

Characterisation and Decontamination of Concrete and Plastic Infrastructure from the Hunterston A Spent Nuclear Fuel Storage Pond

A thesis submitted to The University of Manchester for the degree of
Doctor of Philosophy
in the Faculty of Science and Engineering

2023

Anna E. Denman

School of Natural Sciences
Department of Earth and Environmental Sciences

Contents

List of Figures	7
List of Tables	11
List of Equations	12
Abbreviations	13
Thesis Abstract.....	16
Declaration.....	18
Copyright Statement	19
Acknowledgements.....	20
About the Author	22
1. Introduction	23
1.1. Background of the nuclear industry	23
1.1.1. The nuclear fuel cycle	23
1.1.2. Spent nuclear fuel	25
1.1.3. Reprocessing	26
1.1.4. Nuclear waste.....	26
1.1.5. Magnox reactors.....	27
1.1.6. Contamination and characterisation.....	29
1.2. References	31
2. Literature Review	36
2.1. Hunterston A SNF pond.....	36
2.2. Radioactive contamination.....	36
2.2.1. Solid-liquid interface	36
2.2.2. Adsorption.....	38
2.3. Radionuclides of concern	39
2.3.1. Strontium.....	39
2.3.2. Cesium	39

2.3.3.	Cobalt.....	41
2.4.	Nuclear materials of interest	42
2.4.1.	Concrete	42
2.4.2.	Plastic.....	45
2.4.3.	Stainless steel	48
2.5.	Characterisation of contaminated materials	50
2.5.1.	Laser-induced breakdown spectroscopy	51
2.6.	Decontamination	57
2.7.	Research rationale, aims and hypotheses	58
2.8.	Thesis structure	60
2.9.	References	62
3.	Research methods	79
3.1.	Experimental methods.....	79
3.1.1.	Reagents.....	79
3.1.2.	Hunterston A legacy materials.....	79
3.1.3.	Materials	81
3.1.4.	Sorption experiments	82
3.1.5.	Radioactive sample preparation.....	84
3.1.6.	Decontamination experiments	84
3.2.	Aqueous analytical methods.....	86
3.2.1.	pH analysis.....	86
3.2.2.	Inductively coupled plasma atomic emission spectrometry (ICP-AES) and mass spectrometry (ICP-MS)	86
3.3.	Solid analytical methods	87
3.3.1.	Scanning electron microscopy (SEM) and electron diffraction X-ray spectroscopy (EDX/EDS).....	87
3.3.2.	Quantitative evaluation of materials by scanning electron microscopy (QEMSCAN).....	90

3.3.3.	Laser-induced breakdown spectroscopy (LIBS).....	90
3.3.4.	Powder X-ray diffraction (XRD).....	92
3.3.5.	X-ray computed tomography (XCT)	93
3.3.6.	Sequential extraction.....	94
3.4.	Active analytical methods	95
3.4.1.	Liquid scintillation counting (LSC).....	95
3.4.2.	Gamma spectroscopy	96
3.4.3.	Autoradiography	98
3.5.	References	99
4.	Development of Laser-Induced Breakdown Spectroscopy for Analysis of Radioactively Contaminated Materials	103
4.1.	Abstract	104
4.2.	Introduction	104
4.3.	Experimental	106
4.3.1.	Samples	106
4.3.2.	Calibration standards	107
4.3.3.	Sorption experiments	108
4.3.4.	Laser-induced breakdown spectroscopy	109
4.3.5.	Scanning electron microscopy (SEM) energy dispersive X-ray spectroscopy (EDX)	110
4.4.	Results and discussion.....	110
4.4.1.	Calibration curves and limits of detection	110
4.4.2.	Single element sorption on concrete and HDPE coupons	111
4.4.3.	Contamination chamber sorption analysis	113
4.4.4.	Model waste discharge pipeline samples	118
4.4.5.	Depth-profiling using LIBS	119
4.5.	Conclusions	124
4.6.	References	126

4.7. Supplementary information.....	134
5. Characterisation and Decontamination of HDPE pontoons used in Spent Fuel Pond	
Decommissioning	146
5.1. Abstract	147
5.2. Introduction	147
5.3. Materials and methods	149
5.3.1. Hunterston A pontoons	149
5.3.2. Gamma spectroscopy	150
5.3.3. Autoradiography	150
5.3.4. Laser-induced breakdown spectroscopy (LIBS).....	150
5.3.5. Raman spectroscopy	151
5.3.6. Sorption experiments with HDPE coupons	151
5.3.7. Hydrogel decontamination experiments	152
5.3.8. Liquid scintillation counting (LSC).....	153
5.4. Results and discussion.....	153
5.4.1. Characterisation of the pontoons	153
5.4.2. Surface decontamination of HDPE coupons.....	159
5.4.3. Decontamination of the Hunterston A pontoons	160
5.5. Conclusions	163
5.6. References	165
5.7. Supporting information	172
6. Radionuclide Associations in a Concrete Core Extracted from the Decommissioned	
Hunterston A Spent Nuclear Fuel Pond.....	179
6.1. Abstract	180
6.2. Introduction	180
6.2.1. Hunterston A concrete core	182
6.3. Experimental	182
6.3.1. Materials and sample preparation	182

6.3.2.	Gamma spectroscopy	183
6.3.3.	Autoradiography	183
6.3.4.	Scanning electron microscopy energy dispersive spectroscopy (SEM-EDX).	184
6.3.5.	Powder X-ray diffraction (XRD).....	184
6.3.6.	X-ray computed tomography (XCT)	184
6.3.7.	Sequential extraction.....	184
6.3.8.	Hydrogel decontamination experiments	186
6.4.	Results and discussion.....	187
6.4.1.	Concrete core surface characterisation	187
6.4.2.	Concrete core bulk characterisation.....	188
6.4.3.	Decontamination of the concrete core	195
6.5.	Conclusions	199
6.6.	References	200
6.7.	Supporting information	206
7.	Conclusions and Future Work	214
7.1.	Conclusions	214
7.2.	Future Work	217
7.3.	References	219
8.	Conference presentations, posters and awards	222

List of Figures

Figure 1.1. Schematic of the Nuclear Fuel Cycle consisting of the front-end (green) and back-end (orange) operations (adapted from World Nuclear Association). ⁵	23
Figure 1.2. Fission of U-235 and subsequent beta decay of fission products to form stable cerium and zirconium (adapted from Hyperphysics). ¹⁰	24
Figure 1.3. Simplified PUREX process (adapted from Gill et al. in Nuclear Fission). ¹⁷	26
Figure 1.4. UK radioactive waste inventory (adapted from the NDA inventory 2022). ²⁰	27
Figure 1.5. Hunterston A SNF storage pond (Bertoncini et al., 2013). ²⁸	28
Figure 2.1. Structure of the metal surface in solution at a) neutral pH, b) in alkaline conditions, and c) in acidic conditions (adapted from Hazarika et al.). ⁸	37
Figure 2.2. Schematic of the electric double layer formed at the metal oxide-solution interface. The metal oxide/O plane is defined by the location of surface sites which may be protonated or deprotonated. The inner Helmholtz layer is defined by the centre of specifically adsorbed cations and anions, the outer Helmholtz layer corresponds to the beginning of the diffuse layer of counterions (adapted from Bénard et al. and Brown et al.). ^{10,11}	38
Figure 2.3. Polymerisation of ethene to form polyethylene.	45
Figure 2.4. Example of abiotic degradation of polyethylene chain (adapted from Gewert et al.). ⁶³	45
Figure 2.5. Polymer degradation via a) cross-linking and b) chain scission (adapted from Gewert et al.). ⁶³	46
Figure 2.6. Passive layer formed on stainless steel (adapted from Zahner et al.). ⁹⁷	49
Figure 2.7. Flow diagram of the decontamination process (adapted from the Committee on Decontamination and Decommissioning of Uranium Enrichment Facilities). ¹¹⁵	50
Figure 2.8. Schematic of the LIBS ablation process.	52
Figure 2.9. Laser-induced breakdown spectroscopy apparatus for a) close-up lab analysis and b) remote, standoff measurements (Chinni et al.). ¹³⁰	52
Figure 2.10. LIBS spectra of a titanium sample obtained after a delay time of a) 0-0.5 μ s, b) 0.5-5 μ s, and c) 10-110 μ s (Cremers et al.). ¹³²	53
Figure 3.1. Schematic of the Hunterston A SNF pond.	79
Figure 3.2. Concrete core removed from the Hunterston A SNF pond.	80
Figure 3.3. a) HDPE pontoons used to aid decommissioning of the Hunterston A SNF storage pond (Magnox Ltd, flickr). ¹ b) Close up of a disc removed from the top of the pontoon.	81

Figure 3.4. a) Modified Robbins device used for continuous flow systems (A. McBain et al.). ⁵ b) Design for the contamination chamber device.	83
Figure 3.5. Components of a SEM instrument (M. Kannan). ¹⁵	88
Figure 3.6. Different interactions and phenomenon that occur during SEM analysis (adapted from M. Kannan). ¹⁵	89
Figure 3.7. Schematic of a basic LIBS system (adapted from Cremers and Hull). ^{21,22}	91
Figure 3.8. Schematic of LIBS setup for active analysis (adapted from Hull). ²²	92
Figure 3.9. Schematic of an incident X-ray interacting with a sample to satisfy Bragg's Law (adapted from Housecroft et al.). ²³	93
Figure 3.10. Schematic of the steps involved in LSC analysis (adapted from M. L'Annunziata et al.). ³⁰	95
Figure 3.11. Schematic of a High Purity Germanium (HPGe) Gamma Detector (adapted from National Physical Laboratory). ³¹	96
Figure 3.12. Schematic of the features observed in gamma ray spectra (Buchtela et al.). ³² ..	97
Figure 3.13. Schematic of the autoradiography process.	99
Figure 4.1. LIBS emission spectra for individual a) Sr, b) Cs and c) Co 500 mg/L sorption tests on HDPE and concrete coupons. Normalisation was conducted against known matrix peaks, in this instance the analyte peak intensity was greater than the matrix peak resulting in normalisation values greater than 1.	112
Figure 4.2. Normalised LIBS emission spectra for Sr sorption on a) concrete, b) HDPE and c) stainless steel coupons. Normalisation was conducted against known matrix peaks, in this instance the analyte peak intensity was greater than the matrix peak resulting in normalisation values greater than 1.	115
Figure 4.3. Normalised LIBS emission spectra for the sorption of cobalt on a) concrete, b) HDPE and c) stainless steel coupons.	116
Figure 4.4. Normalised LIBS emission spectra for the sorption of Cs on a) concrete, b) HDPE and c) stainless steel coupons.	117
Figure 4.5. Normalised LIBS emission spectra for a) Co, b) Ru, c) Sr and Eu and d) Cs at their characteristic emission peaks. Normalisation was conducted against known matrix peaks, in this instance the analyte peak intensity was greater than the matrix peak resulting in normalisation values greater than 1.	118
Figure 4.6. Normalised depth-profile LIBS emission spectra for Sr sorption on a) concrete, b) HDPE and c) stainless steel coupons. Normalisation was conducted against known matrix	

peaks, in this instance the analyte peak intensity was greater than the matrix peak resulting in normalisation values greater than 1.....	121
Figure 4.7. Normalised pseudo depth-profiles (where increasing shot numbers represent increasing depth) for a) Sr, b) Cs and c) Co on the concrete coupons over 12 consecutive LIBS ablation shots. Normalisation was conducted against known matrix peaks, in this instance the analyte peak intensity was greater than the matrix peak resulting in normalisation values greater than 1.....	123
Figure 4.8. Normalised pseudo depth-profile LIBS emission spectra for Sr on a) non-biofilm and b) biofilm samples, and Eu on c) non-biofilm and d) biofilm samples.	124
Figure 5.1. Disc images (above) and corresponding false-colour, contrast-adjusted autoradiography images (below) of each pontoon sample. Discs were removed from the top (left), middle (middle) and bottom (right) panels of the pontoons.....	155
Figure 5.2. a) Images of top disc, T2, covered in scratches and rust particulates. b) close up of the particulates present on the disc surface.....	156
Figure 5.3. LIBS emission spectra of the precipitate formed on the bottom disc, B1, at wavelength ranges of a) 292-296 nm, b) 307-310 nm, c) 398-406 nm and d) 400-425 nm highlighting the presence of metal oxides and Sr contamination on the pontoon surfaces...	157
Figure 5.4. False-colour, contrast-adjusted autoradiography images of the bottom disc, B1, cross-section. The largest section a) shows potential ingress of activity into the disc, whereas the smaller sections b and c) show activity is isolated to the pontoon surface.	158
Figure 5.5. False-colour, contrast-adjusted autoradiography images showing the decontamination of bottom disc, B2, after b) 1, c) 24, d) 168 and e) 672 hours.	161
Figure 5.6. False-colour, contrast-adjusted autoradiography images of a section of the a) bottom disc, B1, before and after sequential decontamination experiments and b) the corresponding hydrogel autoradiography images.....	162
Figure 5.7. False-colour, contrast-adjusted autoradiography images of the middle disc, M2, (a) after consecutive decontamination with a 12 cm hydrogel (b)	163
Figure 6.1. False-colour, contrast-adjusted autoradiography images of a) the active top face of the concrete core, highlighting areas of increased activity distributed heterogeneously on the surfaces (b and c). The active hot-spot (d) was cut through for depth analysis with autoradiography and gamma spectroscopy.....	188
Figure 6.2. SEM image (a) and EDX maps of a section of the concrete core indicating the presence of b) CSH/CASH phases, c) mica and feldspathoidal minerals, d) quartz as well as e) TiO ₂ minerals.	189

Figure 6.3. SEM images obtained via a) backscattered electron (BSE) analysis and b) quantitative evaluation of materials by scanning electron microscopy (QEMSCAN) of a section of typical concrete.....	190
Figure 6.4. Contrast adjusted autoradiography images of a) the core cross-section after cutting through the active spot in figure 6.1d, indicating radionuclides had penetrated through the protective layers into the bulk concrete, b) aided by cracks and boundaries between the cement and aggregate phases.	191
Figure 6.5. Cs-137 activity penetration profile for a section of the concrete core (log scale). The gamma spectrometer was not calibrated for the shape and geometry of these samples, therefore activities presented serve as an estimate to allow for comparison and assessment of general trend. Error bars are uncertainties from gamma spectroscopy (3σ).....	192
Figure 6.6. a) Percentage distribution of Cs-137 between the different phases targeted with the sequential extraction reactions of the concrete core samples at a depth of 3 mm. Solid activity was calculated based on the difference between the initial activity of the sample and the total activity leached out with each sequential extraction step. b) Percentage distribution of elements in the concrete core samples obtained using ICP-MS from the different phases targeted with the sequential extraction reactions. Error bars are uncertainties from gamma spectroscopy (3σ) for Cs-137 and estimated standard deviation from repeats for ICP-MS.	193
Figure 6.7. a) Image of the active section before removal of the protective layers for internal analysis (red dotted line indicates cutting path). Images (top) and contrast-adjusted autoradiography images (bottom) of b) the underside of the paint layer and c) the concrete directly beneath the protective layers. Activity is heterogeneously distributed throughout the concrete, congregating around the boundaries between cement and aggregate minerals (d - black), as well as in certain mineral phases (e - red).....	195
Figure 6.8. Contrast-adjusted, false-colour autoradiography images showing the progressive decontamination of a) the painted surface with consecutive hydrogel applications after b) 1, c) 24 and d) 168 hours of contact in areas “paint 1” and “paint 2”.....	197
Figure 6.9. The cumulative activity taken up of for a) Cs-137 and b) Sr-90 into the hydrogels after consecutive decontamination experiments on the painted (black and red) and concrete (blue) surface. Error bars are uncertainties from gamma spectroscopy (3σ).....	198

List of Tables

Table 1.1. Yearly amount of radioactivity released into pond water from 300 tons of SNF handled in a year (adapted from Severa et al.). ³⁹	30
Table 2.1. Composition of typical austenitic stainless steels used in the nuclear industry (adapted from Was et al.). ⁹⁵	48
Table 3.1. Composition of 304L stainless steel (adapted from Was et al.). ⁴	82
Table 3.2. Radionuclide inventory of mixed gamma standard (adapted from IsoTrak Catalogue). ⁶	84
Table 4.1. Measured uptake (q_t) of Sr, Cs and Co on concrete and HDPE surfaces through solution ICP-MS and surface LIBS analysis.....	113
Table 4.2. Measured uptake (q_t) of analytes onto the concrete and HDPE coupon surfaces in the contamination chamber using LIBS, averaged over 4 coupons.....	114
Table 5.1. Gamma survey of the Hunterston A SNF pond pontoon samples.....	154
Table 5.2. Hydrogel decontamination data for the pontoon discs after individual (B2) and consecutive (B1 and M2) applications. DF = decontamination factor, %R = % activity removed.....	160
Table 6.1. Chemical lixiviants and extraction times used in the sequential extraction of the cement phase.	185
Table 6.2. Radioisotopic inventory of the Hunterston A concrete core received from Magnox Ltd.	187
Table 6.3. Hydrogel decontamination data for the painted surface after consecutive applications. DF = decontamination factor, %R = % activity removed.	196

List of Equations

Equation 1.1. Conversion of fertile U-238 to fissile Pu-239 (adapted from Ramanujam et al.). ¹²	25
Equation 2.1. a) Physical and b) chemical sorption of cesium(I) on a metal-hydroxide surface (adapted from Rouppert et al.). ²⁰	40
Equation 2.2. Reactions of cement with water (adapted from Lin et al.). ³⁸	43
Equation 2.3. Decomposition of the calcium hydroxide surface of concretes in nitric acid (adapted from Olusola et al.). ⁴²	43
Equation 2.4. Strontium(II) ion exchange in calcium silicate hydrates (adapted from Tits et al.). ⁴⁹	44
Equation 3.1. The decontamination factor (DF).	85
Equation 3.2. Conversion of DF to the percentage of activity removed (%R).	86
Equation 3.3. Measured uptake (q_t) from solution.	87
Equation 3.4. Bragg's Law	92

Abbreviations

AAS	Atomic Absorption Spectroscopy
AGR	Advanced Gas Cooled Reactor
AISI	American Iron and Steel Institute
AWE	Atomic Weapons Establishment
BSE	Back Scattered Electrons
C(A)SH	Calcium (Aluminium) Silicate Hydrate
DECC	Department for Energy and Climate Change
DF	Decontamination Factor
DI	Deionised
EDL	Electric Double Layer
EDS/EDX	Energy-Dispersive X-ray Spectroscopy
EPSRC	Engineering and Physical Sciences Research Council
(ATR)-FTIR	(Attenuated Total Reflection) Fourier-Transform Infrared Spectroscopy
GDF	Geological Disposal Facility
GD-OES	Glow-Discharge Optical Emission Spectroscopy
HH-LIBS	Handheld Laser-Induced Breakdown Spectroscopy
H/I/(V)LLW	High/Intermediate/(Very) Low Level Waste
HPGe	High-performance Germanium
ICP-AES/MS/OES	Inductively Coupled Plasma Atomic Emission Spectroscopy/ Mass Spectrometry/ Optical Emission Spectroscopy

IPA	Isopropyl Alcohol
(N)IR	(Near) Infrared
LA-ICP-MS	Laser Ablation Inductively Coupled Plasma Mass Spectrometry
LIBS	Laser-Induced Breakdown Spectroscopy
LIF	Laser-Induced Fluorescence
LOD	Limit of Detection
LSC	Liquid Scintillation Counting
MAGNOX	Magnesium Oxide
MOX	Mixed Oxide Fuel
MRD	Modified Robbins Device
NDA	Nuclear Decommissioning Authority
Nd:YAG	Neodymium-doped Yttrium Aluminium Garnet
NFC	Nuclear Fuel Cycle
NGN CDT	Next Generation Nuclear Centre for Doctoral Training
NNL	National Nuclear Laboratory
NNUF RADER	National Nuclear User Facility RADioactive waste management and Environmental Remediation
NFC	Nuclear Fuel Cycle
OPC	Ordinary Portland Cement
(LD/HD)PE	(Low-Density/High-Density) Polyethylene
PET	Polyethylene terephthalate
PEGDA	Polyethylene glycol diacrylate

POCO	Post Operational Clean Out
ppm/ppb/ppt	parts per million/billion/trillion
PUREX	Plutonium Uranium Reduction EXtraction
PVP	Polyvinylpyrrolidone
PWR	Pressurised Water Reactor
QEMSCAN	Quantitative Evaluation of Materials by Scanning Electron Microscopy
SE	Secondary Electrons
(E)SEM	(Environmental) Scanning Electron Microscopy
SMR	Small Modular Reactors
SNF	Spent Nuclear Fuel
TDCR	Triple to double coincidence ratio
THORP	Thermal Oxide Reprocessing Plant
TXRF	Total Reflection X-ray Fluorescence
UV	Ultraviolet
XAS	X-ray Absorption Spectroscopy
XCT	X-ray Computed Tomography
XPS	X-ray Photoelectron Spectroscopy
XRD	X-ray Diffraction
XRF	X-ray Fluorescence

Thesis Abstract

Nuclear power plants can become heavily contaminated with radionuclides during their operational lifetime. These contaminated materials give rise to high doses of radiation and heat, increasing risk to workers and the surrounding environment. Rapid, *in-situ* characterisation is vital to determine the extent of radionuclide contamination and develop appropriate decontamination methods to help reduce the volume of intermediate level waste (ILW) produced during decommissioning and minimise the costs of post operational clean out (POCO) procedures. Complex environments such as spent nuclear fuel (SNF) storage ponds require extensive research into the physical and chemical composition of the pond structure. The long-term storage of spent Magnox fuel in wet storage ponds has resulted in the leakage of SNF and contamination of the surrounding infrastructure creating a huge, complex decommissioning challenge. Of particular concern are the fission products, Sr-90 and Cs-137, and corrosion product, Co-60, due to their abundance and mobility. This project focuses on the interactions of these radionuclides with concrete and plastic materials relevant to the nuclear industry at conditions representative of the alkaline SNF ponds.

In this project, sorption experiments simulating the alkaline conditions of SNF storage pond were conducted. Surface and solution measurements were used to determine the uptake of stable Sr, Cs and Co onto concrete and HDPE coupons representative of the radionuclides and materials found in the pond environments. Laser-induced breakdown spectroscopy (LIBS) was used to analyse the coupons to assess its ability for use as a rapid, *in-situ* characterisation tool in the nuclear industry. Characteristic Sr, Cs and Co emission lines were resolved from the concrete and HDPE matrices with LIBS. Limits of detection (LOD) for each contaminant were determined for each matrix and all contaminants were identified $> 0.01 \text{ mg/cm}^2$ under alkaline conditions at a working distance of 8 cm. In addition, LIBS was used to analyse model waste discharge pipeline samples coated with biofilm. LIBS was able to resolve characteristic Sr, Cs, Co, Ru and Eu emission lines from the coupons with and without a biofilm present and identified variations in emission intensities depending on the presence of the biofilm.

To build on model sorption experiments, authentic samples were obtained from the Hunterston A SNF storage pond. A concrete core was obtained from the middle of the pond wall and plastic discs were obtained from temporary pontoons used during decommissioning operations. Radiometric, chemical and microscopy techniques were used to characterise the distribution of radionuclide contamination on the sample surfaces and in the bulk. Sr-90, Cs-137, Am-241 and

Pu-238-241 were identified as the predominant radionuclide contaminants. Autoradiography of the plastic disc surfaces showed the distribution of radioactivity was associated with areas of increased damage and the presence of metal oxide precipitates, characterised with Raman and LIBS. Autoradiography of the concrete core determined contamination was heterogeneously distributed across the surface. Analysis of the core cross-section determined radionuclide contamination was predominantly isolated within the protective layers on the core surface, but some activity had penetrated 5-10 mm into the bulk concrete. Sequential extraction showed Cs-137 was strongly bound to silicates and aggregate phases in the concrete bulk and could not be leached under natural conditions. Sr was found to be predominantly isolated within the cement, likely in calcium silicate hydrate phases.

Finally, polymer based hydrogels were found to simultaneously remove fission product and actinide contamination from the plastic discs and painted surface of the concrete core. Increasing the contact time and repeat applications resulted in increased removal of activity for all material surfaces. Hydrogels were able to take up 200 Bq Cs-137 and 88 Bq Sr-90 after 1 hour of contact with the plastic disc surfaces, and 34 Bq Cs-137 and 250 Bq Sr-90 from the painted surface, indicating hydrogels can be used for the localised decontamination of complex radionuclide contaminated plastic and painted surfaces.

Declaration

No portion of the work referred to in this thesis has been submitted in support of an application for another degree or qualification of this or any other university or other institute of learning.

Copyright Statement

1. The author of this thesis (including any appendices and/or schedules to this thesis) owns certain copyright or related rights in it (the “Copyright”) and s/he has given the University of Manchester certain rights to use such Copyright, including for administrative purposes.
2. Copies of this thesis, either in full or in extracts and whether in hard or electronic copy, may be made only in accordance with the Copyright, Designs and Patents Act 1988 (as amended) and regulations issued under it or, where appropriate, in accordance with licensing agreements which the University has from time to time. This page must form part of any such copies made.
3. The ownership of certain Copyright, patents, designs, trademarks and other intellectual property (the “Intellectual Property”) and any reproductions of copyright works in the thesis, for example graphs and tables (“Reproductions”), which may be described in this thesis, may not be owned by the author and may be owned by third parties. Such Intellectual Property and Reproductions cannot and must not be made available for use without the prior written permission of the owner(s) of the relevant Intellectual Property and/or Reproductions.
4. Further information on the conditions under which disclosure, publication and commercialisation of this thesis, the Copyright and any Intellectual Property and/or Reproductions described in it may take place is available in the University IP Policy (see <http://documents.manchester.ac.uk/DocuInfo.aspx?DocID=24420>), in any relevant Thesis restriction declarations deposited in the University Library, the University Library’s regulations (see <http://www.library.manchester.ac.uk/about/regulations/>) and in the University’s policy on Presentation of Theses.

Acknowledgements

I would like to start by thanking the Next Generation Nuclear Centre for Doctoral Training, Engineering and Physical Sciences Research Council and National Nuclear Laboratory for funding this PhD project.

I want to acknowledge my supervisors for the chance to embark on this adventure and their constant support throughout. Scott, thank you for joining me on this journey. Your weekly meetings and constant reassurance have really helped to keep me going. Thank you for all your support and invaluable advice (and cups of tea) over the years. Gareth, thank you for seeing something in me and bringing me onto this project. Thank you for your guidance and wisdom during my trips, and the opportunity to work with your amazing radiochemistry department. Katie, Maikki, Markus, Joyce, Alessia, Anisa and, of course, Gianni; thank you all so much for welcoming me in with open arms and being great friends and colleagues. I also want to extend my gratitude to my industrial supervisors, Nick Smith and Tom Carey, thank you for your constant interest and enthusiasm in my monthly updates. This has been some of the most interesting work I've ever done and has (excuse the pun) cemented my passion for nuclear research. Francis, thank you for sharing your wealth of knowledge every time I came to you for advice, especially with your "love" for extractions!

A huge thank you to all the technical staff: Abby Ragazzon-Smith, Rosie Byrne, Lewis Hughes, John Waters, Ashley Wooles and Paul Coffey thank you for your advice and help over the years. I also want to give a big thank you to Tony Stockdale for always being there to answer my silly questions and help me with all things rad. Look after the autorad for me!

Thank you to the NGN lot. Starting this journey with a cohort of fellow excited postgrads really helped me settle into the PhD and build some great friendships. Milk and Honey will always have a special place in my heart for lunchtime catch ups and a safe place to share the slightly more stressful times we've had over the years! Mark and Kadija, your hard work and dedication have kept us all going and it's been a delight to get to know you both over the years. On that note, thank you to the Dalton Nuclear Institute and the Champions. Going on outreach events and organising nuclear events has been a highlight of my PhD experience and I'm so glad I got to be a part of this. Particularly, thank you to Rachel for being a fantastic outreach coordinator and Aneeqa for your constant positivity and passion for science.

Onto the wonderful Geomicro group, old and new! Thank you for taking me in when I didn't really have a group or department to call home. You have been the most wonderful, intelligent, kind group of people. Thank you to Kath, Sam and Jon who have provided their advice and support over the years. Now a special shoutout must go to the ACS crew: Franky, Natalie, Olwen, Chris, Dean, Callum and James. Thank you for making this a trip of a lifetime and as our dear friend Jeff would say, "it's been my utmost pleasure" to grow closer and go on this journey with you all!

I can't go without thanking my wonderful friends. I'll start with two of the most truly incredible people I've ever gotten to know. Kate and Laura, thank you for being there for me since we first lived together as freshers in Owens Park. I would not be where I am today without your constant love, support and kind (and sometimes firm) life-advice. You have honestly seen me through some of my highest and lowest moments and I can't begin to thank you enough. I can't wait to cry my eyes out at your weddings!

Franky, Paige, Amy and Daniel. We started this Chemistry journey together so long ago and getting to grow with you all over the years has been a joy. Franky, I have to give you a little personal thank you. You have been one of my dearest friends and I'm so glad to have had you with me through this all. I can't wait to visit you in Copenhagen! Finally, my lovely korf lot: Hannah, Vick and Alys. Thank you for countless dinners, coffee walks and the "occasional" bottle of wine over the years.

Ed, where do I even begin. Thank you for everything you have done for me over the past 8 years. You have been my number one fan and even when you don't quite know what to say you have stood by me and helped in more ways than you will know. Thank you for being by my side and particularly when I've been stuck (more times than I'd like to admit) in the "pit of despair". Your sense of humour and ability to always find the positives in things has kept me grounded. I know it's not been an easy time for us both and I can't thank you enough for seeing this through to the end with me.

Finally, to my family: Mom, Dad and Maddie. I would not know what to do without your never ending supply of encouraging phone calls, dog photos and warm hugs. Thank you for your constant interest in my work and reading through countless drafts to help along the way. You never doubted me and reassured me with all the right words when I did. I love you all so much.

About the Author

The author graduated from the University of Manchester with a First Class Master's in Chemistry in 2018. During her third year of university, she was successful in her application to the Royal Society Industry Fellowship summer placement with the National Nuclear Laboratory. This placement built on her curiosity and interest for nuclear research. The author continued her journey in academia by starting this PhD project in September 2018 in the Department of Earth and Environmental Sciences at the University of Manchester.

1. Introduction

1.1. Background of the nuclear industry

1.1.1. The nuclear fuel cycle

In 1956, the world's first nuclear power station was attached to the UK's National Grid and has since led to the building of 18 additional power stations over a period of 39 years.¹ At present, the UK is home to just 9 nuclear reactors still in operation, providing around 15% of the country's electricity.² These consist of two reactor types: the Advanced Gas-Cooled Reactor (AGR) and the Pressurised Water Reactor (PWR), with the last of the Magnox reactors shut down in 2015. Whilst the current fleet of reactors are all set for decommissioning by 2028, several new reactors are in the process of being constructed and the development of new small modular reactors (SMR) are being discussed to help provide low carbon energy in the UK by 2030.^{3,4}

The nuclear fuel cycle (NFC) covers the lifecycle of uranium from ore to waste and is split into two sections (Figure 1.1). The front-end of the fuel cycle covers the mining and manufacture of the uranium fuel, whereas the back-end consists of the treatment of the used fuel, such as waste management and reprocessing.

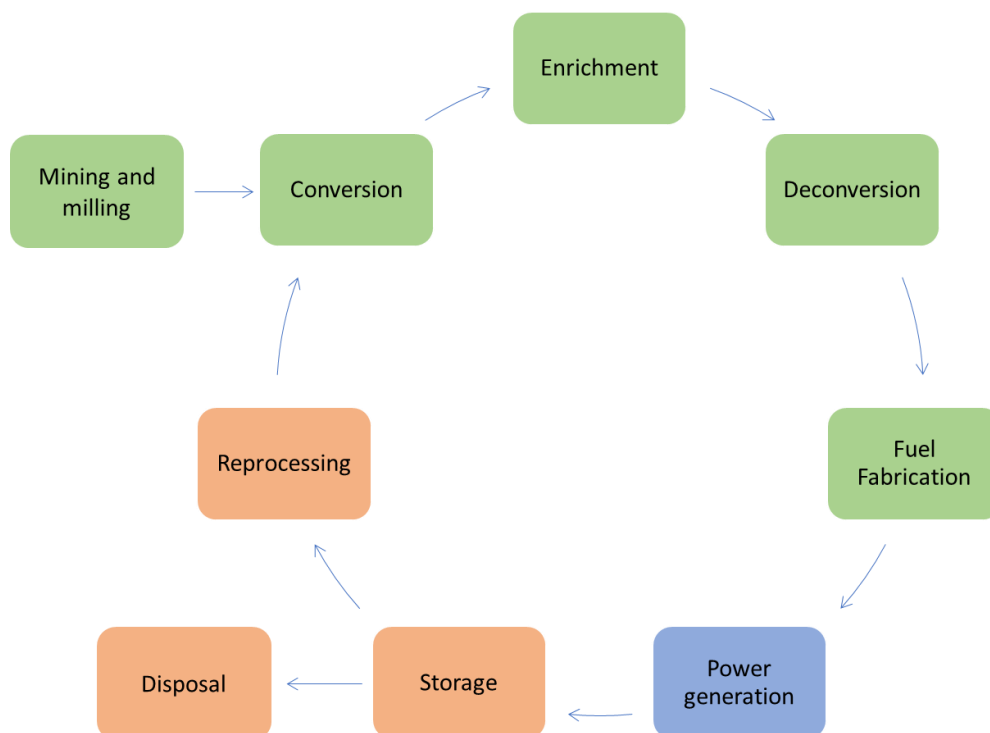


Figure 1.1. Schematic of the Nuclear Fuel Cycle consisting of the front-end (green) and back-end (orange) operations (adapted from World Nuclear Association).⁵

Uranium is obtained through conventional mining operations, such as opencast and underground mining, or by passing a solution through the ores to extract the useful minerals, known as *in-situ* leaching.⁶ After extraction of the ore, it is broken down into a fine powder and the uranium is isolated from the other minerals to yield U_3O_8 . Natural uranium contains around 0.7% of the fissile uranium isotope, U-235, and must usually be enriched to efficiently produce energy. Uranium fuel used for civil nuclear reactors is enriched to around 2-4%; however, enrichment levels of above 90% can be achieved for use in nuclear weapons and submarine reactor cores.⁷ Finally, uranium is converted to uranium dioxide, UO_2 , powder and compressed into small pellets. These are stacked to form the fuel rods used in the reactor.

Energy is produced through the nuclear fission of uranium. When a moving neutron collides with a uranium atom the neutron is absorbed; this forms an unstable isotope that splits into two smaller nuclei, known as fission products (Figure 1.2). Fission rarely produces two identical fragments. Instead, the fission products fall into two mass fractions: light nuclei (atomic mass (A) = 90-100 amu) and heavy nuclei (A = 135-145 amu).⁸ During the thermal fission of uranium around 2.5 neutrons are produced which can cause further fission reactions in neighbouring uranium atoms.⁹ This starts a chain reaction that produces enough energy to convert water into steam, which is used to turn a turbine to produce electricity.

If a large number of neutrons are produced during the fission process the chain reaction can spin out of control and produce very high temperatures. Control rods and coolants are used in reactors to prevent this from happening. The rods are lowered into the reactor to absorb neutrons to control the number of uranium atoms undergoing fission at one time and the coolant transports heat out of the core.

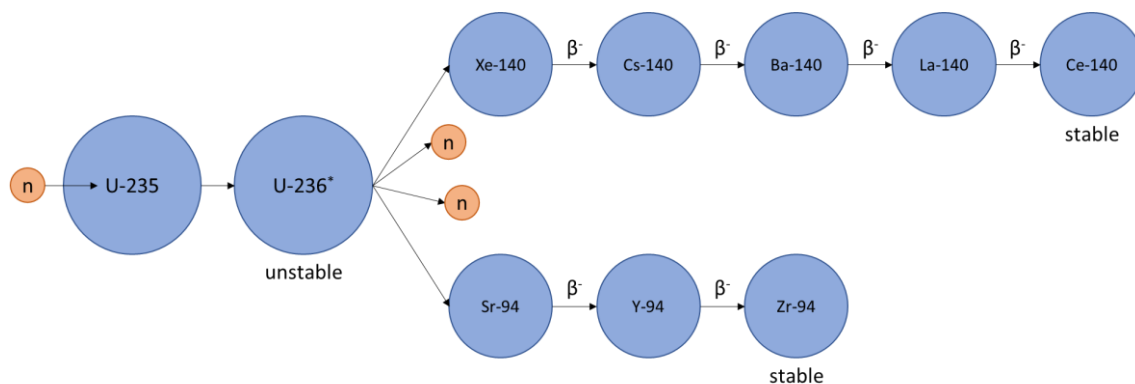


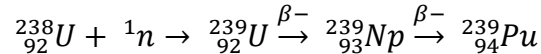
Figure 1.2. Fission of U-235 and subsequent beta decay of fission products to form stable cerium and zirconium (adapted from Hyperphysics).¹⁰

Fission reactions are not isolated to uranium. The Nuclear Regulatory Commission classifies atoms into the following three groups:¹¹

- Fissile – atoms which can undergo fission through capture of a low-energy thermal neutron.
- Fissionable – atoms which can undergo fission through capture of a high-energy or low-energy thermal neutrons.
- Fertile – atoms which are not fissile themselves but can be converted into fissile materials through the absorption of a neutron.

U-238 is the predominant isotope present in uranium fuel. As U-238 is a fertile material it is unable to undergo fission itself and must be converted to fissile Pu-239 through a process called breeding (Equation 1.1). Pu-239 can also undergo fission and allows reactors to continue functioning for longer. Once the majority of U-235 has reacted, the fuel no longer produces energy efficiently and is classified as spent nuclear fuel (SNF).

Equation 1.1. *Conversion of fertile U-238 to fissile Pu-239 (adapted from Ramanujam et al.).¹²*



1.1.2. Spent nuclear fuel

Irradiation of 1 tonne of uranium fuel leads to the formation of around 30-60 kg fission products, with variations dependent on burnup and reactor type.¹³ These fission products can absorb neutrons to form new daughter products which contaminate the nuclear fuel.⁹ Each fission product has a characteristic half-life that can range from a few minutes to thousands of years. Fission products with intermediate half-lives are of greater concern as they can emit high-energy β - and γ -emissions during human lifetime. The majority of activity and heat in SNF is produced by Sr-90 and Cs-137 after an initial decay period and then over the first 1000 years.¹⁴

There are two routes available for the management of SNF. Reprocessing, or closed cycle systems, recover and re-enrich the depleted uranium in SNF to produce new uranium oxide fuel. It can also be mixed with plutonium to form a mixed oxide fuel (MOX), mostly used in reactors around Europe and Japan. Alternatively, an open fuel cycle only uses the fuel once

before it is considered a waste product. The SNF is moved to interim storage before disposal in a long-term facility, such as a geological disposal facility (GDF).

1.1.3. Reprocessing

SNF from Magnox and AGR reactors was reprocessed, where uranium and plutonium are recovered from SNF through the PUREX process (Plutonium Uranium Redox EXtraction, Figure 1.3). The protective cladding is removed to expose the fuel and is dissolved in nitric acid to remove the solid waste and any insoluble fission products. Plutonium and uranium are initially separated from other minor actinides before being separated from each other via redox reactions into the aqueous and solvent phases, respectively.^{15,16} Once separated, U and Pu are individually purified and converted to their oxide form for future use as fuels.

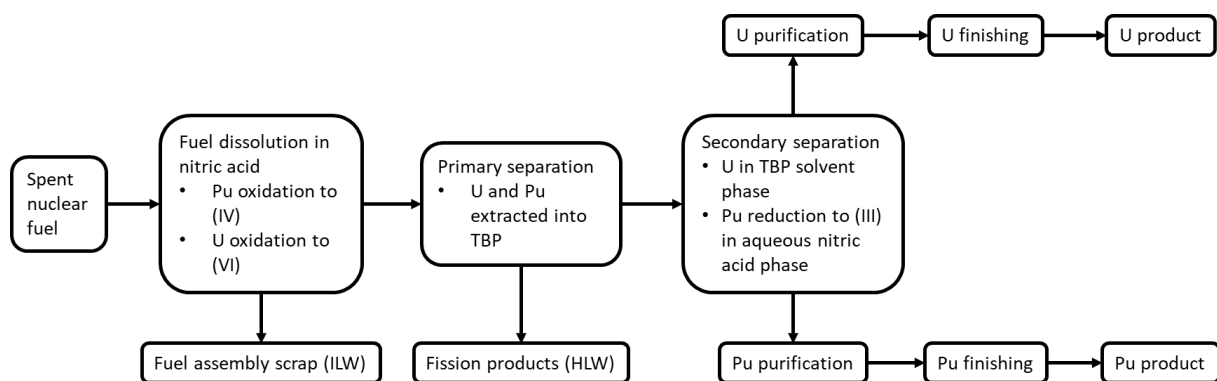


Figure 1.3. Simplified PUREX process (adapted from Gill et al. in *Nuclear Fission*).¹⁷

The UK moved towards a solely open-fuel cycle with the shutdown of the thermal oxide reprocessing plant (THORP) in November 2018 and the final feed of Magnox SNF reprocessed in July 2022.^{18,19} The cost of uranium re-enrichment and/or production of MOX fuels is much higher than the mining of new uranium ore, making a once-through system favourable as it is cheaper to run and reduces proliferation issues as the plutonium remains mixed in the SNF.

1.1.4. Nuclear waste

A drawback of a closed fuel cycle is the volume of radioactive waste produced. The UK is estimated to accumulate a lifetime total of 4,580,000 m³ radioactive waste (according to the NDA 2022 Inventory, Figure 1.4).²⁰ Radioactive waste is categorised into four levels: Very Low Level Waste (VLLW), Low Level Waste (LLW), Intermediate Level Waste (ILW) and High Level Waste (HLW). The majority of nuclear waste is made up of VLLW and LLW, by volume, but the radioactivity levels are minimal: lower than 4 GBq per tonne of alpha activity or 12 GBq per tonne of beta/gamma activity. Whereas, ILW and HLW both exceed the activity

levels of LLW, with HLW being more radioactive and generating sufficient heat to require cooling. Additional treatment and shielding are therefore required to safely manage and dispose of these waste types.

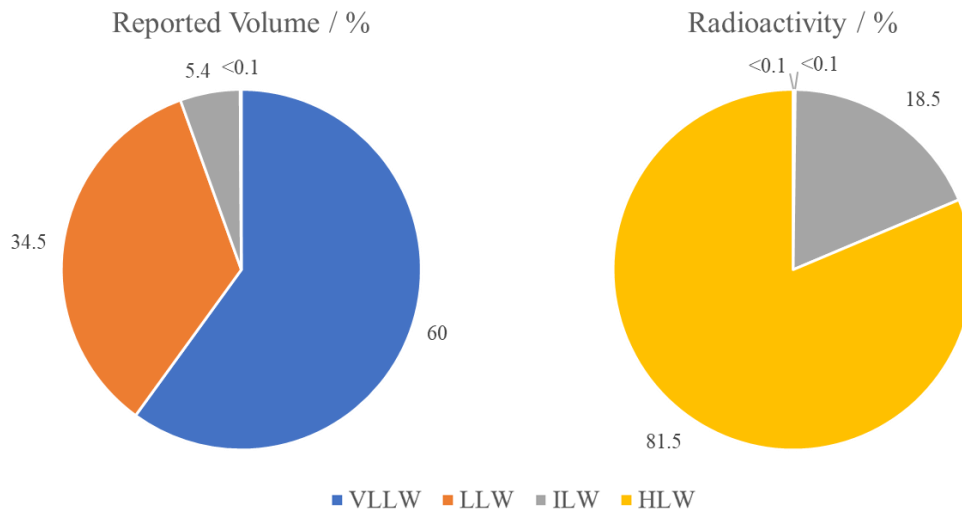


Figure 1.4. UK radioactive waste inventory (adapted from the NDA inventory 2022).²⁰

Near-surface disposal facilities, such as Dounreay, are used to safely dispose of VLLW and LLW as they contain almost negligible amounts of radioactivity.²¹ Decommissioning of reactors and effluent waste treatment predominantly produces ILW. The exact composition of ILW depends on the reactor type and can contain both short and long-lived radionuclides.²² Encapsulation in cement is a common way to manage ILW as it decreases the mobility of radionuclides in the environment. Liquid waste produced during SNF reprocessing is considered HLW and is contained through a process known as vitrification whereby the waste is mixed with molten borosilicate glass to create a compact and durable waste form.²³

1.1.5. Magnox reactors

Magnox reactors were the first commercial nuclear power stations in the UK, with the opening of Calder Hall in 1956. A total of 26 Magnox reactors were built over 11 sites. Since 2015 these have all subsequently been shut down and undergone various stages of defueling and decommissioning.²⁴ Magnox reactors used natural uranium metal as their fuel source, surrounded by magnesium alloy cladding which gave the reactor its name. Magnox reactors use graphite moderators and carbon dioxide gas for cooling. Decommissioning of Magnox reactors is a large financial burden with large volumes of waste produced.

Interim storage is a large aspect of the back-end of the fuel cycle where wastes are temporarily stored in wet or dry facilities until the activity and heat produced has decayed to safer levels before being transported to a final disposal site or reprocessing facility. For Magnox reactors, SNF is stored underwater in cooling ponds to allow radioactivity levels to decrease before reprocessing (Figure 1.5). The pond water was maintained below 50 °C to counter the heat released during the decay of fission products and the waste containers were kept 8 m below the surface to increase shielding against radiation.^{25,26} These conditions minimised corrosion and release of fission products into the environment; however, over time the protective cladding can start to corrode in these aqueous conditions, exposing the fuel underneath.²⁷

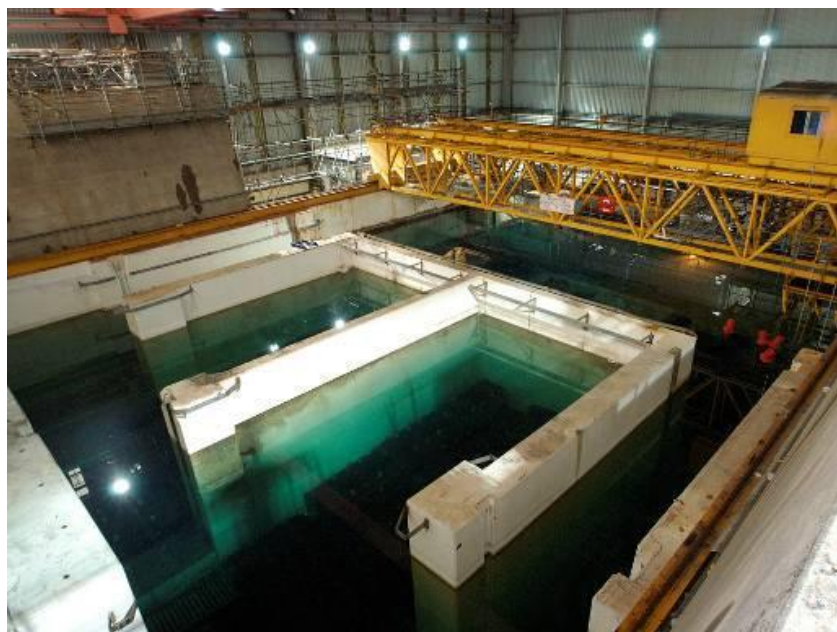


Figure 1.5. Hunterston A SNF storage pond (Bertoncini et al., 2013).²⁸

Hunterston A was a nuclear power station in North Ayrshire, Scotland, and consisted of two Magnox reactors. The reactors differed to previous designs in that re-fuelling was done through the bottom of the reactor, minimising the need for machinery to reload.²⁹ The reactors began producing electricity in 1964 and were decommissioned in 1990. Hunterston A was home to the largest cooling pond for interim storage of Magnox SNF. Due to delays in reprocessing, SNF remained in wet storage for extended periods of time, resulting in the corrosion of the Magnox cladding and uranium fuel and subsequent release of radionuclides into the pond water. To minimise these corrosion effects, sodium hydroxide (NaOH) was added to the storage ponds to maintain alkaline conditions, ~pH 11.³⁰ However, for the Hunterston A pond, this resulted in the corrosion of the aluminium skips and additional dosing was required using silica

(SiO₂) to limit any further corrosion. The combination of corrosion products and chemical dosing resulted in the formation of a complex, radioactive sludge deposit on the bottom of the pond floor.³¹ Due to the complex environment in fuel ponds, *in-situ* characterisation is not always possible and the exact composition of the corrosion material and effluent waste can be difficult to determine. This makes decontamination of fuel ponds particularly difficult. Characterisation of the internal components and chemical and physical properties of the pond is required to determine the most efficient and cost-effective decommissioning operations required.³²

1.1.6. Contamination and characterisation

Contamination of nuclear materials occurs throughout each stage of the fuel cycle and can cause additional challenges during decommissioning. Build-up of radioactive species can lead to increased radiation levels and potential exposure risks for workers.³³ These radioactive species are produced during irradiation of nuclear fuel, in the form of fission products and activation products, or through corrosion of material in contact with fuel or coolant liquids, known as corrosion products.

Stainless steel is used throughout the nuclear industry in the reactor, piping and in the storage of waste materials. Austenitic steels, such as 304L and 316L, are commonly used due to their increased corrosion resistance and ability to withstand high temperature environments.³⁴ Due to its significance in the nuclear industry, the contamination of stainless steel materials has been widely studied.^{35–37}

However, radioactive contamination is not isolated to stainless steel materials. Concrete is a fundamental building material used throughout the nuclear industry and plastics have also been used in areas of lower radioactivity. These materials can also become contaminated through exposure or leaks. Fuel ponds are subject to the formation of corrosion products and the release of radionuclides that can contaminate the surrounding concrete structures (Table 1.1). Temporary plastic structures have been used to help workers reach difficult areas during decommissioning, resulting in the contamination of these materials and additional LLW/ILW products.³⁸

Table 1.1. Yearly amount of radioactivity released into pond water from 300 tons of SNF handled in a year (adapted from Severa et al.).³⁹

Isotope	Radioactivity (Bq)
H-3	4.00E+12
Kr-85	8.00E+13
I-129	8.00E+05
Cs-137	4.00E+08
Pu-239	4.00E+02

One of the main aims of the Nuclear Decommissioning Authority (NDA) is to minimise the total volume of ILW/HLW waste produced during decommissioning operations.⁴⁰ Accurate characterisation of the contaminant species and their relative abundance on materials is vital in determining the extent of possible decontamination, either to allow the material to be disposed as LLW or even recycled, or if the radioactivity present is too high, to be safely contained for disposal as ILW or HLW.

Laser-induced breakdown spectroscopy (LIBS) has been identified as a promising analytical tool for deployment in the nuclear industry due to its ability to conduct rapid, multi-elemental analysis of most material surfaces with only optical access required. Unlike most high-resolution analytical techniques, LIBS does not require any extensive sample preparation and is semi-non-destructive, thereby reducing the volume of secondary waste produced. LIBS can provide both qualitative and semi-quantitative information on surfaces and bulk material via multi-pulse analysis, providing insight into the penetration depth of radionuclide contamination.^{41–43} Further development into remote LIBS devices would allow it to be used for real-time monitoring of contaminated materials without the need for destructive removal of samples.^{44,45} These features make LIBS an appealing technique for the real-time characterisation of contamination to aid decommissioning tasks.

This project focuses on the characterisation and decontamination of concrete and plastic materials contaminated with Sr-90, Cs-137 and Co-60 in conditions representative of those found in alkaline SNF storage ponds. Assessing the use of LIBS for the standoff, *in-situ* analysis of radionuclide contaminated materials in these environments will be conducted throughout.

1.2. References

- 1 T. Roberts and H. Clark, Nuclear electricity in the UK, https://assets.publishing.service.gov.uk/government/uploads/system/uploads/attachment_data/file/789655/Nuclear_electricity_in_the_UK.pdf.
- 2 World Nuclear Association, Nuclear power in the United Kingdom, <https://www.world-nuclear.org/information-library/country-profiles/countries-t-z/united-kingdom.aspx#:~:text=The UK has 15 reactors,reactor designs and their siting>.
- 3 BEIS, *Energy White Paper: Powering our Net Zero Future*, 2020, vol. 44.
- 4 Rolls Royce, Small modular reactors, https://www.rolls-royce.com/innovation/small-modular-reactors.aspx#.
- 5 World Nuclear Association, Nuclear fuel cycle overview, <https://www.world-nuclear.org/information-library/nuclear-fuel-cycle/introduction/nuclear-fuel-cycle-overview.aspx>.
- 6 I. Hore-Lacy, Uranium mining, processing, and enrichment, *Encycl. Energy*, 2004, **6**, 317–328.
- 7 E. S. Craft, A. W. Abu-Qare, M. M. Flaherty, M. C. Garofolo, H. L. Rincavage and M. B. Abou-Donia, Depleted and natural uranium: chemistry and toxicological effects, *J. Toxicol. Environ. Heal. - Part B Crit. Rev.*, 2004, **7**, 297–317.
- 8 E. D. Collins, G. D. Del Cul and B. A. Moyer, in *Advanced Separation Techniques for Nuclear Fuel Reprocessing and Radioactive Waste Treatment*, Woodhead Publishing Limited, 2011, pp. 201–228.
- 9 R. A. Knief, in *Encyclopedia of Physical Science and Technology*, ed. R. Meyers, Academic Press, New York, 3rd edn., 2003, pp. 817–835.
- 10 R. Nave, Fission Fragments, <http://hyperphysics.phy-astr.gsu.edu/hbase/NucEne/fisfrag.html>.
- 11 US NRC, Glossary, <https://www.nrc.gov/reading-rm/basic-ref/glossary.html>.
- 12 A. Ramanujam, An introduction to the PUREX process, *IANCAS Bull.*, 1998, **14**, 11–

- 20.
- 13 G. R. Choppin, C. Ekberg, J. Liljenzin and J. Rydberg, *Radiochemistry and Nuclear Chemistry*, Elsevier, Amsterdam, 4th edn., 2013.
 - 14 MIT, in *The Future of Nuclear Power*, MIT, 2003, pp. 29–35.
 - 15 E. R. Irish and W. H. Reas, *The PUREX Process. A Solvent Extraction Reprocessing Method for Irradiated Uranium*, 1957.
 - 16 M. F. Simpson and J. D. Law, *Nuclear Fuel Reprocessing*, 2010, vol. February.
 - 17 M. Gill, F. Livens and A. Peakman, in *Future Energy: Improved, Sustainable and Clean Options for our Planet*, ed. T. Letcher, Elsevier, 2nd edn., 2014, pp. 181–198.
 - 18 Nuclear Decommissioning Authority, End of reprocessing at THORP signals new era for Sellafield, <https://www.gov.uk/government/news/end-of-reprocessing-at-thorp-signals-new-era-for-sellafield>.
 - 19 Sellafield Ltd and Nuclear Decommissioning Authority, Job done: Sellafield plant safely completes its mission, <https://www.gov.uk/government/news/job-done-sellafield-plant-safely-completes-its-mission>.
 - 20 Jacobs UK Ltd and AFRY Solutions UK Ltd, *2022 UK Radioactive Waste Inventory*, 2022.
 - 21 H. Mildren, Low level radioactive waste storage vaults open, <https://resource.co/article/low-level-radioactive-waste-storage-vaults-open-10148>.
 - 22 P. A. Baisden and G. R. Choppin, in *Radiochemistry and Nuclear Chemistry*, ed. S. Nagy, Encyclopedia of Life Support Systems (EOLSS), 2nd edn., 2209, pp. 228–289.
 - 23 M. T. Harrison, Vittrification of high level waste in the UK, *Procedia Mater. Sci.*, 2014, **7**, 10–15.
 - 24 Nuclear Decommissioning Authority, *Magnox Reactor Dismantling Timing and Sequencing Strategy (Gate 0)*, 2014, vol. 24439283.
 - 25 Office for Nuclear Regulation, *THORP AGR Interim Storage Programme*, 2018, vol.

- 26 Committee on the Safety and Security of Commercial Spent Nuclear Fuel Storage, *Safety and Security of Commercial Spent Nuclear Fuel Storage: Public Report*, National Academies Press, 2006.
- 27 S. A. Parry, L. O'Brien, A. S. Fellerman, C. J. Eaves, N. B. Milestone, N. D. Bryan and F. R. Livens, Plutonium behaviour in nuclear fuel storage pond effluents, *Energy Environ. Sci.*, 2011, **4**, 1457–1464.
- 28 C. Bertoncini, in *Proceedings of the International Conference on Environmental Remediation and Radioactive Waste Management, ICEM*, 2013, pp. 1–11.
- 29 S. E. Jensen and E. Nonbol, *Description of the Magnox Type of Gas Cooled Reactor (MAGNOX)*, 1998, vol. 2.
- 30 M. Jackson, T. Hunter, J. Goode and B. Hanson, in *Waste Management*, 2020, p. 20187.
- 31 C. R. Gregson, D. T. Goddard, M. J. Sarsfield and R. J. Taylor, Combined electron microscopy and vibrational spectroscopy study of corroded Magnox sludge from a legacy spent nuclear fuel storage pond, *J. Nucl. Mater.*, 2011, **412**, 145–156.
- 32 IEAE Nuclear Energy Series, *Decommissioning of Pools in Nuclear Facilities*, 2015, vol. NW-T-2.6.
- 33 S. Adaleye, D. White and J. Taylor, Kinetics of contamination of stainless steel in contact with radioactive solutions at ambient temperatures, *J. Radioa. Nucl. Chem.*, 1995, **189**, 65–70.
- 34 R. Baldev, U. K. Kamachi Mudali, M. Vijayalakshmi, M. D. Mathew, A. K. Bhaduri, P. Chellapandi, S. Venugopal, C. S. Sundar, B. P. C. Rao and B. Venkataraman, Development of stainless steels in nuclear industry: with emphasis on sodium cooled fast spectrum reactors: history, technology and foresight, *Adv. Mater. Res.*, 2013, **794**, 3–25.
- 35 K. Varga, G. Hirschberg, Z. Németh, G. Myburg, J. Schunk and P. Tilky, Accumulation of radioactive corrosion products on steel surfaces of VVER-type nuclear reactors. II. ⁶⁰Co, *J. Nucl. Mater.*, 2001, **298**, 231–238.

- 36 T. Kerry, A. W. Banford, O. R. Thompson, T. Carey, D. Schild, A. Geist and C. A. Sharrad, Transuranic contamination of stainless steel in nitric acid, *J. Nucl. Mater.*, 2017, **493**, 436–441.
- 37 P. Dombóvári, P. Kádár, T. Kovács, J. Somlai, K. Radó, I. Varga, R. Buják, K. Varga, P. Halmos, J. Borszéki, J. Kónya, N. M. Nagy, L. Kövér, D. Varga, I. Cserny, J. Tóth, L. Fodor, A. Horváth, T. Pintér and J. Schunk, Accumulation of uranium on austenitic stainless steel surfaces, *Electrochim. Acta*, 2007, **52**, 2542–2551.
- 38 World Nuclear News, Hunterston A storage pond clearance completed, <https://www.world-nuclear-news.org/Articles/Hunterston-A-storage-pond-clearance-completed>.
- 39 J. Severa and J. Bár, in *Handbook of Radioactive Contamination and Decontamination*, Elsevier, 1991, pp. 1–161.
- 40 Nuclear Decommissioning Authority, Nuclear Decommissioning Authority strategy effective from March 2021, <https://www.gov.uk/government/publications/nuclear-decommissioning-authority-strategy-effective-from-march-2021/nuclear-decommissioning-authority-strategy-effective-from-march-2021#integrated-waste-management>.
- 41 D. Cremers and L. Radziemski, *Handbook of Laser-Induced Breakdown Spectroscopy*, Wiley, 2nd edn., 2013.
- 42 A. Lang, D. Engelberg, N. T. Smith, D. Trivedi, O. Horsfall, A. Banford, P. A. Martin, P. Coffey, W. R. Bower, C. Walther, M. Weiß, H. Bosco, A. Jenkins and G. T. W. Law, Analysis of contaminated nuclear plant steel by laser-induced breakdown spectroscopy, *J. Hazard. Mater.*, 2018, **345**, 114–122.
- 43 M. D. Mowery, R. Sing, J. Kirsch, A. Razaghi, S. Bécharde and R. A. Reed, Rapid at-line analysis of coating thickness and uniformity on tablets using laser-induced breakdown spectroscopy, *J. Pharm. Biomed. Anal.*, 2002, **28**, 935–943.
- 44 I. Gaona, J. Serrano, J. Moros and J. J. Laserna, Evaluation of laser-induced breakdown spectroscopy analysis potential for addressing radiological threats from a distance, *Spectrochim. Acta Part B*, 2014, **96**, 12–20.

- 45 M. Z. Martin, S. Allman, D. J. Brice, R. C. Martin and N. O. Andre, Exploring laser-induced breakdown spectroscopy for nuclear materials analysis and in-situ applications, *Spectrochim. Acta - Part B At. Spectrosc.*, 2012, **74–75**, 177–183.

2. Literature Review

2.1. Hunterston A SNF pond

Magnox SNF from Hunterston A was stored in the interim in wet pond facilities before transport to Sellafield for reprocessing.¹ Reprocessing delays and backlogs meant SNF was stored for longer than intended.² Over time, the aluminium canisters began to corrode allowing pond water to contact SNF. The ponds were dosed with sodium hydroxide (NaOH) and silica (SiO₂) to minimise further corrosion of the facilities forming a highly alkaline environment ~pH 11. This created a complex environment containing a mixture of fission, corrosion and activation products and the build-up of contaminated magnesium hydroxide sludge on the pond floor.³ Radionuclide contamination built up on the surrounding concrete structures as well as the temporary floating structures used to grant workers access to the inner walls during decommissioning. These contaminated materials require extensive characterisation to determine the extent of radionuclide contamination and possible factors influencing radionuclide adsorption.

2.2. Radioactive contamination

Radionuclide contamination occurs through the dispersion of contaminants via leakages, decommissioning operations or accidents. Fission, activation and corrosion products are formed during operation as well as reprocessing or storage of SNF. This can result in the contamination of internal structures, transport and discharge pipelines and SNF storage ponds.^{4,5} These deposits are of particular concern during decommissioning operations, as workers will be at risk of exposure to high levels of radiation.

The extent of contamination is dependent on many chemical, physical and biological factors: the pH of the environment, matrix effects and temperature are just some of the parameters that have to be taken into account when studying contamination processes.⁶

2.2.1. Solid-liquid interface

Contamination occurs primarily at the interface between the contaminant solution and the surrounding structural surfaces. When surfaces are in contact with aqueous environments, they can become charged. The hydroxyl groups on the surface will develop positive or negative charges depending on the pH of the solution (Figure 2.1). The surface is neutral at the pH of point zero charge, pH_{pzc}, where the charges from the anions and cations in solution are in equilibrium. In alkaline environments where the pH is greater than the pH_{pzc}, the hydroxyl groups react with H₂O in solution to become negatively charged.⁷ This allows positively

charged ions present in the solution to favourably bind to hydroxyl sites and adsorb to the material surface.

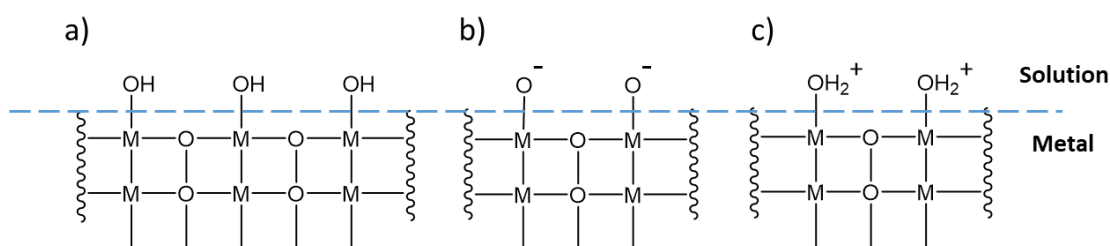


Figure 2.1. Structure of the metal surface in solution at a) neutral pH, b) in alkaline conditions, and c) in acidic conditions (adapted from Hazarika et al.).⁸

The presence of charged ions in solution gives rise to the electric double layer (EDL). The EDL is a surface complexation model first described by Helmholtz in 1850 to explain the interactions of solute ions with charged metal surfaces. Since then the Helmholtz model has been modified to account for sorption reactions of ions and solvent species.⁹ The ions closest to the charged surface become strongly bound and form a compact monolayer. This shields the surface from additional ions, which instead form hydrated species that are loosely attracted to the surface via electrostatic interactions (Figure 2.2). Finally, any species beyond the hydrated layer are too far from the surface to be attracted and remain mobile in the diffuse layer.

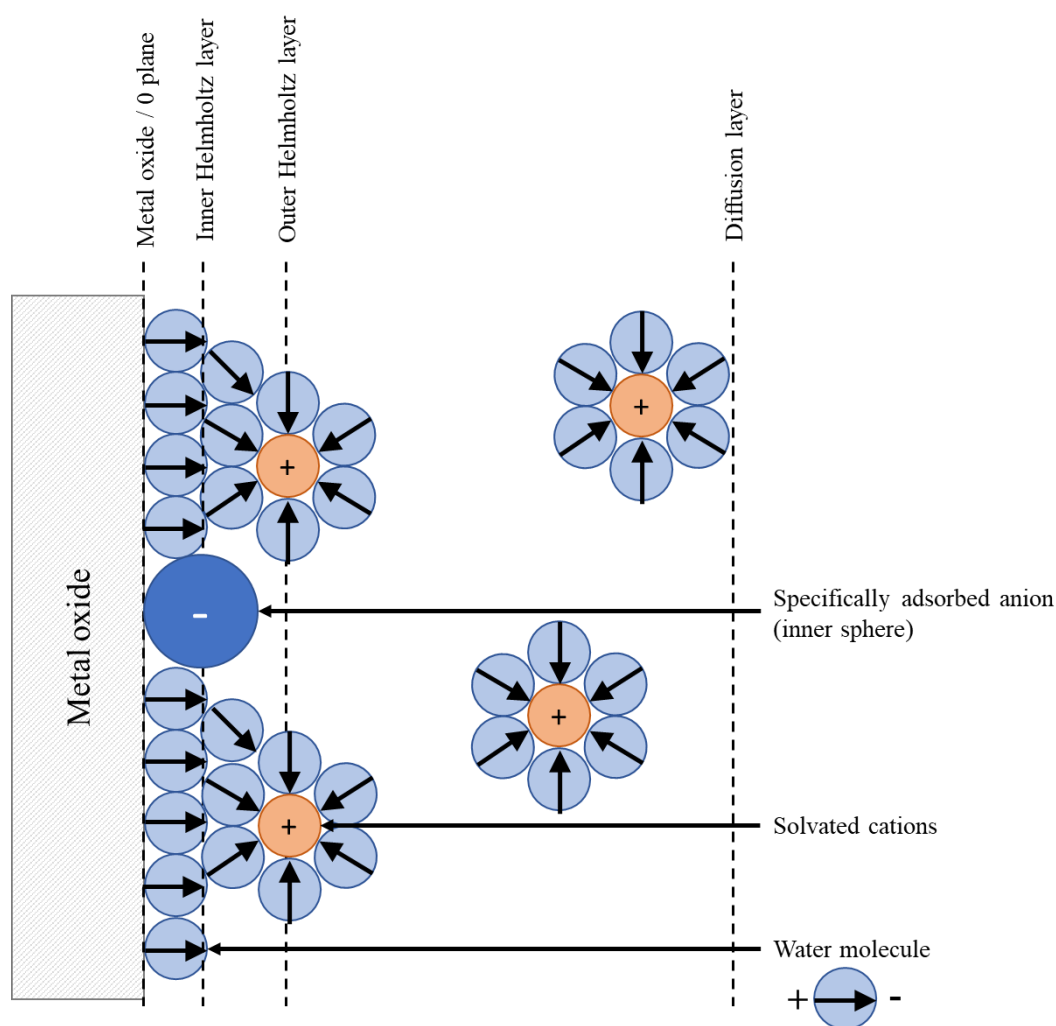


Figure 2.2. Schematic of the electric double layer formed at the metal oxide-solution interface. The metal oxide/0 plane is defined by the location of surface sites which may be protonated or deprotonated. The inner Helmholtz layer is defined by the centre of specifically adsorbed cations and anions, the outer Helmholtz layer corresponds to the beginning of the diffuse layer of counterions (adapted from Bénard et al. and Brown et al.).^{10,11}

2.2.2. Adsorption

Adsorption reactions can occur at the solid-liquid interface. These are either weak, electrostatic interactions (physisorption), or stronger, chemical bonds (chemisorption). Physisorbed contamination consists mainly of solid deposits on the material surface through weak molecular interactions such as van der Waals.¹² This does not directly affect the chemistry of the material surface or radionuclide speciation and is considered as outer-sphere complexation. This is usually a reversible process and contamination can be removed relatively easily using jet-washing or abrasive wiping methods.¹³ By contrast, radionuclides that interact with the surface

through chemical reactions are said to be “fixed” to the surface and require stronger and more thorough decontamination techniques or, in some cases, direct disposal of the contaminated material. Chemisorption tends to form a monolayer of contamination within the protective barrier layer of the material and can lead to the transport of radionuclides in the bulk material. Once contaminants begin to penetrate deeper into the sample material, removal becomes increasingly challenging. This is an issue particularly for porous materials such as concrete where radionuclides can diffuse further into the bulk. Protective paints or coatings can be added to help reduce the volume of contamination accessing the bulk material.¹⁴

2.3. Radionuclides of concern

2.3.1. Strontium

Strontium has four naturally occurring, stable isotopes: Sr-84, Sr-86, Sr-87, and Sr-88, with Sr-88 being the most abundant at 82.58%. However, the main isotope of interest to the nuclear industry is radioactive Sr-90 produced during the fission of U and Pu. Sr-90 has a half-life of 29.1 years and decays via emission of a β^- particle.¹⁵ Sr-90 decays to its daughter product, Y-90, which has a half-life of 64 hours whereby it decays via emission of another high energy β^- particle. This makes Sr-90 a particularly harmful species as it accounts for a significant portion of the activity produced by nuclear waste after initial decay and during the first 100 years and will continue to emit harmful radiation during human lifetime.¹⁶

Sr exists as the mobile 2+ ion in solution and can undergo adsorption reactions with metal-oxide surfaces. This allows radionuclide contamination to build up and increases the risk of radiation exposure to workers during decommissioning of redundant facilities. The properties of strontium(II) are similar to that of calcium(II) and accumulation of strontium in bones and teeth can occur if ingested.¹⁷ This similarity with calcium, and other group 2 metals, means strontium is also able to undergo ion-exchange reactions to contaminate materials such as concrete. Whilst sorption can occur in both acidic and alkaline environments, changes in pH can affect the extent of strontium(II) uptake as charges can build up on the material surface.¹⁸ Alkaline environments are more susceptible to strontium contamination as the hydroxide species on the surface become negatively charged forming strong bonds with strontium(II) ions.

2.3.2. Cesium

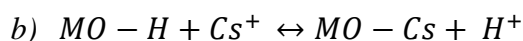
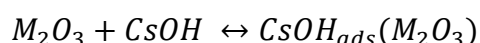
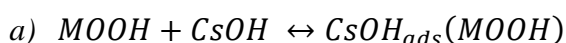
Cesium is a fission product produced during the burning of nuclear fuel and is often found alongside Sr contamination. Radioactive Cs-134, Cs-135 and Cs-137 are all produced during

the fission of U, Pu and Th, with Cs-137 being produced in the highest amount (6.2%).¹⁵ All radioactive isotopes of cesium decay via emission of a high-energy β^- particle, with Cs-137 emitting γ -radiation as the Ba-137 daughter species decays from metastable to stable state. Cs-137 is of great concern as it is a relatively long-lived radionuclide, half-life 30.2 years, making even small quantities of cesium contamination a danger to workers and the environment.

Cesium exists as the mobile, monovalent cesium(I) cation in solution, allowing it to transport in waste streams, contaminating vast areas along the way. Uptake of cesium(I) by organisms is possible due to its chemical similarity to potassium(I), resulting in radioactive cesium uptake in plants, which can make its way into the food supply.¹⁹

Cesium contamination of the environment and nuclear facilities gives rise to remediation and decommissioning issues. Studies into the adsorption of cesium(I) in nuclear materials is vital to determine how it can be easily removed for disposal in HLW facilities. Fourier transform infrared (FTIR) studies have indicated that cesium contamination occurs predominantly via adsorption of the cesium(I) ion on the passive metal-hydroxide surface of stainless steels via both chemical and physical bonds with increased uptake in alkaline conditions (Equation 2.1).²⁰ Studies on cesium(I) adsorption in soil samples found that adsorption was at a maximum around pH 7-8.^{21,22} However, experimental work by Gutierrez *et al.* found changing pH had little effect on the adsorption of Cs on montmorillonite between pH 5-8.²³

Equation 2.1. a) Physical and b) chemical sorption of cesium(I) on a metal-hydroxide surface (adapted from Rouppert *et al.*).²⁰



Besides Fourier-transform infrared spectroscopy (FTIR), X-ray absorption spectroscopy (XAS) and inductively coupled plasma mass spectrometry (ICP-MS) have been used in combination with gamma spectroscopy for the analysis of radio-cesium contaminated materials.^{24,25} These techniques provide information on the bonding of cesium(I) to surfaces as well as isotopic analysis. The drawbacks of these techniques is that they can require stable analogues to be used and in some cases, are destructive, forming secondary waste products requiring disposal.

2.3.3. Cobalt

Cobalt alloys show increased corrosion resistance at high temperatures compared to stainless steels, making them an appealing choice for reactor materials.²⁶ However, harmful radioactive Co-60 can be produced through the direct neutron activation of stable Co-59, or through the corrosion of cobalt containing steels. Cobalt has nine radioactive isotopes, but only Co-57 and Co-60 have substantial half-lives, 272 days and 5.27 years respectively.²⁷ Co-60 forms Ni-60 via the emission of β^- and γ -radiation and is responsible for 39% of the gamma activity found in effluent waste from nuclear facilities.^{15,28}

Despite evidence for cobalt leaching from LLW repository sites, migration of cobalt in groundwater is unlikely under atmospheric conditions as soils contain iron and manganese oxides that readily adsorb cobalt in its stable +2 oxidation state, minimising the possibility of leaching.²⁹ The similar ionic radii of these ions allows cobalt to substitute into the metal lattice of these minerals. Absorption of cobalt into these materials is dependent on pH and increases in alkaline conditions. Corrosion of stainless steel structures in alkaline SNF ponds produces cobalt hydrolysis species that adsorb to the oxide layers. X-ray photoelectron spectroscopy (XPS) and inductively coupled plasma optical emission spectroscopy (ICP-OES) analysis determined that increasing the solution pH resulted in the formation of insoluble cobalt hydroxide ($\text{Co}(\text{OH})_2$) precipitates that preferentially adsorb over cobalt(II) ions.^{30,31} Cobalt(II) ions dominate in the absence of organic ligands and is enhanced with increasing pH and presence of iron and manganese oxides. At pH 9.5 and above, $\text{Co}(\text{OH})_2$ and $\text{Co}(\text{OH})_4^{2-}$ become the dominant species, with reduced adsorption seen for the negatively charged species.³² Organic complexing agents are used during the decontamination of stainless steels and cladding materials and have a substantial impact on the properties of cobalt radionuclides. Ethylenediaminetetraacetic acid (EDTA) and ammonia, NH_3 , have been found to enhance Co-60 mobility in solution, increasing the spread of radioactive contaminants.

Research into the analysis and remediation of radionuclide contamination in groundwater and soil sediments has provided a better understanding of the impacts of pH and environmental conditions on radionuclide behaviour. However, the characterisation of contaminated materials in aqueous pond environments is still relatively under researched. Determining the effects of long-term exposure to radionuclide-contaminated solutions on urban structures is vital to understanding the adsorption mechanisms involved in contamination and developing potential treatments for effective decommissioning processes.

2.4. Nuclear materials of interest

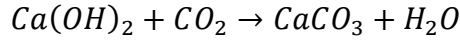
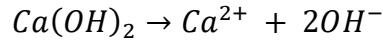
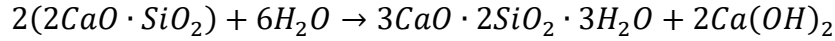
2.4.1. Concrete

Concretes are popular building materials due to their affordability, structural strength and, in the case of nuclear facilities, ability to shield and contain radiation.³³ Ordinary Portland cement (OPC) is the most common cementitious material used to make concrete and consists of calcium, silicon, aluminium and iron oxide phases. Small solid particles, known as aggregates, are mixed with the cement to improve the strength and durability of the material. In the nuclear industry, concrete is primarily used for the construction of buildings and waste containment sites. Over time, concrete structures age and external factors can have lasting effects on the properties of these materials. The atmosphere, radiation level, solution constituents and cement type can all lead to material degradation. Temperature, pH and radiation effects are of particular relevance to the nuclear industry and are discussed below.

Elevated temperatures have an impact on the composition of concrete materials. Concretes remain strong and durable up to around 95 °C; increasing the temperature beyond this causes a loss of interstitial water and a decrease in compressive strength.³⁴ Further research from Kanema *et al.* showed that water loss was occurring at temperatures between 150-300 °C, but mechanical strength only began to fail after 300 °C were exceeded.³⁵ Fluctuation in temperatures can also cause degradation of the material due to rapidly changing conditions and the strength of the material continues to reduce even during the cooling period.³⁶

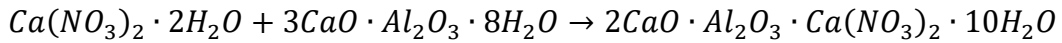
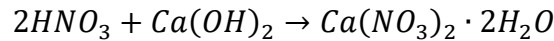
When cementitious materials are in contact with water they undergo hydration and leaching reactions (Equation 2.2). Concrete surfaces are made up of a calcium hydroxide barrier layer, known as the degradation layer.³⁷ These calcium ions dissolve into the aqueous environment, resulting in an increase in alkalinity of the surrounding solution. In addition, this causes an increase in porosity and permeability, and an initial decrease in strength of the concrete material.³⁸ However, the calcium silicate hydroxide (CSH) phases produced during hydration gradually harden, binding the cement and aggregate phases together, resulting in an increase in structural strength and durability.³⁹⁻⁴¹

Equation 2.2. *Reactions of cement with water (adapted from Lin et al.).*³⁸



The pH of the neighbouring environment also influences the strength of concrete. In the nuclear industry, concrete is often present in alkaline environments during the storage of SNF. Therefore, determining the impact of pH on concrete and its composition in these environments is of great importance. Whilst alkaline environments tend to have little impact on the properties of concrete, at low pH nitric acid attacks the cementitious calcium hydroxide ($Ca(OH)_2$), causing it to form soluble calcium nitrate species (Equation 2.3). Low concentrations of nitric acid, around 5%, showed a decrease in the compressive strength of concrete over just 28 days and increasing acidity and exposure times reduces this strength exponentially.⁴²

Equation 2.3. *Decomposition of the calcium hydroxide surface of concretes in nitric acid (adapted from Olusola et al.).*⁴²

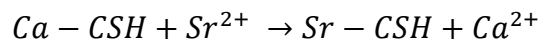


The effect of neutron and gamma radiation on concrete structures has been extensively studied.^{43,44} Neutrons preferentially attack the aggregate particles in the concrete mix, forming defects in the crystal structure and swelling of the material. This, along with the breaking of covalent bonds by gamma radiation, leads to a decrease in the material strength. Neutron radiation doses of 1×10^{19} n/cm² have been shown to vastly reduce the compressive and tensile strength of concrete as well as lead to a potential increase in aggregate volume.^{45,46} Gamma radiation can also modify the microstructure of concrete through a series of mechanisms: atom dislocation, bond breaking, hydrolysis and removal of water.⁴⁷ This has shown to have little effect on the bulk strength of the concrete but increasing levels of radiation can affect the mechanical properties and produce high temperatures that cause thermal cracking of the concrete material.

Activation of concrete materials by radiation is not the only problem affecting the nuclear industry. Corrosion products and radioactive sludge can form in SNF storage ponds

contaminating the surrounding structures. Whilst protective paint coatings prevent significant contamination, some radionuclides can transfer to the interior concrete walls, contaminating the surfaces. Modelling of radionuclide release into fuel ponds has been conducted to aid radiological assessment of contaminant uptake on concrete.⁴⁸ Contamination of the concrete surface is thought to occur predominantly via ion exchange of radionuclide ions with calcium(II), as well as sodium(I) and potassium(I).^{49–51} CSH phases are the major hydration product of OPC and are key for radionuclide adsorption due to the negative charges available on the silanol sites. XAS analysis showed Sr binding preferentially with CSH through the dissolution of calcium (Equation 2.4).⁵² Cesium(I) and cobalt(II) have also been known to adsorb on CSH phases in concrete structures, enhanced by high Ca/Si ratios and substitution of aluminium to form calcium aluminate silicate hydrate (CASH) phases.^{53,54}

Equation 2.4. *Strontium(II) ion exchange in calcium silicate hydrates (adapted from Tits et al.).*⁴⁹



To minimise contamination and radionuclide ingress into concrete structures, protective liners and paints were applied to bare concrete walls. Magnox ponds used epoxy paint coatings containing rutile pigments (TiO₂) to enhance the water resistance of the pond walls and prevent radionuclide ingress.⁵⁵ Coatings were not always successful and exposure to radiation limited their expected lifetimes.⁵⁶ Radionuclide uptake onto paint and other coatings occur via ion-exchange, surface adsorption and permeation mechanisms, with a slight increase in uptake occurring at higher pH for cobalt(II).⁵⁷

Radionuclide contamination on concrete structures has mainly been conducted using gamma and beta detectors, and other radiometric analysis techniques such as autoradiography.^{58,59} Removal of concrete samples from hazardous environments has also been conducted to determine the penetration depth of radionuclides using microscopy and X-ray emission techniques such as XAS and X-ray fluorescence spectroscopy (XRF).⁶⁰ Whilst analysis with these techniques has been successful, it often requires samples to be removed from site and prepared for use in these spectrometers. *In-situ*, non-destructive characterisation of contaminated concrete is a less researched area and identification of advanced techniques for this analysis would benefit the nuclear industry.

2.4.2. Plastic

Plastics are another popular material for use in industry as they are cheap to manufacture and their flexibility make them useful for many applications. Plastics have been used in the nuclear industry in areas of lower radiation outside the reactor core for piping, encapsulation and as temporary structures to provide access to areas for decontamination.⁶¹ High-density polyethylene (HDPE) is a linear form of polyethylene (PE) (Figure 2.3). The increased density makes HDPE ideal for nuclear environments, as it is resistant to most solvents and can withstand temperatures up to 130 °C. High-density polyethylene has been used in the nuclear industry for neutron shielding and in the manufacture of geomembrane liners for LLW.⁶²

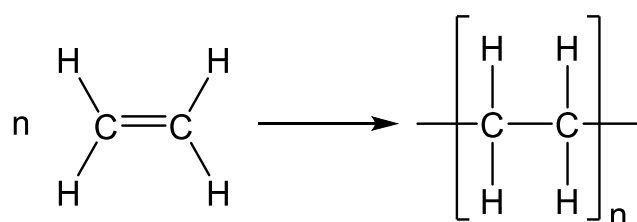


Figure 2.3. Polymerisation of ethene to form polyethylene.

Plastic materials are relatively inert making them resistant to degradation and chemical attack; however, environmental factors such as temperature, pH and radiation can affect the tensile strength and elasticity of plastics. These conditions can cause oxidation of polymer chains, leading to potential cracking of materials particularly in aqueous environments (Figure 2.4).⁶³ UV light can cause C-H bonds to break and results in the formation of radical species. These radicals can continue to react and break down the polymer chain, causing embrittlement and eventually increasing the probability of stress induced cracking.⁶⁴ Jia *et al.* monitored polymer oxidation through the use of attenuated total reflection Fourier transform infrared spectroscopy (ATR-FTIR), XPS and SEM to determine the chemical and elemental composition of the polymer, as well as image the surface morphology.⁶⁵

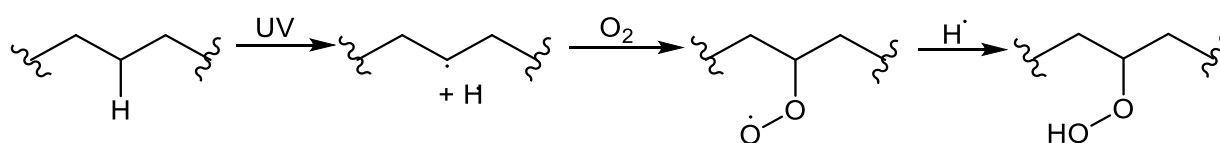


Figure 2.4. Example of abiotic degradation of polyethylene chain (adapted from Gewert *et al.*).⁶³

Most polymers can withstand radiation doses of around 10^4 - 10^5 Gy. However, PE is exceptionally radiation resistant, being able to withstand doses up to 10^8 Gy.⁶⁶ Radiation can result in either the scission or cross-linking of polymer chains (Figure 2.5). Scission results in the breaking of the longer polymer chains into smaller, more soluble fragments, resulting in the weakening and embrittlement of the material. In contrast, cross-linking increases the rigidity of the material by increasing the density of the chain network. This increases the glass transition temperature, T_g , and causes the polymer to become hard and brittle at much lower temperatures.⁶⁶ Alpha and beta radiation from Am-241 and Tc-99 sources have been shown to increase the rate of oxidation with increasing radiation exposure; however, increasing the polymer thickness from 0.2 to 2 mm can prevent sample degradation from occurring.⁶² Degradation of polymers exposed to gamma radiation is also dependent on the thickness of the polymer film. Very thin films, 0.05 mm, are relatively easy to break down and can generate hydrogen, carbon monoxide and carbon dioxide gases.⁶⁷ In contrast, work by Whyatt *et al.* concluded that γ -radiation induced cross-linking in HDPE, reducing the elasticity of the polymer. However, the radiation had minimal impact on the chemical degradation rate of 1.52 mm thick HDPE liners in high pH environments.⁶⁸ Radiation can have an impact on the thermal conductivity of PE through the production of defects that can alter the melting point of the plastic and cause it to fail prematurely.⁶⁹

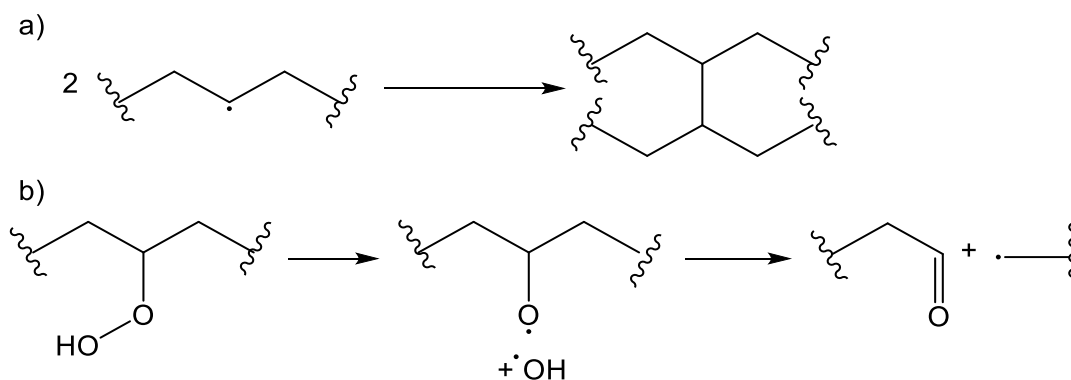


Figure 2.5. Polymer degradation via a) cross-linking and b) chain scission (adapted from Gewert *et al.*).⁶³

Temperature plays a large role in the properties of plastic materials. As the temperature rises polymers become less elastic and an increase in material strain occurs, making plastics more susceptible to breaking.⁷⁰ The ideal temperature range for HDPE membranes was determined to be around 20-40 °C and increasing the temperature beyond this lowers the materials

resistance towards stress cracking.⁷¹ Gassner *et al.* determined that increasing the temperature of the surroundings by just 10 °C could decrease the mechanical lifetime of HDPE by half.⁷²

In comparison to temperature and radiation, pH has a less pronounced effect on plastic materials. HDPE geomembranes subjected to various pH environments over a period of 3 years showed an increase in oxidation rate for higher pH solutions.^{73,74} The studies conducted in acidic solutions were less conclusive and degradation rates were closer in value. However, a different study into the effect of low pH environments on plastic piping identified oxidation of the pipe surface and overall decrease in the fracture resistance of the material.⁷⁵ Contamination and decontamination studies of americium(III) on nylon and PE microplastics have shown that higher pH environments can result in greater adsorption of Am and that desorption can be a time consuming process.⁷⁶

Contamination of pristine plastic is unlikely to occur directly due to the inert nature of the material, particularly over short time scales. However, over time, surfaces can become damaged, resulting in cracks and pores that enable radionuclide adsorption to take place. Radionuclides can interact with plastics through surface complexation, electrostatic interactions, precipitation, or through interactions with chemical precipitates and biofilms (bioaccumulation).^{77,78} Biofilms and metal oxide precipitates can form in complex aqueous environments, particularly in alkaline conditions, resulting in sites for radionuclide adsorption.^{79–82}

The presence of pores and cracks in plastic materials can result in penetration of radionuclides into the bulk. A study indicated that organic compounds can diffuse through low-density polyethylene (LDPE) more readily than other plastics due to its lower glass transition temperature, T_g , at which the polymer exhibits more rubbery properties, increasing its sorption capacity.^{83,84} The semi-crystalline structure of PE allows for a combination of sorption mechanisms as it contains both flexible amorphous sections and glassy segments.⁸⁵ However, PE was found to adsorb heavy metals less than other plastics, such as polyvinyl chloride (PVC) and polystyrene (PS), due to its smaller specific surface area.⁸⁶

Infrared spectroscopy is the predominant analytical technique used for visualising the chemical composition of plastic surfaces and has been used to identify oxidation products.^{65,67,87} Trace analysis has been conducted for heavy metal identification in various PE materials using ICP-OES and atomic absorption spectroscopy (AAS).^{88–90} However, this research focuses primarily on the food industry and other studies on plastics. To date, there have been very few studies

into radionuclide contaminated plastics. The work of Tazaki *et al.*, which used XRF and SEM-EDX to study the uptake of heavy elements alongside radionuclide species in PE, appears to be the only study analysing samples from nuclear sites.⁹¹ A recent study by Zrelli *et al.* contributes to this topic, determining that natural and artificial radionuclides can be taken up and transported by polyethylene terephthalate (PET) plastic waste from coastal environments.⁹²

2.4.3. Stainless steel

Austenitic stainless steels are widely used throughout the nuclear industry and are found in the reactor core, coolant piping and in the back-end operations in reprocessing and waste management infrastructures. The most widely used steels are American iron and steel institute (AISI) type 300 austenitic steels due to the addition of chromium and nickel, which improve the corrosion resistance of the steel in elevated temperatures and acidic environments.¹⁰ Type 304 and 316 stainless steel are primarily used in the nuclear industry and can be made with smaller quantities of carbon to improve durability and minimise intergranular corrosion (Table 2.1).^{93,94}

Table 2.1. *Composition of typical austenitic stainless steels used in the nuclear industry (adapted from Was et al.).*⁹⁵

Alloy type	Composition (wt %)						
	Fe	Ni	Cr	Mn	Mo	Si	C
304	Balance	8.00-10.5	18.0-20.0	<2.00	-	<1.00	<0.08
304L	Balance	8.00-12.0	18.0-20.0	<2.00	-	<1.00	<0.03
316	Balance	10.0-14.0	16.0-18.0	<2.00	2.00-3.00	<1.00	<0.08
316L	Balance	10.0-14.0	16.0-18.0	<2.00	2.00-3.00	<1.00	<0.03

Passivity is a state in which corrosion of a material is significantly reduced through the formation of a protective surface layer. In steels, a protective chromium-rich oxide layer forms through the combined dissolution of iron on the surface and oxidation of the chromium within (Figure 2.6).¹⁰ This layer is in a constant state of change as a controlled equilibrium arises between the adsorption and diffusion of surface and solution ions.⁹⁶ In aqueous conditions, the steel will adsorb oxygen and hydrogen from solution to form a dual hydrated oxide layer.

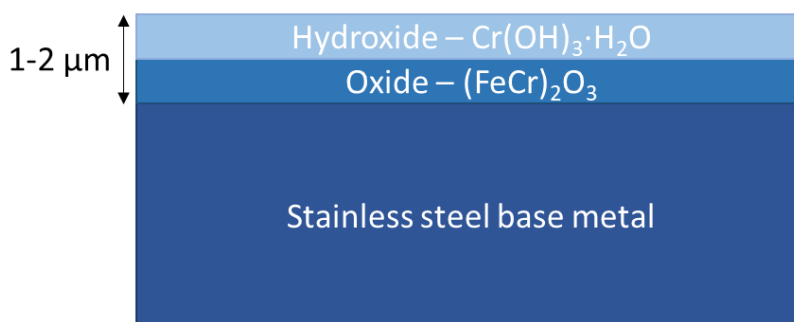


Figure 2.6. Passive layer formed on stainless steel (adapted from Zahner et al.).⁹⁷

Passivity can be chemically induced, but it can also form spontaneously in oxidising environments. The formation and thickness of this layer is dependent on several factors: pH, temperature, halide concentrations and applied potential.^{97,98} For Fe-Cr alloys, such as the type 300 steels, degradation of the passive layer is somewhat reduced by the mixed chromium(III)-iron(III) hydroxylated-oxides; however, studies have been conducted to determine the effect of pH on the passive layer composition.⁹⁸ In alkaline environments, the chromium species are oxidised from chromium(III) to soluble chromium(VI); the protective chromium layer dissolves and is replaced by an iron-nickel oxide that provides reduced corrosion resistance.⁹⁹ In contrast, when steels are exposed to acidic conditions, the chromium layer is stabilised and the iron is reduced from iron(III) to iron(II), which dissolves into solution.¹⁰⁰

At high temperatures, stainless steels are susceptible to corrosion mechanisms: pitting, crevice corrosion, intergranular corrosion and stress-corrosion-cracking. These reactions all occur naturally over time, but can be induced through exposure to high temperatures, chloride ions and irradiation.^{101–103} New materials that replace carbon with increased concentrations of nitrogen can improve the mechanical properties of steel alloys by reducing the rate of corrosion.¹⁰⁴ SNF pond conditions have been optimised to minimise the corrosion of steel and aluminium storage containers; however, over time containers and the protective Mg-based cladding has corroded and given rise to corrosion products.¹⁰⁵

The contamination of stainless steels is a widely researched area and techniques such as combined scanning electron microscopy energy dispersive X-ray spectroscopy (SEM-EDX), FTIR and XPS have proved popular for the analysis of contaminant species.^{106–109} Steel is used throughout nuclear power plants where it is susceptible to contamination by a variety of actinide, transuranic and fission product species.¹¹⁰ For steel surfaces in aqueous conditions, Cs contamination occurs primarily through ion exchange with element such as potassium(I) or

combination with surface hydroxide species.^{111,112} In addition, studies have found that radionuclide contamination on steel often coincides with the adsorption of iron and other corrosion species.^{113,114} This is particularly relevant to fuel pond environments where pH effects lead to the formation of corrosion products that could aid contamination on the surrounding materials.

2.5. Characterisation of contaminated materials

Before decommissioning operations can take place, extensive characterisation of sites is required to determine the radionuclide species present, the binding strength and extent of the material contamination (Figure 2.7). Contaminants that have penetrated deeper into the bulk material become harder to remove and require harsh chemicals or abrasive methods to remove contaminants before disposal.

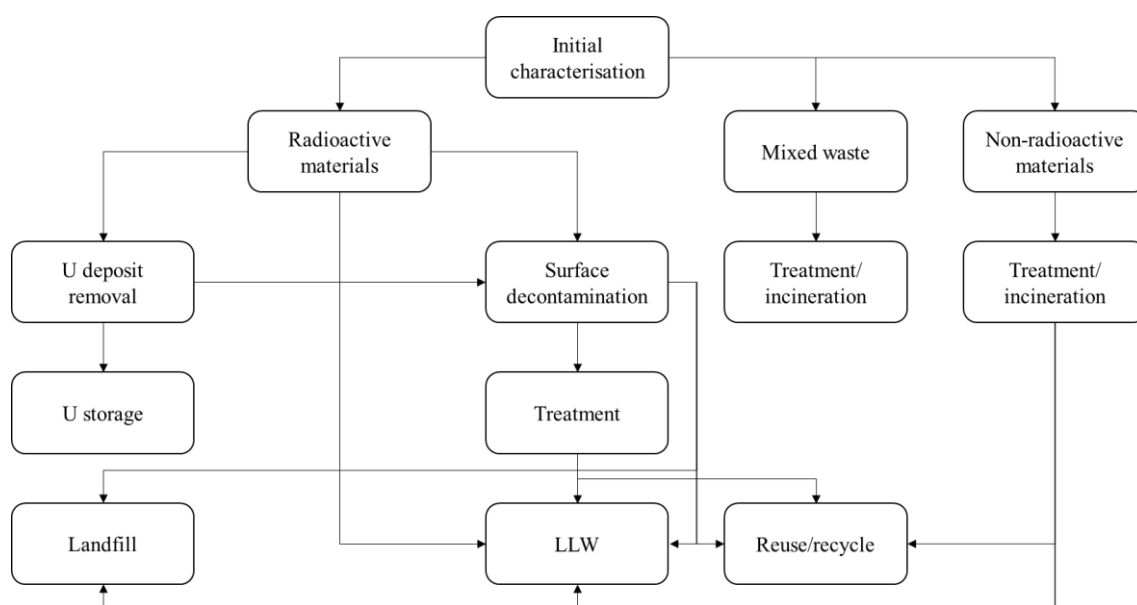


Figure 2.7. Flow diagram of the decontamination process (adapted from the Committee on Decontamination and Decommissioning of Uranium Enrichment Facilities).¹¹⁵

Radiation detectors are used in the initial stages of decommissioning to map large areas and identify hot spots containing increased levels of activity. These detectors can be modified to isolate a particular type of radiation through the addition of screens that block out less penetrating emissions.¹¹⁶ Whilst detectors are able to identify the type of radiation produced, and in some cases the radionuclides responsible, they provide no information on bonding or surface structure.¹¹⁷ Characterisation techniques such as ICP-MS, total reflection X-ray

fluorescence spectroscopy (TXRF) and XPS have been used to provide additional information on the radionuclide species and their bonding; however, these techniques are often time consuming and may require destructive preparation techniques that generate additional waste products.^{118–121} Vibrational methods often produce low signals and most techniques may require samples to be extracted from sites. This can inadvertently produce secondary waste products that must be accounted for in decommissioning planning. The use of LIBS in these scenarios could help aid the *in-situ* characterisation of trace materials as it is able to conduct standoff analysis with little or no sample preparation.

2.5.1. Laser-induced breakdown spectroscopy

Laser-induced breakdown spectroscopy (LIBS) is a high-energy spectroscopy technique that has shown great promise as an analytical tool for industrial application as it only requires optical access to the target material. LIBS has been used to determine the composition of alloys in the steel industry, evaluate the film coating thickness and composition in pharmaceutical tablets and, with sophisticated data analysis, conduct isotopic analysis of uranium samples.¹²² LIBS is able to provide multi-elemental analysis of both major and trace elements on most material surfaces without the need for sample preparation.¹²³ Analysis has been carried out on solids, liquids and gases, as well as in outer space on the Curiosity rover; making LIBS a versatile tool for use in adverse environments.^{124–126}

Laser-induced breakdown spectroscopy uses optical atomic emission spectroscopy to obtain elemental information on the sample material. A high-energy laser pulse is directed at the sample ablating a small portion of the material surface. This interaction between the laser and the surface creates a plasma formed of the ablated particles (Figure 2.8). The high temperature of the plasma causes these particles to atomise and become ionised. As the plasma cools these electrons de-excite down to the ground state, releasing a characteristic light emission.¹²⁷ These emissions are picked up by the detector to create a spectrum of emission wavelength against intensity that can be used to identify the elements present in the sample. The intensities of the emission peaks are proportional to the concentration of the element in the sample, making LIBS not only qualitative, but also semi-quantitative, although obtaining accurate quantitative information requires significant calibration with standards matching the sample matrix of interest or extensive analysis of data using modelling and statistical processes.^{128,129}

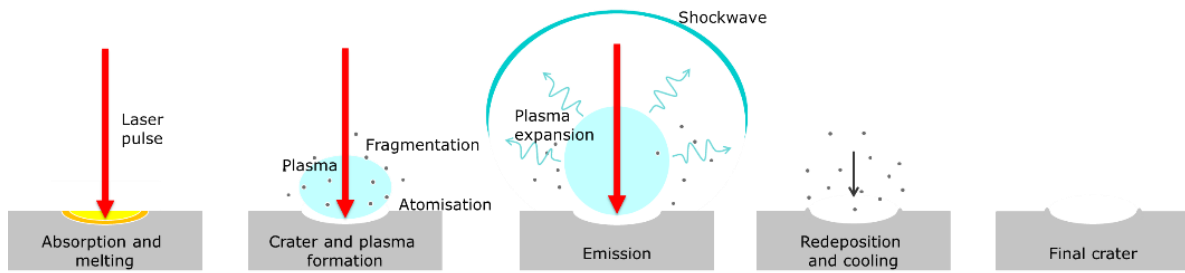


Figure 2.8. Schematic of the LIBS ablation process.

The versatility of LIBS make it a favourable technique as it can be used for standard benchtop analysis or modified to conduct standoff analysis as it only requires an optical line of sight with the target surface (Figure 2.9).¹³⁰ The main components consist of a laser source, detector and a computer to control the parameters and visualise the spectra. Several parameters define the LIBS process and can be adjusted to optimise the analysis for a particular element and environment.

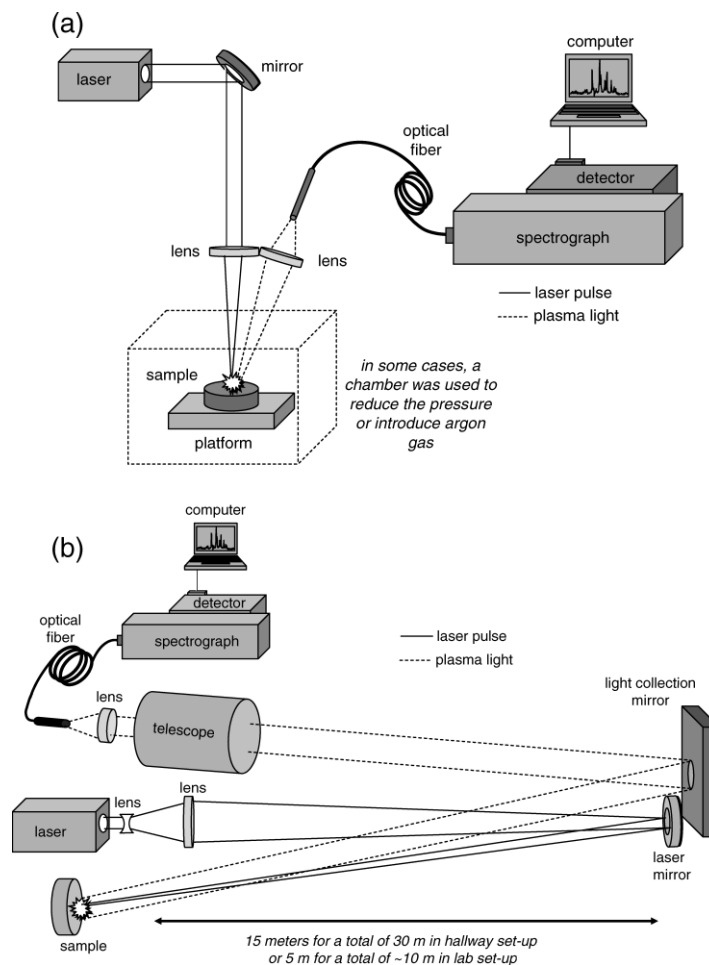


Figure 2.9. Laser-induced breakdown spectroscopy apparatus for a) close-up lab analysis and b) remote, standoff measurements (Chinni et al.).¹³⁰

The delay time and gate width are important parameters for obtaining a high-quality spectrum and defines the time between plasma propagation and light collection. In the first stages of plasma formation, the dominating emissions are caused by background radiation, Bremsstrahlung, and radiative recombination known as the continuum.¹³¹ In the early stages of plasma formation, the continuum can dominate over the whole spectral range and hide any atomic emissions produced (Figure 2.10). By increasing the delay time, the continuum effect can be eliminated and a clear spectrum of atomic emissions can be obtained.

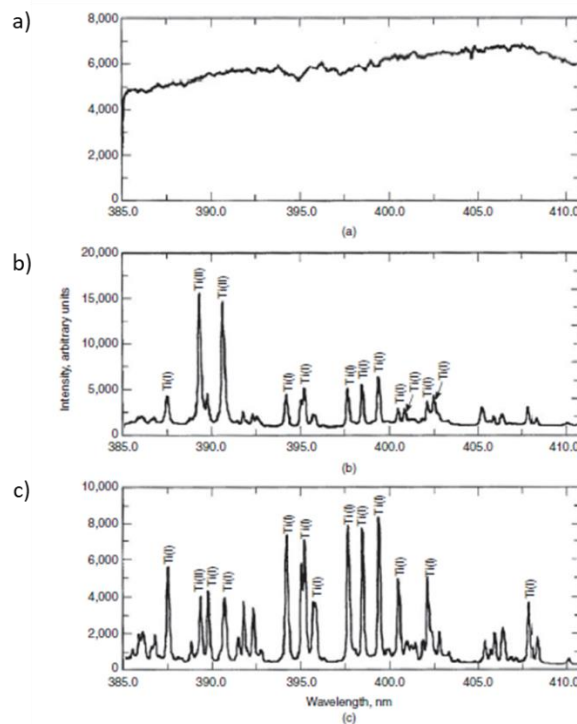


Figure 2.10. LIBS spectra of a titanium sample obtained after a delay time of a) 0-0.5 μs , b) 0.5-5 μs , and c) 10-110 μs (Cremers et al.).¹³²

2.5.1.1. LIBS analysis of radionuclides of interest

The identification of specific elements in a LIBS spectrum should be relatively straightforward as each element has characteristic emission wavelengths; however, in practice this can be a complex and time-consuming process. Each element can contribute hundreds of emissions, relating to different electron de-excitation processes, which can overlap with other element emissions. In addition, a small portion of the sample matrix will be ablated during the process and contribute peaks that can also interfere with the analyte peaks. Whilst this can produce a more complex spectrum, it does not adversely impact the identification of specific elements. Databases of key emission peaks are available for most elements and reference spectra of

uncontaminated sample matrices can be used as a comparison to highlight the presence of new peaks produced by contaminant species.¹³³

Laser-induced breakdown spectroscopy has been used to analyse various elements relevant to the nuclear industry. The identification of uranium has been particularly of interest due to its applications to nuclear forensics. Non-destructive LIBS analysis can be used to determine the composition of uranium containing samples without damaging the integrity of the material, allowing stolen samples to be safely returned to the original location.¹³⁴ The limit of detection (LOD) for LIBS analysis of radionuclides is dependent on the sample matrix, atmosphere and the distance of the sample measurement from the laser source.¹³⁵ Uranium was quantified down to 6120 mg/kg in iron-rich rock, whereas the LOD for uranium in a silicon dioxide (SiO₂) matrix was 268 mg/kg.¹³⁶ The same can be seen for uranium identification in glass samples from vitrified waste, which were detectable down to 150 mg/kg.¹³⁷ LIBS has also been used to characterise the composition of complex mixed actinide samples, showing clear differentiation between uranium, plutonium and actinium emissions. However, neptunium characterisation appears to be a problematic area for LIBS as key emission lines remain to be identified.^{138,139} Another advancement in LIBS beneficial to the nuclear industry is the differentiation of isotopic species in a sample. By introducing algorithms that constrain the spectral lines, uranium emissions were partially resolved to show individual contributions from U-235 and U-238 down to 500 mg/L in soil samples.¹⁴⁰ Recent work combining chemometrics with LIBS has allowed isotopic differentiation to be conducted in less than a minute at concentrations comparable to enrichment values in uranium fuel.¹⁴¹

As with uranium, cesium identification is subject to matrix effects. Cs was unidentifiable at extreme concentrations, 10,000 mg/kg, in calcium carbonate; however, when present in a graphite matrix the LOD for Cs was down to 600 mg/kg.¹⁴² Similarly, identification of Cs contamination on steel samples proves to be difficult due to interference from matrix peaks and low emission intensities.¹⁴³ Current LIBS systems have been inadequate in the detection of Cs at concentrations relevant to the nuclear industry due to its high limit of detection and low sensitivity.¹⁴⁴ Advances to the LIBS apparatus and optimisation to improve analysis are required for LIBS to be used effectively for cesium identification in contaminated nuclear materials.

The analysis of cobalt using LIBS has not been as extensively researched and suffers from similar issues to cesium in that the emission intensities tend to be much lower. Several studies

have looked at identifying cobalt in steel and alloy matrices, and it has been known to suffer from matrix interference from Fe emissions.^{145,146} Another study combined LIBS with laser-induced fluorescence (LIF) to improve the accuracy of LIBS and was capable of detecting cobalt in soil samples down to 0.005 mg/kg.¹⁴⁷

LIBS has proven to be a valuable technique for strontium identification and showed little adverse effects with differing matrices. Strontium was identified down to 10 mg/kg in CaCO₃ and graphite matrices, as well as 0.5 g/cm² on steel surfaces.^{143,148} Whilst LIBS analysis is predominantly focused on atomic identification, experiments using strontium compounds have been used to identify molecular species as well. Increasing the gate width to 45 µs allowed Sr-O and Sr-Cl bonds to be characterised in the LIBS spectra.¹⁴⁹ Molecular LIBS could provide additional information on the bonding and speciation of contaminants in nuclear materials to aid the decontamination process. Previous work by Lang *et al.* has shown LIBS to be a quick, easy tool for the detection of Sr contamination on stainless steel surfaces. Multi-pulse analysis of Sr penetration into the steel bulk showed contamination was isolated to the material surface; however, re-deposition of radionuclide species can occur and requires further research to minimise this negative aspect of LIBS analysis.^{143,150,151}

Here, LIBS could be used as a suitable analytical tool for the accurate characterisation of contaminant speciation and penetration depth into materials common to the nuclear industry. LIBS can provide real-time identification on most nuclear materials present *in-situ*. The additional feature of providing depth-resolved information on the extent of contamination penetration into the material bulk would help deduce necessary decontamination tasks required.

2.5.1.2. LIBS analysis of materials of interest

LIBS has been used to analyse concrete, but this has predominantly focused on the identification of major components in cementitious materials such as calcium or contaminants such as sulphur and chlorine.^{152,153} In addition, LIBS is able to detect the presence of light elements which is beneficial for identifying the potential species present in the concrete matrix and how radionuclides may interact with them.¹⁵⁴ Characterisation of major and trace radionuclide contamination in concrete structures is an area of huge importance in the cost effective decommissioning of nuclear facilities. LIBS is a technique which, to date, has not been applied to this area. This project aims to determine its applicability to the nuclear industry and how it can be used to aid decontamination and decommissioning operations.

LIBS can be used to differentiate polymer species based on the ratio of the carbon and hydrogen peak intensities and can even distinguish between high and low-density polymers.^{155–157} Despite this useful application of LIBS, little research has continued into the use of this spectroscopy technique for industrial application. LIBS has proven to be excellent for studying plastics and in other areas, as a valuable tool for the analysis of radionuclide contaminated steels. The hypothesis is that LIBS can be used to detect radionuclides in contaminated plastics for use in decommissioning of nuclear facilities.

The ability to easily modify the LIBS system to the task at hand makes it an extremely versatile technique with applications as a remote analytical tool. Probes have been developed to measure samples in hostile environments without the need to remove samples from site.¹⁵⁸ This provides real-time, non-destructive analysis of potentially harmful species and allows key areas, such as nuclear sites, to be continuously monitored to determine any changes in composition that may occur over time. Remote analysis with LIBS has shown success in a wide range of industrial applications. In particular, for determination of heavy metal contamination in soils, corrosion in industrial structures and radiological contamination on material surfaces.^{153,159,160} The production of a compact hand-held LIBS (HH-LIBS) apparatus has progressed remote analysis of materials even further. Robots fitted with HH-LIBS could be sent into narrow or harsh environments, such as nuclear pipelines, to conduct elemental characterisation and chemical mapping of the surroundings has been shown for beryllium on fibrous surfaces.¹⁶¹ Whilst the reduced size of these LIBS systems allows access to previously unreachable areas, it is also one of the predominant limitations. Initial designs had vastly reduced wavelength ranges and optimisation of the parameters is currently limited to manually changing the measurement distance and shot number. The resolution of the analysis is therefore reduced, and identification is limited to emissions available in the set range. However, newer models have been developed to encompass the whole wavelength ranges available with benchtop models.

Another advancement in LIBS technology is the ability to identify contaminant penetration depth within a sample via multi-pulse analysis. Repeated laser pulses can be used to “dig” into the sample material and produce in-depth analysis of layer compositions. This feature of LIBS could allow the extent of radionuclide penetration into materials to be determined and allow appropriate decommissioning routes to be used. Multi-pulse analysis has shown LIBS to be a valuable technique for determining the thickness of metallic and geochemical coatings as well as the diffusion of aluminium metal in silicon materials.^{162–164} Recent work from Lang *et al.* showed strontium contamination in steel samples was isolated on the material surface and

decreased with increasing penetration depth.¹⁴³ A side effect of multi-pulse analysis is the potential for contaminant re-deposition on the material surface in ambient conditions. Ablated material has been shown to recombine with the steel surface whilst it remains molten, allowing contaminant material to travel deeper within the bulk of the material. This could prove detrimental to decommissioning tasks and further investigation into the re-deposition phenomenon is required to determine the exact mechanisms taking place. In addition, LIBS suffers from reduced resolution at increased depths and penetration depth is not guaranteed to be consistent with each consecutive laser shot. Additional techniques would need to be used in combination to determine the exact depth of contaminants.

There is no doubt in the ability of LIBS to conduct rapid, high-resolution, multi-elemental analysis on unprepared surfaces make it an appealing technique for *in-situ* identification of low concentrations of radionuclide contamination of nuclear facilities. The lack of research on the radionuclide contamination of concrete and plastic materials, particularly of authentic samples, provides an opportunity for LIBS analysis to prove its capability as a useful analytical tool to the nuclear industry.

2.6. Decontamination

Decommissioning of nuclear facilities is a large and expensive task, requiring extensive planning to maintain a safe working environment for all personnel involved. Successful decontamination allows for disposal of infrastructure into landfill and LLW repositories reducing costs and the overall volume of ILW sent to the GDF.

There are numerous decontamination methods available that are chosen based on the target material, binding strength of radionuclides and the degree of cleaning required. The decontamination effectiveness of these techniques is measured by the decontamination factor (DF) and is one key factor when considering appropriate decontamination methods.

Decontamination techniques can be categorised into physical and chemical methods. Physical decontamination can range from wiping and washing of surfaces with water for weakly sorbed contamination to harsher, mechanical and abrasive methods such as grinding and scabbling for stronger bound contamination in structures.¹⁶⁵ Whilst these methods are hugely effective, they can result in the production of harmful dust as well as secondary wastes that require careful sorting, storage and appropriate disposal. Some physical methods can even result in the re-

distribution of contaminants deeper within the material requiring additional decontamination methods, increasing the financial costs associated with decommissioning tasks. Chemical methods pass strong acids or reagents through structures to dissolve contamination layers and, in some cases, some of the bulk material as well.¹⁶⁵ Whilst effective, these methods can result in significant corrosion which is incompatible with reuse of materials and also generate secondary aqueous wastes.

New methods using gels, foaming agents and ion-imprinted polymers have been demonstrated.^{166–169} These methods use chemical or adsorption effects to draw contaminants out from the material surface into the decontamination medium. For most of these methods, the decontamination medium is brushed or sprayed onto a contaminated surface, creating a film that draws the contaminants into the coating. These diverse techniques tend to reduce the volume of secondary waste produced and, for certain materials such as foaming agents, are capable of penetrating into gaps and pores on surfaces. In contrast, ion-imprinted polymers use targeted binding sites similar to enzymes and antibodies to selectively adsorb hazardous radionuclides.¹⁶⁸ Despite their advantages over traditional physical and chemical methods, there are some setbacks to gel and foam based methods as they can require several applications for effective decontamination and the use of brushing or vacuum equipment to remove the medium once dried.^{170,171}

The use of strippable coatings and polymer-based hydrogels can alleviate some of these issues as they are easily applied and removed post-decontamination.^{171,172} DeconGel and Argonne super-gel (Argonne National Laboratory) are two commercialised strippable coatings that have been successfully used to rapidly decontaminate concrete surfaces, however they can also produce vast amounts of secondary aqueous waste as they require rinsing post decontamination.¹⁷³ Cross-linked polymer hydrogels are of particular interest as they are capable of encapsulating radionuclides in the internal porous network through dehydration post-decontamination. This forms a solid waste form which can either be disposed as is or incinerated and mixed with grout reducing the secondary waste volume.^{174,175}

2.7. Research rationale, aims and hypotheses

The overall aim of this research project is to develop a fundamental understanding of Sr, Cs and Co uptake on concrete and plastic materials under conditions representative of alkaline SNF storage ponds. The Hunterston A SNF storage pond was used as a case study for this work

with authentic samples obtained for analysis. Long-term wet storage of Magnox SNF has resulted in the release of radioactivity into the pond water and subsequent contamination of the surrounding infrastructure, resulting in a significant decommissioning challenge. Characterisation was conducted to determine the distribution, binding strength and diffusivity of radionuclides in these materials to aid future decommissioning tasks. In addition, developments in the use of hydrogels for localised decontamination of fission products and actinides on concrete and plastic materials were carried out. Finally, the assessment of the use of LIBS for the detection of strontium, cesium and cobalt on concrete and plastic surfaces in alkaline conditions was conducted to assess its use for standoff, *in-situ* analysis of contaminated structures in the nuclear industry.

The hypotheses were as follows:

- LIBS can be used to accurately identify and quantify Sr, Cs and Co contamination on concrete and HDPE surfaces in conditions representative of alkaline SNF pond.
- LIBS can be used for rapid, standoff, *in-situ* analysis of authentic radionuclide contaminated materials.
- Hydrogels can be used to successfully decontaminate radioactivity from concrete and HDPE surfaces to minimise waste generation and aid future decommissioning tasks.

The aims of the PhD project were as follows:

- To assess the extent of long-term radionuclide contamination on aged concrete and plastic materials in the Hunterston A SNF storage pond; including identification of key radionuclides and assessing the extent of the binding strength and penetration into the sample bulk.
- To evaluate the capability of LIBS to detect radionuclide contamination on concrete and plastic materials in the nuclear industry and assess the use for analysis of authentic nuclear samples.
- To determine potential decontamination routes for contaminated materials to improve future decommissioning tasks and reduce the overall volume of secondary waste produced.

The findings from this project aim to provide insight into the effects of long-term radionuclide contamination on concrete and plastic infrastructure in aqueous alkaline environments relevant

to the interim storage of nuclear waste. The knowledge obtained from this work will help support future decisions for appropriate decontamination methods to minimise secondary waste generation and encapsulate harmful, radioactive fission products. In addition, this work aims to evaluate the capability of LIBS for deployment as a standoff, *in-situ* characterisation tool in the nuclear industry.

2.8. Thesis structure

This thesis has been submitted in the alternative journal format. The thesis begins by providing an in-depth review of relevant literature in Chapter 2. This is followed by Chapter 3 which covers the experimental methodologies and analytical techniques used throughout this project and the theory behind each technique. The research conducted throughout this project is presented in Chapters 4-6 in journal format as planned papers for submission. The research chapters are summarised below.

Chapter 4 covers the developments to analysis of radionuclide contaminated materials using LIBS. This research focuses on the analysis of concrete and high-density polyethylene (HDPE) materials contaminated with Sr, Cs and Co in conditions representative of alkaline SNF storage ponds to assess the capability of LIBS for rapid analysis of contaminated nuclear materials. To further develop the use of LIBS for the analysis of complex authentic samples, model stainless steel samples representative of waste discharge pipelines were characterised. This chapter is presented as a first author manuscript in preparation for submission to *Spectrochimica Acta B: Atomic Spectroscopy*.

Chapter 4 author contributions:

A. Denman - principal author, experimental design and set-up, sample collection, data processing and interpretation, manuscript writing.

G. Law - project supervisor, input to experimental concept, aided with data interpretation, manuscript review.

T. Carey – project supervisor, manuscript review.

N. Smith – project supervisor, LIBS support, manuscript review.

F. Barton – preparation and provision of waste pipeline samples.

J. Lloyd – provision of waste pipeline samples.

S. Heath - project supervisor, input to experimental concept, aided with data interpretation, manuscript review.

Chapter 5 explores the characterisation and decontamination of HDPE pontoons used during the decommissioning of the Hunterston A SNF storage pond. Surface characterisation of the pontoon samples was conducted using a combination of imaging, radiometric and spectroscopic techniques (autoradiography, gamma spectroscopy, LIBS, Raman and LSC) to determine radioactivity distribution and highlight potential uptake mechanisms. In addition, hydrogels were used to decontaminate model HDPE coupons contaminated with radionuclides relevant to SNF pond environments before being applied to the decontamination of authentic radioactively contaminated HDPE pontoon surfaces. This chapter is presented as a first author manuscript in preparation for submission to the *Journal of Nuclear Materials*.

Chapter 5 author contributions:

A. Denman - principal author, experimental design and set-up, sample collection, data processing and interpretation, manuscript writing.

G. Law - project supervisor, input to experimental concept, aided with data interpretation, manuscript review.

T. Carey – project supervisor, principal coordinator for Hunterston A samples, provided information on samples, manuscript review.

N. Smith – project supervisor, manuscript review.

S. Heath - project supervisor, input to experimental concept, aided with data interpretation, manuscript review.

Chapter 6 covers the research conducted on a concrete drill core removed from the decommissioned Hunterston A SNF storage pond. This chapter presents the characterisation work conducted on the painted core surface and bulk concrete through a combination of imaging, radiometric and microscopic techniques (autoradiography, gamma spectroscopy, SEM-EDX, XRD) to determine the composition and radiological distribution on, and within, the sample. Sequential extractions were conducted to determine possible radionuclide uptake mechanisms and binding strength in the bulk concrete. Finally, decontamination experiments were conducted on the painted surface and bulk concrete using hydrogels to assess their ability to remove long-term radionuclide contamination. The chapter is presented as a first author manuscript in preparation for submission to the *Journal of Hazardous Materials*.

Chapter 6 author contributions:

A. Denman - principal author, experimental design and set-up, sample collection, data processing and interpretation, manuscript writing.

G. Law - project supervisor, input to experimental concept, aided with data interpretation, manuscript review.

T. Carey – project supervisor, principal coordinator for Hunterston A samples, provided information on samples, manuscript review.

N. Smith – project supervisor, manuscript review.

G. Vettese – autoradiography and gamma spectroscopy support.

J. Ang – sample and autoradiography support.

H. Suhonen – XCT analysis and support.

S. Heath - project supervisor, input to experimental concept, aided with data interpretation, manuscript review.

Chapter 7 summarises the research described in this thesis. The key findings obtained and their contributions to research on characterisation of contaminated nuclear materials are highlighted. Possible avenues for future work are described which could further research into the characterisation and decontamination of radioactively contaminated materials.

Chapter 8 (Appendix 1): Conference presentations, posters and awards.

2.9. References

- 1 M. Forwood, The legacy of reprocessing in the United Kingdom, 2008, 1–54.
- 2 M. J. Dunn and I. R. Topliss, The status of spent fuel treatment in the United Kingdom, *Advis. Gr. Meet. status trends spent fuel Reprocess.*, 1998, 61–65.
- 3 C. Bertoncini, in *Proceedings of the International Conference on Environmental Remediation and Radioactive Waste Management, ICEM*, 2013, pp. 1–11.
- 4 H. Ashworth, L. Abrahamsen-Mills, N. Bryan, L. Foster, J. R. Lloyd, S. Kellet and S. Heath, Effect of humic acid & bacterial exudates on sorption-desorption interactions of ⁹⁰Sr with brucite, *Environ. Sci. Process. Impacts*, 2018, **20**, 956–964.
- 5 H. Provens, in *European IRPA Congress*, 2002, vol. October, pp. 1–11.

- 6 R. Saint-Fort, in *Principles and Applications in Nuclear Engineering*, eds. R. Rahman and H. Saleh, Intech Open, 2018, pp. 121–150.
- 7 E. C. Donaldson and W. Alam, in *Wettability*, eds. E. C. Donaldson and W. Alam, Gulf Publishing Company, 2008, pp. 57–119.
- 8 C. Hazarika and S. Sharma, Survey on ion sensitive field effect transistor from the view point of pH sensitivity and drift, *Indian J. Sci. Technol.*, 2017, **10**, 1–18.
- 9 K. B. Oldham, A Gouy-Chapman-Stern model of the double layer at a (metal)/(ionic liquid) interface, *J. Electroanal. Chem.*, 2008, **613**, 131–138.
- 10 J. Bénard, Y. Berthier, F. Delarnare, E. Hondros, M. Huber, P. Marcus, A. Masson, J. Oudar and G. E. Rhead, Eds., in *Studies in Surface Science and Catalysis*, Elsevier, 1983, vol. 13, pp. 211–244.
- 11 G. E. Brown, V. E. Henrich, W. H. Casey, D. L. Clark, C. Eggleston, A. Felmy, D. W. Goodman, M. Grätzel, G. Maciel, M. I. McCarthy, K. H. Nealson, D. A. Sverjensky, M. F. Toney and J. M. Zachara, Metal oxide surfaces and their interactions with aqueous solutions and microbial organisms, *Chem. Rev.*, 1999, **99**, 77–174.
- 12 P. Atkins and J. de Paula, *Physical Chemistry*, W. H. Freeman and Company, 8th edn., 2006, vol. 272.
- 13 International Atomic Energy Agency, *New methods and techniques for decontamination in maintenance or decommissioning operations*, 1998, vol. 1101–4289.
- 14 J. Severa and J. Bár, in *Handbook of Radioactive Contamination and Decontamination*, Elsevier, 1991, pp. 1–161.
- 15 M. I. Ojovan, W. E. Lee and S. N. Kalmykov, in *An Introduction to Nuclear Waste Immobilisation*, Elsevier, 3rd edn., 2019, pp. 145–154.
- 16 MIT, in *The Future of Nuclear Power*, MIT, 2003, pp. 29–35.
- 17 J. Burton and M. A. Katzenberg, in *Biological Anthropology of the Human Skeleton*, eds. M. A. Katzenberg and A. Grauer, Wiley, 3rd edn., 2018, pp. 505–514.
- 18 R. Sureda, X. Martínez-Lladó, M. Rovira, J. de Pablo, I. Casas and J. Giménez,

- Sorption of strontium on uranyl peroxide: implications for a high-level nuclear waste repository, *J. Hazard. Mater.*, 2010, **181**, 881–885.
- 19 P. Bjerregaard and O. Andersen, in *Handbook on the Toxicology of Metals*, Academic Press, 3rd edn., 2007, pp. 251–280.
 - 20 F. Rouppert, A. Rivoallan and C. Largeron, in *Waste Management*, 2000, vol. February.
 - 21 F. R. Livens and P. J. Loveland, The influence of soil properties on the environmental mobility of cesium in Cumbria, *Soil Use Manag.*, 1988, **4**, 69–75.
 - 22 F. Giannakopoulou, C. Haidouti, A. Chronopoulou and D. Gasparatos, Sorption behavior of cesium on various soils under different pH levels, *J. Hazard. Mater.*, 2007, **149**, 553–556.
 - 23 M. Gutierrez and H. R. Fuentes, A mechanistic modeling of montmorillonite contamination by cesium sorption, *Appl. Clay Sci.*, 1996, **11**, 11–24.
 - 24 H. Qin, Y. Yokoyama, Q. Fan, H. Iwatani, K. Tanaka, A. Sakaguchi, Y. Kanai, J. Zhu, Y. Onda and Y. Takahashi, Investigation of cesium adsorption on soil and sediment samples from Fukushima prefecture by sequential extraction and EXAFS technique, *Geochem. J.*, 2012, **46**, 297–302.
 - 25 J. M. B. Moreno, M. Betti and G. Nicolaou, Determination of cesium and its isotopic composition in nuclear samples using isotope dilution-ion chromatography-inductively coupled plasma mass spectrometry, *J. Anal. At. Spectrom.*, 1999, **14**, 875–879.
 - 26 A. H. Fleitman, R. B. Herchenroeder and J. G. Y. Chow, Cobalt-base alloys for use in nuclear reactors, *Nucl. Eng. Des.*, 1971, **15**, 345–362.
 - 27 D. Lison, in *Handbook on the Toxicology of Metals*, eds. G. F. Nordberg, B. A. Fowler, M. Nordberg and L. T. Friberg, Academic Press, 3rd edn., 2007, pp. 511–528.
 - 28 C. Adam, J. Garnier-Laplace and S. Roussel-Debet, *Radionuclide fact sheet: Cobalt-60 and the environment*, 2001.
 - 29 C. A. Backes, R. G. McLaren, A. W. Rate and R. S. Swift, Kinetics of cadmium and cobalt desorption from iron and manganese oxides, *Soil Sci. Soc. Am. J.*, 1995, **59**,

- 778–785.
- 30 S. Handley-Sidhu, T. K. Mullan, Q. Grail, M. Albadarneh, T. Ohnuki and L. E. Macaskie, Influence of pH, competing ions, and salinity on the sorption of strontium and cobalt onto biogenic hydroxyapatite, *Sci. Rep.*, 2016, **6**, 4–11.
 - 31 K. Varga, G. Hirschberg, Z. Németh, G. Myburg, J. Schunk and P. Tilky, Accumulation of radioactive corrosion products on steel surfaces of VVER-type nuclear reactors. II. ^{60}Co , *J. Nucl. Mater.*, 2001, **298**, 231–238.
 - 32 K. M. Krupka and R. J. Serne, *Geochemical Factors Affecting the Behavior of Antimony, Cobalt, Europium, Technetium, and Uranium in Vadose Sediments*, 2002.
 - 33 D. E. Volkman, in *Significance of Tests and Properties of Concrete and Concrete-Making Materials*, eds. J. Lamond and J. Pielert, ASTM International, 2006, pp. 570–577.
 - 34 D. L. Fillmore, *Literature Review of the Effects of Radiation and Temperature on the Aging of Concrete*, 2004.
 - 35 M. Kanema, A. Noumowe, J. L. Gallias and R. Cabrillac, in *18th International Conference on Structural Mechanics in Reactor Technology (SMiRT 18)*, 2005, pp. 2297–2305.
 - 36 V. Kodur, Properties of concrete at elevated temperatures, *ISRN Civ. Eng.*, 2014, 1–16.
 - 37 R. Demmer, J. Drake and R. James, in *Waste Management*, 2014, vol. March, pp. 1–11.
 - 38 W. Lin, A. Cheng, R. Huang, C. Chen and X. Zhou, Effect of calcium leaching on the properties of cement-based composites, *J. Wuhan Univ. Technol. Mater. Sci. Ed.*, 2011, **26**, 990–997.
 - 39 S. Setunge, N. Nguyen, B. L. Alexander and L. Dutton, Leaching of alkali from concrete in contact with waterways, *Water Air Soil Pollut. Focus*, 2009, **9**, 381–391.
 - 40 R. Alizadeh, J. J. Beaudoin and L. Raki, Mechanical properties of calcium silicate hydrates, *Mater. Struct. Constr.*, 2011, **44**, 13–28.
 - 41 A. Madadi and J. Wei, Characterization of calcium silicate hydrate gels with different

- calcium to silica ratios and polymer modifications, *Gels*, 2022, **8**, 1–17.
- 42 K. O. Olusola and O. Joshua, Effect of nitric acid concentration on the compressive strength of laterized concrete, *Civ. Environ. Res.*, 2012, **2**, 48–58.
 - 43 B. Pomaro, A review on radiation damage in concrete for nuclear facilities: from experiments to modeling, *Model. Simul. Eng.*, 2016, **4165746**, 1–10.
 - 44 D. J. Naus, C. B. Oland and B. R. Ellingwood, *Report on Aging of Nuclear Power Plant Reinforced Concrete Structures*, 1996, vol. NUREG/CR-6.
 - 45 H. Hilsdorf, J. Kropp and H. Koch, in *American Concrete Institute*, 1978, vol. SP 55-10, pp. 223–254.
 - 46 K. G. Field, I. Remec and Y. Le Pape, Radiation effects in concrete for nuclear power plants - Part I: Quantification of radiation exposure and radiation effects, *Nucl. Eng. Des.*, 2015, **282**, 126–143.
 - 47 Y. Reches, A multi-scale review of the effects of gamma radiation on concrete, *Results Mater.* 2, 2019, 1–13.
 - 48 A. Bath, G. Deissmann and S. Jefferis, in *9th International Conference on Radioactive Waste Management and Environmental Remediation, ICM'03*, 2003, vol. 4814, pp. 1–8.
 - 49 J. Tits, E. Wieland, C. J. Müller, C. Landesman and M. H. Bradbury, Strontium binding by calcium silicate hydrates, *J. Colloid Interface Sci.*, 2006, **300**, 78–87.
 - 50 N. D. M. Evans, Binding mechanisms of radionuclides to cement, *Cem. Concr. Res.*, 2008, **38**, 543–553.
 - 51 M. Ochs, D. Mallants and L. Wang, in *Radionuclide and Metal Sorption on Cement and Concrete*, Springer, 2015, pp. 45–60.
 - 52 E. Wieland, J. Tits, D. Kunz and R. Dähn, Strontium uptake by cementitious materials, *Environ. Sci. Technol.*, 2008, **42**, 403–409.
 - 53 A. Baldermann, V. Preissegger, S. Šimić, I. Letofsky-Papst, F. Mittermayr and M. Dietzel, Uptake of aqueous heavy metal ions (Co²⁺, Cu²⁺ and Zn²⁺) by calcium-aluminium-silicate-hydrate gels, *Cem. Concr. Res.*, 2021, **147**, 1–14.

- 54 E. Duque-Redondo, K. Yamada and H. Manzano, Cs retention and diffusion in C-S-H at different Ca/Si ratio, *Cem. Concr. Res.*, 2021, **140**, 106294.
- 55 I. Sato, K. Maeda, M. Suto, M. Osaka, T. Usuki and S. I. Koyama, Penetration behavior of water solution containing radioactive species into dried concrete/mortar and epoxy resin materials, *J. Nucl. Sci. Technol.*, 2015, **52**, 580–587.
- 56 IEAE Nuclear Energy Series, *Decommissioning of Pools in Nuclear Facilities*, 2015, vol. NW-T-2.6.
- 57 A. C. Gray and D. F. C. Morris, Sorption of radionuclides by surface coatings, *Radiochim. Acta*, 1982, **31**, 153–156.
- 58 K. Yamada, Y. Takeuchi, G. Igarashi and M. Osako, Field survey of radioactive cesium contamination in concrete after the Fukushima-Daiichi nuclear power station accident, *J. Adv. Concr. Technol.*, 2019, **17**, 659–672.
- 59 E. B. Farfán, S. P. Gaschak, A. M. Maksymenko, E. H. Donnelly, M. D. Bondarkov, G. T. Jannik and J. C. Marra, Assessment of ⁹⁰Sr and ¹³⁷Cs penetration into reinforced concrete (extent of “deepening”) under natural atmospheric conditions, *Health Phys.*, 2011, **101**, 311–320.
- 60 W. R. Bower, K. Morris, J. F. W. Mosselmans, O. R. Thompson, A. W. Banford, K. Law and R. A. D. Patrick, Characterising legacy spent nuclear fuel pond materials using microfocus X-ray absorption spectroscopy, *J. Hazard. Mater.*, 2016, **317**, 97–107.
- 61 A. N. Haddad, in *17th International Conference on Nuclear Engineering*, ASME, 2009, pp. 1–6.
- 62 K. Tian, C. H. Benson, Y. Yang and J. M. Tinjum, Radiation dose and antioxidant depletion in a HDPE geomembrane, *Geotext. Geomembranes*, 2018, **46**, 426–435.
- 63 B. Gewert, M. M. Plassmann and M. Macleod, Pathways for degradation of plastic polymers floating in the marine environment, *Environ. Sci. Process. Impacts*, 2015, **17**, 1513–1521.
- 64 B. Bartoníček, V. Hnát and V. Plaček, Ageing monitoring of plastics used in nuclear power plants by DSC, *J. Therm. Anal. Calorim.*, 2001, **64**, 571–576.

- 65 Y. Jia, J. Chen, H. Asahara, T. A. Asoh and H. Uyama, Polymer surface oxidation by light-activated chlorine dioxide radical for metal-plastics adhesion, *ACS Appl. Polym. Mater.*, 2019, **1**, 3452–3458.
- 66 W. W. Parkinson and O. Sisman, The use of plastics and elastomers in nuclear radiation, *Nucl. Eng. Des.*, 1971, **17**, 247–280.
- 67 V. J. Krasnansky, B. G. Achhammer and M. S. Parker, Effect of gamma radiation on chemical structure of plastics, *SPE Trans.*, 1961, 133–138.
- 68 G. A. Whyatt and R. K. Farnsworth, in *Symposium on Geosynthetic Testing for Waste Containment Applications*, ed. R. M. Koerner, ASTM, 1990, vol. January, pp. 110–124.
- 69 J. N. Tomlinson, D. E. Kline and J. A. Sauer, Effect of nuclear radiation on the thermal conductivity of polyethylene, *SPE Trans.*, 1965, **January**, 44–48.
- 70 N. Merah, F. Saghir, Z. Khan and A. Bazoune, Effect of temperature on tensile properties of HDPE pipe material, *Plast. Rubber Compos.*, 2006, **35**, 226–230.
- 71 H. Jeon, Y. Jang and K. Lee, in *Proceedings of the 4th Asian Regional Conference on Geosynthetics*, eds. G. Li, Y. Chen and X. Tang, Springer, 2008, pp. 30–34.
- 72 F. Gassner and B. Wrench, Lined storage facilities for mine waste – considerations and benefits, *Mine Waste*, 2010, 275–281.
- 73 R. K. Rowe and F. B. Abdelaal, Antioxidant depletion in high-density polyethylene (HDPE) geomembrane with hindered amine light stabilizers (HALS) in low-pH heap leach environment, *Can. Geotech. J.*, 2016, **53**, 1612–1627.
- 74 F. B. Abdelaal, R. K. Rowe, Y. G. Hsuan and R. Awad, Effect of high temperatures on the physical and mechanical properties of HDPE geomembranes in air, *Geosynth. Int.*, 2015, **22**, 207–224.
- 75 W. Ghabeche, L. Alimi and K. Chaoui, Degradation of plastic pipe surfaces in contact with an aggressive acidic environment, *Energy Procedia*, 2015, **74**, 351–364.
- 76 I. Ioannidis, A. Xenofontos and I. Anastopoulos, Americium sorption by microplastics in aqueous solutions, *Coatings*, 2022, **12**, 1452 1–9.

- 77 Y. Cao, M. Zhao, X. Ma, Y. Song, S. Zuo, H. Li and W. Deng, A critical review on the interactions of microplastics with heavy metals: mechanism and their combined effect on organisms and humans, *Sci. Total Environ.*, 2021, **788**, 147620.
- 78 M. P. Johansen, E. Prentice, T. Cresswell and N. Howell, Initial data on adsorption of Cs and Sr to the surfaces of microplastics with biofilm, *J. Environ. Radioact.*, 2018, **190–191**, 130–133.
- 79 L. A. Holmes, A. Turner and R. C. Thompson, Adsorption of trace metals to plastic resin pellets in the marine environment, *Environ. Pollut.*, 2012, **160**, 42–48.
- 80 T. Artham, M. Sudhakar, R. Venkatesan, C. Madhavan Nair, K. V. G. K. Murty and M. Doble, Biofouling and stability of synthetic polymers in sea water, *Int. Biodeterior. Biodegrad.*, 2009, **63**, 884–890.
- 81 J. L. Means, D. A. Crerar, M. P. Borcsik and J. O. Duguid, Adsorption of Co and selected actinides by Mn and Fe oxides in soils and sediments, *Geochim. Cosmochim. Acta*, 1978, **42**, 1763–1773.
- 82 J. Zou, X. Liu, D. Zhang and X. Yuan, Chemosphere adsorption of three bivalent metals by four chemical distinct microplastics, *Chemosphere*, 2020, **248**, 126064.
- 83 O. D. Agboola and N. U. Benson, Physisorption and chemisorption mechanisms influencing micro (nano) plastics-organic chemical contaminants interactions: a review, *Front. Environ. Sci.*, 2021, **9**, 1–27.
- 84 M. A. Pascall, M. E. Zabik, M. J. Zabik and R. J. Hernandez, Uptake of polychlorinated biphenyls (PCBs) from an aqueous medium by polyethylene, polyvinyl chloride, and polystyrene films, *J. Agric. Food Chem.*, 2005, **53**, 164–169.
- 85 T. H. Uber, T. Hüffer, S. Planitz and T. C. Schmidt, Characterization of sorption properties of high-density polyethylene using the poly-parameter linearfree-energy relationships, *Environ. Pollut.*, 2019, **248**, 312–319.
- 86 X. Guo, G. Hu, X. Fan and H. Jia, Sorption properties of cadmium on microplastics: the common practice experiment and a two-dimensional correlation spectroscopic study, *Ecotoxicol. Environ. Saf.*, 2020, **190**, 110118.
- 87 S. M. Mitroka, T. D. Smiley, J. M. Tanko and A. M. Dietrich, Reaction mechanism for

- oxidation and degradation of high-density polyethylene in chlorinated water, *Polym. Degrad. Stab.*, 2013, **98**, 1369–1377.
- 88 O. Alam, L. Yang and X. Yanchun, Determination of the selected heavy metal and metalloid contents in various types of plastic bags, *J. Environ. Heal. Sci. Eng.*, 2019, **17**, 161–170.
 - 89 S. Khan and A. Khan, Toxic heavy metal contamination in locally made plastic food container, *Int. J. Sci. Eng. Res.*, 2015, **6**, 45–47.
 - 90 M. Whitt, K. Vorst, W. Brown, S. Baker and L. Gorman, Survey of heavy metal contamination in recycled polyethylene terephthalate used for food packaging, *J. Plast. Film Sheeting*, 2012, **0**, 1–11.
 - 91 K. Tazaki, M. Nakano, T. Takehara, Y. Ishigaki and H. Nakagawa, Experimental analysis of plastic materials containing radionuclides for decontamination viability, *Earth Sci.*, 2015, **69**, 99–108.
 - 92 R. El Zrelli, L. Yacoubi, S. Castet, M. Grégoire, C. Josse, J. Olive, P. Courjault-Radé, P. van Beek, T. Zambardi, M. Souhaut, J. E. Sonke and L. J. Rabaoui, PET plastics as a Trojan horse for radionuclides, *J. Hazard. Mater.*, 2023, **441**, 129886 1–11.
 - 93 H. Bhadeshia and R. Honeycombe, *Steels: Microstructure and Properties*, Elsevier, 3rd edn., 2006.
 - 94 R. K. Desu, H. N. Krishnamurthy, A. Balu, A. K. Gupta and S. K. Singh, Mechanical properties of austenitic stainless steel 304L and 316L at elevated temperatures, *J. Mater. Res. Technol.*, 2016, **5**, 13–20.
 - 95 G. S. Was and S. Ukai, in *Structural Alloys for Nuclear Energy Applications*, eds. G. R. Odette and S. J. Zinkle, Elsevier, 2019, pp. 293–347.
 - 96 D. L. Roll, Passivation and the passive layer, https://astropak.com/wp-content/uploads/2014/07/the_passive_layer.pdf.
 - 97 L. W. Zahner, in *Stainless Steel Surfaces*, Wiley, 2019, pp. 249–276.
 - 98 B. Elsener and A. Rossi, in *Encyclopedia of Interfacial Chemistry: Surface Science and Electrochemistry*, ed. K. Wandelt, Elsevier, 2018, pp. 365–375.

- 99 L. Freire, M. J. Carmezim, M. G. S. Ferreira and M. F. Montemor, The passive behaviour of AISI 316 in alkaline media and the effect of pH: A combined electrochemical and analytical study, *Electrochim. Acta*, 2010, **55**, 6174–6181.
- 100 D. Hamm, K. Ogle, C. O. Olsson, S. Weber and D. Landolt, Passivation of Fe-Cr alloys studied with ICP-AES and EQCM, *Corros. Sci.*, 2002, **44**, 1443–1456.
- 101 Z. Duan, F. Arjmand, L. Zhang and H. Abe, Investigation of the corrosion behavior of 304L and 316L stainless steels at high-temperature borated and lithiated water, *J. Nucl. Sci. Technol.*, 2016, **53**, 1435–1446.
- 102 R. Parrott and H. Pitts, *Chloride Stress Corrosion Cracking in Austenitic Stainless Steel*, 2011.
- 103 D. H. Lister and W. G. Cook, in *The Essential CANDU*, ed. W. J. Garland, UNENE, 2014, pp. 1–54.
- 104 J. W. Simmons, Overview: high-nitrogen alloying of stainless steels, *Mater. Sci. Eng. A*, 1996, **207**, 159–169.
- 105 R. D. Shaw, Corrosion prevention and control at Sellafield nuclear fuel reprocessing plant, *Br. Corros. J.*, 1990, **25**, 97–107.
- 106 C. J. Dodge, A. J. Francis, J. B. Gillow, G. P. Halada, C. Eng and C. R. Clayton, Association of uranium with iron oxides typically formed on corroding steel surfaces, *Environ. Sci. Technol.*, 2002, **36**, 3504–3511.
- 107 C. W. Eng, G. P. Halada, A. J. Francis, C. J. Dodge and J. B. Gillow, Uranium association with corroding carbon steel surfaces, *Surf. Interface Anal.*, 2003, **35**, 525–535.
- 108 H. Filipská and K. Štamberg, Sorption of Cs(I) and Sr(II) on a mixture of bentonite and magnetite using SCM + IExM: a parametric study, *J. Radioanal. Nucl. Chem.*, 2006, **270**, 531–542.
- 109 A. R. Lang, D. L. Engelberg, C. Walther, M. Weiss, H. Bosco, A. Jenkins, F. R. Livens and G. T. W. Law, Cesium and strontium contamination of nuclear plant stainless steel: implications for decommissioning and waste minimization, *ACS Omega*, 2019, **4**, 14420–14429.

- 110 P. Kádár, K. Varga, Z. Németh, N. Vajda, T. Pintér and J. Schunk, Accumulation of uranium, transuranium and fission products on stainless steel surfaces. I. A comprehensive view of the experimental parameters influencing the extent and character of the contamination, *J. Radioanal. Nucl. Chem.*, 2010, **284**, 303–308.
- 111 F. Rouppert, A. Rivoallan and C. Largeron, in *Waste Management*, 2002, vol. February, pp. 1–8.
- 112 R. Répánszki, Z. Kerner and G. Nagy, Adsorption of fission products on stainless steel and zirconium, *Adsorption*, 2007, **13**, 201–207.
- 113 P. Dombovári, P. Kádár, T. Kovács, J. Somlai, K. Radó, I. Varga, R. Buják, K. Varga, P. Halmos, J. Borszéki, J. Kónya, N. M. Nagy, L. Kövér, D. Varga, I. Cserny, J. Tóth, L. Fodor, A. Horváth, T. Pintér and J. Schunk, Accumulation of uranium on austenitic stainless steel surfaces, *Electrochim. Acta*, 2007, **52**, 2542–2551.
- 114 A. R. Lang, University of Manchester, 2017.
- 115 National Research Council, *Affordable Cleanup? Opportunities for cost reduction in the decontamination and decommissioning of the nation's uranium enrichment facilities*, National Academies Press, 1996.
- 116 M. T. Cross, T. H. Green and I. Adsley, in *Nuclear Decommissioning: Planning, Execution and International Experience*, ed. M. Laraia, Woodhead Publishing Limited, 2012, pp. 87–116.
- 117 I. M. Omoniyi, S. M. B. Oludare and O. M. Oluwaseyi, Determination of radionuclides and elemental composition of clay soils by gamma- and X-ray spectrometry, *Springerplus*, 2013, **2**, 1–11.
- 118 I. W. Croudace, B. C. Russell and P. W. Warwick, Plasma source mass spectrometry for radioactive waste characterisation in support of nuclear decommissioning: a review, *J. Anal. At. Spectrom.*, 2017, **32**, 494–526.
- 119 S. Dhara and N. L. Misra, Elemental characterization of nuclear materials using total reflection X-ray fluorescence spectrometry, *Trends Anal. Chem.*, 2019, **116**, 31–43.
- 120 M. R. Smith, E. J. Wyse and D. W. Koppenaal, Radionuclide detection by inductively coupled plasma mass spectrometry: a comparison of atomic and radiation detection

- methods, *J. Radioanal. Nucl. Chem. Artic.*, 1992, **160**, 341–354.
- 121 T. Kerry, A. W. Banford, O. R. Thompson, T. Carey, D. Schild, A. Geist and C. A. Sharrad, Transuranic contamination of stainless steel in nitric acid, *J. Nucl. Mater.*, 2017, **493**, 436–441.
 - 122 S. Legnaioli, B. Campanella, F. Poggialini, S. Pagnotta, M. A. Harith, Z. A. Abdel-Salam and V. Palleschi, Industrial applications of laser-induced breakdown spectroscopy: A review, *Anal. Methods*, 2020, **12**, 1014–1029.
 - 123 L. Jolivet, M. Leprince, S. Moncayo, L. Sorbier, C. P. Lienemann and V. Motto-Ros, Review of the recent advances and applications of LIBS-based imaging, *Spectrochim. Acta Part B*, 2019, **151**, 41–53.
 - 124 Q. Lin, Z. Wei, M. Xu, S. Wang, G. Niu, K. Liu, Y. Duan and J. Yang, Laser-induced breakdown spectroscopy for solution sample analysis using porous electrospun ultrafine fibers as a solid-phase support, *RSC Adv.*, 2014, **4**, 14392–14399.
 - 125 V. Sturm and R. Noll, Laser-induced breakdown spectroscopy of gas mixtures of air, CO₂, N₂, and C₃H₈ for simultaneous C, H, O, and N measurement, *Appl. Opt.*, 2003, **42**, 6221–6225.
 - 126 A. Bolshakov, LIBS at work on Mars, <https://appliedspectra.com/mars-lib.html#:~:text=LIBS technology has been deployed,Rover Curiosity since August 2012.&text=Since then LIBS has worked,about 1%2C500 individual target locations>.
 - 127 R. Noll, *Laser-Induced Breakdown Spectroscopy (LIBS): Fundamentals and Applications*, Springer, 1st edn., 2012.
 - 128 C. M. Davies, H. H. Telle, D. J. Montgomery and R. E. Corbett, Quantitative analysis using remote laser-induced breakdown spectroscopy (LIBS), *Spectrochim. Acta Part B At. Spectrosc.*, 1995, **50**, 1059–1075.
 - 129 V. Tankova, K. Blagoev, M. Grozeva, G. Malcheva and P. Penkova, Qualitative and quantitative laser-induced breakdown spectroscopy of bronze objects, *J. Phys. Conf. Ser.*, 2016, **700**, 1–5.
 - 130 R. C. Chinni, D. A. Cremers, L. J. Radziemski, M. Bostian and C. Navarro-Northrup, Detection of uranium using laser-induced breakdown spectroscopy, *Appl. Spectrosc.*,

- 2009, **63**, 1238–1250.
- 131 F. Anabitarte, A. Cobo and J. M. Lopez-Higuera, Laser-induced breakdown spectroscopy: fundamentals, applications and challenges, *ISRN Spectrosc.*, 2012, **285240**, 1–12.
 - 132 D. Cremers and L. Radziemski, in *Handbook of Laser-Induced Breakdown Spectroscopy*, Wiley, 2nd edn., 2013, p. 5.
 - 133 NIST, Atomic spectra database, <https://www.nist.gov/pml/atomic-spectra-database>.
 - 134 B. Bhatt, K. H. Angeyo and A. Dehayem-Kamadjeu, Rapid nuclear forensics analysis via laser based microphotonic techniques coupled with chemometrics, *Energy Procedia*, 2017, **127**, 76–86.
 - 135 D. Cremers and L. Radziemski, *Handbook of Laser-Induced Breakdown Spectroscopy*, Wiley, 2nd edn., 2013.
 - 136 J. E. Barefield, E. J. Judge, K. R. Campbell, J. P. Colgan, D. P. Kilcrease, H. M. Johns, R. C. Wiens, R. E. McInroy, R. K. Martinez and S. M. Clegg, Analysis of geological materials containing uranium using laser-induced breakdown spectroscopy (LIBS), *Spectrochim. Acta Part B*, 2016, **120**, 1–8.
 - 137 E. C. Jung, D. H. Lee, J. I. Yun, J. G. Kim, J. W. Yeon and K. Song, Quantitative determination of uranium and europium in glass matrix by laser-induced breakdown spectroscopy, *Spectrochim. Acta Part B*, 2011, **66**, 761–764.
 - 138 E. J. Judge, J. M. Berg, L. A. Le, L. N. Lopez and J. E. Barefield, *LIBS spectral data for a mixed actinide fuel pellet containing uranium, plutonium, neptunium and americium*, 2012.
 - 139 J. E. Barefield, E. J. Judge, J. M. Berg, S. P. Willson, L. A. Le and L. N. Lopez, Analysis and spectral assignments of mixed actinide oxide samples using laser-induced breakdown spectroscopy (LIBS), *Appl. Spectrosc.*, 2013, **67**, 433–440.
 - 140 G. C. Y. Chan, I. Choi, X. Mao, V. Zorba, O. P. Lam, D. K. Shuh and R. E. Russo, Isotopic determination of uranium in soil by laser-induced breakdown spectroscopy, *Spectrochim. Acta Part B*, 2016, **122**, 31–39.

- 141 C. Rinaldi, M. Pozzi, N. Boggio and J. Vorobioff, Isotopic analysis of uranium by laser-induced breakdown spectroscopy, *Spectrochim. Acta Part B*, 2020, **167**, 105841 1–6.
- 142 M. Z. Martin, S. Allman, D. J. Brice, R. C. Martin and N. O. Andre, Exploring laser-induced breakdown spectroscopy for nuclear materials analysis and in-situ applications, *Spectrochim. Acta - Part B At. Spectrosc.*, 2012, **74–75**, 177–183.
- 143 A. Lang, D. Engelberg, N. T. Smith, D. Trivedi, O. Horsfall, A. Banford, P. A. Martin, P. Coffey, W. R. Bower, C. Walther, M. Weiß, H. Bosco, A. Jenkins and G. T. W. Law, Analysis of contaminated nuclear plant steel by laser-induced breakdown spectroscopy, *J. Hazard. Mater.*, 2018, **345**, 114–122.
- 144 S. Ikezawa, M. Wakamatsu and T. Ueda, Detection of cesium from pollucite using laser-induced breakdown spectroscopy, *Solid State Phenom.*, 2013, **199**, 285–290.
- 145 E. A. Mokhbat and D. W. Hahn, Laser-induced breakdown spectroscopy for the analysis of cobalt-chromium orthopaedic wear debris particles, *Appl. Spectrosc.*, 2002, **56**, 984–993.
- 146 J. Li, L. Guo, N. Zhao, X. Yang, R. Yi, K. Li, Q. Zeng, X. Li, X. Zeng and Y. Lu, Determination of cobalt in low-alloy steels using laser-induced breakdown spectroscopy combined with laser-induced fluorescence, *Talanta*, 2016, **151**, 234–238.
- 147 R. Zhou, K. Liu, Z. Tang, P. Gao, J. Yan and X. Li, High-sensitivity determination of available cobalt in soil using laser-induced breakdown spectroscopy assisted with laser-induced fluorescence, *Appl. Opt.*, 2021, **60**, 9062–9066.
- 148 M. Z. Martin, S. Allman, D. J. Brice, R. C. Martin and N. O. Andre, Exploring laser-induced breakdown spectroscopy for nuclear materials analysis and in-situ applications, *Spectrochim. Acta - Part B At. Spectrosc.*, 2012, **74–75**, 177–183.
- 149 C. R. Bhatt, B. Alfarraj, K. K. Ayyalasomayajula, C. Ghany, F. Y. Yueh and J. P. Singh, Study of atomic and molecular emission spectra of Sr by laser-induced breakdown spectroscopy (LIBS), *Appl. Opt.*, 2015, **54**, 10264.
- 150 G. Wilsch, D. Schaurich, F. Weritz and H. Wiggensauser, in *International Symposium (Non-Destructive Testing in Civil Engineering)*, 2003.

- 151 S. Singh, M. Argument, Y. Y. Tsui and R. Fedosejevs, Effect of ambient air pressure on debris redeposition during laser ablation of glass, *J. Appl. Phys.*, 2005, **98**, 1–8.
- 152 B. S. Hartadi and A. Khumaeni, Analysis of calcium element in concrete using laser-induced breakdown spectroscopy, *J. Phys. Conf. Ser.*, 2019, **1217**, 1–6.
- 153 S. Millar, T. Eichler, G. Wilsch and C. Gottlieb, in *Proceedings of the 4th International Conference on Concrete Repair, Rehabilitation and Retrofitting*, 2015, pp. 273–279.
- 154 G. Wilsch, T. Eichler, S. Millar and C. Gottlieb, in *International Symposium Non-Destructive testing in Civil Engineering (NDT-CE)*, 2015, vol. September, pp. 611–615.
- 155 M. A. Gondal and M. N. Siddiqui, Identification of different kinds of plastics using laser-induced breakdown spectroscopy for waste management, *J. Environ. Sci. Heal. - Part A Toxic/Hazardous Subst. Environ. Eng.*, 2007, **42**, 1989–1997.
- 156 J. Anzano, B. Bonilla, B. Montull-Ibor and J. Casas-González, Plastic identification and comparison by multivariate techniques with laser-induced breakdown spectroscopy, *J. Appl. Polym. Sci.*, 2011, **121**, 2710–2716.
- 157 Q. Zeng, J. B. Sirven, J. C. P. Gabriel, C. Y. Tay and J. M. Lee, Laser-induced breakdown spectroscopy for plastic analysis, *TrAC - Trends Anal. Chem.*, 2021, **140**, 116280.
- 158 B. J. Marquardt, S. R. Goode and S. Michael Angel, In-situ determination of lead in paint by laser-induced breakdown spectroscopy using a fiber-optic probe, *Anal. Chem.*, 1996, **68**, 977–981.
- 159 B. Bousquet, G. Travaillé, A. Ismaël, L. Canioni, K. Michel-Le Pierrès, E. Brasseur, S. Roy, I. le Hecho, M. Larregieu, S. Tellier, M. Potin-Gautier, T. Boriachon, P. Wazen, A. Diard and S. Belbèze, Development of a mobile system based on laser-induced breakdown spectroscopy and dedicated to in-situ analysis of polluted soils, *Spectrochim. Acta Part B*, 2008, **63**, 1085–1090.
- 160 I. Gaona, J. Serrano, J. Moros and J. J. Laserna, Evaluation of laser-induced breakdown spectroscopy analysis potential for addressing radiological threats from a

- distance, *Spectrochim. Acta Part B*, 2014, **96**, 12–20.
- 161 B. T. Manard, M. F. Schappert, E. M. Wylie and G. E. McMath, Investigation of handheld laser induced breakdown spectroscopy (HH-LIBS) for the analysis of beryllium on swipe surfaces, *Anal. Methods*, 2019, **11**, 752–759.
 - 162 J. Zhang, X. Hu, J. Xi, Z. Kong and Z. Ji, Depth profiling of Al diffusion in silicon wafers by laser-induced breakdown spectroscopy, *J. Anal. At. Spectrom.*, 2013, **28**, 1430–1435.
 - 163 C. Lefebvre, A. Catalá-Espí, P. Sobron, A. Koujelev and R. Léveillé, Depth-resolved chemical mapping of rock coatings using laser-induced breakdown spectroscopy: implications for geochemical investigations on Mars, *Planet. Space Sci.*, 2016, **126**, 24–33.
 - 164 H. Balzer, M. Hoehne, V. Sturm and R. Noll, Online coating thickness measurement and depth profiling of zinc coated sheet steel by laser-induced breakdown spectroscopy, *Spectrochim. Acta Part B*, 2005, **60**, 1172–1178.
 - 165 Nuclear Energy Agency, *Decontamination Techniques Used in Decommissioning Activities*, 1999.
 - 166 US Environmental Protection Agency, *Decontamination of cesium, cobalt, strontium, and americium from porous surfaces.*, 2013.
 - 167 A. Gossard, A. Lilin and S. Faure, Gels, coatings and foams for radioactive surface decontamination: state of the art and challenges for the nuclear industry, *Prog. Nucl. Energy*, 2022, **149**, 104255.
 - 168 V. V. Kusumkar, M. Galamboš, E. Viglašova, M. Daňo and J. Šmelková, Ion-imprinted polymers: synthesis, characterization, and adsorption of radionuclides, *Materials (Basel)*., 2021, **14**, 1083 1–29.
 - 169 M. Kaminski, C. Mertz, M. Finck, M. Kalensky, N. Kivenas, P. De Lurgio and J. Reed, in *Waste Management*, 2020.
 - 170 I. Yaar, R. Hakmon, M. D. Kaminski, T. Stilman, S. Serre, I. Halevy, R. Bar-Ziv, N. Vainblat, Y. Iflach, M. Assulin and T. Avraham, Evaluation of hydrogel technologies for the decontamination of ¹³⁷Cs from building material surfaces, *J. Nucl. Eng.*

Radiat. Sci., 2017, **3**, 030909 1–9.

- 171 H. M. Yang, C. W. Park and K. W. Lee, Enhanced surface decontamination of radioactive Cs by self-generated, strippable hydrogels based on reversible cross-linking, *J. Hazard. Mater.*, 2019, **362**, 72–81.
- 172 J. J. Moore, T. P. Raine, A. Jenkins, F. R. Livens, K. A. Law, K. Morris, G. T. W. Law and S. G. Yeates, Decontamination of cesium and strontium from stainless steel surfaces using hydrogels, *React. Funct. Polym.*, 2019, **142**, 7–14.
- 173 S. S. Mahrous, E. H. Borai and M. S. Mansy, Polymeric gel for surface decontamination of long-lived gamma and beta-emitting radionuclides, *Appl. Radiat. Isot.*, 2023, **197**, 110834.
- 174 C. Madic and M. Hudson, *High-level liquid waste partitioning by means of completely incinerable extractants*, 1998.
- 175 Nuclear Decommissioning Authority, Nuclear Decommissioning Authority strategy effective from March 2021, <https://www.gov.uk/government/publications/nuclear-decommissioning-authority-strategy-effective-from-march-2021/nuclear-decommissioning-authority-strategy-effective-from-march-2021#integrated-waste-management>.

3. Research methods

This chapter outlines the experimental methodologies used throughout this project and the relevant theory for each technique is discussed.

3.1. Experimental methods

3.1.1. Reagents

All reagents used throughout the experiments were of analytical grade standard. Any glassware used was washed in an acid bath overnight (10% HCl) and rinsed thoroughly with deionised (DI) water (18 MΩ) before use.

3.1.2. Hunterston A legacy materials

Plastic discs and a concrete core were obtained from the decommissioned Hunterston A spent nuclear fuel (SNF) pond for analysis in Chapters 5 and 6, respectively (Figure 3.1). The samples were provided by Magnox Ltd and the National Nuclear Laboratory. Drainage of the pond began in 2011 and researchers were able to extract unique, authentic samples to provide insight into the long-term contamination of nuclear facilities.

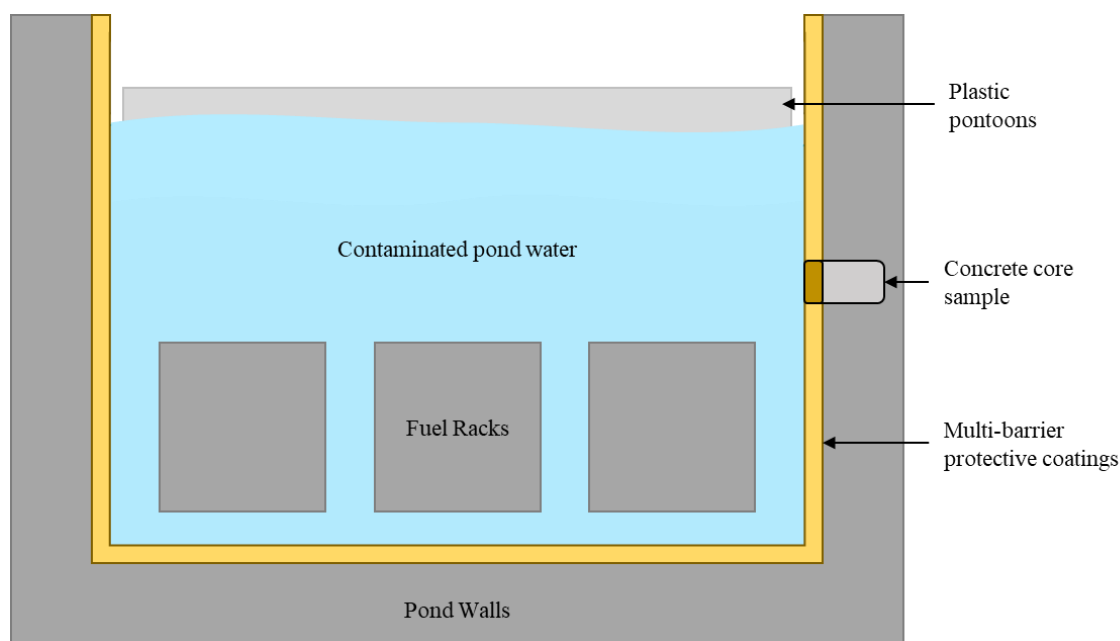


Figure 3.1. Schematic of the Hunterston A SNF pond.

The concrete core (120 x 190 mm (ø x h)) was extracted from the centre of the inner wall of the storage pond where it had been exposed to the contaminated pond water for around 50 years (Figure 3.2).

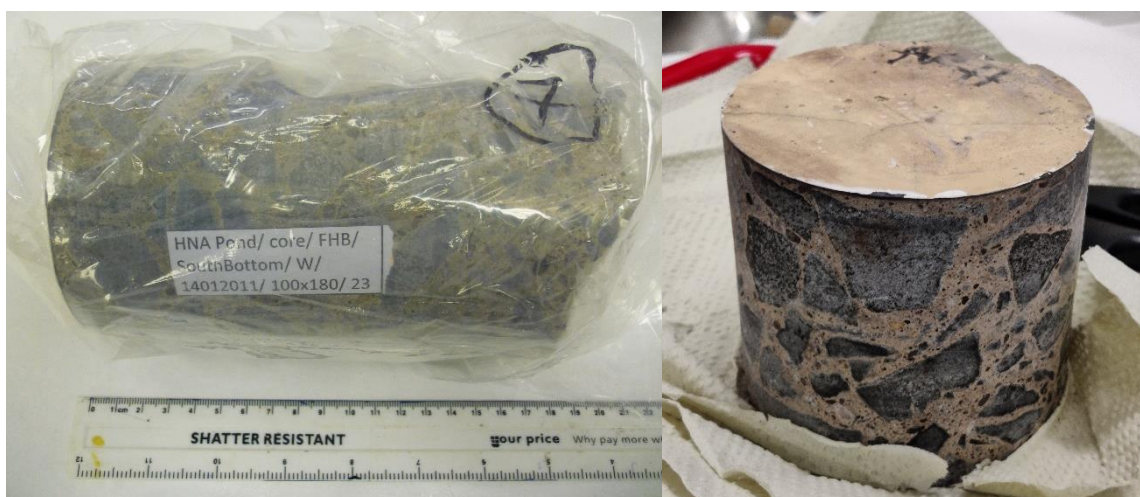


Figure 3.2. Concrete core removed from the Hunterston A SNF pond.

Multiple layers of protective coatings were applied to the concrete pond walls during plant operations to prevent contamination and minimise the uptake of activity into the surrounding structure. This consisted of a cement layer finish, a waterproof rubber coating and a protective epoxy paint topcoat containing titanium dioxide (TiO_2) pigment. The pond walls were made from ordinary Portland cement (OPC) with a mix of aggregates from the local environment.

In addition to the concrete core, samples were cut from the top, middle and bottom panels of a high-density polyethylene (HDPE) pontoon used during decommissioning operations to grant workers access to the inner, contaminated pond walls (Figure 3.3). The pontoons floated on top of the pond water, allowing workers to decontaminate the concrete walls as the pond water was drained. The discs are 10 cm in diameter and 1-2 cm thick; the top face of the pontoons was textured to provide grip, and the sides and bottom were smooth. Ultra-high-pressure jet-washing of the pond walls resulted in contaminated waste water splashing onto the surface and over the sides of the pontoons leading to contamination of the pontoons.

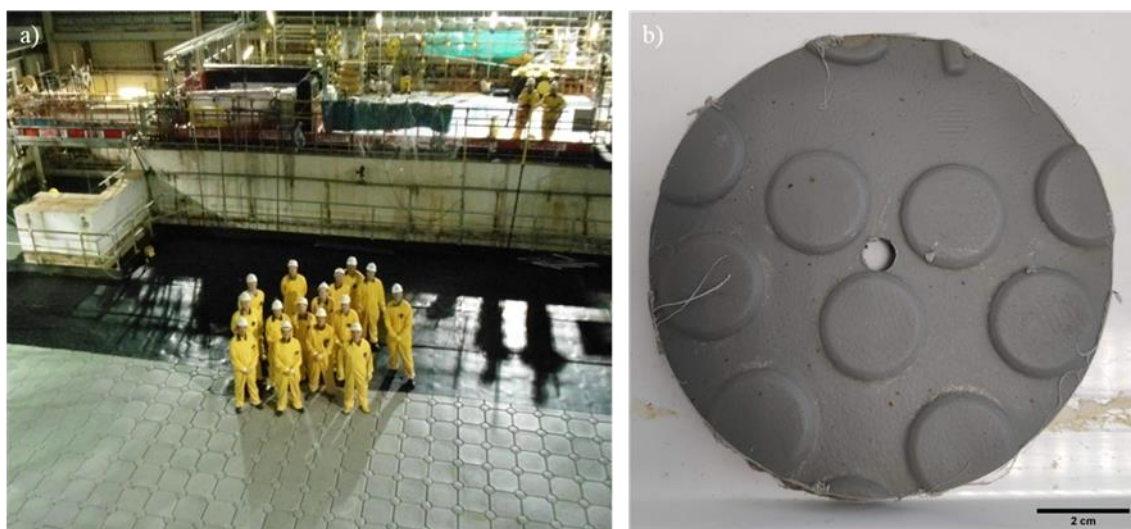


Figure 3.3. a) HDPE pontoons used to aid decommissioning of the Hunterston A SNF storage pond (Magnox Ltd, flickr).¹ b) Close up of a disc removed from the top of the pontoon.

3.1.3. Materials

In addition to the characterisation of the authentic samples, stable and active contamination experiments were conducted on HDPE and concrete coupons for comparison.

Sections from the uncontaminated bottom of the concrete core were used for the sorption studies to keep the concrete matrix the same. During cutting operations, the top, active paint section of the core was protected from water using Mylar film coatings and waterproof tape to minimise any damage or alteration to the sample surface. 30 x 30 x 10 mm (w x l x h) coupons were prepared using a Buehler IsoMet Low Speed precision cutter with a Diamond Wafering Blade (15 HC, 10.2 x 0.3 mm), using DI water as the lubricant. The coupons were ground to 2500 grit using silicon carbide grinding paper and polished down to 0.5 μm using Buehler micropolish II alumina suspension on a Buehler EcoMet 30 Auto/Manual Grinder & Polisher. Finally, the samples were washed with DI water (18 M Ω) and isopropyl alcohol (IPA) and left to air dry prior to contamination experiments.

HDPE plastic was obtained from Direct Plastics Ltd as a 2 cm diameter rod and cut into 1 cm discs to represent the pontoon materials. The coupons were ground to 2500 grit using silicon carbide grinding paper and polished down to 5 μm using Buehler micropolish II alumina suspension on a Buehler EcoMet 30 Auto/Manual Grinder & Polisher. Samples were washed with DI water (18 M Ω) and isopropyl alcohol (IPA) and left to air dry prior to contamination experiments.

Type 304L stainless steel was used for experiments in Chapter 4 (Table 3.1). This steel is commonly used in reprocessing and waste management facilities due to its increased corrosion resistance at high temperatures and low pH.^{2,3}

Table 3.1. *Composition of 304L stainless steel (adapted from Was et al.).⁴*

Element	Fe	Ni	Cr	Mn	Si	C
wt %	Balance	8.00-12.00	18.00-20.00	<2.00	<1.00	<0.03

Steel coupons (20 x 10 mm (ø x h)) were cut using ATM Brilliant 200 (rough) and 220 (precision) cutting machines. The coupons were ground to 2400 grit using silicon carbide grinding paper, followed by polishing to 1 µm using diamond suspension on a polishing cloth. Finally, the samples were degreased with ethanol before contamination experiments took place.

3.1.4. Sorption experiments

3.1.4.1. Single element system

Single element sorption experiments were conducted to determine the uptake of Sr, Cs and Co on concrete and plastic surfaces using LIBS in Chapter 4.

Simulant contaminant solutions containing 500 mg/L Sr(NO₃)₂, CsNO₃ or Co(NO₃)₂ were prepared in DI (18 MΩ) water adjusted to pH 11 using 0.1 M NaOH to replicate the alkaline SNF pond conditions. No further pH adjustments were made once the experiment started. HDPE and concrete coupons were exposed to the contaminant solutions such that a single face was in contact with the liquor and were left for 28 days at 60 °C. Sorption experiments were conducted in triplicate. Aliquots of the solution were removed at set intervals throughout the experiment and analysed using inductively coupled plasma mass spectrometry (ICP-MS; Section 3.2.2) to monitor the uptake of each analyte and any potential leaching from the concrete coupons. After 28 days the samples were removed and washed with DI water (18 MΩ) and IPA. The samples were left to air dry before being analysed with LIBS.

3.1.4.2. Contamination chamber – multi-element system

In addition to single-element sorption experiments, a contamination chamber device was designed to help improve the replicability of contamination experiments over long periods of time. The design was based on the modified Robbins device (MRD), which contains individual sample plugs that position the sample surface in contact with the solution.⁵ As a constant flow of solution was not required for this experiment, the inlets and outlets were removed to form a

simple chamber where the contaminant solution was held (Figure 3.4). The body of the holder was made from Nylon-6 due to its relative inertness and ability to withstand temperatures from 0-90 °C. Individual sample holders were fitted into slots in the lid to allow one face of the coupons direct contact with the contaminant solution. The samples could then be removed independently, allowing multiple contamination experiments to take place at different times. The chamber was built in a University of Manchester workshop.

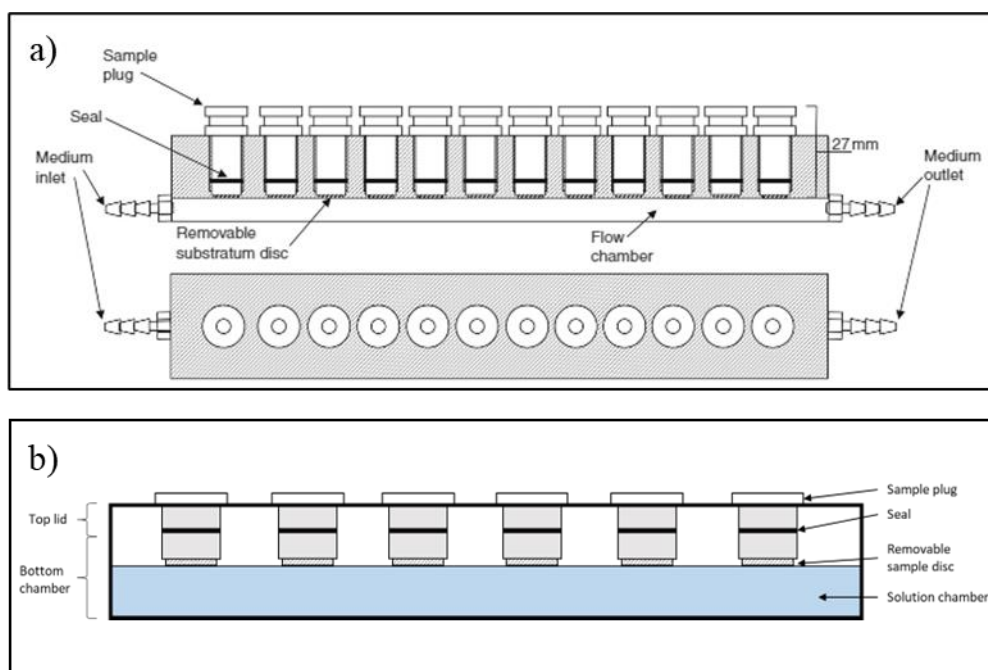


Figure 3.4. a) *Modified Robbins device used for continuous flow systems (A. McBain et al.).*⁵
b) *Design for the contamination chamber device.*

To replicate the complex SNF storage pond environment, 500 mg/L $\text{Sr}(\text{NO}_3)_2$, CsNO_3 and $\text{Co}(\text{NO}_3)_2$ were dissolved in DI water (18 M Ω) and adjusted to pH 11 using 0.1 M NaOH. No further pH adjustments were made once the experiment started. 304L stainless steel, HDPE and concrete coupons (20 x 10 mm (ϕ x h)) were prepared and 4 coupons of each material were fit into the sample holders with a single surface in contact with the liquor. The device was sealed and heated to 60 °C for 28 days. Aliquots of the solution were removed at set intervals throughout the experiment and analysed using ICP-MS to monitor the uptake of each analyte and any potential leaching or corrosion of the sample coupons. After completion of the experiment, the samples were removed, washed with DI water (18 M Ω) and IPA, and left to air dry for 1 week before analysis.

3.1.5. Radioactive sample preparation

Radioactive samples were prepared to replicate contamination of the Hunterston A materials and to allow assessment of hydrogels for decontaminating concrete and HDPE surfaces (3.1.6) in Chapters 5 and 6.

A top stock of Sr-90, Cs-137 and a mixed gamma standard (Table 3.2) were diluted to achieve a working solution of 200 Bq/mL in 0.1 M HCl. The mixed gamma standard was obtained from the National Physical Laboratory as 10 kBq 10 g nominal mass (QCP20803). 100 Bq of each Sr-90, Cs-137 or the mixed gamma standard solution was spotted onto concrete coupon surfaces and allowed to air dry for 1 week, resulting in an overall activity of 11.1 Bq/cm². 20 Bq of each active solution was spotted onto HDPE coupon surfaces, due to the smaller surface area, resulting in an overall activity of 6.4 Bq/cm².

Table 3.2. Radionuclide inventory of mixed gamma standard (adapted from IsoTrak Catalogue).⁶

Radionuclide											
Am-241	Cd-109	Co-57	Ce-139	Cr-51	Sn-113	Sr-85	Cs-137	Co-60	Y-88	Zn-65	Mn-54

3.1.6. Decontamination experiments

Polyvinylpyrrolidone (PVP) based hydrogels have been highlighted as a potential decontaminant for removal of Sr-90 and Cs-137 contamination on stainless steel surfaces.⁷ Hydrogels have been used in Chapters 5 and 6 for the decontamination of the Hunterston A samples and concrete and HDPE coupons contaminated with Sr-90, Cs-137 and other γ -emitting radionuclides.

Hydrogel pucks (20 x 20 mm (ϕ x h)) were synthesised as described in Moore *et al.*⁷ Polyvinylpyrrolidone (PVP) was dissolved in deionised (DI) water (18 M Ω) and combined with hydroxyethyl methacrylate (HEMA), *N,N'*-methylenebisacrylamide (MBAM) and azobisisobutyronitrile (AIBN). The mixture was stirred to remove any bubbles before being transferred to well plates (20 x 20 mm (ϕ x h)) and heated at 60 °C. Once cured the hydrogels were stored in deionised (DI) water (18 M Ω) until use. In addition to the H06 hydrogels, modifications were made to double the MBAM cross-linker concentration, which will be referred to as H06-2. Hydrogels were loaded in 2% HNO₃ 1 week prior to experiments to aid decontamination without affecting the hydrogel structure and functionality. Individual

hydrogels were placed on the surface of the contaminated coupon for 1, 24, 168 or 672 hours. After each time point, the hydrogel was removed and both the coupon and hydrogel were analysed using autoradiography (Section 3.4.3.). The hydrogels were stored in a sealed container to prevent them drying out prior to analysis with gamma spectroscopy (Section 3.4.2.) for Cs-137 and mixed gamma uptake, and liquid scintillation counting (LSC, Section 3.4.1.) for Sr-90 uptake.

Decontamination studies for the Hunterston A samples were conducted in a similar manner. Hydrogels were placed on sections of the HDPE discs for 1, 24, 168 and 682 hours to test the decontamination ability of the hydrogels over time. In addition, several tests were conducted where the same hydrogel was used to determine whether repeated applications resulted in further decontamination.

For the concrete core, decontamination studies were conducted on both the painted surface and a section of the concrete bulk directly below the protective layers. Hydrogels were placed on the surfaces for selected time periods of 1, 24 and 168 hours. For the painted surface, after each decontamination step, hydrogels were replaced with new hydrogels in the same location to determine the overall uptake of contamination with increasing contact time. In contrast, the same hydrogel was replaced on the bulk concrete surface after each decontamination period to determine whether repeated use was able to remove additional radioactivity from long-term contaminated concrete. Hydrogels were not left on the core surfaces for longer than 168 hours, since sorption between the painted surface and the hydrogel affected the structural integrity of the hydrogel. Analysis with autoradiography and gamma spectroscopy was conducted before moving onto the next decontamination test. After the final decontamination timepoint, hydrogels were leached in 20 mL DI water (18 MΩ) for 5 days and 2 mL aliquots were removed for analysis with liquid scintillation counting (LSC). The decontamination factor (DF) and percentage of activity removed (%R) were calculated for each hydrogel (Equations 3.1 and 3.2).

Equation 3.1. *The decontamination factor (DF).*

$$DF = \frac{A_0}{A_f}$$

where A_0 is the radioactivity on the sample surface before decontamination and A_f is the activity on the sample surface after decontamination.⁸

Equation 3.2. Conversion of *DF* to the percentage of activity removed (%*R*).

$$\%R = \left(1 - \frac{1}{DF}\right) \times 100\%$$

3.2. Aqueous analytical methods

3.2.1. pH analysis

Aqueous phase pH measurements were made using the Mettler Toledo SevenCompact digital meter with a Mettler Toledo InLab Micro-Pro-ISM electrode probe (pH). pH calibrations were conducted prior to analysis using buffer solutions at pH 2, 4, 7 and 10 (purchased from Mettler Toledo). The pH probe was washed with DI water (18 MΩ) prior to each measurement.

3.2.2. Inductively coupled plasma atomic emission spectrometry (ICP-AES) and mass spectrometry (ICP-MS)

ICP-AES and ICP-MS were used to measure ions in solution samples, using AES for major and trace elemental analysis and MS for lower concentrations.

ICP-AES and MS analysis consists of two stages. During the initial ICP stages the sample solution is passed through a nebuliser where it is split into tiny droplets.⁹ These droplets pass through the spray chamber and into a high-energy argon plasma which atomises and ionises the elements present in the sample. For ICP-AES, these excited ions can emit a photon which is characteristic to each individual element, allowing the concentration for each analyte to be determined.¹⁰

In ICP-MS, the ions are passed through a series of ion optics towards the mass spectrometer. The MS splits the ions based on their mass to charge ratio (*m/z*) through a quadrupole. ICP-MS is able to detect elements at lower concentrations to AES, at the milligram to nanogram level, per litre.¹¹

ICP-MS was used to measure the uptake of Sr, Cs and Co onto the sample materials in Chapter 4, as well as the hydrogel loading ability and determination of the Fe and Ca concentrations in each sequential extraction step in Chapters 5 and 6.

200 µL aliquots were removed from solution at the following time intervals: 0.5, 1, 3, 6, 24, 48, 168, 336, 504 and 672 hours. The aliquots were diluted to appropriate concentrations using 2% HNO₃ and transferred to centrifuge tubes. Samples were analysed using the Agilent 7500CX for ICP-MS and the Perkin-Elmer Optima 5300 DV for ICP-AES. Each sample was

performed in triplicate. The measured uptake (q_t) for Sr, Cs and Co from solution was measured for each sorption experiment (Equation 3.3).

Equation 3.3. *Measured uptake (q_t) from solution.*

$$q_t = \frac{(C_0 - C_t) \times V}{A}$$

where q_t is the amount adsorbed at time t (mg/cm²); C_0 is the initial concentration (mg/L); C_t is the concentration at time t (mg/L); V is the volume of the solution (L) and A is the surface area of the sample (cm²).

3.3. Solid analytical methods

3.3.1. Scanning electron microscopy (SEM) and electron diffraction X-ray spectroscopy (EDX/EDS)

Scanning electron microscopy (SEM) is a technique that creates high resolution and high magnification images of a sample surface.¹² A beam of high-energy electrons is focused onto the sample surface through a series of lenses (Figure 3.5). When the beam hits the surface, the electrons are either reflected back as backscattered electrons (BSE) or lead to the emission of secondary electrons (SE). SE originate in the first 5-50 nm of the sample surface and give information on the topography and morphology of the sample surface. BSE originate at greater depths and give sub-surface information about the sample composition.¹³ Other emissions, such as X-rays, infrared (IR) and ultraviolet (UV) rays, are produced during the SEM process, so the detector must be set to only collect the emissions of interest (Figure 3.6).¹⁴

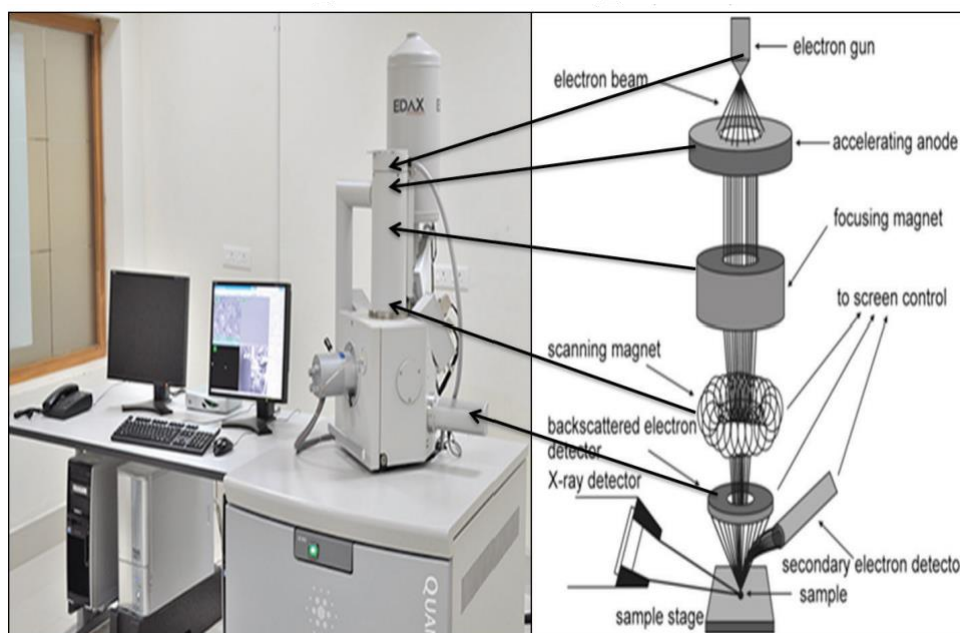


Figure 3.5. Components of a SEM instrument (M. Kannan).¹⁵

The non-destructive nature of SEM makes it a popular imaging technique and its greater depth of focus creates 3D-like images. Samples must be conductive to prevent charge build-up of the electrons on the sample surface. Overcharging leads to overly bright and poor-quality images. This process is relatively simple for metallic samples, but for powders and polymers, the sample must be coated with a conductive layer, such as gold, carbon or platinum. The combination of SEM and electron diffraction X-ray spectroscopy (EDX) have been used to identify the presence of uranium and thorium in homogenous samples, showing its efficiency and utility as an analysis technique for identification of radionuclides.¹⁶

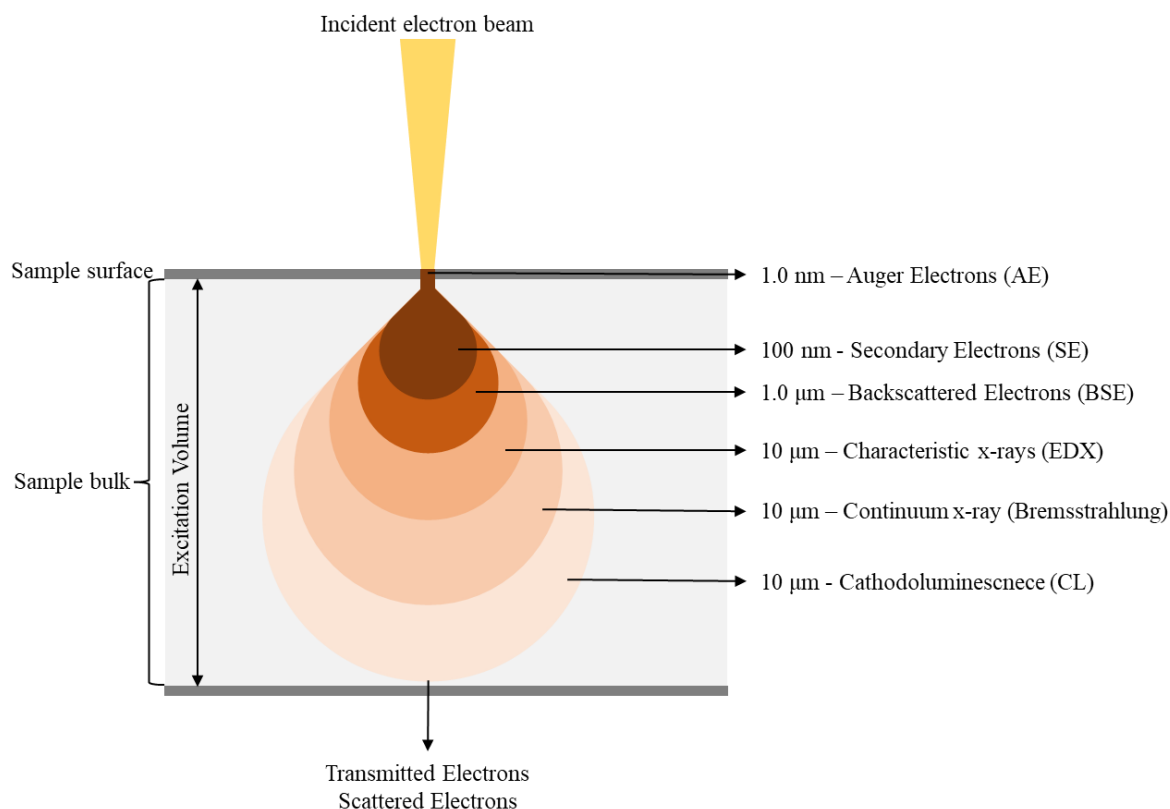


Figure 3.6. Different interactions and phenomenon that occur during SEM analysis (adapted from M. Kannan).¹⁵

Electron diffraction X-ray spectroscopy is an extension of SEM that detects any X-rays emitted during the SEM process. As X-ray emissions are characteristic to the atomic structure of the element, EDX is able to identify and quantify the elemental composition of the sample surface.¹⁷ A distribution map of the elements of interest is created based on relative emission intensity over the scanned area.¹⁸ By analysing the types of elements present and their relative abundancies, the user is able to infer the species or compound that may have formed on the sample surface. In addition, EDX is able to create a spectrum by focusing the beam on a single spot on the surface.¹⁹ This localised analysis provides information on an area of interest and can help determine whether a specific analyte may or may not be present. This is beneficial to the nuclear industry to determine the presence of key radionuclides on material surfaces.

Imaging of the HDPE, concrete and stainless steel coupon surfaces was conducted with SEM-EDX after LIBS analysis to study the craters formed on the sample surface in Chapter 4. In addition, SEM-EDX was used to image and analyse the composition of the concrete samples in Chapter 6.

High-resolution, high-magnification SEM images of the steel, concrete and HDPE samples were produced using the FEI Thermofisher Quanta 650 (E)SEM at 15 kV in high vacuum mode (10 to 10 mbar) with high resolution Bruker Quantax energy dispersive spectrometer (EDX). Thin-sections of the samples were prepared and carbon coated prior to analysis.

3.3.2. Quantitative evaluation of materials by scanning electron microscopy (QEMSCAN)

Quantitative evaluation of materials by scanning electron microscopy (QEMSCAN) is an automated analysis that combines SEM with EDX spectroscopy to produce a mineral and phase map of the sample. X-ray spectra of the sample are obtained and cross-referenced with a database of spectra of known minerals and phases to generate a composition map of the analysed sample.²⁰ It is therefore vital to conduct initial EDX analysis to determine the minerals present in the sample prior to QEMSCAN analysis. However, QEMSCAN is a time-consuming analysis technique, requiring 1-2 days for complete analysis of a single sample. Analysis of a typical concrete coupon from the bottom of the Hunterston A concrete core is described in Chapter 6. QEMSCAN was conducted on a FEI Thermofisher Quanta 650 (E)SEM.

3.3.3. Laser-induced breakdown spectroscopy (LIBS)

Laser-induced breakdown spectroscopy (LIBS) is a characterisation technique that can provide rapid, multi-elemental analysis of a sample surface. A high-energy laser pulse is used to ablate a small area of the sample, which is then atomised and ionised within a plasma (Figure 3.7). Characteristic photons are emitted by the analyte elements and picked up by a detector. LIBS can be used on a wide variety of sample materials and states and has the possibility for *in-situ* and standoff analysis as it only requires optical access to the sample surface.

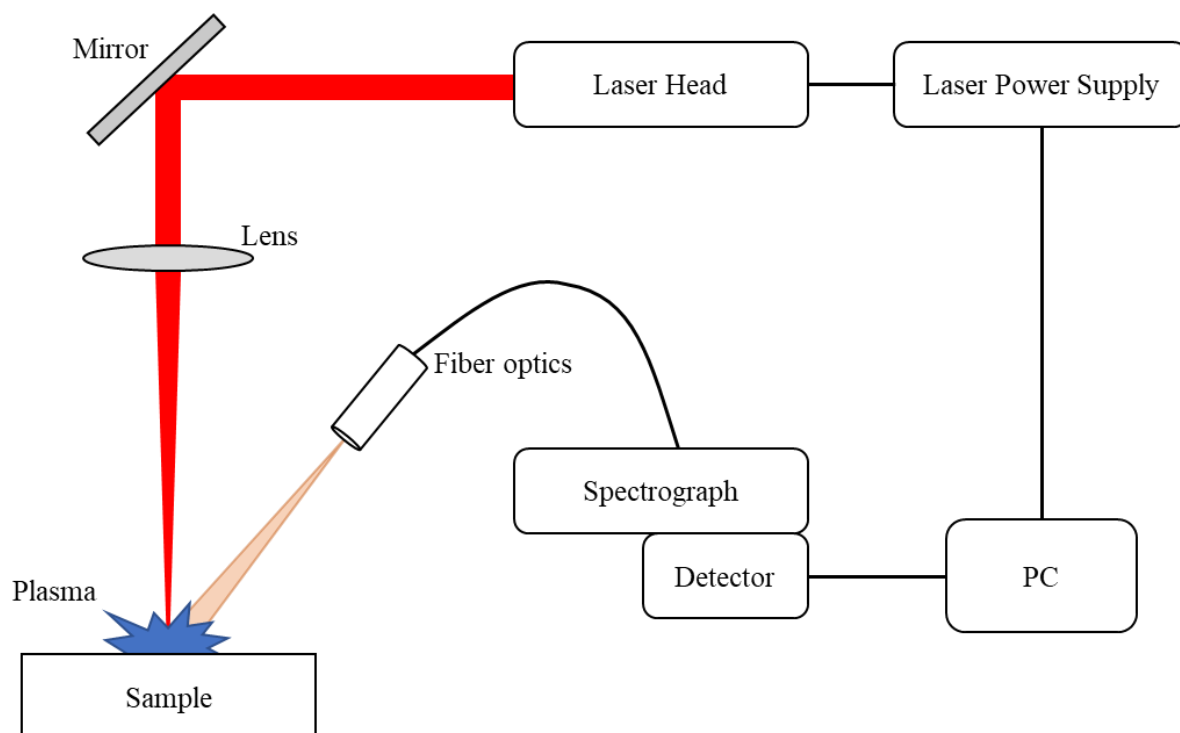


Figure 3.7. Schematic of a basic LIBS system (adapted from Cremers and Hull).^{21,22}

LIBS analysis was conducted in Chapters 4 and 5 using an Innolas Spitlight 600 laser and Aryelle Echelle spectrometer, which uses a Q-switched 1064 nm Nd:YAG pulsed laser system (10 Hz repetition rate, 7 ns pulse width) with ICCD camera (Andor iStar series). The integration time and delay time were kept constant for all experiments at 1.10 ms and 1.27 μ s, respectively. Analysis was conducted with a pulsed laser energy of 100 mJ/pulse in air at a working distance of 8 cm and over a wavelength range of 250-900 nm. The gate delay and gate width were kept constant at 1500 ns and 100 ms, respectively. Depth-profiling was conducted via multi-pulse analysis, using a series of consecutive shots aimed at the same location. Spectra were analysed using the Aryelle Sophi Software V1.03 R630 (LTB Lasertechnik Berlin).

Calibration standards were prepared for Chapter 4 by labelling concrete and HDPE surfaces with $\text{Sr}(\text{NO}_3)_2$, CsNO_3 and $\text{Co}(\text{NO}_3)_2$ solutions at concentrations ranging from 1 to 500 mg/L. 100 μ L was spotted onto a concrete surfaces and 200 μ L was spotted onto the HDPE surfaces, giving an average droplet area of $1.13 \pm 0.3 \text{ cm}^2$ (over 3 replicates). The samples were left to air dry for 1 week before analysis with LIBS. Emissions were collected for 9 shots across a 3 x 3 grid within the contamination area per spectrum. Calibration spectra were developed using the strongest emission lines for each analyte: Sr II - 407.78 nm, Cs I - 852.13 nm and Co I - 345.32 nm. Peak intensities $<3\sigma$ above background intensity were considered below the limit of detection (LOD).

Active LIBS analysis was conducted for the Hunterston A samples in Chapters 5 and 6. The samples were loaded into a chamber and sealed prior to LIBS analysis (Figure 3.8). The laser is fired through a quartz window to impact the sample, generating the plasma inside the holder without spreading contamination. The holder can be decontaminated after use. The laser setup and parameters remained the same.

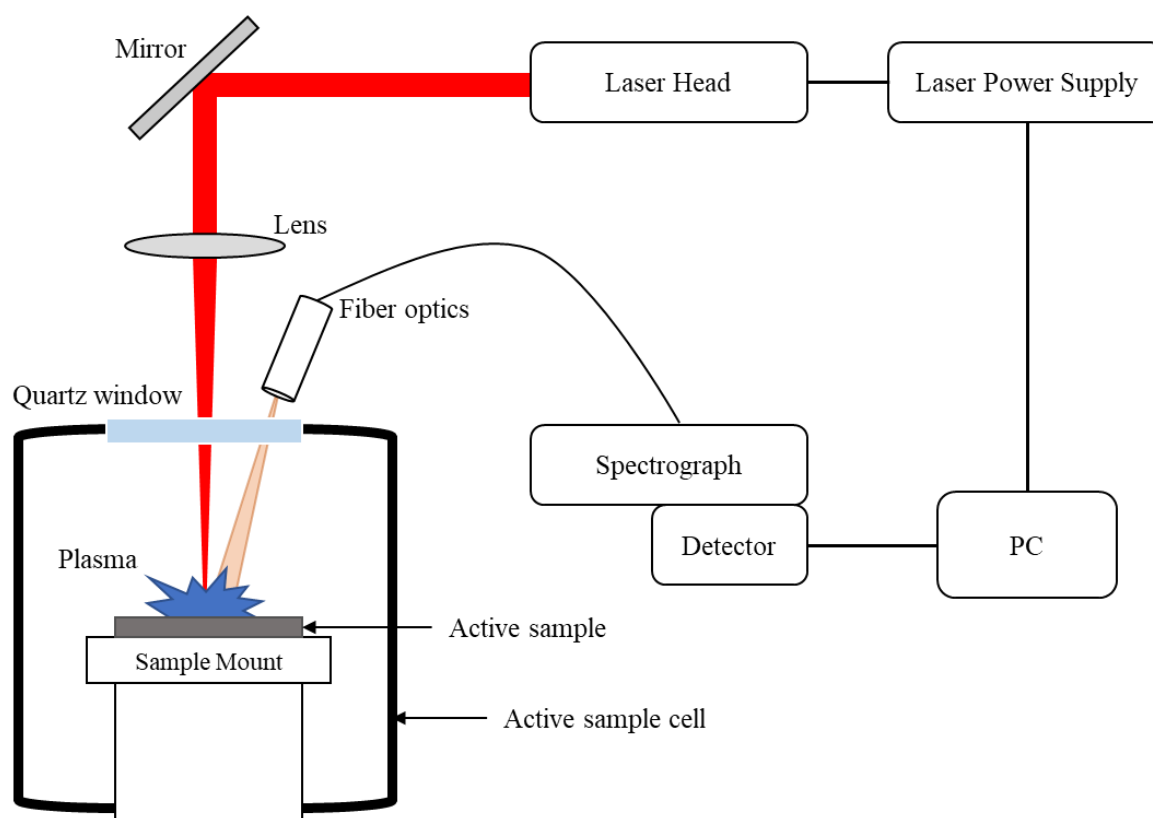


Figure 3.8. Schematic of LIBS setup for active analysis (adapted from Hull).²²

3.3.4. Powder X-ray diffraction (XRD)

Powder X-ray diffraction (XRD) provides information on the structure, phase and crystal orientation of crystalline materials. Monochromatic X-rays are fired at the sample, where they interact with the electrons in an atom (Figure 3.9). This interaction produces a diffracted X-ray only when Bragg's Law (Equation 3.4) is satisfied and constructive interference takes place.²³

Equation 3.4. Bragg's Law

$$n\lambda = 2d \sin \theta$$

where λ is the radiation wavelength; d is the lattice spacing and θ is the diffraction angle in a crystalline sample.

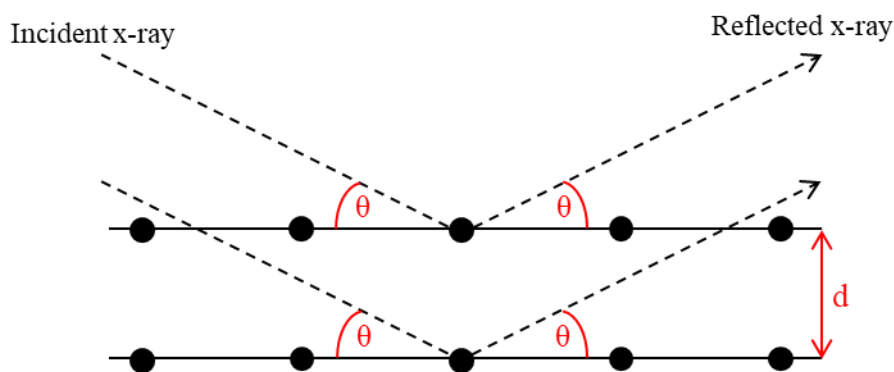


Figure 3.9. Schematic of an incident X-ray interacting with a sample to satisfy Bragg's Law (adapted from Housecroft et al.).²³

Scanning a range of angles of incidence generates a diffraction pattern which can be analysed to yield d-spacings. As each crystal structure has a distinctive diffraction pattern, they can be compared to standard patterns found in databases to identify the minerals and phases in a sample.

Powder-XRD analysis was conducted on the non-active concrete sections from the Hunterston A core as described in Chapter 6. Samples were prepared by grinding with a pestle and mortar, and addition of amyl acetate to form a homogeneous slurry which was deposited on a glass slide. Analysis was conducted using a Bruker D2 Phaser diffractometer, equipped with a Göbel Mirror and Lynxeye XE-T detector with an axial 2.5° Soller slit and anti-scatter screen. Powder-XRD was conducted using Cu K α X-rays (wavelength 1.5406 \AA) over incident angle range from $5 - 70^\circ$, with a step size of 0.03° at 0.3 s per step.

3.3.5. X-ray computed tomography (XCT)

X-ray computed tomography (XCT) is a non-destructive technique that can provide information on the internal structure of samples. X-rays are used to image the sample in 2D from multiple directions. Once the scans have been obtained, they are reconstructed to form a 3D map of the sample. This can help detect pores, cracks and other notable internal features in a sample.²⁴ Analysis of XCT data requires extensive computational processing using specific, licensed software to work through the large datasets and correctly separate material phases in the sample. This can be a time-consuming process, particularly for complex matrices such as concrete.

Micro-XCT analysis was conducted on a section of the uncontaminated core as described in Chapter 6, using a Phoenix Nanotom nanoCT scanner with a maximum voltage of 180 kV and

20 W power (Waygate Technologies, Baker Hughes). Analysis of the data was conducted using ImageJ and Avizo (Thermo Fisher Scientific).

3.3.6. Sequential extraction

Sequential extraction is commonly used to indicate phases associations in an environmental sample, such as soils, sediments and concretes.^{25–27} Samples are subjected to increasingly harsher chemical reagents to sequentially leach out elements of interest. It is vital to tailor the chemicals used to target the phases specific to the sample matrix.

Sequential extractions were conducted in Chapter 6 to determine the binding strength of radionuclides identified in the Hunterston A concrete core. Thin sections (10 x 10 x 1 mm (w x l x h)) of the concrete core were prepared using the cutting methods described above (Section 3.1.3.). The thin-sections ran from a section of the bulk concrete directly below the protective layers, to a depth of 2 cm. After initial gamma analysis, the thin-sections were physically separated into aggregate and cementitious phases before each fraction was ground to a fine powder using a pestle and mortar. The procedure used was adapted from the methods used by Li *et al.* with alterations made to suit the nature of the sample.^{28,29} The total sample mass used was decreased from 1.0 g to 0.2 g due to the volume of sample available, as well as to minimise the exposure limit to the powdered solid. The extractant volumes were reduced proportional to the sample mass. Extraction times for fractions 4 and 5 were extended compared to the reference method as described below and no HF was used.

The following fractions were investigated:

Fraction 1: Exchangeable – 0.2 g of sample was extracted with 1.6 mL MgCl₂ (1.0 M, pH 7.0). The mixture was continuously agitated for 5 hours at room temperature.

Fraction 2: Carbonates – Residue from fraction 1 was extracted with 1.6 mL NaOAc (pH 5). The mixture was continuously agitated overnight for 17 hours at room temperature.

Fraction 3: Reducible – Residue from fraction 2 was extracted with 4.0 mL hydroxylamine hydrochloride (0.04 M in 25% (v/v) HOAc) for 6 hours at 85 °C with continuous agitation.

Fraction 4: Oxidisable – Residue from fraction 3 was extracted with 1.0 mL HNO₃ (0.02 M) and 3 mL H₂O₂ (30%, pH 2.5) added dropwise. The solution was heated to 85 °C for 2 hrs with regular agitation. After 2 hours 1 mL H₂O₂ was added and shaken regularly for 5 hours at 85 °C. The volume was reduced to ~ 1 mL and left to cool overnight. 2 mL NH₄OAc (3.2% in 20% (v/v) HNO₃) was added and shaken continuously for 1 hour at room temperature.

Fraction 5: Residual– Residue from fraction 4 was extracted with 0.8 mL HNO₃ (70%) and 0.6 mL HClO₄ (60 %). The solution was heated to 90 °C for 2 hours, 120 °C for 12 hours and 160 °C for 6 hours in a heating block.

Before moving onto the next step, each extraction was centrifuged (5000 rpm, 10 minutes) and the leachate kept. The residue was then washed with 2 mL DI water (18 MΩ) and shaken for 20 minutes before centrifuging (5000 rpm, 10 minutes). This leachate was discarded. The leachates from each step were analysed using gamma spectroscopy and LSC (Sections 3.4.1 and 3.4.2). A blank sample was run alongside and the leachates analysed using ICP-MS.

3.4. Active analytical methods

3.4.1. Liquid scintillation counting (LSC)

Liquid scintillation counting (LSC) is used to detect and measure the activity of radioactive solutions, particularly for α - and β -emitting radionuclides. Analysis requires a scintillation cocktail to be added, consisting of organic fluorophores dissolved in solvent. Radiation emitted by the sample is absorbed by the cocktail solvent and transferred to the fluorophore (Figure 3.10). As the excited scintillators return to ground state they emit a flash of light, where the intensity corresponds to a specific radioactive decay event.³⁰

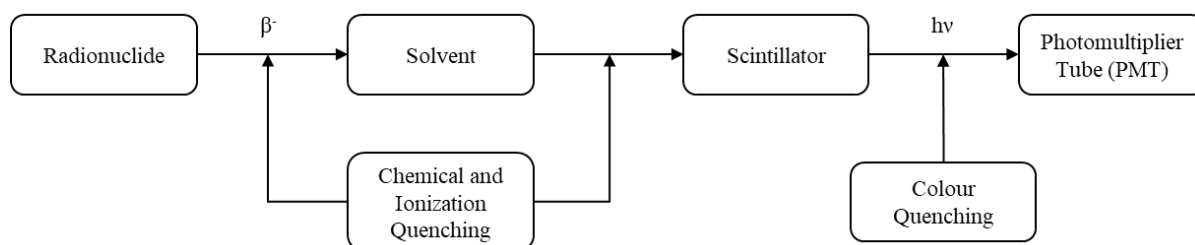


Figure 3.10. Schematic of the steps involved in LSC analysis (adapted from M. L'Annunziata *et al.*).³⁰

Analysis of the hydrogel decontamination tests was conducted using LSC and is described in Chapters 5 and 6, as well as the sequential extraction experiments described in Chapter 6. Samples were prepared by adding 0.5 mL of leachate from the sequential extractions and 2 mL from the hydrogel leach tests to 10 mL proSafe HC+ liquid scintillation cocktail. Leachates from fractions 3 and 5 were diluted in DI water (18 MΩ) before scintillation cocktail was added to avoid colour quenching. Samples were left for 19 days to reach secular equilibrium for Sr-90 prior to analysis and were dark adapted for 2 hours to minimise photoluminescence effects. Samples containing multiple radionuclides were analysed through Cerenkov counting to isolate

Sr-90 radioactivity, whereby 2 mL of solution was diluted to 10 mL using DI (18 Ω M) water. Samples were run using the LabLogic Hidex 300 SL with MikroWin 300SL control software. The Hidex 300 SL system uses three PMT detectors to automatically quench correct by triple to double coincidence ratio (TDCR). In addition, Sr-90 standards in solution had been prepared for calibration of solution analysis. Hydrogel standards had been prepared to calibrate the leaching of Sr-90 from hydrogels.

3.4.2. Gamma spectroscopy

Gamma spectroscopy is a non-destructive analytical technique used to detect and quantify γ -emitting radionuclides. Radioactive samples emit characteristic γ -rays which are picked up by the detector and compared to known energies to identify the radionuclides present (Figure 3.11). Gamma spectroscopy can be done on both solid and liquid samples but requires standards for quantification to account for the sample geometry and composition.

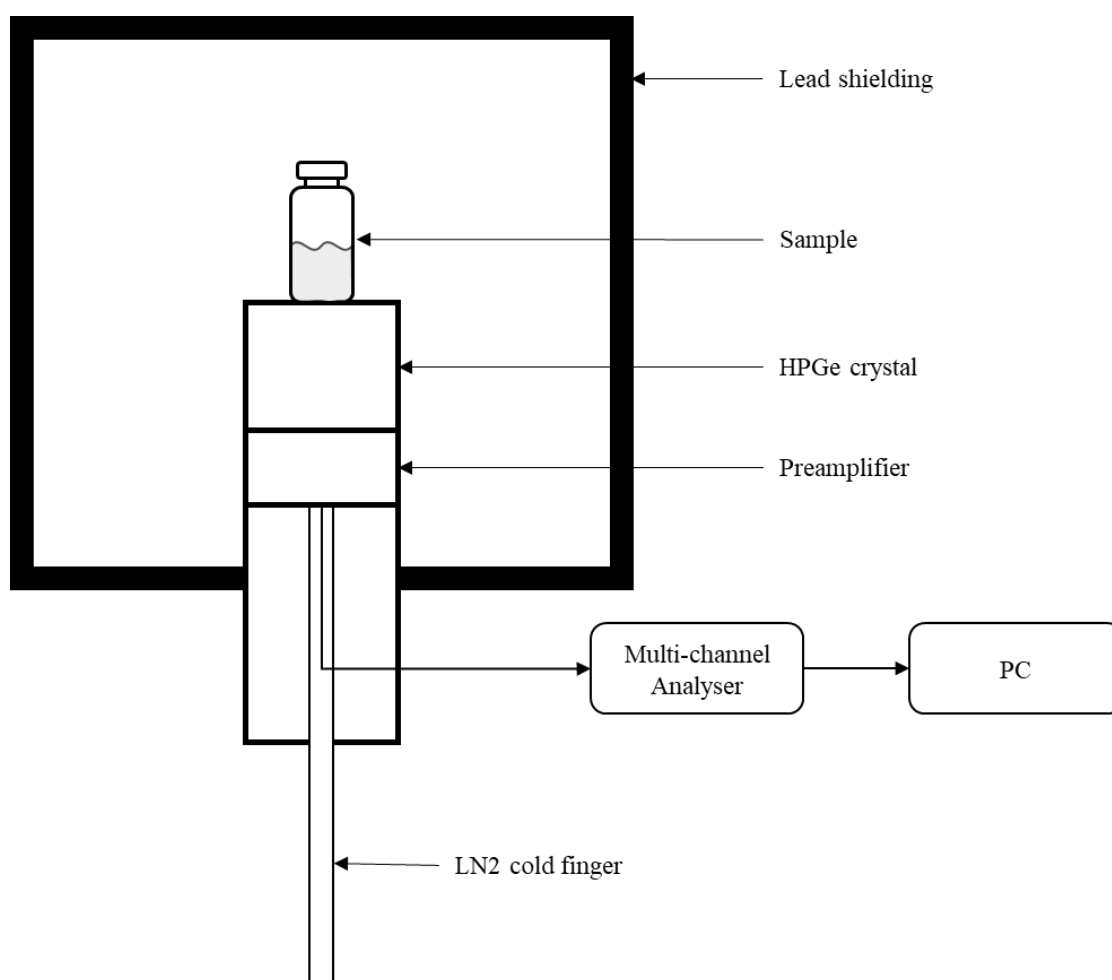


Figure 3.11. Schematic of a High Purity Germanium (HPGe) Gamma Detector (adapted from National Physical Laboratory).³¹

There are several features that need to be taken into account when analysing a gamma spectrum: the photopeak, Compton edge and pair production (Figure 3.12).³²

- The photopeak corresponds to the peak produced when all of the incident γ -ray has been absorbed by the detector.
- The Compton edge is formed when only a portion of the incident γ -ray is transferred to the detector, known as the Compton effect. This results in the formation of a very broad low-energy peak known as the Compton distribution with sharp edges corresponding to the maximum amount of energy transferred (Compton edge) and the minimum amount of energy transferred (backscatter peak). The sum of the Compton edge and backscatter peak will equal the photopeak energy.
- Finally, pair production occurs when a γ -ray with energy > 1.022 MeV produces an electron-positron pair. The positrons will find an electron and annihilate to produce two 0.511 MeV γ photons. This can result in the formation of an escape peak, when one annihilation γ -ray is not absorbed (photopeak $- 0.511$ MeV), or a double escape peak, when both annihilation γ -rays are not absorbed (photopeak $- 1.022$ MeV).

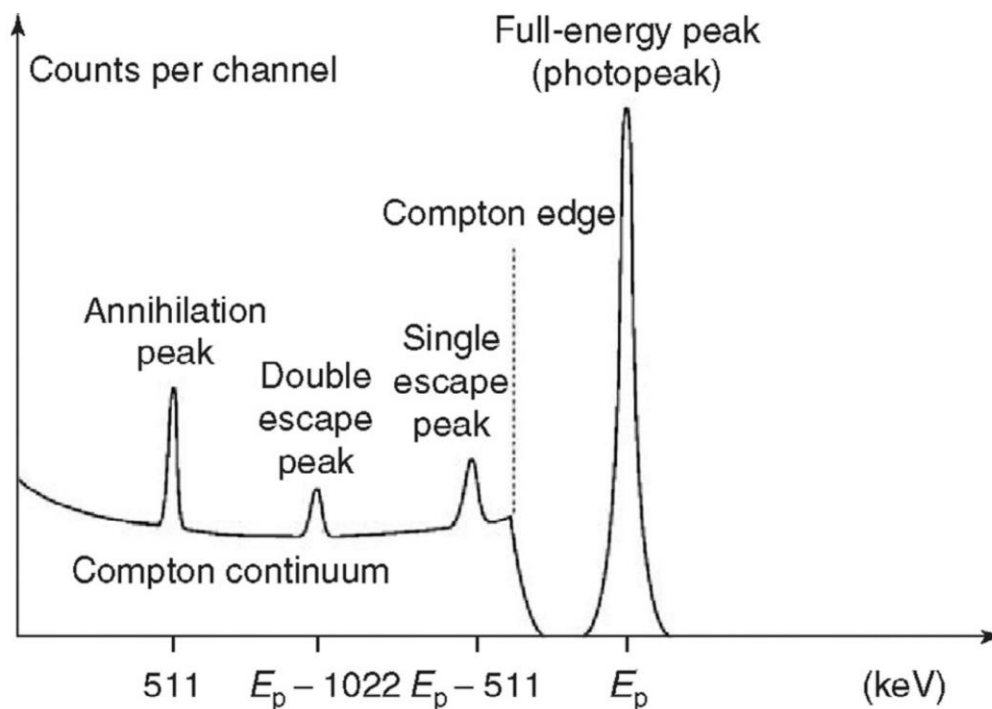


Figure 3.12. Schematic of the features observed in gamma ray spectra (Buchtela et al.).³²

Gamma spectroscopy was used to determine the radionuclides present in the Hunterston A samples and quantify the activity removed during decontamination experiments described in Chapters 5 and 6. Gamma analysis was conducted on two different spectrometers due to

analysis being conducted on two different sites at the University of Manchester and the University of Helsinki.

The concrete core samples were analysed at the University of Helsinki using a GEM coaxial HPGe detector. Data was analysed using the Genie™ 2000 gamma analysis software (Mirion Technologies, Canberra). Quantification of activities in the concrete core was not possible due to the unique geometry and composition of the sample. Gamma spectroscopy of the depth-profile samples was performed to estimate activities and compare between samples in the same geometry.

Gamma spectroscopy of the HDPE discs, HDPE and concrete coupons, and hydrogels used in Chapters 5 and 6 was performed using a Canberra 2020 coaxial HPGe detector with an Ortec DSPEC-50 multi-channel analyser. Accurate quantification of the pontoon samples was not possible due to the unique geometry and composition of the pontoon discs. Gamma spectroscopy did; however, allow relative measurements and hence comparison between the samples pre- and post-decontamination. Analysis of the leachates obtained from sequential extractions as described in Chapter 6 was performed against standards of known activity counted in the same geometry. Gamma spectroscopy of the hydrogels was performed against standards of known activity counted in the same geometry and timescale. Cs-137, Am-241 and Eu-152 were identified using the diagnostic photon energies of 661.6 keV, 59.5 and 121.8 keV, respectively. LODs were calculated by the GammaVision software. Peaks with greater intensity than 3σ above the background count were considered significant.

3.4.3. Autoradiography

Autoradiography is a non-destructive, 2D imaging technique that indicates the presence of radioactivity in a sample. Phosphor screens or film are used to image the radiation source; although, due to their increased sensitivity and need for shorter exposure times, phosphor screens have become the most popular option.³³ The sample is placed on the phosphor screen in a cassette such that the radioactive face is in contact with the screen (Figure 3.13). The cassette is closed and placed inside a dark cupboard to minimise the interference from incoming light. The exposure time is dependent on the type and quantity of radiation present in the sample.³⁴

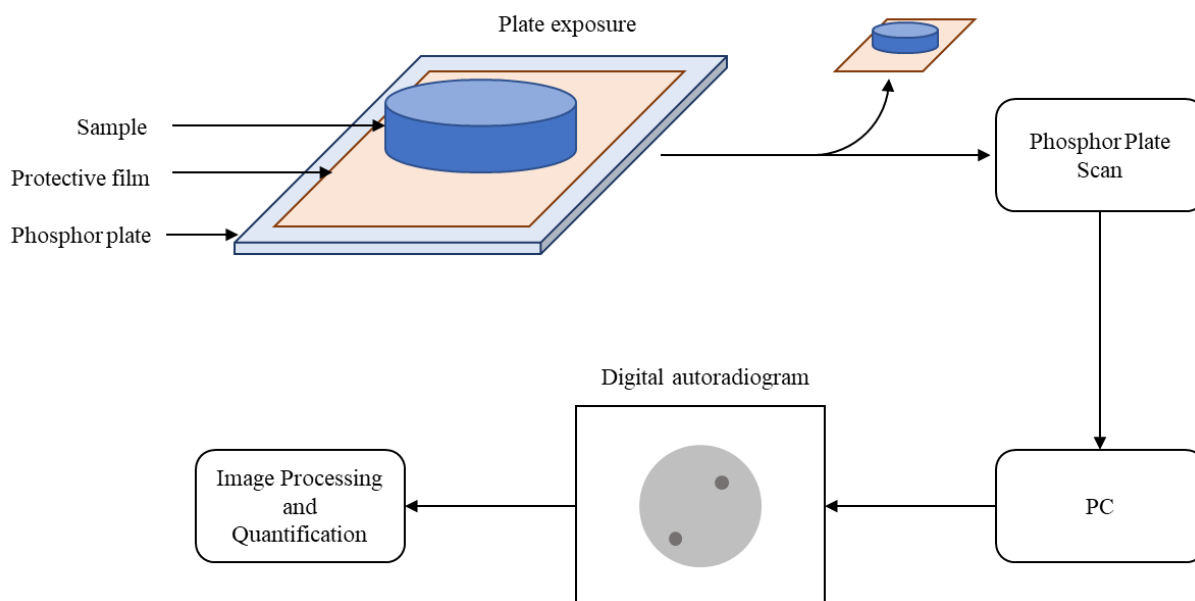


Figure 3.13. Schematic of the autoradiography process.

Autoradiography was used to identify radioactivity present on and within the concrete core and HDPE discs as described in Chapters 5 and 6. In addition, autoradiography was used to image the concrete and HDPE coupons pre- and post-decontamination experiments, as well as visualizing the uptake of radioactivity in the hydrogels.

Autoradiography analysis was conducted on two instruments as this research was conducted on two different sites at the University of Manchester and the University of Helsinki.

For the concrete core, samples were exposed to a BAS-IP TR 2040 E (Fujifilm Corporation) imaging plate for 2 hours and scanned using the Fujifilm Fluorescent Image Analyser FLA-5000 (Fuji Photo Film Co., LTD) with pixel size 50 μm . Image optimisation was conducted using the AIDA image analysis software version 5.0 SP 2 (Elysia-Raytest GmbH).

The HDPE discs and samples used during decontamination studies were exposed to BAS-IP MS 2040 E (GE Healthcare) storage phosphor screens for 24 hours and scanned using the Amersham™ Typhoon Laser Scanner (Cytiva Life Sciences) with pixel size 50 μm . Images were optimised using the Amersham ImageQuant TL analysis software version 10.2 (Cytiva Life Sciences).

3.5. References

- 1 M. Ltd, Hunterston A pond pontoon,
<https://www.flickr.com/photos/magnoxsites/8557186854/in/photostream/>.

- 2 R. Baldev, U. K. Kamachi Mudali, M. Vijayalakshmi, M. D. Mathew, A. K. Bhaduri, P. Chellapandi, S. Venugopal, C. S. Sundar, B. P. C. Rao and B. Venkataraman, Development of stainless steels in nuclear industry: with emphasis on sodium cooled fast spectrum reactors: history, technology and foresight, *Adv. Mater. Res.*, 2013, **794**, 3–25.
- 3 Z. Duan, F. Arjmand, L. Zhang and H. Abe, Investigation of the corrosion behavior of 304L and 316L stainless steels at high-temperature borated and lithiated water, *J. Nucl. Sci. Technol.*, 2016, **53**, 1435–1446.
- 4 G. S. Was and S. Ukai, in *Structural Alloys for Nuclear Energy Applications*, eds. G. R. Odette and S. J. Zinkle, Elsevier, 2019, pp. 293–347.
- 5 A. J. McBain, in *Advances in Applied Microbiology*, Elsevier Inc., 2009, vol. 69, pp. 99–132.
- 6 Isotrak, *Calibration Standards and Instruments*, Exckert & Ziegler, 2009.
- 7 J. J. Moore, T. P. Raine, A. Jenkins, F. R. Livens, K. A. Law, K. Morris, G. T. W. Law and S. G. Yeates, Decontamination of cesium and strontium from stainless steel surfaces using hydrogels, *React. Funct. Polym.*, 2019, **142**, 7–14.
- 8 US Environmental Protection Agency, *Decontamination of cesium, cobalt, strontium, and americium from porous surfaces.*, 2013.
- 9 S. C. Wilschefski and M. R. Baxter, Inductively coupled plasma mass spectrometry: introduction to analytical aspects, *Clin. Biochem. Rev.*, 2019, **40**, 115–133.
- 10 C. B. Boss and K. J. Fredeen, Concepts, instrumentation and techniques in inductively coupled plasma optical emission spectrometry, *PerkinElmer*, 1999, **997**, 1–125.
- 11 ThermoFisher, Inductively coupled plasma mass spectrometry (ICP-MS) information, <https://www.thermofisher.com/uk/en/home/industrial/spectroscopy-elemental-isotope-analysis/spectroscopy-elemental-isotope-analysis-learning-center/trace-elemental-analysis-tea-information/inductively-coupled-plasma-mass-spectrometry-icp-ms-information.htm>.
- 12 J. Webb and J. Holgate, in *Encyclopedia of Food Sciences and Nutrition*, eds. B. Caballero, L. Trugo and P. M. Finglas, Academic Press, 2nd edn., 2003, pp. 3922–3928.
- 13 K. Akhtar, S. A. Khan, S. B. Khan and A. M. Asiri, in *Handbook of Materials*

- Characterization*, ed. S. K. Sharma, Springer, 2019, pp. 113–145.
- 14 W. C. Nixon, The general principles of scanning electron microscopy, *Philos. Trans. R. Soc. London. B, Biol. Sci.*, 1971, **261**, 45–50.
 - 15 M. Kannan, in *Textbook on Fundamentals And Applications of Nanotechnology*, Astral, 2018, pp. 81–92.
 - 16 S. E. Shaban, N. M. Ibrahiem, S. A. El-Mongy and E. E. Elshereafy, Validation of scanning electron microscope (SEM), energy dispersive X-ray (EDX) and gamma spectrometry to verify source nuclear material for safeguards purposes, *J. Radioanal. Nucl. Chem.*, 2013, **296**, 1219–1224.
 - 17 S. Ebnesajjad, in *Surface Treatment of Materials for Adhesive Bonding*, Elsevier, 2nd edn., 2014, pp. 39–75.
 - 18 R. Schneider, in *Surface and Thin Film Analysis: a Compendium of Principles, Instrumentation, and Applications*, eds. G. Friedbacher and H. Bubert, Wiley, 2nd edn., 2011, pp. 293–310.
 - 19 B. Hafner, *Energy Dispersive Spectroscopy on the SEM: A Primer*, University of Minnesota, 2007.
 - 20 D. Pirrie, A. R. Butcher, M. R. Power, P. Gottlieb and G. L. Miller, Rapid quantitative mineral and phase analysis using automated scanning electron microscopy (QEMSCAN); potential applications in forensic geoscience, *Geol. Soc. Spec. Publ.*, 2004, **232**, 123–136.
 - 21 D. Cremers and L. Radziemski, in *Handbook of Laser-Induced Breakdown Spectroscopy*, Wiley, 2nd edn., 2013, p. 5.
 - 22 G. Hull, University of Manchester, 2020.
 - 23 C. E. Housecroft and A. G. Sharpe, in *Inorganic chemistry*, Pearson, 4th edn., 2012, pp. 87–138.
 - 24 P. J. Withers, C. Bouman, S. Carmignato, V. Cnudde, D. Grimaldi, C. K. Hagen, E. Maire, M. Manley, A. Du Plessis and S. R. Stock, X-ray computed tomography, *Nat. Rev. Methods Prim.*, 2021, **1**, 1–21.
 - 25 L. Skipperud and B. Salbu, Sequential extraction as a tool for mobility studies of radionuclides and metals in soils and sediments, *Radiochim. Acta*, 2015, **103**, 187–197.

- 26 P. Blanco, F. Vera Tomé and J. C. Lozano, Sequential extraction for radionuclide fractionation in soil samples: a comparative study, *Appl. Radiat. Isot.*, 2004, **61**, 345–350.
- 27 A. Tessier, P. G. C. Campbell and M. Bisson, Sequential extraction procedure for the speciation of particulate trace metals, *Anal. Chem.*, 1979, **51**, 844–851.
- 28 X. D. Li, C. S. Poon, H. Sun, I. M. C. Lo and D. W. Kirk, Heavy metal speciation and leaching behaviors in cement based solidified/stabilized waste materials, *J. Hazard. Mater.*, 2001, **82**, 215–230.
- 29 X. Li, B. J. Coles, M. H. Ramsey and I. Thornton, Sequential extraction of soils for multielement analysis by ICP-AES, *Chem. Geol.*, 1995, **124**, 109–123.
- 30 M. F. L’Annunziata and M. J. Kessler, in *Handbook of Radioactivity Analysis*, Elsevier, 3rd edn., 2013, pp. 423–573.
- 31 National Physics Laboratory, HPGe gamma ray spectroscopy education, <http://www.nuclearphysicslab.com/npl/npl-home/spectroscopy/gamma-ray-spectroscopy/gamma-ray-spectroscopy-education/>.
- 32 K. Buchtela, *Radiochemical methods: gamma-ray spectrometry*, Elsevier, 3rd edn., 2019, vol. 9.
- 33 P. Johnström, J. L. Bird and A. P. Davenport, Quantitative phosphor imaging autoradiography of radioligands for positron emission tomography, *Methods Mol. Biol.*, 2012, **897**, 205–220.
- 34 R. Pöllänen, A. Kansanaho and H. Toivonen, *Detection and Analysis of Radioactive Particles using Autoradiography*, 1996, vol. 27.

4. Development of Laser-Induced Breakdown Spectroscopy for Analysis of Radioactively Contaminated Materials

Anna E. Denman ^a, Gareth T. W. Law ^b, Thomas Carey ^c, Nicholas T. Smith ^c, Franky L. Barton ^a, Jonathan R. Lloyd ^a, and Scott L. Heath ^{a,d}

^a. Research Centre for Radwaste Disposal and Williamson Research Centre for Molecular Environmental Science, Department of Earth and Environmental Sciences, The University of Manchester, Manchester, M13 9PL, UK

^b. Radiochemistry Unit, Department of Chemistry, The University of Helsinki, Helsinki, 00014, FI

^c. National Nuclear Laboratory, Chadwick House, Warrington Road, Birchwood Park, Warrington, WA3 6AE, UK

^d. Dalton Nuclear Institute, The University of Manchester, Manchester, M13 9PL, UK

Status: Manuscript in preparation for submission to *Spectrochimica Acta B: Atomic Spectroscopy*.

Highlights:

- Laser-induced breakdown spectroscopy (LIBS) analysed contaminated high-density polyethylene (HDPE) and concrete materials relevant to the nuclear industry at distance of 8 cm.
- Sr, Cs and Co detected below 0.01 mg/cm² on the concrete and HDPE surfaces using LIBS.
- LIBS analysed metal contamination in model nuclear waste discharge pipeline samples.
- Multi-pulse LIBS analysis of contaminant penetration depth in concrete, HDPE and stainless steel.

Keywords: LIBS, Contamination, Elemental Analysis, Concrete, Plastic, Steel

4.1. Abstract

Characterisation of radioactive materials is vital in nuclear decommissioning. Laser-induced breakdown spectroscopy (LIBS) is a promising characterisation tool for the rapid, multi-elemental analysis of major and trace species in the nuclear industry. Analysis of model systems is vital to determine the applicability of LIBS for *in-situ* analysis. Here, LIBS has been used to analyse contaminated plastic, concrete and steel coupons representative of spent nuclear fuel (SNF) storage pond and waste discharge pipeline materials. In this new study, sorption experiments were conducted using stable Sr, Cs and Co in conditions mimicking alkaline SNF ponds and analyte emissions could be distinguished in each of the sample matrices. The limits of detection (LOD) for each element were determined with LIBS and found to be lower than those obtained through ICP-MS analysis of the solution: concrete – 40 ng/cm² for strontium, 680 ng/cm² for cesium and 320 ng/cm² for cobalt; HDPE – 71 ng/cm² for strontium, 6000 ng/cm² for cesium and 2800 ng/cm² for cobalt. Strontium, cesium, cobalt, ruthenium and europium emissions could be resolved from model nuclear waste discharge pipeline samples with changes to uptake dependent on the presence of model biofilms using anaerobic metal reducing bacteria (*Shewanella oneidensis* MR-1). Finally, depth-profiling determined contamination was predominantly isolated to the sample surface with possible diffusion of analytes into the concrete material.

4.2. Introduction

Decommissioning nuclear facilities can result in large volumes of waste.¹ Fission products and other hazardous radionuclides can be transported throughout the facilities, leading to a build-up of contamination in reactors, pipelines and waste storage sites. Thorough characterisation of materials is therefore vital to provide insight into which materials are contaminated, the type of contaminants present and the extent of contaminant penetration.²

Laser-induced breakdown spectroscopy (LIBS) has been identified as a useful characterisation tool for the nuclear industry.^{3–6} LIBS is a high energy spectroscopic technique that can provide multi-elemental analysis of major and trace species on unprepared surfaces.⁷ The ability of LIBS to conduct analysis using only an optical line of sight make it a favourable technique for use in the nuclear industry. Advances beyond traditional bench-top LIBS now allow standoff analysis from distances up to 20 m and small, handheld versions are available that can be mounted onto robots and sent into confined or highly contaminated areas that would otherwise

be unreachable or harmful to workers.^{6,8} In addition, fibre optic LIBS probes can now be used to conduct measurements below 1000 m water depths and could be applied to the characterisation of submerged nuclear materials.^{9–11} The versatility of LIBS makes it a competitive technique for rapid, *in-situ* analysis that could provide invaluable insight into the contamination of a wide range of materials across the nuclear industry.

The contamination of stainless steel is a widely researched area due to its abundance in nuclear infrastructure.^{12–14} Austenitic stainless steels account for around 80% of the structural materials used and they are found in the reactor core, coolant piping, and in reprocessing plants and waste management infrastructure. 304L stainless steel is used in particular due to its increased corrosion resistance at high temperatures and acidic pH.^{15,16} LIBS has proved itself as a useful technique for the identification of key radionuclide species, such as strontium and cesium, on stainless steel materials.^{17–19} In contrast, research into the contamination of concrete and plastic with LIBS has been limited, despite the widespread use of these materials in the nuclear industry.

Concrete is used throughout the nuclear industry due to its low cost, durability and radiation shielding properties.^{20,21} Over time these structures become contaminated through daily operations, leaks or more drastic events.^{22–24} Analysis of radionuclides in concrete has historically been conducted using universal alpha, beta, gamma, and neutron dosimeter-radiometer detectors, and imaging analytical techniques such as autoradiography.²⁵ Concrete samples have been collected from hazardous environments to determine the penetration depth of radionuclides using microscopy and techniques, such as X-ray fluorescence spectroscopy (XRF).²⁶ Whilst analysis with these techniques has been successful, it requires samples to be extracted from site and, often, destroyed during analysis. LIBS avoids some of these drawbacks and has, for example, been used to measure chlorine content in cementitious materials as a rapid alternative to chemical methods.^{27,28} Whilst analysis of radionuclide-contaminated concrete with LIBS is less researched, these results show promise that LIBS can be used for the *in-situ* characterisation technique for these materials.

Although less abundant, plastics have been used in the nuclear industry in areas of lower radiation for piping, encapsulation and in temporary structures. Polyethylene (PE) is exceptionally radiation resistant: able to withstand doses of up to 10^8 Gy of gamma radiation, making it a suitable material for use in nuclear facilities.²⁹ To date, there have been few studies on radionuclide contamination of plastics. The work of Tazaki *et al.*, which uses XRF and

scanning electron microscopy with energy dispersive X-ray spectroscopy (SEM-EDX) to study the uptake of heavy elements alongside radionuclide species in PE, appears to be the only relevant study.³⁰ Laser-induced breakdown spectroscopy has been used to differentiate plastic polymers for recycling purposes as well as for the identification of bromine and copper contamination in polystyrene, polyethylene terephthalate (PET) and Grilon® polyamide.^{31–33} In the food industry, trace analysis of heavy metals in PE materials has been carried out using inductively coupled plasma optical emission spectroscopy (ICP-OES) and atomic absorption spectroscopy (AAS), but little remains known about radionuclide contamination of plastics.^{34–}

36

Concrete and high-density polyethylene (HDPE) contaminated with Sr, Cs and Co are representative of materials found steel discharge pipelines and the SNF storage pond of Hunterston A nuclear power station, where release from stored SNF containers has resulted in the contamination of the pond infrastructure. Sr-90 and Cs-137 are β - and β -, γ -emitting fission products which are mobile in solution and have moderate half-lives, 29.1 and 30.2 years, respectively.³⁷ Co-60 is a γ -emitter that is formed through neutron activation of steel used in nuclear reactors, and has a shorter half-life of 5.27 years.³⁸ Accurate identification of these key radionuclides in waste materials could aid decontamination tasks and help minimise the volume of low and intermediate level waste (LLW/ILW) produced during decommissioning. In this paper we explore the use of LIBS for the analysis of concrete and HDPE materials contaminated with Sr, Cs and Co by comparing the results of single and multielement sorption studies which aimed to replicate contamination conditions in the SNF storage pond. LIBS was used to obtain the limits of detection for each of the analytes and measure the uptake onto the concrete and HDPE surfaces during sorption studies. Scanning electron microscopy (SEM) energy dispersive X-ray spectroscopy (EDX) analysis was used to determine the material composition of the materials and the effects of LIBS analysis on the sample surfaces. In addition, samples representative of steel discharge pipelines were analysed to assess the use of LIBS for the analysis of complex contaminated samples with and without the presence of biofilms.

4.3. Experimental

4.3.1. Samples

304L stainless steel, concrete and HDPE samples were selected as the matrices for

investigation due to their abundant use in the nuclear industry. Aristar grade chemicals were used throughout.

Concrete material was obtained from the walls of the decommissioned SNF pond at Hunterston A nuclear power station. The pond walls consisted of ordinary Portland cement (OPC) mixed with aggregate from the local environment consisting predominantly of olivine and pyroxene gabbro phases, as well as silicates.²⁶ Coupons were prepared using a Buehler IsoMet Low Speed precision cutter with a Diamond Wafering Blade (15 HC, 10.2 x 0.3 mm), using DI water as the lubricant. The coupons were ground to 2500 grit using silicon carbide grinding paper and polished down to 0.5 μm using Buehler micropolish II alumina suspension on a Buehler EcoMet 30 Auto/Manual Grinder & Polisher. Finally, the samples were washed with DI water (18 M Ω) and isopropyl alcohol (IPA), and left to air dry prior to contamination experiments.

1 cm thick high-density polyethylene (HDPE) disc coupons were cut from 2 cm diameter plastic rod obtained from Direct Plastics Ltd. The coupons were ground to 2500 grit using silicon carbide grinding paper and polished down to 5 μm using Buehler micropolish II alumina suspension on a Buehler EcoMet 30 Auto/Manual Grinder & Polisher. Samples were washed with deionised (DI) (18 M Ω) water and isopropyl alcohol (IPA) prior to contamination experiments.

The multi-element contamination analysis experiments (Section 4.3.3.2) were performed on 304L stainless steel coupons (20 x 10 mm (ϕ x h)) (Table S4.1). Coupons were ground with 2400 grit silicon carbide grinding paper, followed by polishing to 1 μm with diamond suspension on a polishing cloth. Finally, the samples were degreased with ethanol before contamination experiments took place.

4.3.2. Calibration standards

Calibration standards were prepared by labelling concrete and HDPE surfaces with $\text{Sr}(\text{NO}_3)_2$, CsNO_3 and $\text{Co}(\text{NO}_3)_2$ in aqueous solution at concentrations ranging from 1 to 500 mg/L. 100 μL was spotted on the concrete surfaces and 200 μL on the HDPE surfaces, giving an average droplet area of $1.13 \text{ cm}^2 \pm 0.3$. The samples were left to air dry for one week before analysis with LIBS. Emissions were collected for nine shots on a 3 x 3 grid within the contamination area per spectrum. Calibration curves were obtained using the strongest emission lines for each analyte: Sr II - 407.78 nm, Cs I - 852.13 nm and Co I - 345.32 nm. Peak intensities $<3\sigma$ above

background were considered to be below the limit of detection (LOD).

4.3.3. Sorption experiments

Sorption studies were conducted to assess the extent of Sr, Cs and Co contamination on concrete and HDPE coupons in conditions representative of the alkaline SNF storage pond environment. Initial single element sorption studies were used to assess the extent of analyte uptake onto individual material surfaces in a model system. Multi-element sorption studies were then conducted to be more representative of a real storage pond environment and account for any preferential uptake onto matrices and competition between the contaminants.

4.3.3.1. Single-element systems

Contaminant solutions containing 500 mg/L $\text{Sr}(\text{NO}_3)_2$, CsNO_3 or $\text{Co}(\text{NO}_3)_2$ were prepared in DI (18 M Ω) water adjusted to pH 11 using 0.1 M NaOH to replicate the alkaline SNF pond conditions. No further pH adjustments were made once the experiment started. HDPE and concrete coupons were exposed to 20 mL of the contaminant solutions such that a single face was in contact with the liquor. The containers were sealed and left for 28 days at 60 °C. Sorption experiments were conducted in triplicate. After 28 days the samples were removed and washed with DI water (18 M Ω) and IPA. The samples were air dried for 1 week before being analysed with LIBS.

Aliquots of the solution were removed at set intervals throughout the experiment and analysed using inductively coupled plasma mass spectrometry (ICP-MS) to monitor the uptake of each analyte and any leaching or corrosion of the coupons. The deposition of Sr, Cs and Co onto the sample surface (q_t) was measured using the following equation:

$$q_t = \frac{(C_0 - C_t) \times V}{A} \quad [1]$$

where C_0 is the concentration at the start of the experiment (time = 0, mg/L); C_t is the concentration at time t (mg/L); V is the volume (L) and A is the surface area of the coupon (cm²).

4.3.3.2. Contamination chamber: multi-element system

A contamination chamber device was designed to improve the repeatability of long-term contamination experiments (Figure S4.1). The design was based on the modified Robbins device (MRD) where the sample surface is kept in contact with a continuously flowing solution.³⁹ The use of individual sample holders allowed the samples to be removed

independently allowing multiple experiments to take place simultaneously.

304L stainless steel, concrete and HDPE coupons were cut to fit the sample holders (20 x 10 mm (ϕ x h)) and prepared as described previously. A solution containing 500 mg/L stable $\text{Sr}(\text{NO}_3)_2$, CsNO_3 and $\text{Co}(\text{NO}_3)_2$ in DI water (18 M Ω) was prepared and adjusted to pH 11 using 0.1 M NaOH. No further pH adjustments were made once the experiment started. 4 coupons of each material were fit into the sample holders with a single surface in contact with the liquor. The device was sealed and heated to 60 °C for 28 days. Aliquots of the solution were removed at set intervals throughout the experiment and analysed using ICP-MS to monitor the uptake of each analyte and any potential leaching or corrosion of the coupons. After completion of the experiment the samples were removed, washed with DI water (18 M Ω) and IPA, and left to air dry for 1 week before analysis.

4.3.3.3. Model waste discharge pipeline samples

The model waste discharge pipeline samples analysed in this experiment were prepared according to Barton *et al.*⁴⁰ 304L stainless steel coupons were fitted into two MRDs, one for the formation of biofilms onto the steel surfaces using *Shewanella oneidensis* MR-1 culture and one without. Analysis of underground discharge pipelines from Sellafield identified radioactive contamination from a range of radionuclides, including Ru-106, Sr-90, Cs-134, Cs-137, Co-60, Eu-154 and Eu-155. A solution containing clinoptilolite fines (500 mg/L) was passed through each device before 3-(N-morpholino)propanesulfonic acid (MOPS, 50 mM) with lactate (10 mM) solutions containing stable $\text{SrCl}_2 \cdot 6\text{H}_2\text{O}$, CsCl , $\text{CoCl}_2 \cdot 6\text{H}_2\text{O}$, $\text{EuCl}_3 \cdot 6\text{H}_2\text{O}$ and $\text{RuCl}_3 \cdot x\text{H}_2\text{O}$ (all 100 μM per 200 mL) were circulated through the MRDs for 8 days.⁴⁰ The biofilm coupons were fixed in 2.5% v/v glutaraldehyde in phosphate buffered saline overnight and washed in 60 and 30% diluted phosphate buffered saline before being dehydrated in 30 minute steps of DI (18 M Ω) with increasing ethanol concentrations. Non-biofilm coupons were rinsed with DI (18 M Ω) and air dried prior to analysis.

4.3.4. Laser-induced breakdown spectroscopy

Laser-induced breakdown spectroscopy (LIBS) analysis was conducted using a 1064 nm Nd:YAG laser (Innolas Spitlight 600) with a 10 Hz repetition rate, a 7 ns pulse duration and an Echelle spectrometer (LaserTechnik Berlin Aryelle Butterfly) with ICCD camera (Andor iStar series). The spectral range covers between 250-900 nm. The beam delivery periscope system, sample chamber, sample cell and LIBS module were manufactured by Applied Photonics Ltd. (Figure S4.2). Sophi software V1.03 R630 (LaserTechnik Berlin) was used to control the laser,

spectrometer and camera during analysis. The gate delay and gate width were kept constant at 1500 ns and 100 ms, respectively. Analysis was conducted using a pulsed laser energy of 100 mJ/pulse in air at a working distance of 8 cm. Depth-profiling of the contaminated coupons was conducted via multi-pulse analysis, where repetitive laser shots are fired at a single target. All spectra were analysed using the Sophi software.

4.3.5. Scanning electron microscopy (SEM) energy dispersive X-ray spectroscopy (EDX)

SEM-EDX analysis was used to image the material surfaces post-LIBS analysis to identify potential contamination outside and within the crater formed. High resolution, high magnification images were produced using a FEI Thermofisher Quanta 650 (E)SEM with Bruker Quantax energy dispersive spectrometer (EDX).

4.4. Results and discussion

4.4.1. Calibration curves and limits of detection

Calibration curves were generated using the following characteristic emission peaks for each analyte: Sr II 407.78 nm ($^2P_{3/2} \rightarrow ^2S_{1/2}$, whereby $^2P_{3/2}$ represents the upper energy level term and $^2S_{1/2}$ represents the lower energy level term), Cs I 852.13 nm ($^2P_{3/2} \rightarrow ^2S_{1/2}$) and Co I 345.32 nm ($^4G_{11/2} \rightarrow ^4F_{9/2}$). These emissions were selected based on their relatively high intensities and limited interference from the sample matrix, a detailed explanation on peak selection can be found in the supplementary information (Figure S4.3). The intensities of the emissions for the concrete coupons showed a general positive correlation with an increase in concentration resulting in a greater emission intensity (Figure S4.4). For the concrete samples, Sr on average gave a signal $>3\sigma$ above background at surface concentrations above 40 ng/cm² Cs could be detected down to 680 ng/cm² and Co down to 320 ng/cm² on the concrete surface.

Analysis of the HDPE calibration standards showed a similar positive trend to the concrete coupons (Figure S4.5). For example, Sr could be identified down to 71 ng/cm² on the HDPE surface. The LODs (3σ above background) for Cs and Co on HDPE were higher at 6000 and 2800 ng/cm², respectively.

Unlike stainless steel and concrete, the plastic matrix does not contain multiple interfering elements. Despite thorough washing with DI and IPA, the blank HDPE spectra indicate the presence of Ca II (393.38 nm), Fe I (404.56 nm) and Al I (396.13 nm) which may be

contaminants from manufacture and processing as well as contaminants from other sources. In addition, LIBS analysis of plastics can result in the melting and burning of the surface due to the high-energy laser pulse.⁴¹

4.4.2. Single element sorption on concrete and HDPE coupons

Individual concrete and HDPE coupon surfaces were contacted with solutions containing either 500 mg/L $\text{Sr}(\text{NO}_3)_2$, CsNO_3 or $\text{Co}(\text{NO}_3)_2$ (see 4.3.3.1. above).

Normalisation of each matrix was conducted to improve comparison between the uncontaminated and contaminated coupons.⁴² For concrete this was done using the Ca II 373.67 nm emission line as the higher intensity Ca II 393.38 nm could not be used due to the high concentrations causing self-absorption to take place and thus was of little use. Normalisation of the HDPE emission spectra proved to be more difficult due to the C and H emissions falling outside of the wavelength range or below the LOD for LIBS at the conditions used in this work. To overcome this, normalisation was carried out using the Ca II 396.83 nm peak. Whilst this allowed relatively good normalisation here, it must be noted that this is a contaminant peak present in the HDPE samples and that variations in concentrations throughout the sample could affect the results.

Analysis of the concrete and HDPE coupons with LIBS identified the presence of all three analytes at their characteristic emissions of 407.78 nm, 852.13 nm and 340.51 nm (Figure 4.1). The Cs and Co peaks can be readily resolved from both sample matrices; however, the Sr peak can still be seen in the uncontaminated concrete coupon, although at a much lower normalised intensity. Despite this, Sr intensities in the contaminated concrete coupons were above the LOD for LIBS.

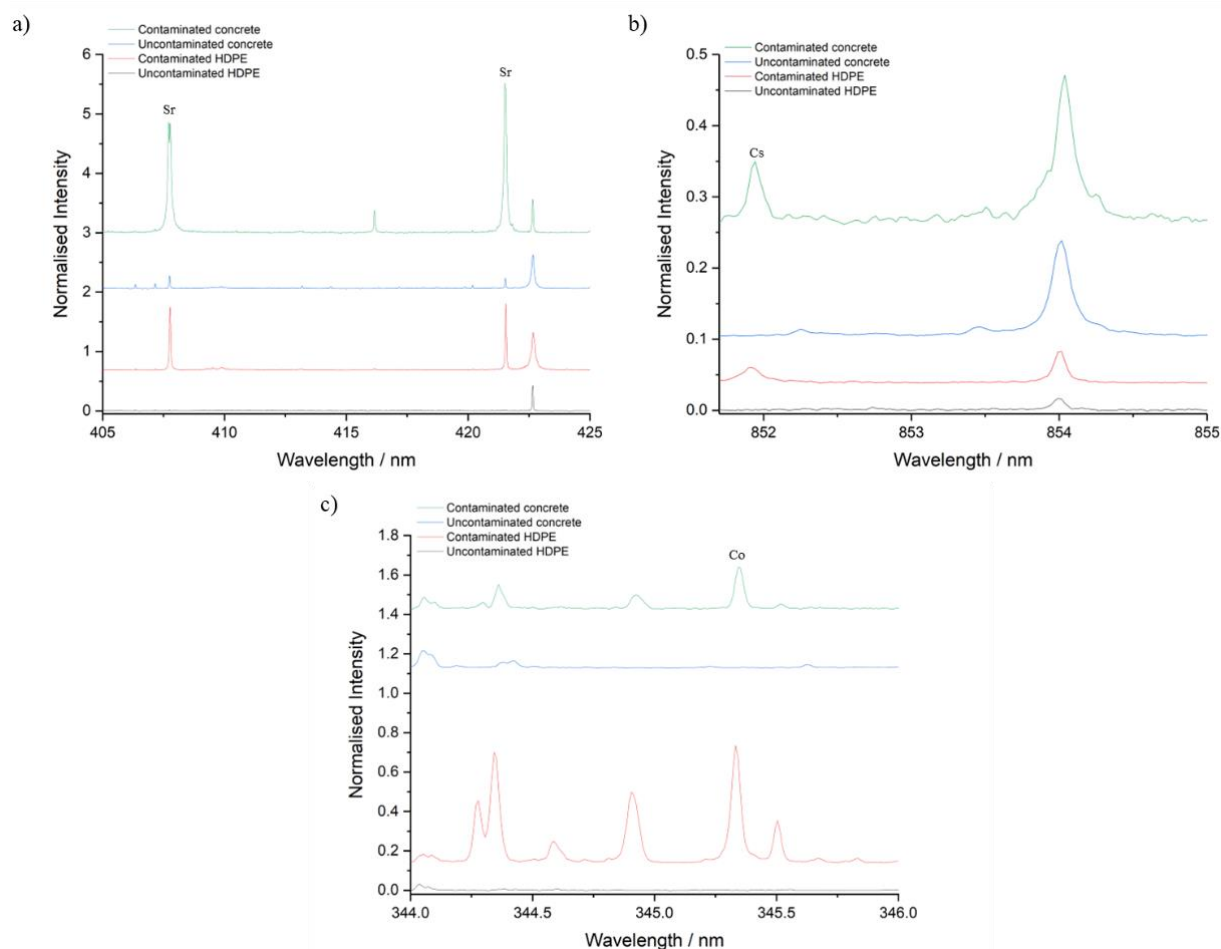


Figure 4.1. LIBS emission spectra for individual a) Sr, b) Cs and c) Co 500 mg/L sorption tests on HDPE and concrete coupons. Normalisation was conducted against known matrix peaks, in this instance the analyte peak intensity was greater than the matrix peak resulting in normalisation values greater than 1.

Uptake of contaminants (q_t) onto the concrete and HDPE surfaces were determined using ICP-MS analysis of the solutions, as well as LIBS analysis of the coupon surfaces using the calibration curves generated previously (Table 4.1). The measured uptake determined through the LIBS calibration curves were lower than those determined through ICP-MS analysis of the solution, except for Co on the HDPE surface. This could be due to a combination of LIBS small spot size and heterogeneous uptake of the analytes onto surfaces.⁴³ The difference in measured uptake for the concrete coupons is attributed to the porosity of the matrix. LIBS is only able to accurately identify the presence of analytes on the sample surface, whereas ICP-MS will account for additional uptake and diffusion of analytes into the concrete matrix. This may also be the case for HDPE as diffusion can take place; however, this is unlikely to have occurred over the time scales of this experiment.⁴⁴ Despite these differences, we have shown that LIBS

can identify the uptake of Sr, Cs and Co on concrete and HDPE surfaces at concentrations >1 mg/cm^2 .

Table 4.1. Measured uptake (q_t) of Sr, Cs and Co on concrete and HDPE surfaces through solution ICP-MS and surface LIBS analysis.

Element	Concrete $q_t / \text{mg cm}^{-2}$		HDPE $q_t / \text{mg cm}^{-2}$	
	ICP-MS	LIBS	ICP-MS	LIBS
Sr	1.14 ± 0.09	0.72 ± 0.12	0.43 ± 0.04	0.23 ± 0.06
Cs	2.20 ± 0.02	0.16 ± 0.07	0.64 ± 0.17	0.03 ± 0.02
Co	2.00 ± 0.13	0.04 ± 0.03	0.20 ± 0.01	0.25 ± 0.11

4.4.3. Contamination chamber sorption analysis

To build on the single-element contamination system analyses, sorption experiments were conducted with a mix of stable $\text{Sr}(\text{NO}_3)_2$, CsNO_3 and $\text{Co}(\text{NO}_3)_2$ in alkaline pH 11 conditions in the presence of concrete, HDPE and stainless steel matrices (see 4.3.3.2. above). Stainless steel coupons were included in these experiments to encompass the breadth of materials likely to be present in a SNF pond and allow for potential interactions between the different matrices in solution.

ICP-MS analysis of the solution could not be used to calculate contaminant uptake on the individual surfaces of each coupon since the same contaminant solution contacts multiple coupons. However, using the LIBS calibration curves, the concentration of analyte uptake onto the concrete and HDPE surfaces in the multi-elemental contamination chamber was calculated (Table 4.2). Uptake of each analyte was significantly decreased in the pond chamber compared to the individual sorption experiments. This is attributed to the presence of several different surfaces available for sorption reactions and the presence of other analytes that could compete for sorption sites.

Table 4.2. Measured uptake (q_t) of analytes onto the concrete and HDPE coupon surfaces in the contamination chamber using LIBS, averaged over 4 coupons.

Element	$q_t / \text{mg cm}^{-2}$	
	Concrete	HDPE
Sr	0.28 ± 0.082	0.10 ± 0.065
Cs	0.02 ± 0.007	<LOD
Co	0.01 ± 0.005	0.01 ± 0.003

Analysis of the concrete, HDPE and stainless steel samples after the contamination chamber experiment showed the clear presence of the 407.78 nm Sr II emission peak in the spectra of each matrix (Figure 4.2), showing Sr sorption took place on all three matrices over 28 days. Normalisation of the LIBS spectra was carried out for each matrix as before, with the Fe I 404.56 nm emission line utilised for normalisation of the stainless steel coupons.

Normalisation of the data shows the difference in intensity of the Sr emission between the uncontaminated and contaminated concrete coupons, correlating to increased uptake of Sr onto the concrete surface. Sr sorption on concrete occurs predominantly through ion-exchange mechanisms with calcium(II) in cement.⁴⁵ This is enhanced with the presence of calcium silicate hydroxide (CSH) phases which have higher concentrations of Ca and Al available for ion-exchange.^{46,47}

Analysis of the Sr emission for the stainless steel samples showed particularly high intensities, although sorption of the analytes onto stainless steel was not calibrated and therefore analysis is only semi-quantitative. Uptake of metals onto stainless steel has been shown to increase in alkaline conditions due to corrosion of the protective oxide layer which could account for the greater emission intensities seen for Sr and Co sorption on stainless steel in these experiments.^{19,48}

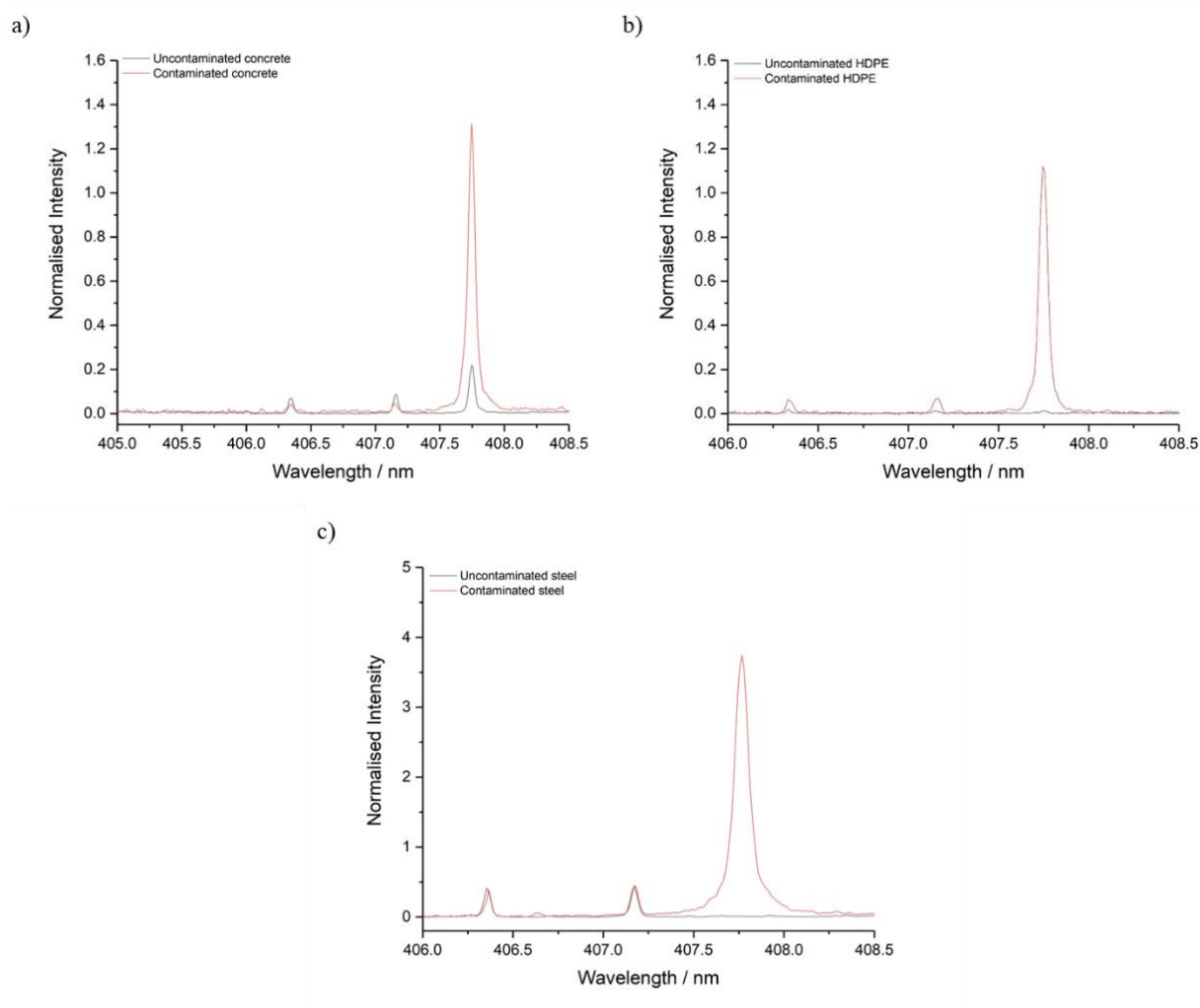


Figure 4.2. Normalised LIBS emission spectra for Sr sorption on a) concrete, b) HDPE and c) stainless steel coupons. Normalisation was conducted against known matrix peaks, in this instance the analyte peak intensity was greater than the matrix peak resulting in normalisation values greater than 1.

Cobalt uptake was identified on all three matrices in the chamber contamination (Figure 4.3). For concrete cobalt sorption occurs primarily through ion-exchange and adsorption mechanisms with hydrated CSH phases in alkaline conditions, similar to Sr.⁴⁹ LIBS analysis of the Co emissions indicate that sorption had taken place in the cement phases of the concrete samples, but at much lower concentrations. This could, in part, be due to competition for adsorption sites from strontium(II) ions; however, Co is prone to precipitation above pH 8.⁵⁰ Co precipitates as $\text{Co}(\text{OH})_2$ in alkaline conditions, which can result in reduced concentrations of cobalt(II) ions available for ion-exchange or adsorption. However, interactions between $\text{Co}(\text{OH})^+$ or $\text{Co}(\text{OH})_2$ and the matrices can still occur through the deposition of particulates onto the sample surfaces.^{48,51}

Uptake of analytes was significantly reduced for HDPE in the contamination chamber, indicating preferential sorption onto concrete and steel may have taken place. At pH 11, the hydroxide sites on concrete and steel surfaces can become negatively charged, attracting positive ions for binding along with ion-exchange mechanisms in the concrete and steel layers.⁵² This will result in increased uptake on these sites compared to the more inert HDPE surface. In this instance, Co uptake is likely to be due to deposition of $\text{Co}(\text{OH})_2$ precipitates.

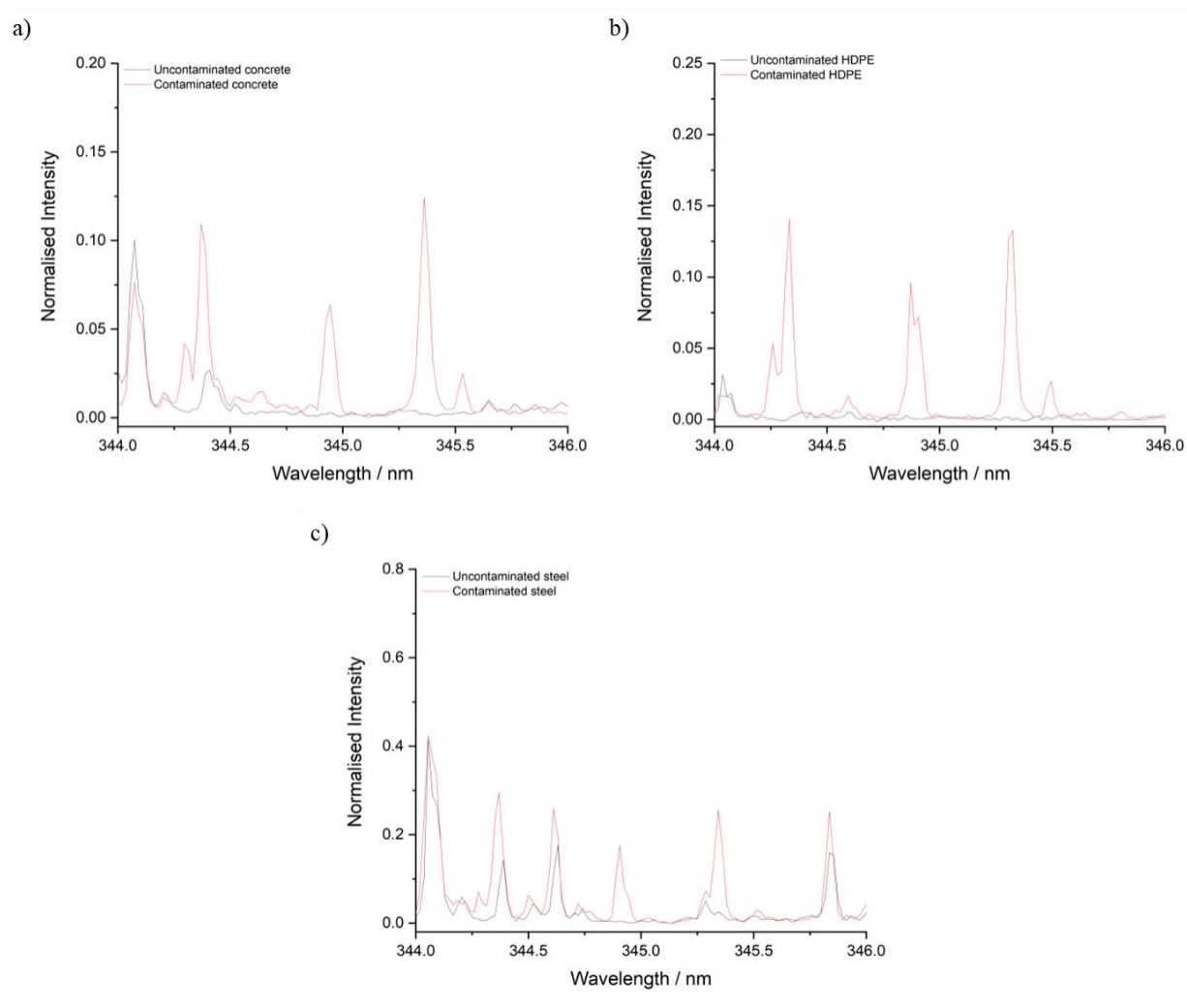


Figure 4.3. Normalised LIBS emission spectra for the sorption of cobalt on a) concrete, b) HDPE and c) stainless steel coupons.

In contrast to Sr and Co, the Cs I 852.13 nm peak was only identifiable on the concrete surfaces, indicating sorption fell below the LOD for HDPE and stainless steel in alkaline conditions (Figure 4.4).⁵³

Measured Cs uptake was lower in the multi-elemental contamination experiments, indicating

competition for adsorption sites might be occurring and that the smaller ionic radius and increased charge of Sr and Co ions result in preferential. Cs is known to preferentially bind with aggregate phases in concrete.^{26,54} However, LIBS analysis of the aggregate phases in the concrete coupons showed similar results with little to no uptake of Cs, indicating the concentration of Cs sorbed falls below the LOD.⁵⁵ In addition, ICP-MS analysis of the solution showed high concentrations of Ca and Na, due to leaching of the concrete matrix and pH adjustments (Figure S4.6). These elements may have competed with the analytes for the available sorption sites, resulting in lower concentrations of analytes sorbed to the sample surfaces.

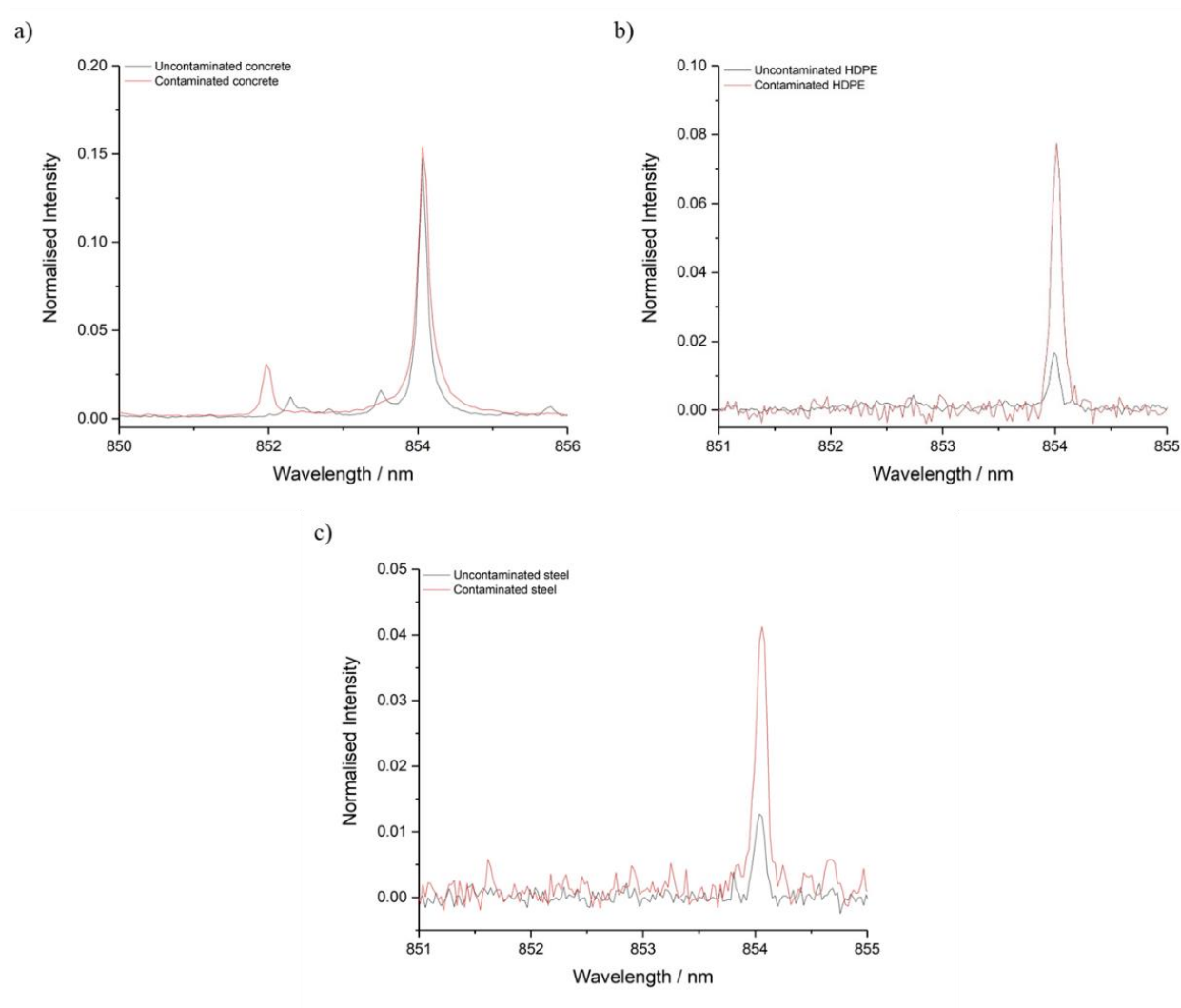


Figure 4.4. Normalised LIBS emission spectra for the sorption of Cs on a) concrete, b) HDPE and c) stainless steel coupons.

4.4.4. Model waste discharge pipeline samples

Any evaluation of the suitability or appropriateness of techniques such as LIBS for nuclear characterisation requires analysis of samples representing as many materials and environments where contamination is likely to occur as possible. To illustrate the diversity of such environments, samples replicating the contamination of nuclear waste discharge pipelines through the uptake of radionuclides onto clinoptilolite and biofilms on 304L stainless steel were analysed using LIBS. These samples were prepared according to the methodology described by Barton *et al.* (see Section 4.3.3.3 above).⁴⁰ 304L stainless steel coupons with and without the presence of *Shewanella oneidensis* MR-1 culture were contaminated with stable $\text{SrCl}_2 \cdot 6\text{H}_2\text{O}$, CsCl , $\text{CoCl}_2 \cdot 6\text{H}_2\text{O}$, $\text{EuCl}_3 \cdot 6\text{H}_2\text{O}$ and $\text{RuCl}_3 \cdot x\text{H}_2\text{O}$. Analysis of these samples with LIBS identified the presence of Sr, Cs, Ru, Co and Eu in samples both with and without biofilms present (Figure 4.5).

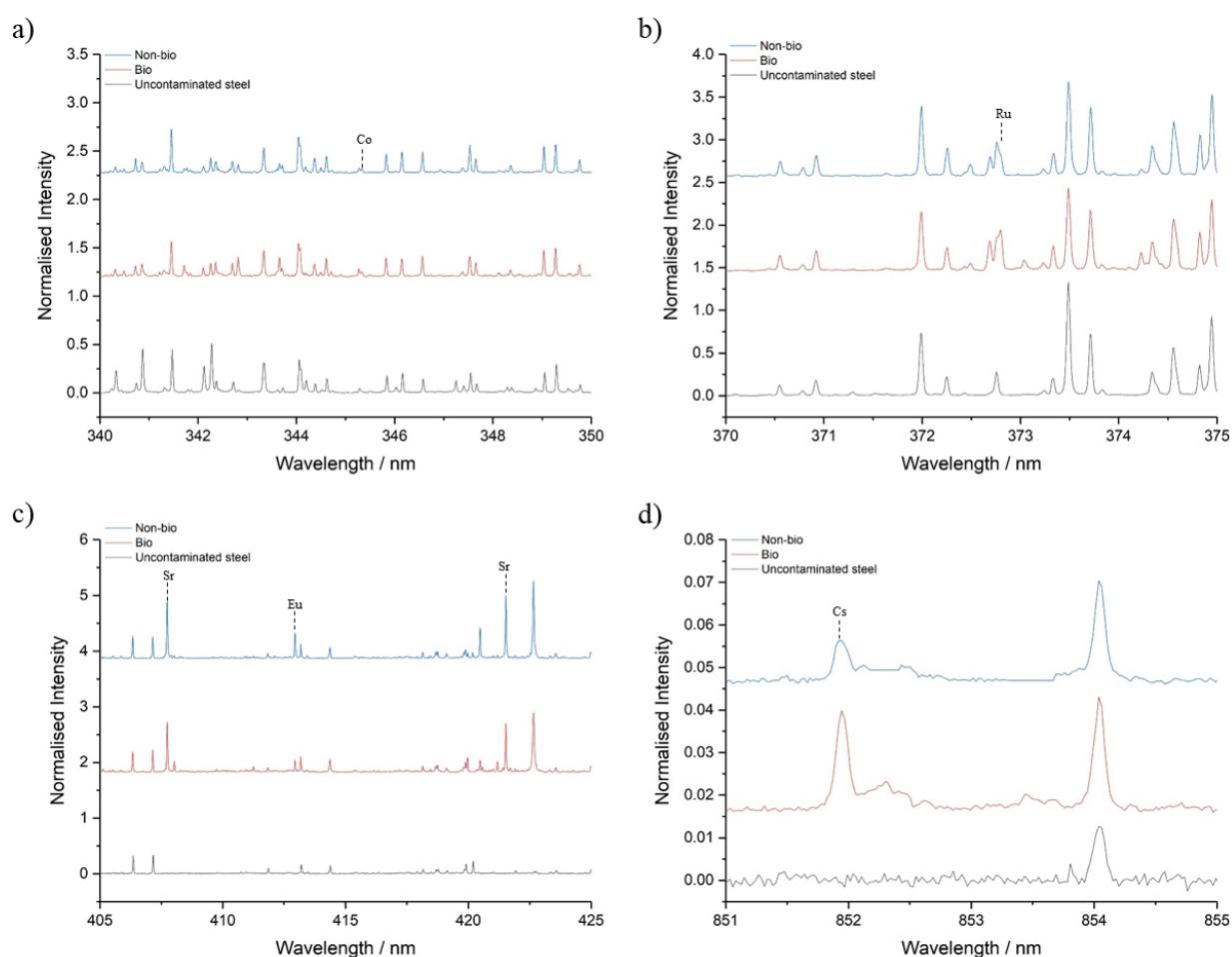


Figure 4.5. Normalised LIBS emission spectra for a) Co, b) Ru, c) Sr and Eu and d) Cs at their characteristic emission peaks. Normalisation was conducted against known matrix peaks, in

this instance the analyte peak intensity was greater than the matrix peak resulting in normalisation values greater than 1.

The characteristic Sr, Cs and Co emission peaks described earlier were used due to their lack of interference with peaks representing elements present in the steel and biofilm matrices. Identifying a suitable emission peak for Ru proved to be more challenging. The Ru II 240.27 and 245.66 nm peaks fell below the wavelength range for the chosen spectrometer and the other notable peaks at 267.88 (Ru II) and 349.89 (Ru I) nm were not visible.⁵⁶ In fact, the only peak that could be resolved was the Ru I 372.80 ($^5F_0 \rightarrow ^5F_4$) nm emission.⁵⁷ In contrast, there were several identifiable peaks available for Eu in the samples, the clearest of which were the Eu II 412.97 ($^8S_4 \rightarrow ^9S_4$) and 420.51 ($^8S_3 \rightarrow ^9S_4$) nm peaks.^{58,59}

As calibration curves were not produced for the analytes on stainless steel, these data are semi-quantitative. The results can be compared to one another, but absolute values can not be generated. The intensity of the peaks varied slightly with the presence of the biofilm. Eu emission intensities was slightly higher in the non-biofilm sample, consistent with LA-ICP-MS results obtained by Barton *et al.*⁴⁰ Ru could be identified in the biofilm samples, but not the non-biofilm samples, indicating uptake of Ru may be dependent on biological mechanisms.⁶⁰ The peak appears as a small shoulder on a neighbouring matrix peak, making accurate identification with LIBS difficult (Figure S4.7a). The concentration of Sr did not vary greatly, but the Cs concentration appears to be greater for the bio coupons compared to the non-bio coupons. This could be due to increased uptake of clinoptilolite on the biofilm samples, allowing for ion-exchange of sodium(I) and potassium(I) with cesium(I) in the zeolite.⁶¹ However, strontium(II) also readily undergoes ion-exchange with calcium(II) and magnesium(II) in clinoptilolite and did not show much variation. This difference could be attributed to heterogeneous uptake onto the coupon and the small spot size of LIBS. The Co emission peak appears relatively similar for both samples although Co identification proved difficult with LIBS at these concentrations in the sample matrix and could not be confirmed through the 412.06 nm peak (Figure S4.7b).

4.4.5. Depth-profiling using LIBS

Whilst LIBS is predominantly used for surface analysis, it is also capable of conducting depth analysis. The following describes the results of using LIBS to determine elemental concentration with increasing depth of material penetration through repeated laser pulses. Multi-pulse analysis allows the laser to essentially “drill” into the sample, providing

information on element-specific signal intensity with increasing depth into the sample. As expected, this was not a straightforward process. LIBS resolution decreases with increasing depth and each ablation shot is not guaranteed to remove a consistent volume of sample, meaning quantification of the penetration depth is not possible through LIBS alone.^{62,63} Additional support using techniques such as interferometry or microscopy is typically required to accurately measure the crater depth with each laser shot. Combinations of laser ablation techniques with ICP-MS have also been used to improve the resolution with greater crater depths, enhancing the accuracy of results.⁶⁴

Depth-profiling using LIBS was conducted for each of the steel, concrete and HDPE coupons taken from the chamber contamination experiment, as well as the pipeline samples. Each of the analyte emission lines was normalised to a matrix line from the sample material as before.

Analysis of the steel coupons indicated that most of the contamination was present in the sample surface. Increasing the number of shots, and therefore the analysis depth, resulted in a steady decrease in Sr intensity in the spectra (Figure 4.6). Spectra for the steel coupon record a drastic decrease in the Sr signal intensity by a factor of 9 from the 1st to 10th shot. In contrast, the intensity of the Sr peak in the concrete coupon remained relatively constant even after 12 shots. Concrete is a porous material, so it is likely that contaminants will have penetrated deeper into the sample bulk resulting in higher concentration of Sr throughout. SEM-EDX analysis identified Sr and Co in a LIBS crater formed after a single shot indicating the contaminants penetrated further into the concrete or have been redeposited post-ablation (Figure S4.8). However, the intensity of the 3rd to 12th shots fell below the LOD for Sr using LIBS, indicating the emissions may be due to the background concrete matrix.

Multi-pulse analysis of the HDPE samples recorded a decrease in Sr concentrations with increasing laser shot. Sr sorption is isolated at the sample surface with limited diffusion into the bulk material over the timescales of this experiment. Here we found that further depth-analysis resulted in the melting of the sample surface and produced a degraded, noisy spectra with broad peaks overlapping the emission data, indicating that the high laser energy used in LIBS is not compatible with accurate contamination depth assessment in plastic materials (Figures S4.9 and S4.10). Use of a lower energy laser pulse simply resulted in a lower signal intensity and a reduction in identification of contaminants at low concentrations.

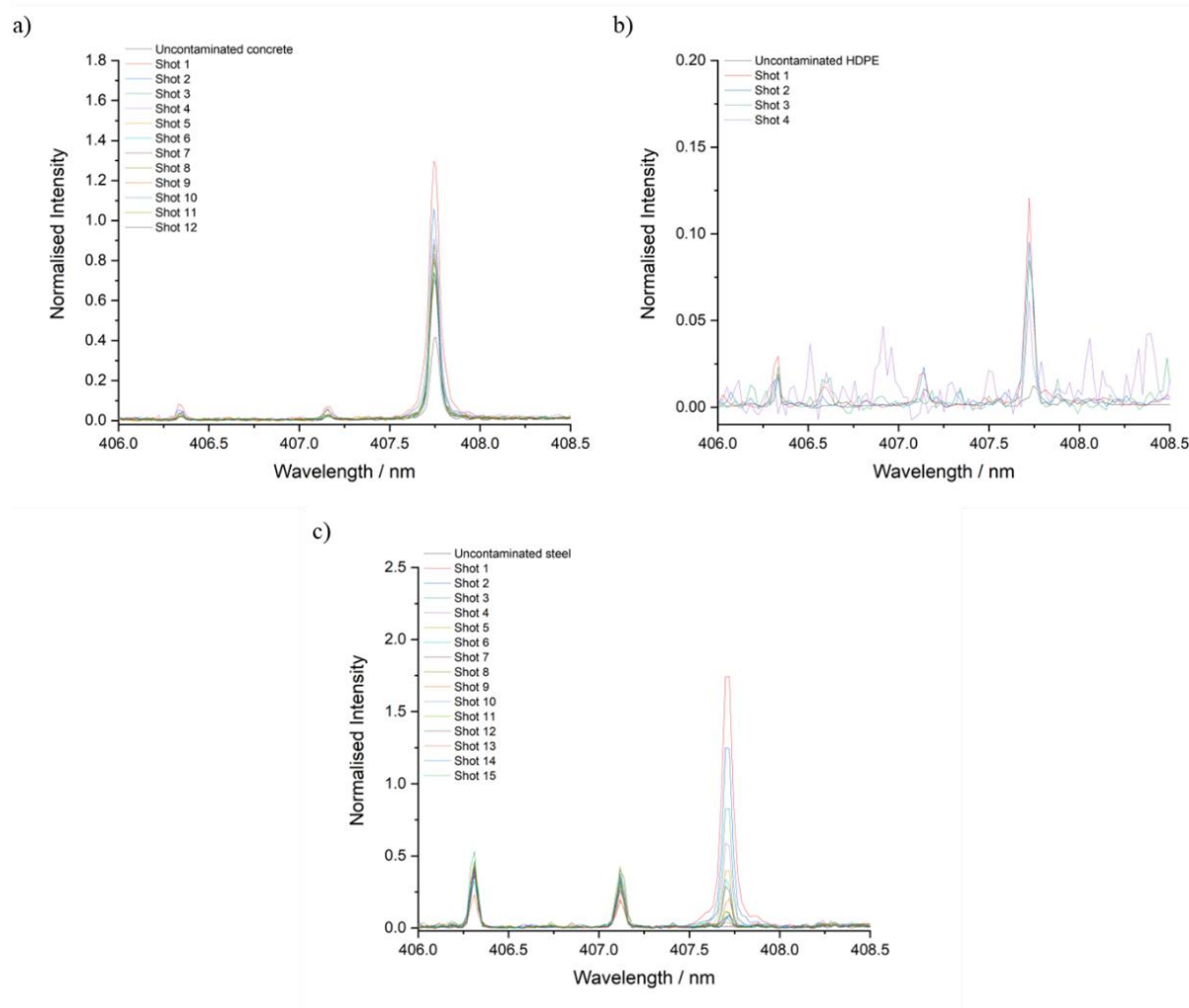


Figure 4.6. Normalised depth-profile LIBS emission spectra for Sr sorption on a) concrete, b) HDPE and c) stainless steel coupons. Normalisation was conducted against known matrix peaks, in this instance the analyte peak intensity was greater than the matrix peak resulting in normalisation values greater than 1.

Since no measurable Cs was taken up for the steel and HDPE coupons, depth-profiling of the 852.13nm peak was not conducted for these matrices. Analysis of the 345.32 nm Co I emission peak suggests that contamination was isolated to the HDPE and steel surfaces. Further depth-analysis was conducted for Cs and Co contamination on the concrete coupons (Figure 4.7). Analysis of the 345.32 nm Co I peak shows a general decrease in peak intensity with increasing number of ablation shots, indicating that Co contamination is also largely isolated to the sample surface with little penetration into the concrete. However, an increase in peak intensity can be seen after the 8th shot indicating that Co had either penetrated further into the concrete or that re-deposition of previously ablated Co from the surface occurred during repeated laser pulses,

as can be seen in the SEM-EDX images (Figure S4.11). Based on the initial decrease in intensity, it is more likely that Co contamination was limited to the sample surface with minor penetration into the concrete.

Analysis of the 852.13 nm Cs I peak over the 12 consecutive shots was more complex. On spectra, intensities appear to increase over the first 5 shots before immediately decreasing back to the original intensity observed at the surface. This seems to indicate that Cs may have gathered beneath the sample surface. Spectra for additional shots also record a small increase in the peak intensity; however, this was after several shots where Cs emissions were not identified, indicating re-deposition is likely to have occurred during ablation of the later shots. This suggest that the complex, heterogeneous concrete matrix is likely to affect the results obtained by LIBS because the concentrations in the matrix themselves will vary throughout and penetration of radionuclides is unlikely to be uniform. This may have an impact on the emission intensity values, particularly for elements that are also present in the sample matrix. Combining LIBS with depth-analysis techniques such as GD-OES or LA-ICP-MS may be able to improve the accuracy of results.^{53,64}

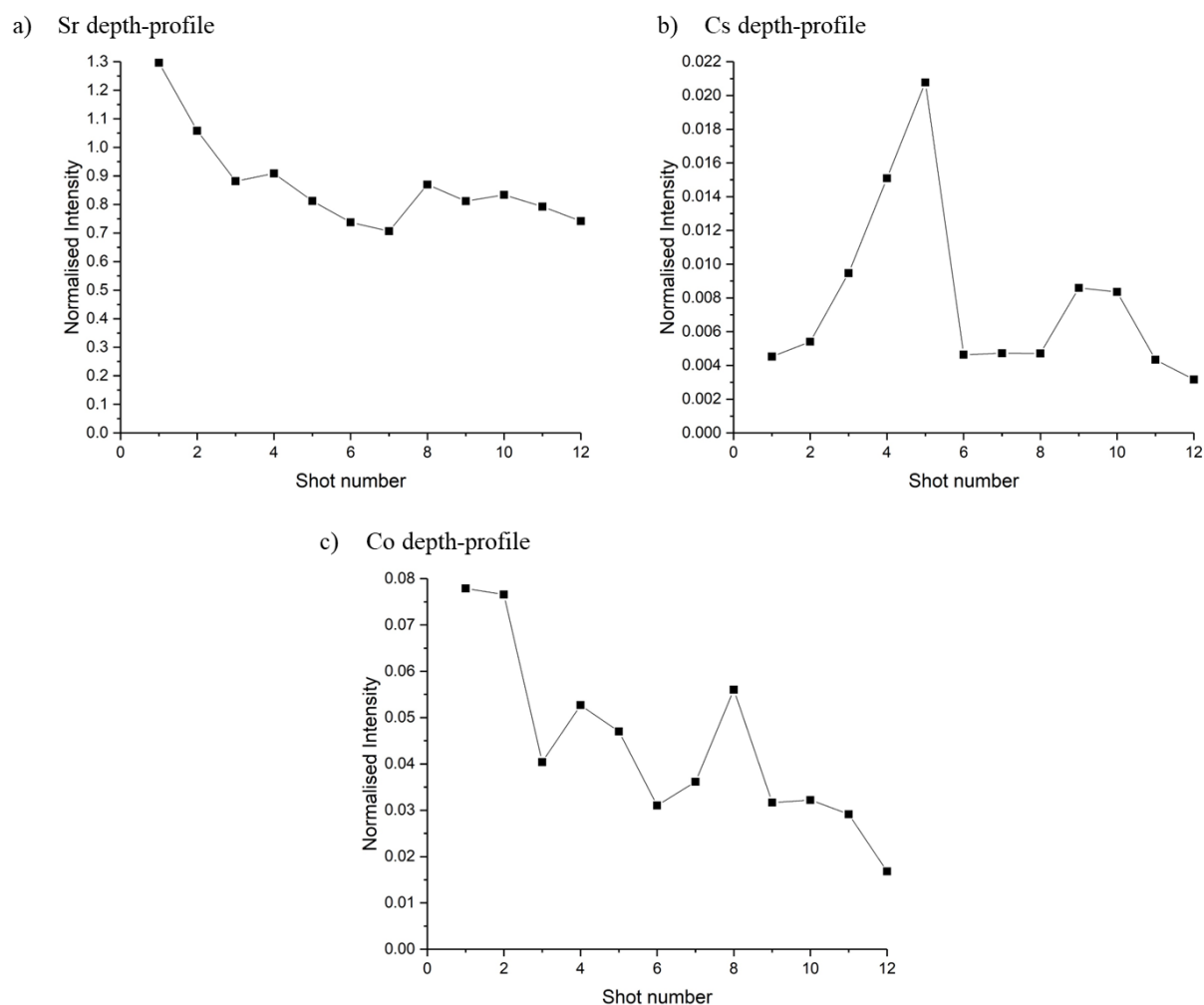


Figure 4.7. Normalised pseudo depth-profiles (where increasing shot numbers represent increasing depth) for a) Sr, b) Cs and c) Co on the concrete coupons over 12 consecutive LIBS ablation shots. Normalisation was conducted against known matrix peaks, in this instance the analyte peak intensity was greater than the matrix peak resulting in normalisation values greater than 1.

Depth analysis of the waste pipeline samples recorded a rapid decay in the Sr signal after the first two shots, indicating Sr is isolated to the sample surface in both the biofilm and non-biofilm samples, possibly trapped in the clinoptilolite on both samples (Figures 4.8a and b). The Sr signal decreases more rapidly with depth for the non-biofilm samples, indicating that increased concentrations of Sr may have been present on the biofilm samples. The continued presence of the Sr emission peak with increased shots seems to indicate that Sr sorption had taken place in the biofilm layer, as well as the steel surface below, with potential increased penetration aided by corrosion of the steel surface by the biofilm.⁶⁵ For Eu, the 412.8 nm

emission peak disappears rapidly after the initial two shots on the biofilm sample, with no reappearance throughout (Figure 4.8d). Whereas for the non-biofilm sample, the Eu intensity remains high until the 4th shot, with a small peak visible in the 5th shot, indicating Eu sorption was enhanced for the non-biofilm sample, as determined by the initial surface analysis. Depth analysis for Ru and Co was not as clear due to the initial small emission intensities obtained at the surface, but initial analysis suggested sorption was isolated to the surface with little to no penetration into the bulk material.

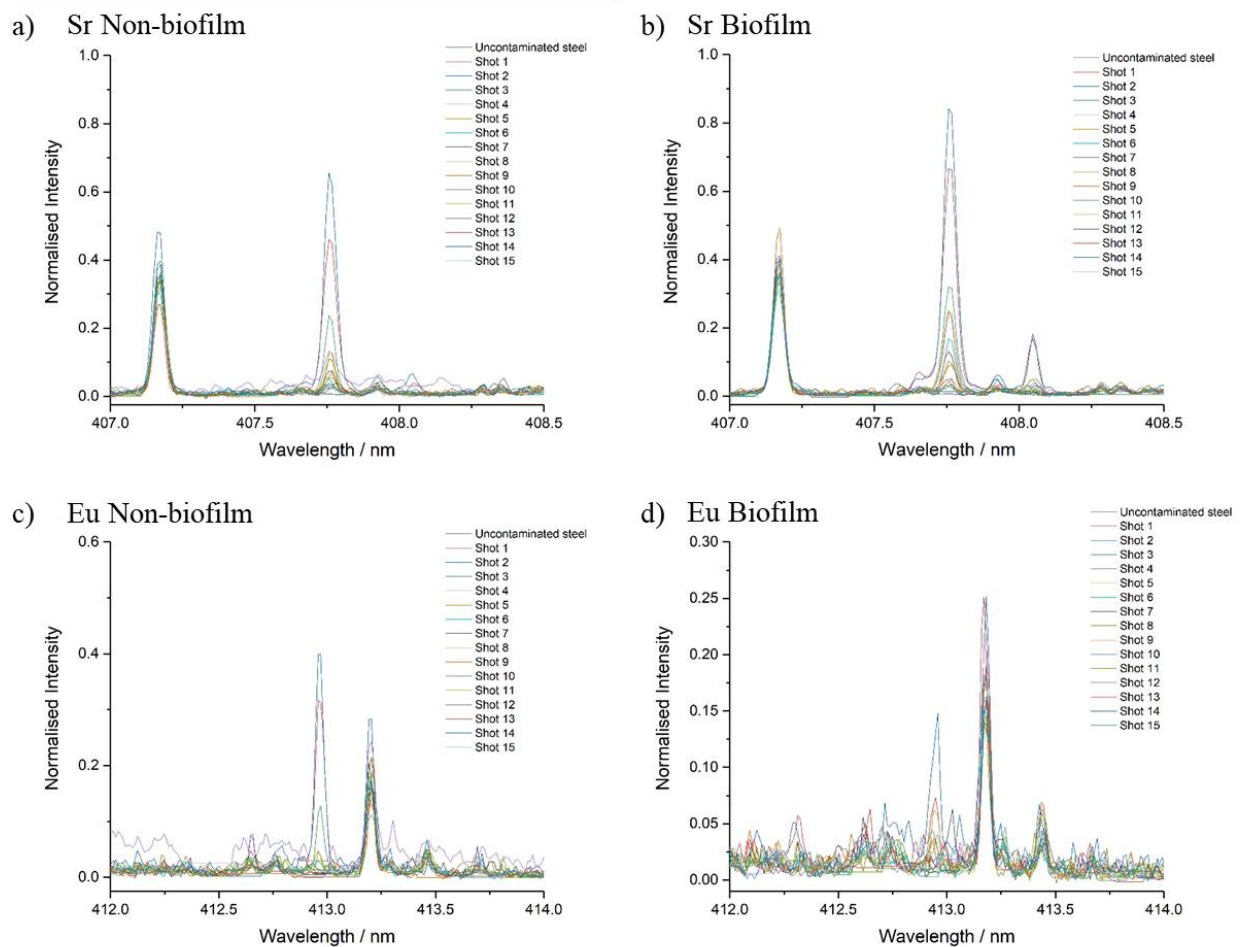


Figure 4.8. Normalised pseudo depth-profile LIBS emission spectra for Sr on a) non-biofilm and b) biofilm samples, and Eu on c) non-biofilm and d) biofilm samples.

4.5. Conclusions

This study illustrated that it is possible to identify characteristic Sr, Cs and Co emission lines during the deployment of LIBS on concrete and HDPE materials in conditions representative

of SNF storage ponds. Limits of detection for LIBS analysis of these radionuclides on concrete and HDPE surfaces were determined for the conditions used; concrete – 40 ng/cm² for Sr, 680 ng/cm² for Cs and 320 ng/cm² for Co; HDPE – 71 ng/cm² for Sr, 6000 ng/cm² for Cs and 2800 ng/cm² for Co. Lower LODs were obtained via LIBS analysis of the sample surface compared to those obtained through ICP-MS analysis of the solution. Calibration curves estimated uptake of Sr, Cs and Co as 0.72, 0.16 and 0.04 mg/cm² on concrete and 0.23, 0.03 and 0.25 mg/cm² on HDPE surfaces in single sorption systems. The multi-elemental contamination chamber experiments highlighted that contaminant uptake was reduced in complex environment representative of *in-situ* pond conditions due to competition for adsorption sites and preferential uptake on concrete materials.

In addition, LIBS resolved characteristic Sr, Cs, Eu, Ru and Co emission lines from model samples representative of waste discharge pipelines. Increased emission intensities of Cs and Ru were detected in the biofilm samples, whereas Eu emissions were greater in the non-biofilm samples. Finally, Sr and Co emission intensities remained relatively constant.

Depth-profiling showed promise for the use of LIBS for determining contaminant penetration, particularly for the analysis of Sr with this study obtaining vital new information on the intricacies of the technique. Contamination was predominantly isolated to the sample surface, with some signs of potential redeposition taking place on the concrete coupon. Analysis of the Cs 852.13 nm emission peak indicated concentrations were greater below the concrete surface; however, additional depth-profile techniques would be needed to corroborate these initial findings. Increased number of shots on HDPE resulted in surface damage and loss of spectral resolution at greater depths, suggesting that this technique may not be suitable for depth-profiling of HDPE. Depth-profiling of the waste pipeline samples indicates that Sr penetration into the steel material may have been aided by biofilm induced corrosion. However, the study illustrates huge promise in the identification of key contaminants in the shallow subsurface of samples through LIBS depth-profiling which previous studies have only hinted at.

This study provides what is believed to be the first use of LIBS to detect Sr, Cs and Co on concrete and HDPE materials relevant at 40-6000 ng/cm². These mass concentrations would correspond to activities of 0.2-23700 MBq which suggests LIBS will not be competitive with radiometric techniques. In contrast, tens of ng/cm² concentrations of heavier, longer-lived radionuclides would correspond to much lower activities (~20 Bq for Pu-239) and LIBS would be a very attractive technique. Such results indicate that there can now be no doubt that LIBS

would make a useful characterisation tool for *in-situ* analysis of radionuclide contaminated infrastructure in alkaline conditions.

Declaration of competing interest

None.

Acknowledgements

Philip Martin (UoM) and Edward McNaghten (AWE) are acknowledged for the loan of the Aryelle Echelle LIBS apparatus.

The University of Manchester Physics Workshop is acknowledged for their help in designing and manufacturing the contamination chamber.

Dr Abby Ragazzon-Smith is acknowledged for analysis of the ICP-MS samples.

Funding sources

The National Nuclear Laboratory (NNL) (Core Science Decontamination and Decommissioning R&D Theme) and the EPSRC Next Generation Nuclear Centre for Doctoral Training (NGN CDT) are acknowledged for their funding.

4.6. References

- 1 Jacobs UK Ltd and AFRY Solutions UK Ltd, *2022 UK Radioactive Waste Inventory*, 2022.
- 2 Nuclear Energy Agency, *Decontamination Techniques Used in Decommissioning Activities*, 1999.
- 3 E. C. Jung, D. H. Lee, J. I. Yun, J. G. Kim, J. W. Yeon and K. Song, Quantitative determination of uranium and europium in glass matrix by laser-induced breakdown spectroscopy, *Spectrochim. Acta Part B*, 2011, **66**, 761–764.

- 4 I. Gaona, J. Serrano, J. Moros and J. J. Laserna, Evaluation of laser-induced breakdown spectroscopy analysis potential for addressing radiological threats from a distance, *Spectrochim. Acta Part B*, 2014, **96**, 12–20.
- 5 P. Fichet, P. Mauchien and C. Moulin, Determination of impurities in uranium and plutonium dioxides by laser-induced breakdown spectroscopy, *Appl. Spectrosc.*, 1999, **53**, 1111–1117.
- 6 R. C. Chinni, D. A. Cremers, L. J. Radziemski, M. Bostian and C. Navarro-Northrup, Detection of uranium using laser-induced breakdown spectroscopy, *Appl. Spectrosc.*, 2009, **63**, 1238–1250.
- 7 L. Jolivet, M. Leprince, S. Moncayo, L. Sorbier, C. P. Lienemann and V. Motto-Ros, Review of the recent advances and applications of LIBS-based imaging, *Spectrochim. Acta Part B*, 2019, **151**, 41–53.
- 8 B. T. Manard, M. F. Schappert, E. M. Wylie and G. E. McMath, Investigation of handheld laser induced breakdown spectroscopy (HH-LIBS) for the analysis of beryllium on swipe surfaces, *Anal. Methods*, 2019, **11**, 752–759.
- 9 B. Thornton, T. Takahashi, T. Sato, T. Sakka, A. Tamura, A. Matsumoto, T. Nozaki, T. Ohki and K. Ohki, Development of a deep-sea laser-induced breakdown spectrometer for in situ multi-element chemical analysis, *Deep. Res. Part I Oceanogr. Res. Pap.*, 2015, **95**, 20–36.
- 10 C. Liu, J. Guo, Y. Tian, C. Zhang, K. Cheng, W. Ye and R. Zheng, Development and field tests of a deep-sea laser-induced breakdown spectroscopy (LIBS) system for solid sample analysis in seawater, *Sensors*, 2020, **20**, 1–11.
- 11 M. Saeki, A. Iwanade, C. Ito, I. Wakaida, B. Thornton, T. Sakka and H. Ohba, Development of a fiber-coupled laser-induced breakdown spectroscopy instrument for analysis of underwater debris in a nuclear reactor core, *J. Nucl. Sci. Technol.*, 2014, **51**, 930–938.
- 12 A. R. Lang, D. L. Engelberg, C. Walther, M. Weiss, H. Bosco, A. Jenkins, F. R. Livens and G. T. W. Law, Cesium and strontium contamination of nuclear plant stainless steel: implications for decommissioning and waste minimization, *ACS*

- Omega*, 2019, **4**, 14420–14429.
- 13 H. Filipská and K. Štamberg, Sorption of Cs(I) and Sr(II) on a mixture of bentonite and magnetite using SCM + IExM: a parametric study, *J. Radioanal. Nucl. Chem.*, 2006, **270**, 531–542.
 - 14 C. J. Dodge, A. J. Francis, J. B. Gillow, G. P. Halada, C. Eng and C. R. Clayton, Association of uranium with iron oxides typically formed on corroding steel surfaces, *Environ. Sci. Technol.*, 2002, **36**, 3504–3511.
 - 15 R. Baldev, U. K. Mudali, M. Vijayalakshmi, M. D. Mathew, A. K. Bhaduri, P. Chellapandi, S. Venugopal, C. S. Sundar, B. P. C. Rao and B. Venkataraman, Development of stainless steels in nuclear industry: with emphasis on sodium cooled fast spectrum reactors: history, technology and foresight, *Adv. Mater. Res.*, 2013, **794**, 3–25.
 - 16 Z. Duan, F. Arjmand, L. Zhang and H. Abe, Investigation of the corrosion behavior of 304L and 316L stainless steels at high-temperature borated and lithiated water, *J. Nucl. Sci. Technol.*, 2016, **53**, 1435–1446.
 - 17 Y. Xie, J. Wang, Y. Hu, J. Zhang, Q. Zhang, M. Men, S. Wang, Z. Li, G. Liu and A. Mi, Corrosion and contamination of 316L stainless steel in simulated HNO₃-based spent nuclear fuel reprocessing environments with cesium and strontium, *Ind. Eng. Chem. Res.*, 2022, **61**, 9342–9355.
 - 18 M. Z. Martin, S. Allman, D. J. Brice, R. C. Martin and N. O. Andre, Exploring laser-induced breakdown spectroscopy for nuclear materials analysis and in-situ applications, *Spectrochim. Acta - Part B At. Spectrosc.*, 2012, **74–75**, 177–183.
 - 19 Y. Xie, J. Wang, Y. Hu, J. Zhang, Y. Gao, H. Li and S. Wang, Laser-induced breakdown spectroscopy for contamination analysis of Sr and Cs on 316L stainless steels in alkaline environment for spent nuclear fuel storage, *Appl. Surf. Sci.*, 2021, **566**, 150709.
 - 20 D. E. Volkman, in *Significance of Tests and Properties of Concrete and Concrete-Making Materials*, eds. J. Lamond and J. Pielert, ASTM International, 2006, pp. 570–577.

- 21 D. L. Fillmore, *Literature Review of the Effects of Radiation and Temperature on the Aging of Concrete*, 2004.
- 22 A. Bath, G. Deissmann and S. Jefferis, in *9th International Conference on Radioactive Waste Management and Environmental Remediation, ICEM'03*, 2003, vol. 4814, pp. 1–8.
- 23 K. S. Dickerson, M. J. Wilson-Nichols and M. I. Morris, Contaminated concrete: occurrence and emerging technologies for DOE decontamination, 1995, 377.
- 24 K. Yamada, Y. Takeuchi, G. Igarashi and M. Osako, Field survey of radioactive cesium contamination in concrete after the Fukushima-Daiichi nuclear power station accident, *J. Adv. Concr. Technol.*, 2019, **17**, 659–672.
- 25 E. B. Farfán, S. P. Gaschak, A. M. Maksymenko, E. H. Donnelly, M. D. Bondarkov, G. T. Jannik and J. C. Marra, Assessment of ⁹⁰Sr and ¹³⁷Cs penetration into reinforced concrete (extent of “deepening”) under natural atmospheric conditions, *Health Phys.*, 2011, **101**, 311–320.
- 26 W. R. Bower, K. Morris, J. F. W. Mosselmans, O. R. Thompson, A. W. Banford, K. Law and R. A. D. Patrick, Characterising legacy spent nuclear fuel pond materials using microfocus X-ray absorption spectroscopy, *J. Hazard. Mater.*, 2016, **317**, 97–107.
- 27 G. Wilsch, F. Weritz, D. Schaurich and H. Wiggensauser, Determination of chloride content in concrete structures with laser-induced breakdown spectroscopy, *Constr. Build. Mater.*, 2005, **19**, 724–730.
- 28 S. Millar, T. Eichler, G. Wilsch and C. Gottlieb, in *Proceedings of the 4th International Conference on Concrete Repair, Rehabilitation and Retrofitting*, 2015, pp. 273–279.
- 29 W. W. Parkinson and O. Sisman, The use of plastics and elastomers in nuclear radiation, *Nucl. Eng. Des.*, 1971, **17**, 247–280.
- 30 K. Tazaki, M. Nakano, T. Takehara, Y. Ishigaki and H. Nakagawa, Experimental analysis of plastic materials containing radionuclides for decontamination viability,

- Earth Sci.*, 2015, **69**, 99–108.
- 31 Q. Zeng, J. B. Sirven, J. C. P. Gabriel, C. Y. Tay and J. M. Lee, Laser-induced breakdown spectroscopy for plastic analysis, *TrAC - Trends Anal. Chem.*, 2021, **140**, 116280.
- 32 T. Sormunen, J. Viljanen, J. Havisto, K. Korpijärvi, I. Rytöluoto, J. P. Kankaanpää, A. Lämsä, S. Kauppi, J. Toivonen, P. Fjäder and S. Järvinen, Characterizing plastics containing brominated flame retardants with combined LIBS and Raman spectroscopy, *J. Phys. Conf. Ser.*, 2022, **2346**, 1–7.
- 33 S. Tognana, C. D'Angelo, S. Montecinos, M. Pereyra and W. Salgueiro, Laser-induced breakdown spectroscopy (LIBS) as a technique to detect copper in plastic and microplastic waste, *Chemosphere*, 2022, **303**, 1–6.
- 34 O. Alam, L. Yang and X. Yanchun, Determination of the selected heavy metal and metalloid contents in various types of plastic bags, *J. Environ. Heal. Sci. Eng.*, 2019, **17**, 161–170.
- 35 S. Khan and A. Khan, Toxic heavy metal contamination in locally made plastic food container, *Int. J. Sci. Eng. Res.*, 2015, **6**, 45–47.
- 36 M. Whitt, K. Vorst, W. Brown, S. Baker and L. Gorman, Survey of heavy metal contamination in recycled polyethylene terephthalate used for food packaging, *J. Plast. Film Sheeting*, 2012, **0**, 1–11.
- 37 M. I. Ojovan, W. E. Lee and S. N. Kalmykov, in *An Introduction to Nuclear Waste Immobilisation*, Elsevier, 3rd edn., 2019, pp. 145–154.
- 38 C. Adam, J. Garnier-Laplace and S. Roussel-Debet, *Radionuclide fact sheet: Cobalt-60 and the environment*, 2001.
- 39 A. J. McBain, in *Advances in Applied Microbiology*, Elsevier Inc., 2009, vol. 69, pp. 99–132.
- 40 F. Barton, The University of Manchester, 2022.
- 41 Polymer Database, Melting points of polymers, <https://polymerdatabase.com/polymer>

physics/Polymer Tm C.html.

- 42 R. Noll, *Laser-Induced Breakdown Spectroscopy (LIBS): Fundamentals and Applications*, Springer, 1st edn., 2012.
- 43 D. Cremers and L. Radziemski, *Handbook of Laser-Induced Breakdown Spectroscopy*, Wiley, 2nd edn., 2013.
- 44 X. Guo, G. Hu, X. Fan and H. Jia, Sorption properties of cadmium on microplastics: the common practice experiment and a two-dimensional correlation spectroscopic study, *Ecotoxicol. Environ. Saf.*, 2020, **190**, 110118.
- 45 J. Tits, E. Wieland, C. J. Müller, C. Landesman and M. H. Bradbury, Strontium binding by calcium silicate hydrates, *J. Colloid Interface Sci.*, 2006, **300**, 78–87.
- 46 N. D. M. Evans, Binding mechanisms of radionuclides to cement, *Cem. Concr. Res.*, 2008, **38**, 543–553.
- 47 E. Wieland, J. Tits, D. Kunz and R. Dähn, Strontium uptake by cementitious materials, *Environ. Sci. Technol.*, 2008, **42**, 403–409.
- 48 S. A. Adeleye, D. A. White and J. B. Taylor, Kinetics of contamination of stainless steel in contact with radioactive solutions at ambient temperatures, *J. Radioanal. Nucl. Chem. Artic.*, 1995, **189**, 65–70.
- 49 C. Kim, S. Choi and M. Shin, Editors' Choice—Review—Electro-Kinetic Decontamination of Radioactive Concrete Waste from Nuclear Power Plants, *J. Electrochem. Soc.*, 2018, **165**, E330–E344.
- 50 H. Yüzer, M. Kara, E. Sabah and M. S. Çelik, Contribution of cobalt ion precipitation to adsorption in ion exchange dominant systems, *J. Hazard. Mater.*, 2008, **151**, 33–37.
- 51 L. Chen and S. Lu, Sorption and desorption of radiocobalt on montmorillonite — effects of pH, ionic strength and fulvic acid, 2008, **66**, 288–294.
- 52 C. Hazarika and S. Sharma, Survey on ion sensitive field effect transistor from the view point of pH sensitivity and drift, *Indian J. Sci. Technol.*, 2017, **10**, 1–18.
- 53 A. Lang, D. Engelberg, N. T. Smith, D. Trivedi, O. Horsfall, A. Banford, P. A. Martin,

- P. Coffey, W. R. Bower, C. Walther, M. Weiß, H. Bosco, A. Jenkins and G. T. W. Law, Analysis of contaminated nuclear plant steel by laser-induced breakdown spectroscopy, *J. Hazard. Mater.*, 2018, **345**, 114–122.
- 54 A. S. Makarious, M. A. El-Kolaly, I. I. Bashter and W. A. Kansouh, Radiation distribution through ilmenite-limonite concrete and its application as a reactor biological shield, *Int. J. Radiat. Appl. Instrumentation. Part*, 1989, **40**, 257–260.
 - 55 M. D. Kaminski, C. J. Mertz, J. Jerden, M. Kalensky, N. Kivenas and M. Magnuson, A case study of cesium sorption onto concrete materials and evaluation of wash agents: implications for wide area recovery, *J. Env. Chem Eng*, 2019, **60**, 1–24.
 - 56 A. Sarkar, V. M. Telmore, D. Alamelu and S. K. Aggarwal, Laser-induced breakdown spectroscopic quantification of platinum group metals in simulated high level nuclear waste, *J. Anal. At. Spectrom.*, 2009, **24**, 1545–1550.
 - 57 A. F. Abu Kasim, M. A. Wakil, K. Grant, M. Hearn and Z. T. Alwahabi, Aqueous ruthenium detection by microwave-assisted laser-induced breakdown spectroscopy, *Plasma Sci. Technol.*, 2022, **24**, 1–8.
 - 58 J. I. Yun, T. Bundschuh, V. Neck and J. I. Kim, Selective determination of europium(III) oxide and hydroxide colloids in aqueous solution by laser-induced breakdown spectroscopy, *Appl. Spectrosc.*, 2001, **55**, 273–278.
 - 59 K. G. Myhre, M. J. Mehta, M. Z. Martin and M. Du, Laser-induced breakdown spectroscopy analysis of europium and samarium in aluminum oxide, *Spectrochim. Acta - Part B At. Spectrosc.*, 2018, **149**, 30–34.
 - 60 J. F. Gibson, R. K. Poole, M. N. Hughes and J. F. Rees, Ruthenium nitrosyl complexes: toxicity to *Escherichia coli* and yeasts and uptake by marine bacteria, *Arch. Environ. Contam. Toxicol.*, 1986, **15**, 519–523.
 - 61 A. Dyer, A. Chimedtsogzol, L. Campbell and C. Williams, Uptake of cesium and strontium radioisotopes by natural zeolites from Mongolia, *Microporous Mesoporous Mater.*, 2006, **95**, 172–175.
 - 62 L. St-Onge and M. Sabsabi, Towards quantitative depth-profile analysis using laser-

- induced plasma spectroscopy: investigation of galvanized coatings on steel, *Spectrochim. acta, Part B At. Spectrosc.*, 2000, **55**, 299–308.
- 63 C. Lefebvre, A. Catalá-Espí, P. Sobron, A. Koujelev and R. Léveillé, Depth-resolved chemical mapping of rock coatings using laser-induced breakdown spectroscopy: implications for geochemical investigations on Mars, *Planet. Space Sci.*, 2016, **126**, 24–33.
- 64 M. P. Mateo, C. C. Garcia and R. Hergenröder, Depth analysis of polymer-coated steel samples using near-infrared femtosecond laser ablation inductively coupled plasma mass spectrometry, *Anal. Chem.*, 2007, **79**, 4908–4914.
- 65 R. Jia, D. Yang, D. Xu and T. Gu, Anaerobic corrosion of 304 stainless steel caused by the *Pseudomonas aeruginosa* biofilm, *Front. Microbiol.*, 2017, **8**, 1–9.

4.7. Supplementary information

Table S4.1. Composition of 304L stainless steel.⁷³

Element	Fe	Ni	Cr	Mn	Si	C
wt %	Balance	8.00-12.00	18.00-20.00	<2.00	<1.00	<0.03

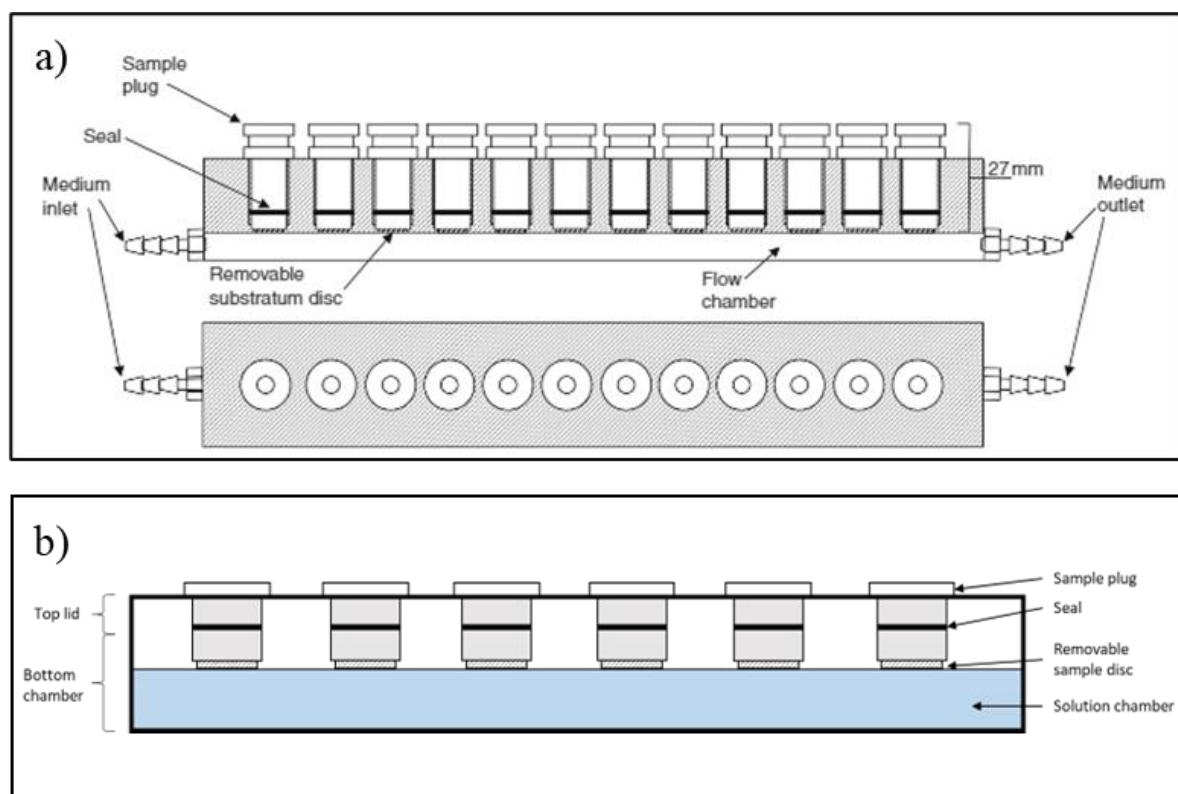


Figure S4.1. a) Modified Robbins device used for continuous flow systems.³⁹ b) Design for the contamination chamber.

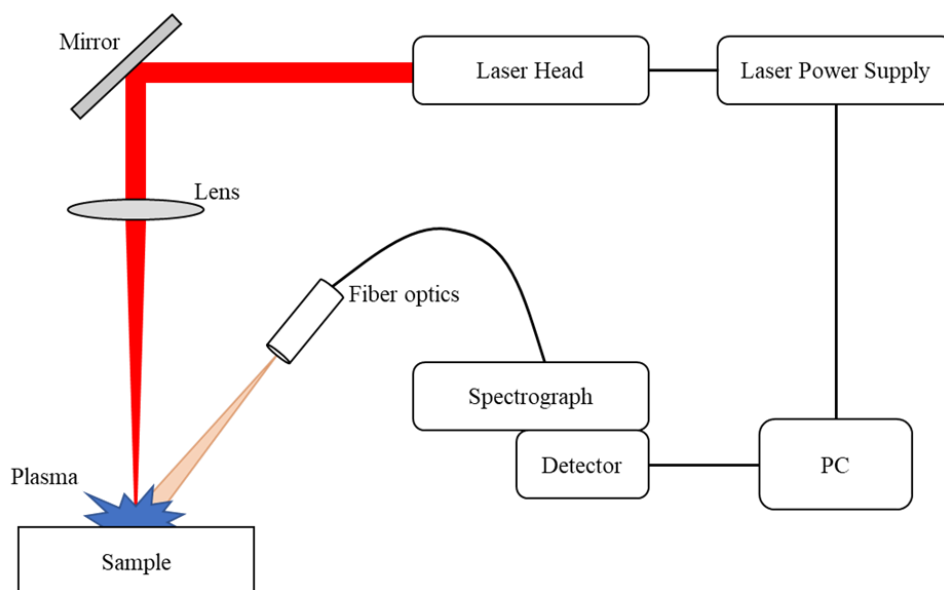


Figure S4.2. Schematic of LIBS setup.

S.I. – Matrix interference in laser-induced breakdown spectroscopy.

During LIBS analysis, a portion of the sample matrix is ablated along with any potential surface contamination. This can result in a complex spectrum with overlap of analyte emission peaks with signals from the sample matrix (Figure S4.3). In addition, the limit of detection for LIBS analysis of analytes is dependent on the sample matrix, atmosphere and distance of the sample measurement from the laser source.¹ It is therefore necessary to determine which peaks can be used for accurate identification of analytes on each sample surface in the conditions used, particularly for complex matrices such as steel and concrete.

For strontium contamination, the 407.78 nm ($^2P_{3/2} \rightarrow ^2S_{1/2}$, whereby $^2P_{3/2}$ represents the upper energy level term and $^2S_{1/2}$ represents the lower energy level term) and 421.54 nm ($^2P_{1/2} \rightarrow ^2S_{1/2}$) Sr II emission peaks were predominantly used for the identification of Sr due to their high intensity and relatively low interference with other elements.²⁻⁴ These peaks can clearly be distinguished from the HDPE and steel matrices (Figure 4.1d). However, the 407.78 and 421.54 nm Sr emission peaks are also present in the spectra for the uncontaminated concrete sample as Sr is present in the sample matrix. This interference will make accurate identification of Sr arising from contamination difficult using solely LIBS.

Cesium contaminant identification using LIBS has often proved challenging due to its high

LOD and the presence in the spectrum of high intensity peaks that overlap with peaks representing abundant elements such as Fe and Cr in steel.⁵⁻⁷ In addition, Cs is prone to self-absorption at higher concentrations, a phenomenon whereby elemental emissions are re-absorbed by the same element in another area of the plasma.⁸ This can result in inaccurate measurement of the peak intensity and hence of elemental concentrations. Previous analysis of Cs sorption on steel highlighted these issues and the need for improvements to LIBS sensitivity to identify Cs at concentrations relevant to those found in nuclear environments.⁴ Cs has several emission peaks available for characterisation with LIBS. The Cs I 455.53 ($^2P_{3/2} \rightarrow ^2S_{1/2}$), 852.13 ($^2P_{3/2} \rightarrow ^2S_{1/2}$) and 894.34 ($^2P_{1/2} \rightarrow ^2S_{1/2}$) nm peaks have been used previously.⁹⁻¹¹ In this study, the 852.13 nm Cs I emission line could be clearly identified from the concrete and HDPE matrix; however, the 455.53 nm and 894.34 nm emissions could not be distinguished due to their lower relative intensities in these matrices (Figure 4.1).

Co emissions can be relatively weak and some researchers have had difficulty identifying Co due to interference from Fe emissions from steel.¹² No interference occurred for the matrices used in this work. Co analysis was achieved using identification of the range of peaks from 340-360 nm. Previous work focused on the 340.51 nm ($^4F^{\circ}_{9/2} \rightarrow ^4F_{9/2}$) peak; however, the 345.32 nm Co I ($^4G_{11/2} \rightarrow ^4F_{9/2}$) emission intensity was greater in this work.^{13,14}

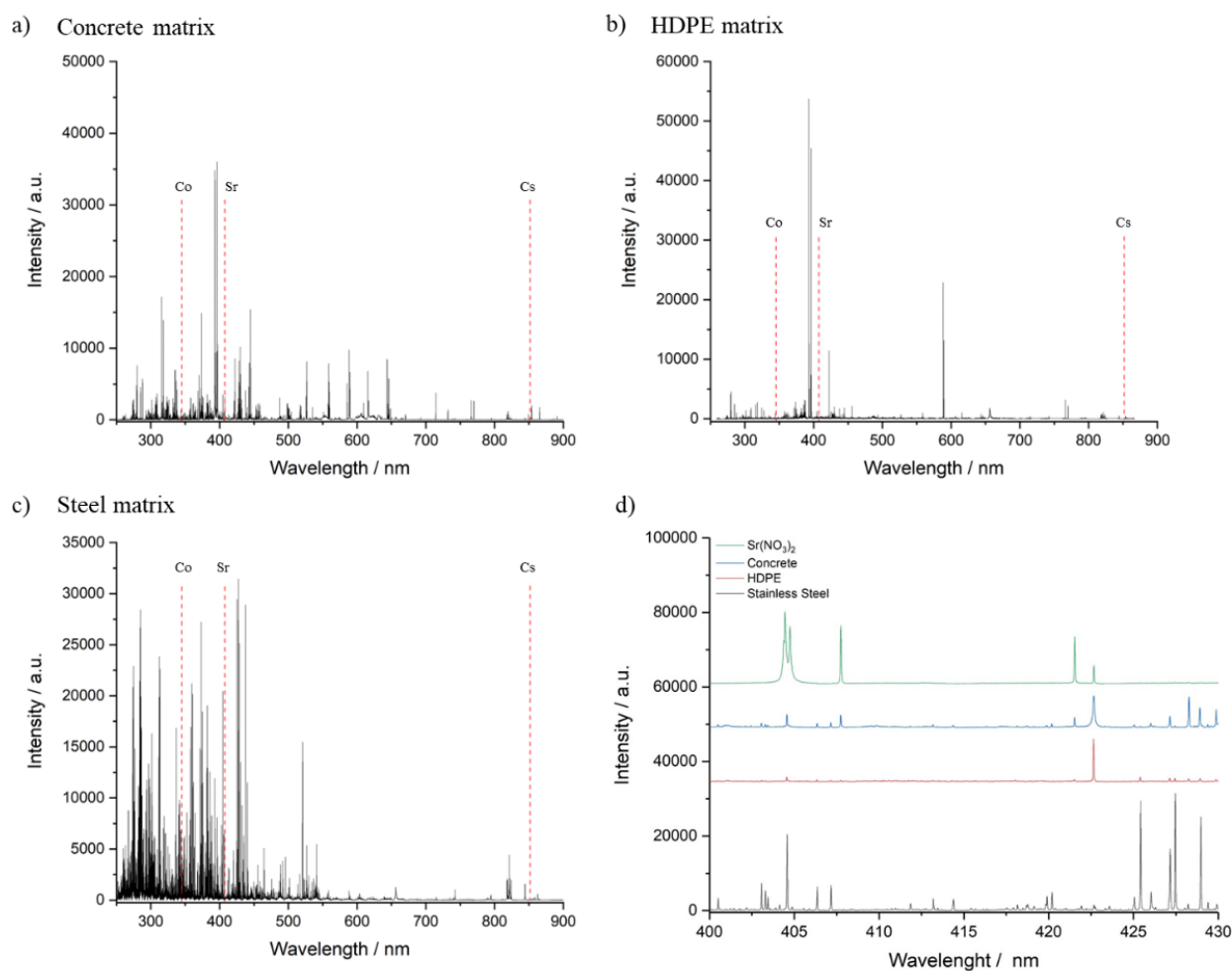


Figure S4.3. LIBS emission spectra for uncontaminated a) concrete, b) HDPE, c) 304L stainless steel coupons and d) comparison of all three matrices with a $\text{Sr}(\text{NO}_3)_2$ standard from 400-430 nm.

References:

- 1 D. Cremers and L. Radziemski, *Handbook of Laser-Induced Breakdown Spectroscopy*, Wiley, 2nd edn., 2013.
- 2 P. Fichet, P. Mauchien and C. Moulin, Determination of impurities in uranium and plutonium dioxides by laser-induced breakdown spectroscopy, *Appl. Spectrosc.*, 1999, **53**, 1111–1117.
- 3 A. M. Popov, A. N. Drozdova, S. M. Zaytsev, D. I. Biryukova, N. B. Zorov and T. A. Labutin, Rapid, direct determination of strontium in natural waters by laser-induced

- breakdown spectroscopy, *J. Anal. At. Spectrom.*, 2016, **31**, 1123–1130.
- 4 A. Lang, D. Engelberg, N. T. Smith, D. Trivedi, O. Horsfall, A. Banford, P. A. Martin, P. Coffey, W. R. Bower, C. Walther, M. Weiß, H. Bosco, A. Jenkins and G. T. W. Law, Analysis of contaminated nuclear plant steel by laser-induced breakdown spectroscopy, *J. Hazard. Mater.*, 2018, **345**, 114–122.
 - 5 M. Z. Martin, S. Allman, D. J. Brice, R. C. Martin and N. O. Andre, Exploring laser-induced breakdown spectroscopy for nuclear materials analysis and in-situ applications, *Spectrochim. Acta Part B*, 2012, **74–75**, 177–183.
 - 6 M. Singh and A. Sarkar, Analytical evaluation of cesium emission lines using laser-induced breakdown spectroscopy, *Pramana - J. Phys.*, 2019, **93**, 1–9.
 - 7 M. Ramli, A. Khumaeni, K. H. Kurniawan, M. O. Tjia and K. Kagawa, Spectrochemical analysis of Cs in water and soil using low pressure laser-induced breakdown spectroscopy, *Spectrochim. Acta - Part B At. Spectrosc.*, 2017, **132**, 8–12.
 - 8 R. Hai, Z. He, X. Yu, L. Sun, D. Wu and H. Ding, Comparative study on self-absorption of laser-induced tungsten plasma in air and in argon, *Opt. Express*, 2019, **27**, 2509.
 - 9 I. Gaona, J. Serrano, J. Moros and J. J. Laserna, Evaluation of laser-induced breakdown spectroscopy analysis potential for addressing radiological threats from a distance, *Spectrochim. Acta Part B*, 2014, **96**, 12–20.
 - 10 Y. Xie, J. Wang, Y. Hu, J. Zhang, Q. Zhang, M. Men, S. Wang, Z. Li, G. Liu and A. Mi, Corrosion and contamination of 316L stainless steel in simulated HNO₃-based spent nuclear fuel reprocessing environments with cesium and strontium, *Ind. Eng. Chem. Res.*, 2022, **61**, 9342–9355.
 - 11 S. Ikezawa, M. Wakamatsu and T. Ueda, Detection of cesium from pollucite using laser-induced breakdown spectroscopy, *Solid State Phenom.*, 2013, **199**, 285–290.
 - 12 R. Noll, *Laser-Induced Breakdown Spectroscopy (LIBS): Fundamentals and Applications*, Springer, 1st edn., 2012.
 - 13 J. Li, L. Guo, N. Zhao, X. Yang, R. Yi, K. Li, Q. Zeng, X. Li, X. Zeng and Y. Lu, Determination of cobalt in low-alloy steels using laser-induced breakdown spectroscopy combined with laser-induced fluorescence, *Talanta*, 2016, **151**, 234–238.

- 14 R. Zhou, K. Liu, Z. Tang, P. Gao, J. Yan and X. Li, High-sensitivity determination of available cobalt in soil using laser-induced breakdown spectroscopy assisted with laser-induced fluorescence, *Appl. Opt.*, 2021, **60**, 9062–9066.

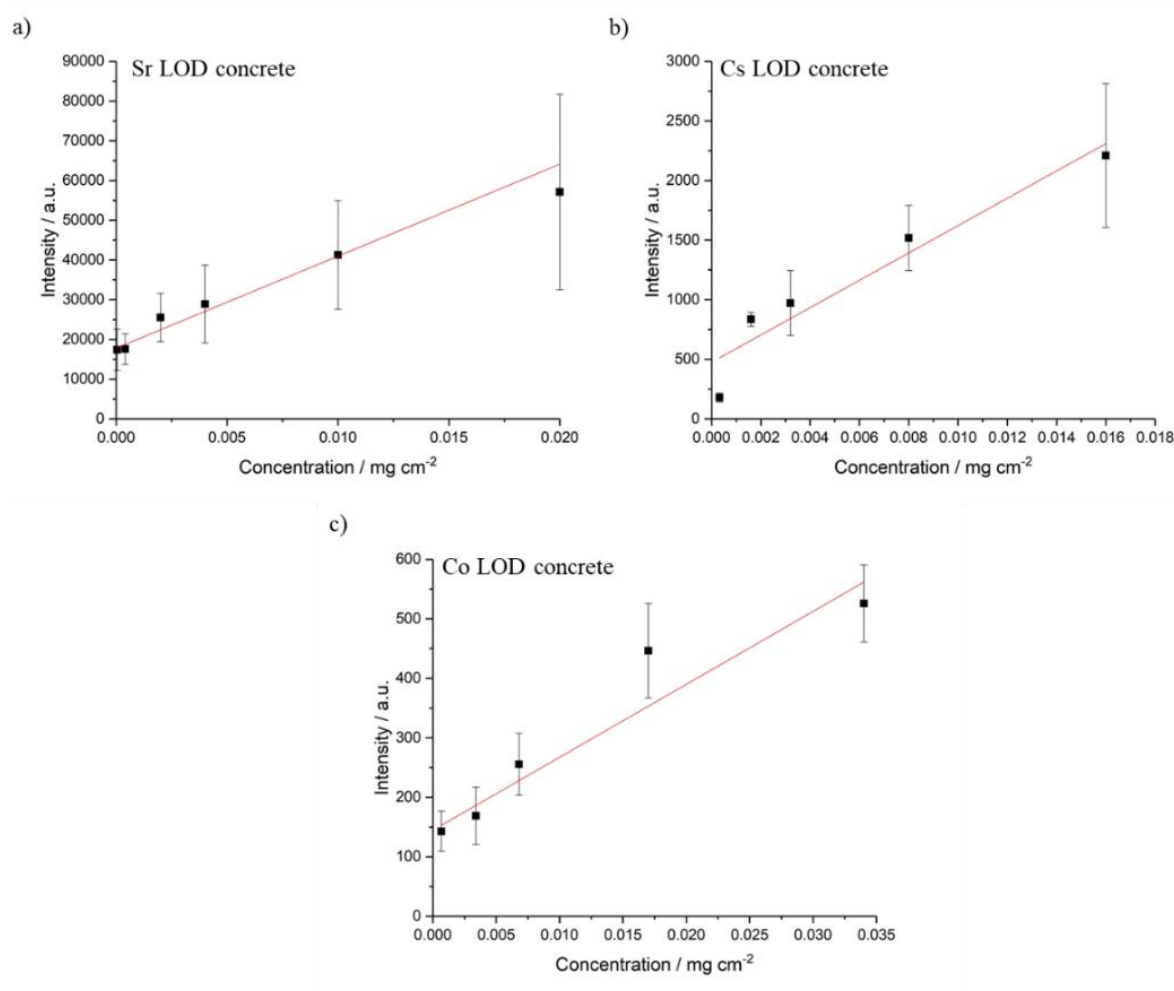


Figure S4.4. LIBS calibration curves for a) Sr ($R^2 = 0.93$), b) Cs ($R^2 = 0.94$) and c) Co ($R^2 = 0.92$) on concrete surfaces. Error bars are estimated standard deviation over 9 shots.

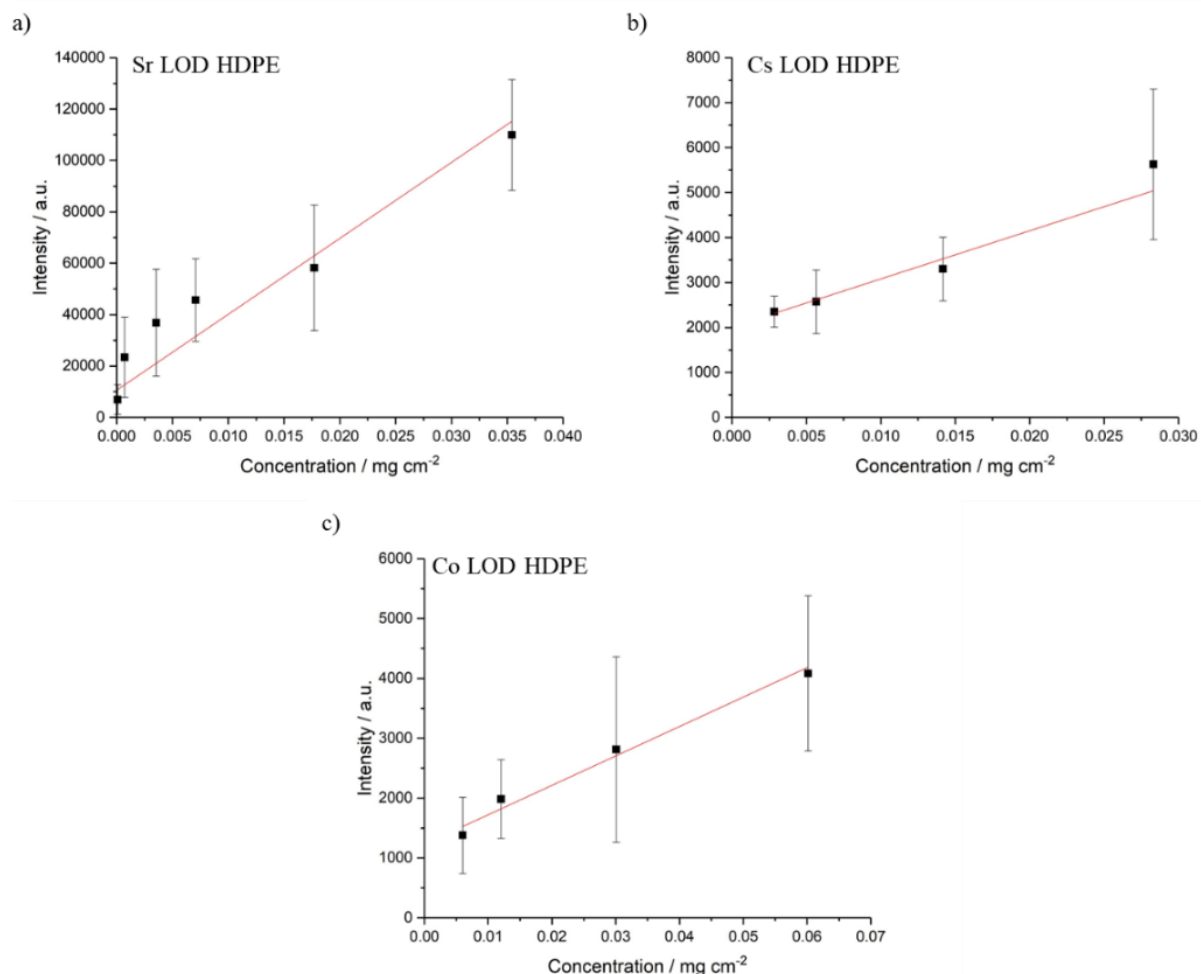


Figure S4.5. LIBS calibration curves for a) Sr ($R^2 = 0.92$), b) Cs ($R^2 = 0.97$) and c) Co ($R^2 = 0.95$) on HDPE surfaces. Error bars are estimated standard deviation over 9 shots.

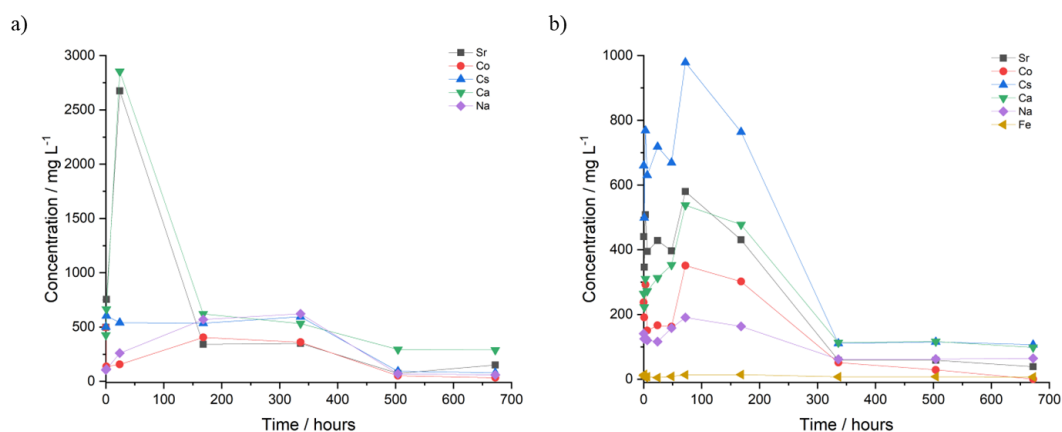


Figure S4.6. Concentration (mg/L) of analytes obtained from ICP-MS analysis of solutions containing a) Sr, Cs and Co in concrete sorption experiments and b) Sr, Cs and Co for mixed-element experiments containing concrete, HDPE and steel coupons.

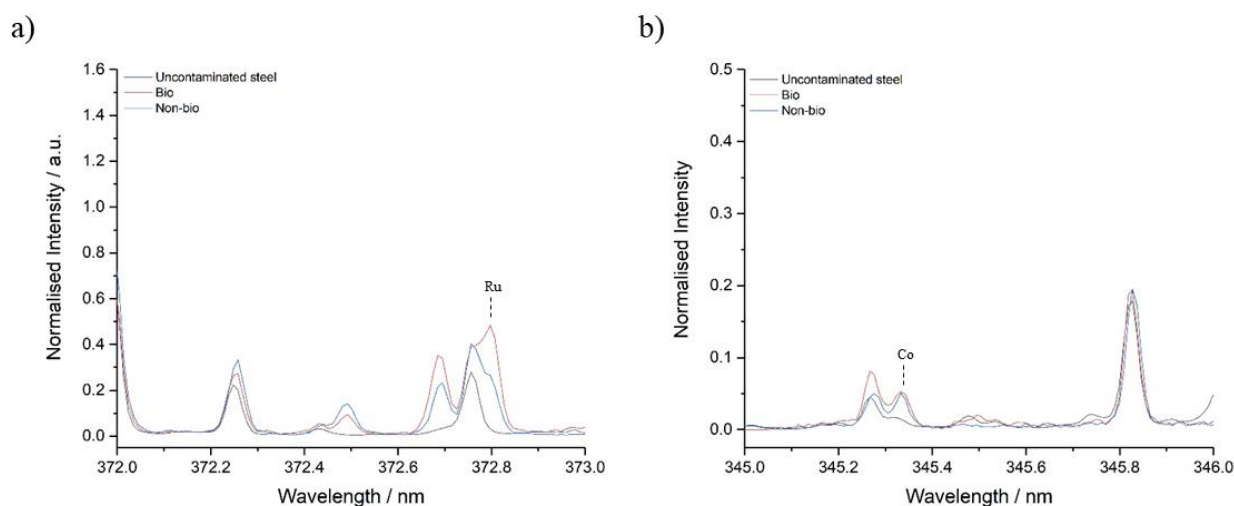


Figure S4.7. Normalised LIBS emission spectra for a) Ru at 372.80 nm and b) Co at 345.32 nm on stainless steel with and without biofilm present. Normalisation was conducted against known matrix peaks, in this instance the analyte peak intensity was greater than the matrix peak resulting in normalisation values greater than 1.

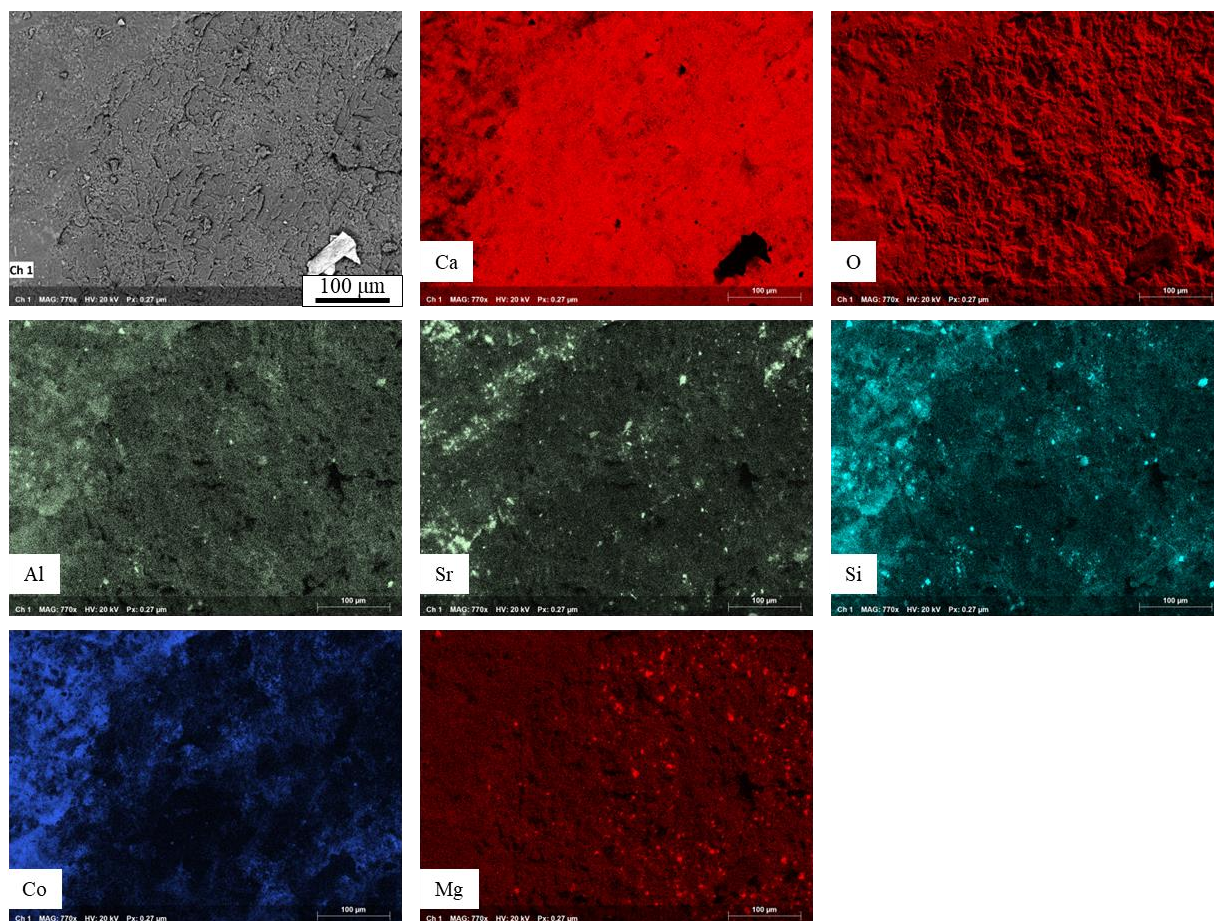


Figure S4.8. SEM-EDX maps of edge of a LIBS crater on the concrete surface indicating the presence of Sr and Co in the crater after 1 shot. Sr and Co can also be seen in regions containing Ca and Si, indicating binding to CSH phases is taking place.

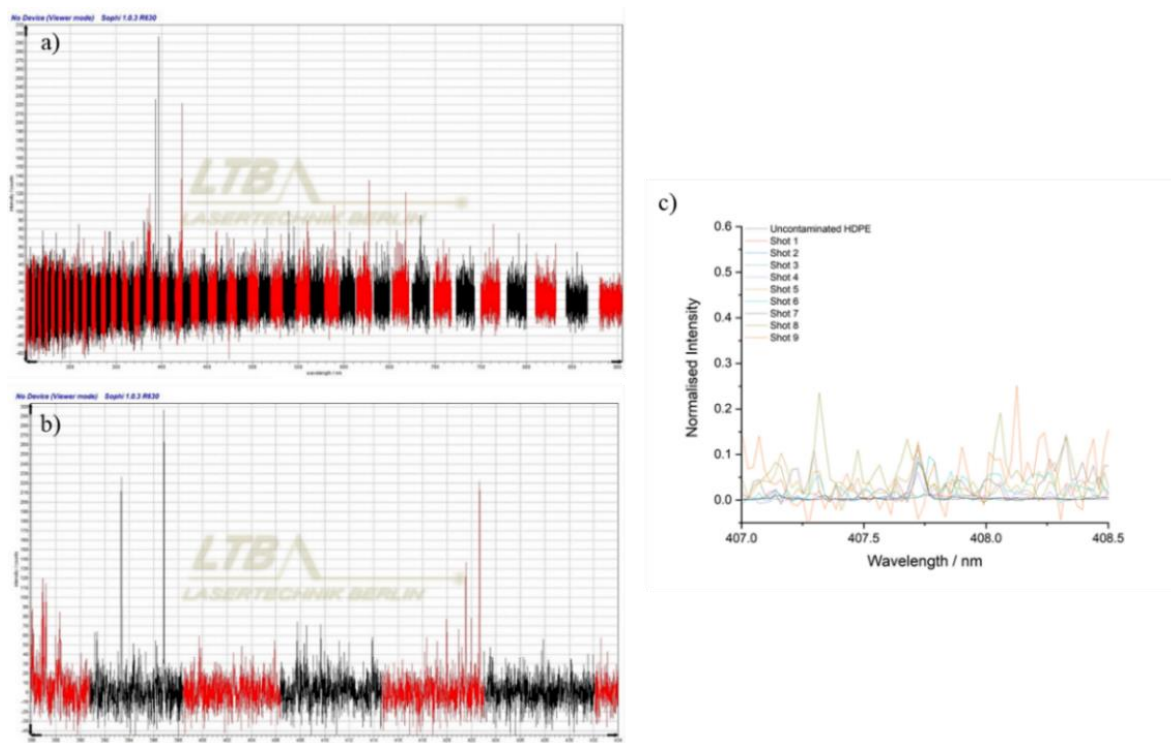


Figure S4.9. LIBS emission spectra for an HDPE coupon after 9 consecutive shots over a) whole wavelength range, b) 386-434 nm range on Sophi and c) normalised depth-profile LIBS spectra highlighting the impact of surface melting on Sr emission detection.

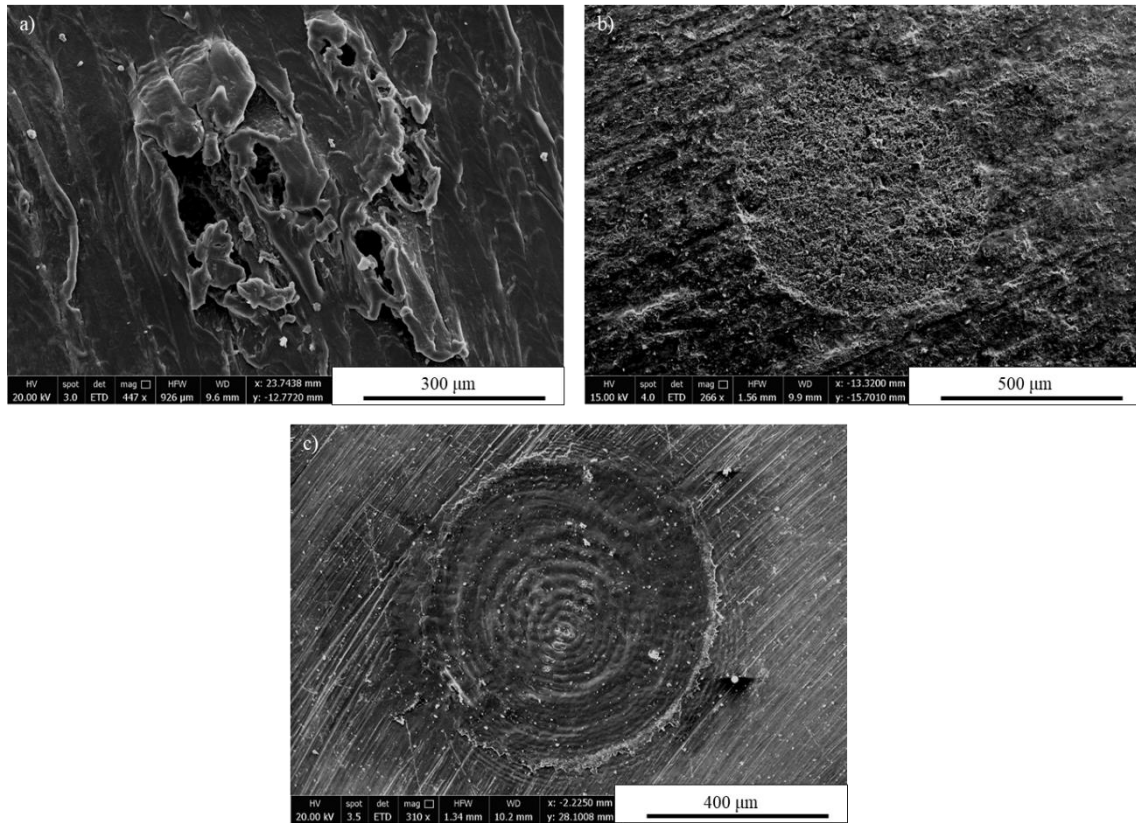


Figure S4.10. SEM images of the difference in ablation craters formed on a) HDPE, b) concrete and c) steel surfaces, highlighting the destructive nature on softer materials such as plastic.

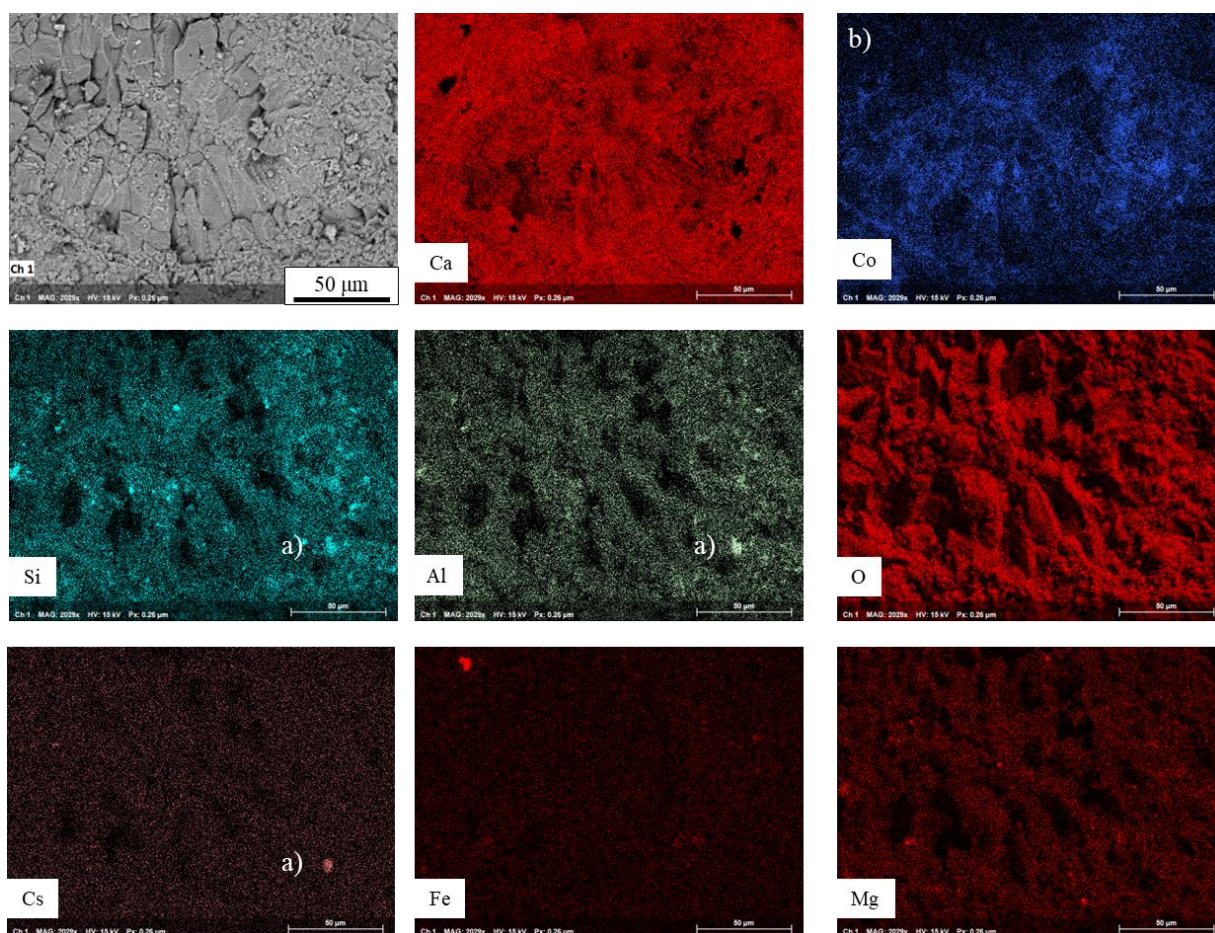


Figure S4.31. SEM-EDX maps of the inside of a LIBS crater formed after 12 shots on the concrete surface. a) Cs can be seen on the outside of the crater in a particulate containing Si and Al. b) Co can be identified in the centre of the crater, indicating Co has penetrated further into the bulk concrete or redeposition has occurred.

5. Characterisation and Decontamination of HDPE Pontoons used in Spent Fuel Pond Decommissioning

Anna E. Denman ^a, Gareth T.W. Law ^b, Thomas Carey ^c, Nicholas T. Smith ^c and Scott L. Heath ^{a,d}

^a. Research Centre for Radwaste Disposal and Williamson Research Centre for Molecular Environmental Science, Department of Earth and Environmental Sciences, The University of Manchester, Manchester, M13 9PL, UK

^b. Radiochemistry Unit, Department of Chemistry, The University of Helsinki, Helsinki, 00014 FI, Finland

^c. National Nuclear Laboratory, Chadwick House, Warrington Road, Birchwood Park, Warrington, WA3 6AE, UK

^d. Dalton Nuclear Institute, The University of Manchester, Manchester, M13 9PL, UK

Status: Manuscript in preparation for submission to the *Journal of Nuclear Materials*.

Highlights:

- High-density polyethylene (HDPE) pontoons contaminated with Cs-137, Sr-90, Am-241 and Eu-152 during decommissioning of the Hunterston A spent nuclear fuel (SNF) pond.
- Autoradiography used to identify areas of increased activity across the pontoon surfaces.
- Polymer hydrogels effectively decontaminated Sr-90, Cs-137 and Am-241 from authentic radionuclide contaminated pontoons.

Keywords: Decommissioning, Spent Nuclear Fuel, HDPE, Contamination

5.1. Abstract

Characterisation of unique, radioactive samples obtained from the Hunterston A spent nuclear fuel (SNF) pond has helped give insight into the radionuclide contamination of plastic materials in nuclear power plants. Decommissioning operations resulted in the contamination of plastic pontoons floated on the pond surface to reach the inner contaminated walls. Six samples from the pontoons showed heterogeneous radioactivity present on the surface, correlating to their relative positions on the pontoons. Sr-90, Cs-137 and Am-241 were identified as the primary contaminating radionuclides, generating activities ranging from 0.2-5.9 Bq/g. Raman and LIBS analysis identified the presence of precipitates such as Fe and Mn oxides on the sample surface which aided contamination. In terms of decommissioning of a nuclear site, efforts to help develop suitable decontamination methods, without producing vast quantities of secondary waste would greatly benefit the nuclear industry. Here, cross-linked polyvinylpyrrolidone based hydrogels have been shown to remove 32% Sr-90 and 55% Cs-137 activity from high-density polyethylene (HDPE) surfaces after 1 hour of contact. In addition, hydrogels have been shown to simultaneously take up a multitude of radionuclides and doubling the cross-linker concentration in the hydrogels resulted in an increase in activity uptake. The hydrogels have been used to remove up to 70% of activity from the pontoon surfaces after 1 hour of application and are capable of taking up >200 Bq Cs-137 and 88 Bq Sr-90 in this time frame. Repeat applications of the same hydrogel can also be used to further remove contamination.

5.2. Introduction

Hunterston A was a twin Magnox reactor that ceased operation in 1990 and was home to one of the largest SNF ponds for interim storage of the reactors waste, holding 6500 m³ of water. SNF from the Magnox reactors was carefully contained and stored underwater in storage ponds to allow the activity and heat generated to decay before it was sent for reprocessing.¹ Decommissioning of the pond began in 2013 and was the first to use floating plastic pontoons to grant workers access to the contaminated pond walls, allowing them to simultaneously decontaminate and drain down the facility.² Spray from the jet-washing used to decontaminate the concrete walls of the pond resulted in the contamination of the plastic pontoons, as well as through contact with the pond water. These plastic pontoons were washed with water prior to disposal; however, radionuclide contamination remains present at activity ranges of 0.2-5.9 Bq/g gamma radiation on the plastic surfaces.

Radionuclide contamination studies have been extensively conducted on steel,^{3–5} concrete^{6,7}, soils^{8,9} and sediments.^{10,11} However, the analysis of radionuclide contaminated plastics is a less researched subject. Initial studies involving Sr and Cs on microplastics indicated that adsorption on plastic materials is several orders lower than those on sediments, due to the lack of surface binding sites.¹² Tazaki *et al.* is one of the few studies that covers radionuclide contaminated plastics, identifying adsorption of radionuclides on plastics through exposure to polluted water systems from the Fukushima Daiichi Nuclear Power Plant, with increased adsorption taking place in the presence of clay phases.¹³ A recent study by Zrelli *et al.* contributes to this topic, determining that natural and artificial radionuclides can be taken up and transported by polyethylene terephthalate (PET) plastic waste from coastal environments.¹⁴ Contamination and decontamination studies of americium(III) on nylon and polyethylene (PE) microplastics have also shown that higher pH environments can result in greater adsorption of Am and that desorption can be a time consuming process.¹⁵ Whilst these studies have provided insight into radionuclide uptake on microplastics and plastic waste, the contamination of plastic materials used in nuclear facilities has not been extensively researched. Understanding the mechanisms of radionuclide adsorption and desorption taking place on plastics in nuclear environments is vital to aid future decommissioning tasks.

Detection of heavy metal contamination on various plastic materials has been done via Fourier-transform infrared spectroscopy (FTIR) and inductively-coupled plasma optical and atomic emission spectroscopy (ICP-OES/AES).^{16–18} However, these techniques require samples to be removed from site and in some cases result in the total destruction of the sample. Laser-induced breakdown spectroscopy (LIBS) has been suggested as an *in-situ* characterisation tool for use in the nuclear industry as it only requires optical access to samples to simultaneously detect major and trace elements, with little or no sample preparation.^{19,20} In addition, handheld and standoff analysis allow LIBS to be used for continuous monitoring of contamination over time.^{21,22} LIBS has shown its promise for use in the nuclear industry and has been used to identify Sr and Cs on steel at concentrations relevant to the nuclear industry, as well as analyse mixed actinide samples and rare earth elements relevant to molten salt reactors.^{23–26} Recent studies have also used LIBS to identify the uptake of heavy metals on microplastic and plastic waste in aquatic environments.^{27–29}

The Hunterston A pond is a complex, alkaline environment contaminated with fission, corrosion and activation products. Metal deposits and biofilms can form on plastic surfaces in

aqueous environments, particularly in areas of increased damage.^{30,31} These deposits allow for greater uptake of heavy metals and radionuclides, particularly in alkaline conditions where increased electronegativity of the surface attracts metal cations.^{32,33} Submersion of the plastic pontoons in the pond water is likely to have resulted in the damage of the pontoon structures and build-up of chemical precipitates which could form sites for radionuclide adsorption.

In this study, plastic samples were obtained from pontoons used during the decommissioning of the Hunterston A SNF storage pond. Surface characterisation was conducted to identify the presence of SNF radionuclides and determine the extent of contamination to improve our understanding of radionuclide contaminated plastic materials. Novel use of LIBS to analyse the presence of radionuclide contamination on the pontoon surfaces was conducted to assess its ability as an *in-situ* analytical tool for use in the nuclear industry. In addition, decontamination experiments were conducted using hydrogels as their ability to take up radionuclides without the need for gel removal equipment or the production of vast quantities of secondary waste is promising for nuclear applications.^{34,35} The hydrogels can act as a final waste container for the radionuclides removed. As the hydrogels dry, they become solid pucks that trap the radionuclides in their previously open-network structure. It is possible to dispose of the hydrogels through acid dissolution or by burning the solid waste forms and mixing with cement grout, resulting in a >90% reduction in volume. This treatment could also include the removal of Sr and Cs to minimise the risk of these mobile species and to decrease the activity levels of the waste for disposal as low level waste (LLW.) Decontamination was initially carried out on simulant coupons to determine their applicability before use on the authentic HDPE discs to determine their ability to remove radioactivity from HDPE surfaces.

5.3. Materials and methods

5.3.1. Hunterston A pontoons

Samples were cut from the top, middle and bottom panels of the HDPE pontoons used during decommissioning operations at the Hunterston A SNF (Figure S5.1 and S5.2). The disc samples will be referred to throughout the paper as:

- Top: T1 and T2
- Middle: M1 and M2
- Bottom: B1 and B2

The discs have a diameter of 10 cm and are 1 cm thick; the top panel of the pontoon was textured to provide grip, and the sides and bottom were smooth. The pontoons were contaminated with fission products and actinides during decommissioning, resulting in additional formation of intermediate level waste (ILW). The bottom discs would have been fully submerged in the pond water and the middle pieces may have fallen under the water level, particularly when workers and heavy equipment were stationed on top. During decommissioning, ultra-high-pressure jet washing of the pond walls resulted in contaminated wastewater splashing onto the surface and over the sides of the pontoons, where it is likely to have remained and dried over time, contaminating the surfaces.

5.3.2. Gamma spectroscopy

Gamma spectroscopy was used to quantify the activity of the discs pre- and post-decontamination, as well as measure the uptake of contamination in the hydrogels. Analysis was performed using a Canberra 2020 coaxial HPGe detector with an Ortec DSPEC-50 multi-channel analyser. Accurate quantification of the pontoon samples was not possible due to the unique geometry and composition of the pontoon discs. Gamma spectroscopy did, however, allow relative measurements and hence comparison between the samples pre- and post-decontamination. Gamma spectroscopy of the hydrogels was performed against standards of known activity counted in the same geometry and timescale. Cs-137 was quantified using the diagnostic photon energy peaks of 661.6 keV. Am-241 and Eu-152 were identified using their diagnostic photon energy peak at 59.5 and 121.8 keV, respectively. Limits of detection (LOD) were calculated by the GammaVision software. Peaks with greater intensity than 3σ above the background count were considered significant.

5.3.3. Autoradiography

Autoradiography was used to visualise the removal of contamination from the sample surfaces, as well as radionuclide uptake in the hydrogels. The samples were exposed on BAS-IP MS 2040 E (GE Healthcare) storage phosphor screens for 24 hours and scanned using an Amersham™ Typhoon Laser Scanner (Cytiva Life Sciences) pixel size 50 μm . Images were optimised using the Amersham ImageQuant TL analysis software version 10.2 (Cytiva Life Sciences).

5.3.4. Laser-induced breakdown spectroscopy (LIBS)

LIBS analysis was conducted on an Innolas Spitlight 600 laser and Aryelle Echelle spectrometer, which uses a Q-switched 1064 nm Nd:YAG pulsed laser system (10 Hz

repetition rate, 7 ns pulse width) with a total wavelength range of 250-900 nm. The following camera settings were used: 150 MPC gain, 1500 ns gate delay and 100 μ s gate width. Analysis was conducted with a pulsed laser energy of 100 mJ/pulse. Depth-profiling was conducted via multi-pulse analysis, using a series of consecutive shots in the same location. Spectra were analysed using the Applied Photonics Ltd. Sophi Software version 6.0 (LTB Lasertechnik Berlin).

LIBS analysis of the active pontoon discs was conducted in a specialised, sealed sample chamber (Figure S5.3). The laser is fired through a quartz window to impact the sample, generating the plasma inside the holder without spreading contamination. The holder can be decontaminated after use.

5.3.5. Raman spectroscopy

Raman spectroscopy was performed using a Horiba XploRA™ Plus confocal Raman spectrometer with a dual excitation source (532 nm - green and 785 nm - NIR), various diffraction gratings (600, 1200, 1800 and 2400 g/mm) and a CCD (Si) detector. The instrument resolution is $\sim 1 \text{ cm}^{-1}$ (wavenumber).

5.3.6. Sorption experiments with HDPE coupons

In addition to the characterisation of the pontoon samples, active contamination experiments were conducted on HDPE coupons for comparison. HDPE plastic was obtained from Direct Plastics Ltd as a 2 cm diameter rod and cut into 1 cm discs to represent the pontoon samples. The coupons were ground to 2500 grit using silicon carbide grinding paper and polished down to 5 μ m using Buehler micropolish II alumina suspension on a Buehler EcoMet 30 Auto/Manual Grinder & Polisher. Samples were washed with deionised (DI) water (18 M Ω) and isopropyl alcohol (IPA) prior to contamination experiments.

HDPE coupons were contaminated with a known volume of Sr-90, Cs-137 or a mixed gamma standard solution (Table S5.1) to test the decontamination ability of the hydrogels (Section 5.3.7.) on HDPE surfaces. A top stock of each radionuclide solution was diluted to achieve a working solution of 200 Bq/mL in 0.1 M HCl. 20 Bq of Sr-90, Cs-137 or the mixed gamma standard was spotted onto each HDPE coupon surface and allowed to air dry for 1 week, resulting in an overall activity of 6.37 Bq/cm².

5.3.7. Hydrogel decontamination experiments

H06 hydrogels (20 x 20 mm (ø x h)) were synthesised as described in Moore *et al.*³⁴ Polyvinylpyrrolidone (PVP) was dissolved in deionised (DI) water (18 MΩ) and combined with hydroxyethyl methacrylate (HEMA), *N,N'*-methylenebisacrylamide (MBAM) and azobisisobutyronitrile (AIBN). The mixture was stirred to remove any bubbles before being transferred to well plates (20 x 20 mm (ø x h)) and heated at 60 °C. Once cured the hydrogels were stored in deionised (DI) water (18 MΩ) until use. In addition to the H06 hydrogels, modifications were made to double the MBAM cross-linker concentration, which will be referred to as H06-2. H06 hydrogels were loaded in 2% HNO₃ for 1 week to aid decontamination without affecting the hydrogel structure and functionality. Initial decontamination tests were conducted on HDPE coupons contaminated with Sr-90 and Cs-137 over periods of 1, 24, 168 and 672 hours. To test the hydrogel ability for decontamination of complex nuclear samples and determine whether preferential uptake of certain radionuclides was occurring, hydrogels were applied to HDPE coupons contaminated with a mixed gamma standard. In addition to the original H06 hydrogel, a modified hydrogel was synthesised containing double the concentration of the cross-linker *N,N'*-Methylenebisacrylamide (MBAM), named H06-2, to determine whether increased cross-linker concentration aided the removal of radioactivity. Each hydrogel was placed on the HDPE coupon surface for 24 hours to test the ability of the two hydrogels for the removal of multiple gamma radionuclides.

For the pontoon samples, individual hydrogels were placed on sections of the HDPE surface for 1, 24, 168 and 672 hours to test the hydrogel decontamination ability on authentic samples. To determine whether hydrogels could be reused to remove additional contamination, tests were conducted where the same hydrogel was replaced on the plastic surface over consecutive decontamination periods.

The decontamination factor (DF) for the hydrogels was:

$$DF = \frac{A_0}{A_f} \quad [1]$$

where A_0 is the radioactivity on the sample surface before decontamination and A_f is the activity on the sample surface after decontamination.³⁶

This was then converted to the percentage of activity removed (%R):

$$\%R = \left(1 - \frac{1}{DF}\right) \times 100\% \quad [2]$$

5.3.8. Liquid scintillation counting (LSC)

Hydrogels used during sample decontamination experiments were analysed with LSC to measure the uptake of β -emitting radionuclides. The hydrogels were leached in 20 mL DI water (18 M Ω) for 5 days. A 2 mL aliquot of the leachate was added to 10 mL proSafe HC+ liquid scintillation cocktail and analysed using a LabLogic HIDEX 300 SL counter, with MikroWin 300SL control software. The Hidex 300 SL system uses three PMT detectors to automatically quench correct by triple to double coincidence ratio (TDCR). In addition, Sr-90 standards in solution had been prepared for calibration of solution analysis. Hydrogel standards had been prepared to calibrate the uptake of Sr-90 by the hydrogels. Solutions were all colourless, so no colour quenching was required.

5.4. Results and discussion

5.4.1. Characterisation of the pontoons

Gamma analysis highlighted Cs-137 and Am-241 were responsible for the majority of the gamma activity generated, with small quantities of Eu-152 also detected (Table 5.1). As the gamma spectrometer was not calibrated for the geometry of the discs, these values serve as estimates to allow for comparison between the samples and for later decontamination measurements (Section 5.4.3.). Gamma spectroscopy of the pontoon samples identified varying levels of activity between 0.2-5.9 Bq/g, with no apparent trend depending on location of the discs.

Table 5.1. Gamma survey of the Hunterston A SNF pond pontoon samples.

Sample ID	Activity (Bq/g)			
	Cs-137	Am-241	Eu-152	Total
T1	7.0E-01	1.1E-01	1.6E-02	8.3E-01
T2	1.3E+00	4.4E-03	7.3E-04	1.3E+00
M1	1.5E-01	2.7E-03	8.5E-04	1.5E-01
M2	3.5E+00	3.1E-02	9.4E-03	3.5E+00
B1	4.8E-01	2.1E-03	7.9E-04	4.9E-01
B2	5.6E+00	2.2E-01	1.5E-02	5.9E+00

Autoradiography analysis showed the highest areas of contamination on the top discs correlated to areas with increased damage as well as in the grooves surrounding the raised notches where wastewater gathered along the edges and dried in place, depositing a layer of contamination (Figure 5.1). Analysis of the middle discs showed contamination was related to the water level of the pond along the pontoons during operation. The middle disc, M1, shows small amounts of activity present on most of the surface, ending in an abrupt line attributed to the nominal water level of the pond along the pontoon. Smaller hotspots of increased activity above this are attributed to the variation in water level as workers stepped onto the pontoons. For the second middle disc, M2, the activity is primarily isolated to a strip feature along the bottom. This could be an indicator of where the pond water level reached on that disc, with possible build-up of chemical precipitates and organic matter which could result in increased radionuclide sorption.

Autoradiography of the bottom discs show activity covering the majority of the surfaces due to being submerged in the contaminated water throughout decommissioning operations. Comparison of the two bottom discs indicates that increased damage and formation of precipitates on the sample surface have contributed to a greater uptake of radionuclides.

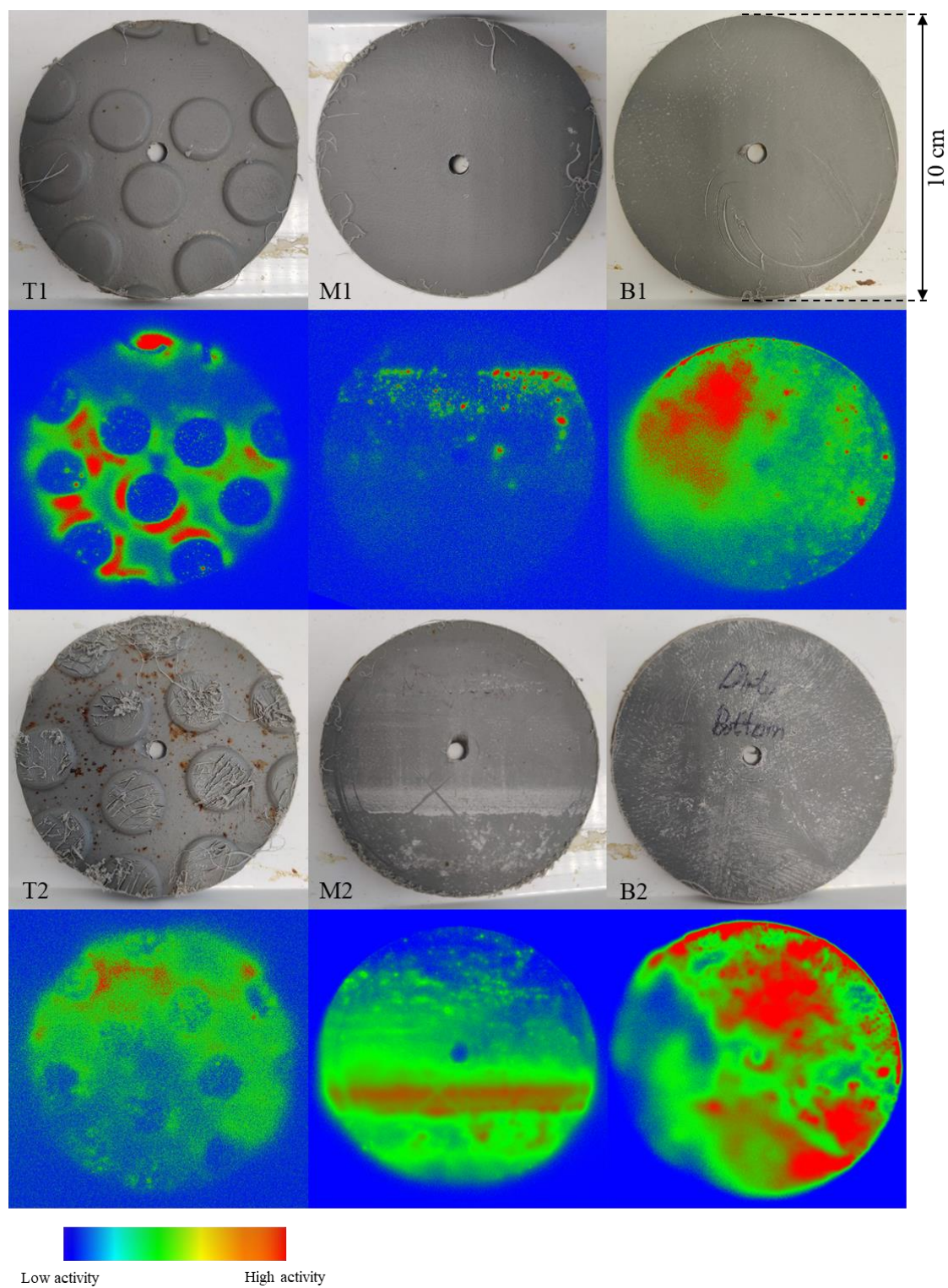


Figure 5.1. Disc images (above) and corresponding false-colour, contrast-adjusted autoradiography images (below) of each pontoon sample. Discs were removed from the top (left), middle (middle) and bottom (right) panels of the pontoons.

Raman analysis of the solid particulates and precipitates on the pontoon surfaces identified predominately iron (oxy)hydroxide and carbonate species (Figures 5.2 and S5.4), indicative of rust deposits from equipment used on the pontoon surface. Bands at 240, 290, 390 and 1100 cm^{-1} indicate the presence of goethite ($\alpha\text{-FeOOH}$).³⁷ It is possible that some lepidocrocite ($\gamma\text{-FeOOH}$) may be present as both species form during the oxidation of iron rich minerals.³⁸ However, goethite is more commonly found in alkaline conditions and the presence of bands at 240 and 290 cm^{-1} correlate well with goethite spectra found in literature.^{39–41} The second spectra identified bands at 290, 720 and 1090 cm^{-1} indicating the presence of siderite (FeCO_3); however, there are similarities between the Raman spectra for siderite and calcite (CaCO_3) minerals and the 514 cm^{-1} peak characteristic of siderite could not be easily resolved in the spectra.^{42,43} It is likely that both siderite and calcite are present on the pontoon samples due to the corrosion products present in the pond and leaching of Ca from the concrete walls. Analysis of the pontoon surface with LIBS also identified emissions from both Fe and Ca supporting this. Radionuclides such as uranium and strontium have been shown to adsorb onto carbonate and oxide materials, which could result in increased uptake of radionuclides on the pontoon surfaces.⁴⁴

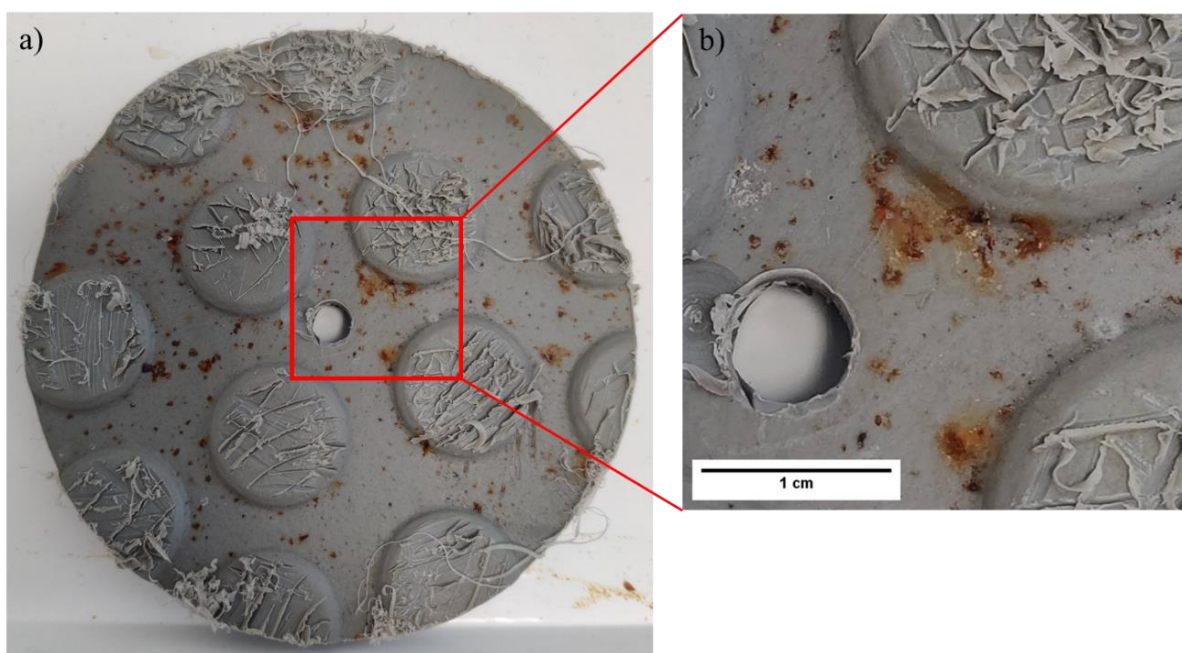


Figure 5.2. a) Images of top disc, T2, covered in scratches and rust particulates. b) close up of the particulates present on the disc surface.

Further analysis of the bottom disc, B1, with LIBS identified emissions from Fe (295.39 nm and 404.58 nm),⁴⁵ Mn (294.93 nm, 403.08 nm and 403.31 nm),^{46,47} Al (309.27 nm)⁴⁸, Ti

(307.52 nm, 307.86 nm and 308.80 nm)⁴⁹ and O (399.80 nm) on the pontoon surface (Figure 5.3). This is an indicator that metal oxide precipitates have formed on the pontoons over time resulting in adsorption sites for radionuclide contamination, particularly on the bottom and side panels that were submerged in the pond water.^{30–32} Corrosion of the steel and aluminium waste containers in the SNF pond could result in the formation of Fe and Al oxides, which act as adsorption sites for radionuclides, particularly in alkaline conditions.^{50,51} In addition, titanium dioxide (TiO₂) phases were present in the protective paint layers applied to the SNF pond walls and have been known to accumulate radionuclides in nuclear reactors.^{52,53}

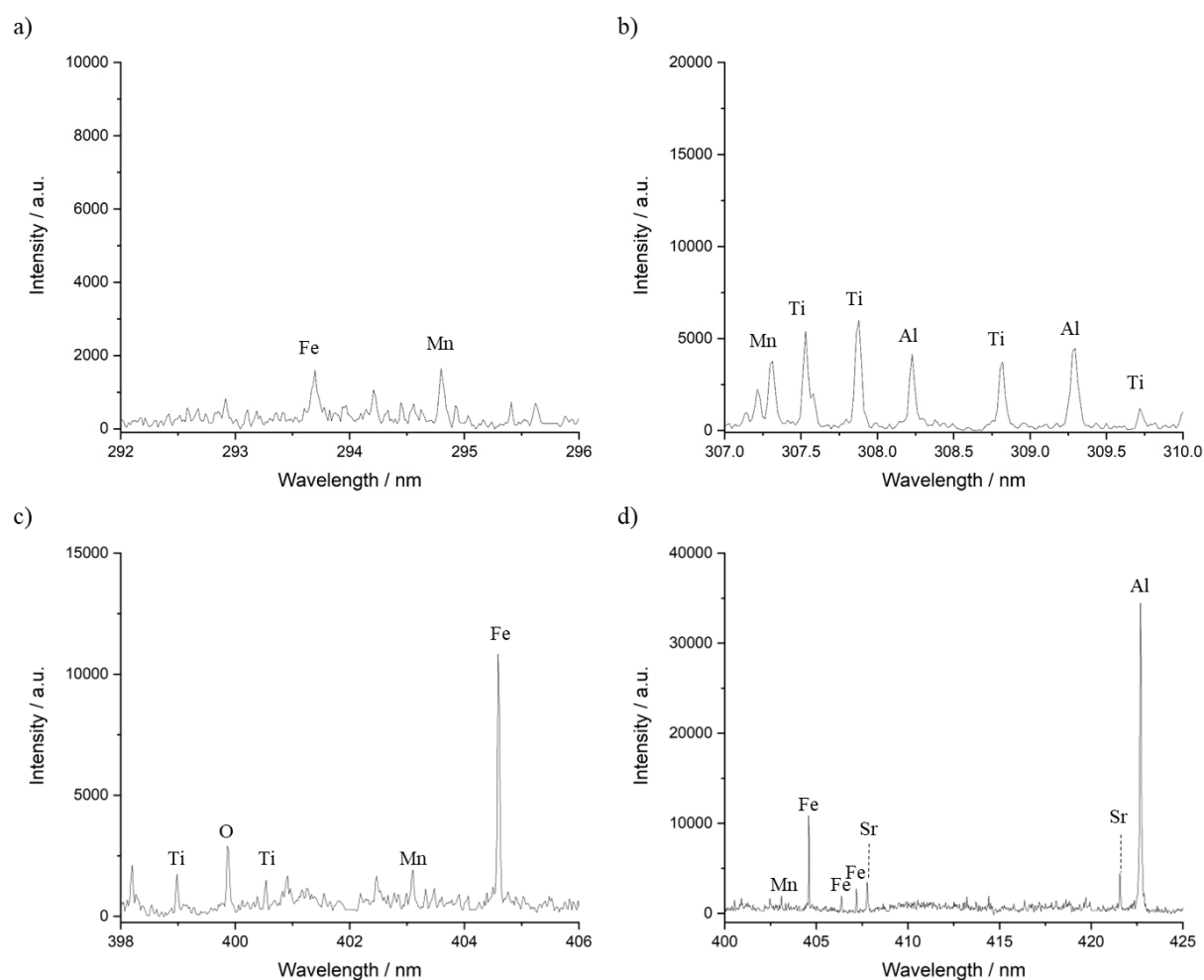


Figure 5.3. LIBS emission spectra of the precipitate formed on the bottom disc, B1, at wavelength ranges of a) 292-296 nm, b) 307-310 nm, c) 398-406 nm and d) 400-425 nm highlighting the presence of metal oxides and Sr contamination on the pontoon surfaces.

Analysis with LIBS also identified the presence of Sr on the B1 pontoon surface (Figure 5.3d). The characteristic 407.78 and 421.42 nm Sr II emission peaks were resolved from the

contaminated HDPE matrix. As stable Sr will also be present in the pond environment, it is not possible to separate contamination caused by stable or radio-Sr using LIBS alone. Additional radioanalytical techniques are required to accurately quantify the concentration of Sr-90 on the pontoon surfaces.⁵⁴ No clear Cs or Am emission peaks could be identified in the spectra, indicating these contaminant concentrations fell below the LOD for LIBS analysis of plastic surfaces in alkaline SNF pond environments.

To determine whether contamination was isolated to the sample surface or had penetrated further into the material, the bottom disc, B1, was sectioned to allow for analysis of the cross-section. Autoradiography analysis indicated that the majority of the contamination was isolated to the sample surface, but some activity appears to have penetrated further into the disc (Figure 5.4a). Autoradiography analysis of the back of the top disc, T1, also indicated penetration of activity may have occurred through the sample (Figure S5.5). This could be caused by the presence of cracks or the diffusion of activity into the pores on the surface as has been observed in PE, PVC and polystyrene films.^{18,55,56} The presence of activity on the surfaces and in areas of the bulk emphasises that surface washing of the pontoons was not sufficient in removing radionuclide contamination and stronger decontamination methods are required.

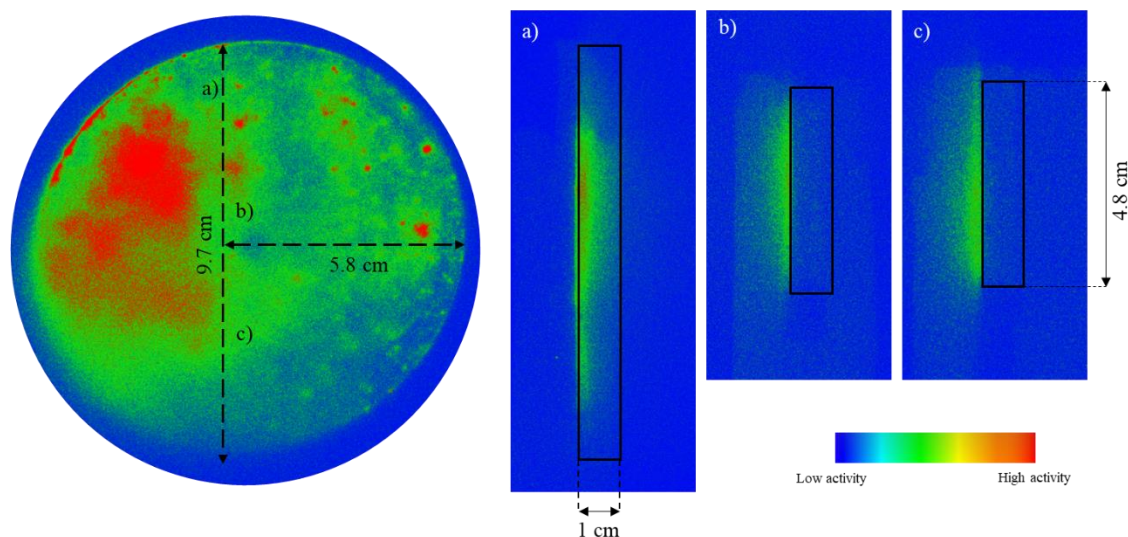


Figure 5.4. False-colour, contrast-adjusted autoradiography images of the bottom disc, B1, cross-section. The largest section a) shows potential ingress of activity into the disc, whereas the smaller sections b and c) show activity is isolated to the pontoon surface.

5.4.2. Surface decontamination of HDPE coupons

HDPE coupons were contaminated to replicate the real pontoon surfaces to assess the applicability of hydrogels for decontamination of plastic materials. Autoradiography analysis of the contaminated coupons showed activity was removed from the coupon surface and taken up into the hydrogel for Sr-90, Cs-137 and mixed gamma radionuclide contamination (Figures S5.6 and S5.7). Comparison with autoradiography data shows greater uptake in the hydrogels with increased contact time although the difference between the activity taken up by each hydrogel for the Cs-137 uptake experiments was less pronounced. This apparent increased activity from Sr-90 is likely due to the β -decay of Sr-90 to Y-90 which has a short half-life of 64 hours when it emits a high-energy β -particle, contributing to the intensity of the autoradiography image.^{34,57}

Calibration curves were calculated for Sr-90 and Cs-137 uptake in H06 and H06-2 hydrogels (Figure S5.8). As the activity of Sr-90 on the coupon surfaces could not be accurately assessed after decontamination, DF values for the removal of Sr-90 and Cs-137 from the coupon surfaces were calculated by quantifying the activity taken up by the hydrogel to allow for comparison (Tables S5.2 and S5.3). The following modifications were made to equation [1]:

$$DF = \frac{\text{Activity on the surface before (Bq)}}{\text{Activity on the surface before (Bq)} - \text{activity in the hydrogel (Bq)}} \quad [3]$$

Hydrogel applications to HDPE coupons demonstrated 32% removal of Sr-90 (DF of 1.47), and 56% removal of Cs-137 (DF of 2.2) after 1 hour of application. ICP-MS studies indicated that 1300 mg/L \pm 90 Sr and 11000 mg/L \pm 3800 Cs could be taken up by the hydrogels. This increased uptake of Cs-137 over Sr-90 in the H06 hydrogels is in agreement with other studies and can be attributed to the greater molecular diffusivity and ionic mobility of cesium(I) compared to strontium(II).^{34,58,59} Increasing the contact time resulted in a general increase in DF value with the greatest removal of activity seen after 672 hours of contact. However, DF values remained relatively constant across the four application times, indicating >50% of Cs-137 and Sr-90 removal is possible in 1 hour and 24 hours, respectively. Similar studies using cryogels for the removal of Sr and Cs from solution determined uptake was greatest in the first 24-48 hours, before reaching an equilibrium point.⁵⁸

After initial assessment with individually contaminated coupons, tests were conducted on HDPE coupons contaminated with a mixed gamma solution to determine the hydrogel ability to take up multiple radionuclides simultaneously. Autoradiography assessment of the coupon

surfaces after hydrogel decontamination indicated that the ability to remove contamination was not as successful for the original H06 hydrogel compared to the modified H06-2. However, the DF values for the H06 and H06-2 hydrogels were considerably high at 42 and 64, respectively. Gamma analysis of the hydrogels showed no preferential absorption of radionuclides had taken place. Quantification showed doubling concentrations in the cross-linker, MBAM, resulted in an increase of Cs-137 uptake from the HDPE surfaces by a factor of 3. This is in contrast with molecular dynamic studies on ion diffusion in hydrogels which determined that increasing the cross-linker concentration in poly(ethylene glycol) diacrylate (PEGDA) hydrogels resulted in decreased diffusion of chloride and sodium ions.⁶⁰ Whilst doubling the cross-linker concentration resulted in increased uptake of radionuclides in this study, it is possible that increasing the cross-linker concentration significantly could result in a reduced uptake of larger radionuclides due to a decrease in the network pore size.^{61,62} Further studies to investigate the optimum concentration of MBAM for maximum radionuclide uptake would need to be conducted to confirm this.

5.4.3. Decontamination of the Hunterston A pontoons

Quantifying the removal of activity from the Hunterston A pontoon samples was not possible in the same manner as for the HDPE coupons. Due to the heterogeneous uptake of activity on the sample surfaces and the hydrogels only decontaminating a small area of the discs (3.14 cm²), DF values and the percentage of activity removed (%R) were determined using autoradiography to evaluate the decontamination of the area in contact with the hydrogel (Table 5.2). The following modifications were made to equation [1]:

$$DF = \frac{\text{Average intensity of decontamination area before (\%)}}{\text{Average intensity of decontamination area after (\%)}} \quad [4]$$

Table 5.2. Hydrogel decontamination data for the pontoon discs after individual (B2) and consecutive (B1 and M2) applications. DF = decontamination factor, %R = % activity removed.

Sample	Contact time / hours	Radioactivity / Bq		DF	%R
		Cs-137	Sr-90		
Bottom disc (B2)	1	216	88	1.7	41
	24	78	24	6.1	84
	168	171	87	5.7	83
	672	130	59	6.8	85
Bottom disc (B1)	1	1.8	-	3.2	67

	24	1.7	-	4.1	76
	168	2.4	-	5	80
	672	2.8	14	5.9	83
Middle disc (M2)	1	-	-	4.5	78
	24	-	-	10.7	91
	168	-	-	15.4	93
	672	-	-	16.6	94

Hydrogels were placed on the surface of the bottom disc, B2, targeting areas of low and high activity. Radiological analysis of the hydrogels showed Sr-90, Cs-137 and Am-241 had all been taken up from the pontoon surface with each hydrogel application. Autoradiography analysis showed the greatest uptake of radioactivity occurred in the hydrogel applied to the pontoon surface for 1 hour (Figure 5.5). This is predominantly due to the hydrogel being placed in an area of higher activity on the disc surface in comparison to the other hydrogel applications. Whilst the percentage of activity removed for the 1 hour hydrogel was only 40% compared to >80% for the hydrogels applied for longer, radiological analysis showed 200 Bq Cs-137 and 88 Bq Sr-90 had been taken up in 1 hour. Based on these results we predict that 1 hour of contact is sufficient to significantly decontaminate regions of low and high activity using the hydrogels.

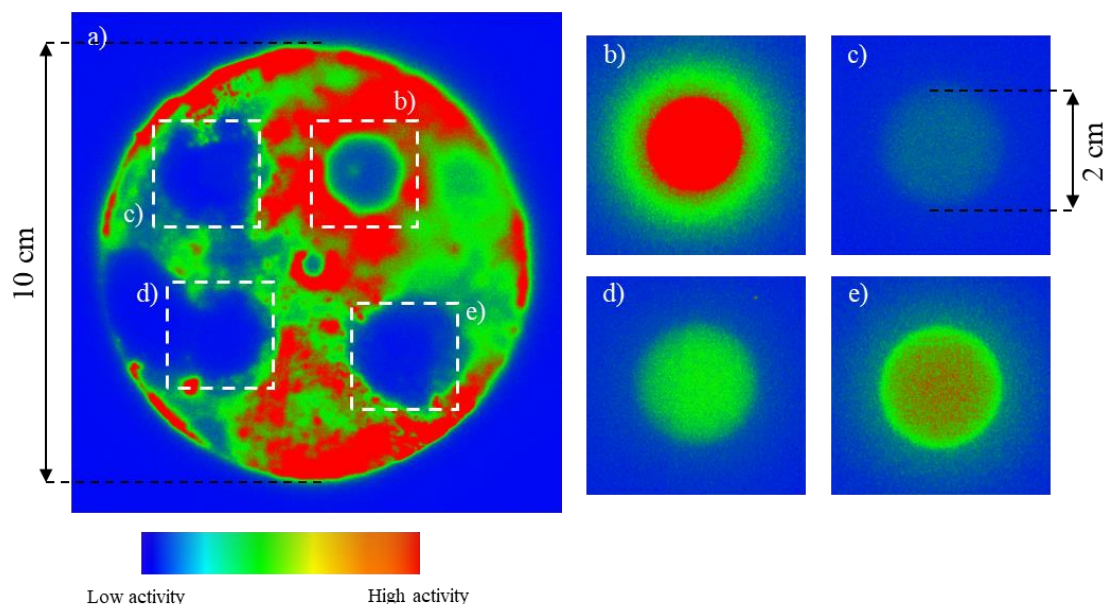


Figure 5.5. False-colour, contrast-adjusted autoradiography images showing the decontamination of bottom disc, B2, after b) 1, c) 24, d) 168 and e) 672 hours.

Decontamination of a hotspot region on the bottom, B1, surface with consecutive applications of the same hydrogel showed increased removal of activity was taking place with each additional hydrogel application (Figure 5.6). The initial 1 hour contact time resulted in 68% removal of activity from the sample surface, with each consecutive application exhibiting an increase in DF value. Despite a small decrease in measured Cs-137 activity after 24 hours, additional applications of the hydrogel generally resulted in increased uptake of Cs-137 and DF values. A total of 83% of activity removed from the sample surface after 4 consecutive applications with no activity redeposited or spread in the decontamination area.

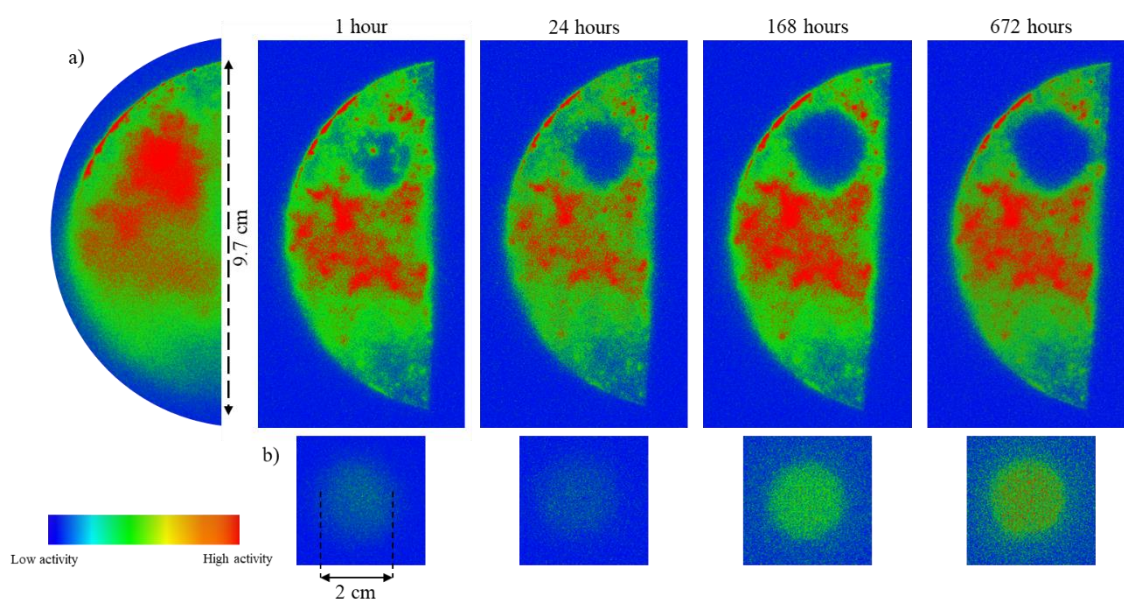


Figure 5.6. False-colour, contrast-adjusted autoradiography images of a section of the a) bottom disc, B1, before and after sequential decontamination experiments and b) the corresponding hydrogel autoradiography images.

As the same hydrogel was used for sequential decontamination, LSC analysis for Sr-90 quantification was not possible between each time point. Analysis of the hydrogel after the final decontamination process showed a total of 14 Bq Sr-90 and 2.8 Bq Cs-137 had been taken up. No Am-241 removal was detected in this area.

Final decontamination studies looked at the possibility of tailoring the hydrogel geometry to the sample being decontaminated. A 12 cm diameter H06 hydrogel was prepared using the same method as before and applied to the surface of the middle, M2, disc to test the repeated use of a hydrogel for removal of contamination on a larger scale. As with the smaller hydrogels, consecutive applications resulted in increased radioactive removal from the pontoon surface

(Figure 5.7). The autoradiography images showed the initial application of the gel resulted in a distinct mirrored pattern of the activity placement on the disc whilst ensuing applications showed the radioactivity in the hydrogels was diffused throughout the cross-linked polymer network. This diffusion allows the hydrogel to take up additional contamination without the need to apply fresh hydrogels.

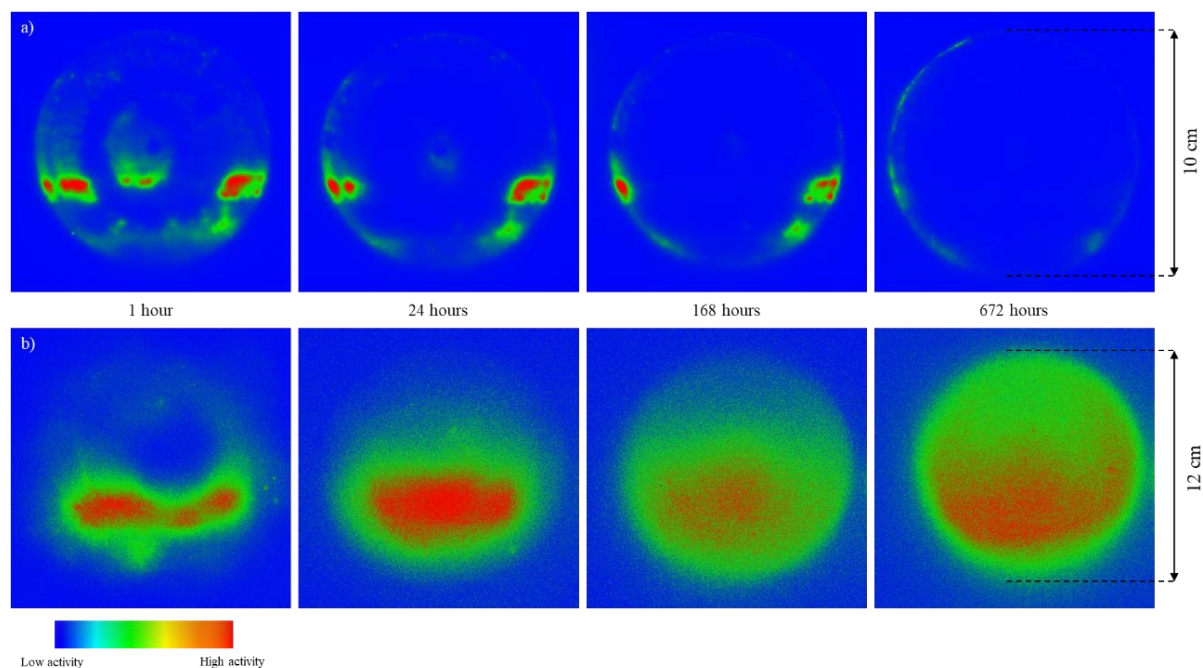


Figure 5.7. False-colour, contrast-adjusted autoradiography images of the middle disc, M2, (a) after consecutive decontamination with a 12 cm hydrogel (b)

Increased removal of activity was occurring with each reapplication of the hydrogel. Gamma analysis of the M2 surface and hydrogel indicated that Am-241 and majority of the Cs-137 had been removed from the disc surface by the hydrogel after all four applications. A total of 139 Bq Cs-137 and 149 Bq of Sr-90 had taken up by the hydrogel, indicating the hydrogels are capable of simultaneously removing high activities of multiple radionuclides from the pontoon surfaces.

5.5. Conclusions

Authentic samples from pontoons used during the decommissioning of the Hunterston A SNF pond were characterised using a combination of surface and radiological characterisation techniques. Cs-137, Sr-90 and Am-241 were determined as the predominant radionuclide

contaminants, with small emissions of Eu-152 identified on several of the discs. Autoradiography analysis of the pontoon surfaces showed radioactivity was associated with areas of increased damage and the presence of metal oxide precipitates deposited by the contaminated pond water. The results of this work have shown the promise of LIBS for analysis of radionuclide contaminated plastic materials and possible deployment as an *in-situ* characterisation technique.

Hydrogels have been shown to remove >55% Cs-137 and 32% Sr-90 activity from the HDPE coupons after 1 hour of contact, with increased application time resulting in greater radionuclide uptake. Hydrogels were capable of simultaneously taking up multiple radionuclides and initial studies indicated that doubling the cross-linker concentration resulted in greater uptake of Cs-137. Decontamination of the pontoon samples using the hydrogels was successful after 1 hour of contact, resulting in 40-60% removal for higher activity areas, with uptake of >200 Bq Cs-137 and 88 Bq Sr-90 determined. This work highlights the use of hydrogels for the localised removal and entrapment of harmful radionuclides on plastic surfaces, helping to minimise the production of secondary waste produced during decommissioning operations.

Declaration of competing interest

None.

Acknowledgements

Martin C. McGarvey at Magnox Ltd and the National Nuclear Laboratory (NNL) are acknowledged for the provision of the Hunterston A samples.

The EPSRC NNUF RADER Facility (EP/T011300/1) is acknowledged for access and analysis performed.

The authors would like to acknowledge Professor Peter Quayle and Dr Aula Alwatter for the synthesis of the hydrogels used throughout this work and Dr Lewis Hughes for conducting the Raman analysis.

The authors would also like to acknowledge Professor Francis Livens for helpful discussions and guidance throughout this work.

Funding sources

The National Nuclear Laboratory (NNL) (Core Science Decontamination and Decommissioning R&D Theme) and the EPSRC Next Generation Nuclear Centre for Doctoral Training (NGN CDT) are acknowledged for their funding.

5.6. References

- 1 Nuclear Decommissioning Authority, Magnox Fuel Strategy Contingency Options, 2014, 1–13.
- 2 C. Bertoncini, in *Proceedings of the International Conference on Environmental Remediation and Radioactive Waste Management, ICEM*, 2013, pp. 1–11.
- 3 A. Lang, D. Engelberg, N. T. Smith, D. Trivedi, O. Horsfall, A. Banford, P. A. Martin, P. Coffey, W. R. Bower, C. Walther, M. Weiß, H. Bosco, A. Jenkins and G. T. W. Law, Analysis of contaminated nuclear plant steel by laser-induced breakdown spectroscopy, *J. Hazard. Mater.*, 2018, **345**, 114–122.
- 4 C. J. Dodge, A. J. Francis, J. B. Gillow, G. P. Halada, C. Eng and C. R. Clayton, Association of uranium with iron oxides typically formed on corroding steel surfaces, *Environ. Sci. Technol.*, 2002, **36**, 3504–3511.
- 5 P. Kádár, K. Varga, Z. Németh, N. Vajda, T. Pintér and J. Schunk, Accumulation of uranium, transuranium and fission products on stainless steel surfaces. I. A comprehensive view of the experimental parameters influencing the extent and character of the contamination, *J. Radioanal. Nucl. Chem.*, 2010, **284**, 303–308.
- 6 N. D. M. Evans, Binding mechanisms of radionuclides to cement, *Cem. Concr. Res.*, 2008, **38**, 543–553.
- 7 M. Ochs, D. Mallants and L. Wang, in *Radionuclide and Metal Sorption on Cement and Concrete*, Springer, 2015, pp. 45–60.

- 8 A. E. Berns, A. Flath, K. Mehmood, D. Hofmann, D. Jacques, M. Sauter, H. Vereecken and I. Engelhardt, Numerical and experimental investigations of cesium and strontium sorption and transport in agricultural soils, *Vadose Zo. J.*, 2018, **17**, 1–14.
- 9 S. K. Sahoo, N. Kavasi, A. Sorimachi, H. Arae, S. Tokonami, J. W. Mietelski, E. Lokas and S. Yoshida, Strontium-90 activity concentration in soil samples from the exclusion zone of the Fukushima daiichi nuclear power plant, *Sci. Rep.*, 2016, **6**, 1–10.
- 10 V. G. Petrov, I. E. Vlasova, A. A. Rodionova, V. O. Yapaskurt, V. V. Korolev, V. A. Petrov, V. V. Poluektov, J. Hammer and S. N. Kalmykov, Preferential sorption of radionuclides on different mineral phases typical for host rocks at the site of the future Russian high level waste repository, *Appl. Geochemistry*, 2019, **100**, 90–95.
- 11 A. D. Ebner, J. A. Ritter and J. D. Navratil, Adsorption of cesium, strontium, and cobalt ions on magnetite and a magnetite-silica composite, *Ind. Eng. Chem. Res.*, 2001, **40**, 1615–1623.
- 12 M. P. Johansen, E. Prentice, T. Cresswell and N. Howell, Initial data on adsorption of Cs and Sr to the surfaces of microplastics with biofilm, *J. Environ. Radioact.*, 2018, **190–191**, 130–133.
- 13 K. Tazaki, M. Nakano, T. Takehara, Y. Ishigaki and H. Nakagawa, Experimental analysis of plastic materials containing radionuclides for decontamination viability, *Earth Sci.*, 2015, **69**, 99–108.
- 14 R. El Zrelli, L. Yacoubi, S. Castet, M. Grégoire, C. Josse, J. Olive, P. Courjault-Radé, P. van Beek, T. Zambardi, M. Souhaut, J. E. Sonke and L. J. Rabaoui, PET plastics as a Trojan horse for radionuclides, *J. Hazard. Mater.*, 2023, **441**, 129886 1–11.
- 15 I. Ioannidis, A. Xenofontos and I. Anastopoulos, Americium sorption by microplastics in aqueous solutions, *Coatings*, 2022, **12**, 1452 1–9.
- 16 M. Whitt, K. Vorst, W. Brown, S. Baker and L. Gorman, Survey of heavy metal contamination in recycled polyethylene terephthalate used for food packaging, *J. Plast. Film Sheeting*, 2012, **0**, 1–11.
- 17 O. Alam, L. Yang and X. Yanchun, Determination of the selected heavy metal and

- metalloid contents in various types of plastic bags, *J. Environ. Heal. Sci. Eng.*, 2019, **17**, 161–170.
- 18 X. Guo, G. Hu, X. Fan and H. Jia, Sorption properties of cadmium on microplastics: the common practice experiment and a two-dimensional correlation spectroscopic study, *Ecotoxicol. Environ. Saf.*, 2020, **190**, 110118.
 - 19 L. Jolivet, M. Leprince, S. Moncayo, L. Sorbier, C. P. Lienemann and V. Motto-Ros, Review of the recent advances and applications of LIBS-based imaging, *Spectrochim. Acta Part B*, 2019, **151**, 41–53.
 - 20 D. Cremers and L. Radziemski, *Handbook of Laser-Induced Breakdown Spectroscopy*, Wiley, 2nd edn., 2013.
 - 21 B. T. Manard, M. F. Schappert, E. M. Wylie and G. E. McMath, Investigation of handheld laser induced breakdown spectroscopy (HH-LIBS) for the analysis of beryllium on swipe surfaces, *Anal. Methods*, 2019, **11**, 752–759.
 - 22 I. Gaona, J. Serrano, J. Moros and J. J. Laserna, Evaluation of laser-induced breakdown spectroscopy analysis potential for addressing radiological threats from a distance, *Spectrochim. Acta Part B*, 2014, **96**, 12–20.
 - 23 A. R. Lang, D. L. Engelberg, C. Walther, M. Weiss, H. Bosco, A. Jenkins, F. R. Livens and G. T. W. Law, Cesium and strontium contamination of nuclear plant stainless steel: implications for decommissioning and waste minimization, *ACS Omega*, 2019, **4**, 14420–14429.
 - 24 Y. Xie, J. Wang, Y. Hu, J. Zhang, Y. Gao, H. Li and S. Wang, Laser-induced breakdown spectroscopy for contamination analysis of Sr and Cs on 316L stainless steels in alkaline environment for spent nuclear fuel storage, *Appl. Surf. Sci.*, 2021, **566**, 150709.
 - 25 E. J. Judge, J. M. Berg, L. A. Le, L. N. Lopez and J. E. Barefield, *LIBS spectral data for a mixed actinide fuel pellet containing uranium, plutonium, neptunium and americium*, 2012.
 - 26 G. Hull, H. Lambert, K. Haroon, P. Coffey, T. Kerry, E. D. McNaghten, C. A. Sharrad and P. Martin, Quantitative prediction of rare earth concentrations in salt matrices using

- laser-induced breakdown spectroscopy for application to molten salt reactors and pyroprocessing, *J. Anal. At. Spectrom.*, 2021, **36**, 92–102.
- 27 D. Chen, T. Wang, Y. Ma, G. Wang, Q. Kong, P. Zhang and R. Li, Rapid characterization of heavy metals in single microplastics by laser-induced breakdown spectroscopy, *Sci. Total Environ.*, 2020, **743**, 140850.
 - 28 X. Chen, S. Ali, L. Yuan, F. Guo, G. Huang, W. Shi and X. Chen, Characterization and source analysis of heavy metals contamination in microplastics by laser-induced breakdown spectroscopy, *Chemosphere*, 2022, **287**, 132172.
 - 29 S. Tognana, C. D'Angelo, S. Montecinos, M. Pereyra and W. Salgueiro, Laser-induced breakdown spectroscopy (LIBS) as a technique to detect copper in plastic and microplastic waste, *Chemosphere*, 2022, **303**, 1–6.
 - 30 L. A. Holmes, A. Turner and R. C. Thompson, Adsorption of trace metals to plastic resin pellets in the marine environment, *Environ. Pollut.*, 2012, **160**, 42–48.
 - 31 T. Artham, M. Sudhakar, R. Venkatesan, C. Madhavan Nair, K. V. G. K. Murty and M. Doble, Biofouling and stability of synthetic polymers in sea water, *Int. Biodeterior. Biodegrad.*, 2009, **63**, 884–890.
 - 32 Y. Cao, M. Zhao, X. Ma, Y. Song, S. Zuo, H. Li and W. Deng, A critical review on the interactions of microplastics with heavy metals: mechanism and their combined effect on organisms and humans, *Sci. Total Environ.*, 2021, **788**, 147620.
 - 33 J. Zou, X. Liu, D. Zhang and X. Yuan, Chemosphere adsorption of three bivalent metals by four chemical distinct microplastics, *Chemosphere*, 2020, **248**, 126064.
 - 34 J. J. Moore, T. P. Raine, A. Jenkins, F. R. Livens, K. A. Law, K. Morris, G. T. W. Law and S. G. Yeates, Decontamination of cesium and strontium from stainless steel surfaces using hydrogels, *React. Funct. Polym.*, 2019, **142**, 7–14.
 - 35 A. Gossard, F. Frances, P. Venditti, C. Lepeyre and A. Grandjean, in *GLOBAL 2017 International Nuclear Fuel Cycle Conference*, 2017.
 - 36 US Environmental Protection Agency, *Decontamination of cesium, cobalt, strontium, and americium from porous surfaces.*, 2013.

- 37 D. L. A. De Faria, S. Venâncio Silva and M. T. De Oliveira, Raman microspectroscopy of some iron oxides and oxyhydroxides, *J. Raman Spectrosc.*, 1997, **28**, 873–878.
- 38 J. F. W. Bowles, in *Encyclopedia of Geology*, eds. D. Alderton and S. A. Elias, Elsevier, 2nd edn., 2021, pp. 442–451.
- 39 U. Schwertmann and E. Murad, Effect of pH on the formation of goethite and hematite from ferrihydrite., *Clays Clay Miner.*, 1983, **31**, 277–284.
- 40 J. Dünnwald and A. Otto, An investigation of phase transitions in rust layers using raman spectroscopy, *Corros. Sci.*, 1989, **29**, 1167–1176.
- 41 L. Bellot-Gurlet, D. Neff, S. Réguer, J. Monnier, M. Saheb and P. Dillmann, Raman studies of corrosion layers formed on archaeological irons in various media, *J. Nano Res.*, 2009, **8**, 147–156.
- 42 Romanian Database of Raman Spectroscopy, Siderite raman spectrum, <http://www.rdrs.ro/minerals/carbonates/anhydrous-carbonates/siderite-raman-spectrum/#:~:text=The Raman spectrum of siderite,1 to v3 mode>.
- 43 N. Buzgar and A. Ionut Apopei, The raman study of carbonates, *Geologie*, 2009, **55**, 97–112.
- 44 F. Grandia, C. Sena, D. Arcos, J. Molinero, L. Duro and J. Bruno, *Quantitative assessment of radionuclide retention in the near-surface system at Forsmark*, 2007, vol. R-07-64.
- 45 N. Idris, K. Lahna, Fadhli and M. Ramli, Study on emission spectral lines of iron, Fe, in laser-induced breakdown spectroscopy (LIBS) on soil samples, *J. Phys. Conf. Ser.*, 2017, **846**, 012020.
- 46 F. Bredice, F. O. Borges, H. Sobral, M. Villagran-Muniz, H. O. Di Rocco, G. Cristoforetti, S. Legnaioli, V. Palleschi, L. Pardini, A. Salvetti and E. Tognoni, Evaluation of self-absorption of manganese emission lines in laser-induced breakdown spectroscopy measurements, *Spectrochim. Acta - Part B At. Spectrosc.*, 2006, **61**, 1294–1303.
- 47 G. S. Senesi, M. Dell’Aglio, R. Gaudiuso, A. De Giacomo, C. Zacccone, O. De Pascale,

- T. M. Miano and M. Capitelli, Heavy metal concentrations in soils as determined by laser-induced breakdown spectroscopy (LIBS), with special emphasis on chromium, *Environ. Res.*, 2009, **109**, 413–420.
- 48 T. A. Labutin, V. N. Lednev, A. A. Ilyin and A. M. Popov, Femtosecond laser-induced breakdown spectroscopy, *J. Anal. At. Spectrom.*, 2016, **31**, 90–118.
- 49 D. W. Hahn, J. E. Carranza, G. R. Arsenault, H. A. Johnsen and K. R. Hencken, Aerosol generation system for development and calibration of laser-induced breakdown spectroscopy instrumentation, *Rev. Sci. Instrum.*, 2001, **72**, 3706–3713.
- 50 S. Musić and M. Ristić, Adsorption of trace elements or radionuclides on hydrous iron oxides, *J. Radioanal. Nucl. Chem. Artic.*, 1988, **120**, 289–304.
- 51 J. L. Means, D. A. Crerar, M. P. Borcsik and J. O. Duguid, Adsorption of Co and selected actinides by Mn and Fe oxides in soils and sediments, *Geochim. Cosmochim. Acta*, 1978, **42**, 1763–1773.
- 52 W. R. Bower, K. Morris, J. F. W. Mosselmans, O. R. Thompson, A. W. Banford, K. Law and R. A. D. Patrick, Characterising legacy spent nuclear fuel pond materials using microfocus X-ray absorption spectroscopy, *J. Hazard. Mater.*, 2016, **317**, 97–107.
- 53 N. A. Glukhoedov, V. N. Epimakhov, S. N. Orlov, A. A. Tsapko, A. A. Zmitrodan, G. A. Zmitrodan and M. Y. Skripkin, Sorption of ^{137}Cs and ^{60}Co on titanium oxide films in light water reactor primary circuit environment, *Materials (Basel)*, 2022, **15**, 1–10.
- 54 E. B. Farfán, S. P. Gaschak, A. M. Maksymenko, E. H. Donnelly, M. D. Bondarkov, G. T. Jannik and J. C. Marra, Assessment of ^{90}Sr and ^{137}Cs penetration into reinforced concrete (extent of “deepening”) under natural atmospheric conditions, *Health Phys.*, 2011, **101**, 311–320.
- 55 O. D. Agboola and N. U. Benson, Physisorption and chemisorption mechanisms influencing micro (nano) plastics-organic chemical contaminants interactions: a review, *Front. Environ. Sci.*, 2021, **9**, 1–27.
- 56 M. A. Pascall, M. E. Zabik, M. J. Zabik and R. J. Hernandez, Uptake of polychlorinated biphenyls (PCBs) from an aqueous medium by polyethylene, polyvinyl chloride, and

- polystyrene films, *J. Agric. Food Chem.*, 2005, **53**, 164–169.
- 57 M. I. Ojovan and W. E. Lee, in *An Introduction to Nuclear Waste Immobilisation*, Elsevier, 3rd edn., 2019, pp. 71–79.
 - 58 A. Baimenov, F. Montagnaro, V. J. Inglezakis and M. Balsamo, Experimental and modeling studies of Sr^{2+} and Cs^{+} sorption on cryogels and comparison to commercial adsorbents, *Ind. Eng. Chem. Res.*, 2022, **61**, 8204–8219.
 - 59 M. J. Kadhim and M. I. Gamaj, Estimation of the diffusion coefficient and hydrodynamic radius (Stokes radius) for inorganic ions in solution depending on molar conductivity as electro-analytical technique - a review, *J. Chem. Rev.*, 2020, **2**, 182–188.
 - 60 Y. Wu, S. Joseph and N. R. Aluru, Effect of cross-linking on the diffusion of water, ions, and small molecules in hydrogels, *J. Phys. Chem. B*, 2009, **113**, 3512–3520.
 - 61 F. Burla, T. Sentjabrskaja, G. Pletikapic, J. Van Beugen and G. H. Koenderink, Particle diffusion in extracellular hydrogels, *Soft Matter*, 2020, **16**, 1366–1376.
 - 62 F. Schneider, A. Balaceanu, A. Feoktystov, V. Pipich, Y. Wu, J. Allgaier, W. Pyckhout-Hintzen, A. Pich and G. J. Schneider, Monitoring the internal structure of poly(N-vinylcaprolactam) microgels with variable cross-link concentration, *Langmuir*, 2014, **30**, 15317–15326.
 - 63 M. Ltd, Hunterston A pond pontoon,
<https://www.flickr.com/photos/magnoxsites/8557186854/in/photostream/>.
 - 64 Isotrak, *Calibration Standards and Instruments*, Exckert & Ziegler, 2009.

5.7. Supporting information



Figure S5.1. Hunterston A SNF pond with floating pontoon devices used for decommissioning operations (Magnox Ltd.).⁶³

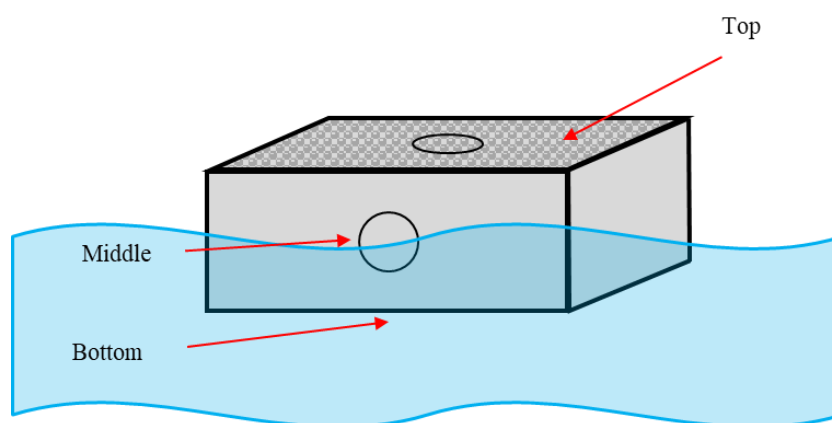


Figure S5.2. Schematic of the plastic pontoons, highlighting the sampling location of the discs.

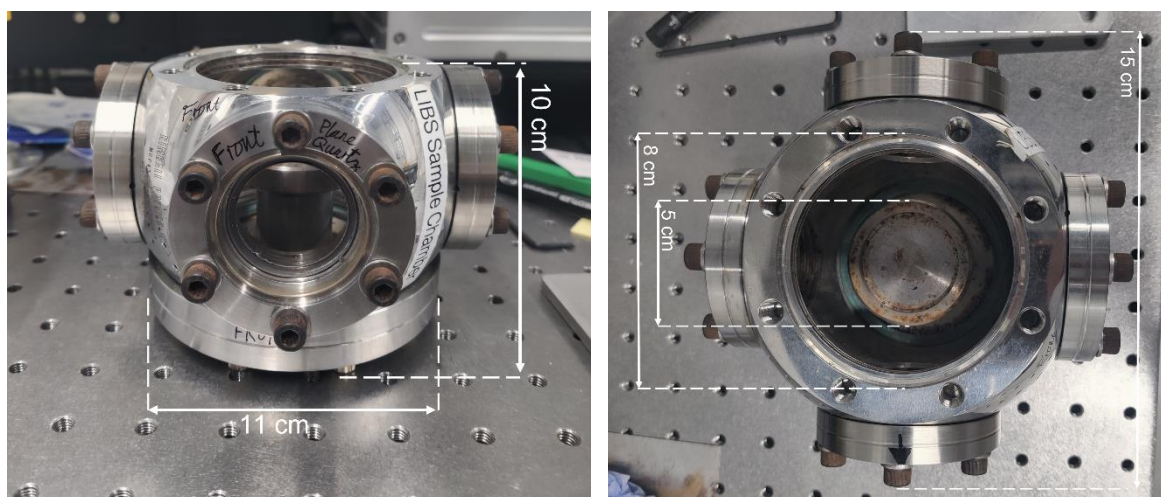


Figure S5.3. Active sample chamber for LIBS analysis of the Hunterston A pontoon samples.

Table S5.1. Radionuclide inventory of mixed gamma standard (adapted from IsoTrak Catalogue, 2009).⁶⁴

Radionuclide											
Am-241	Cd-109	Co-57	Ce-139	Cr-51	Sn-113	Sr-85	Cs-137	Co-60	Y-88	Zn-65	Mn-54

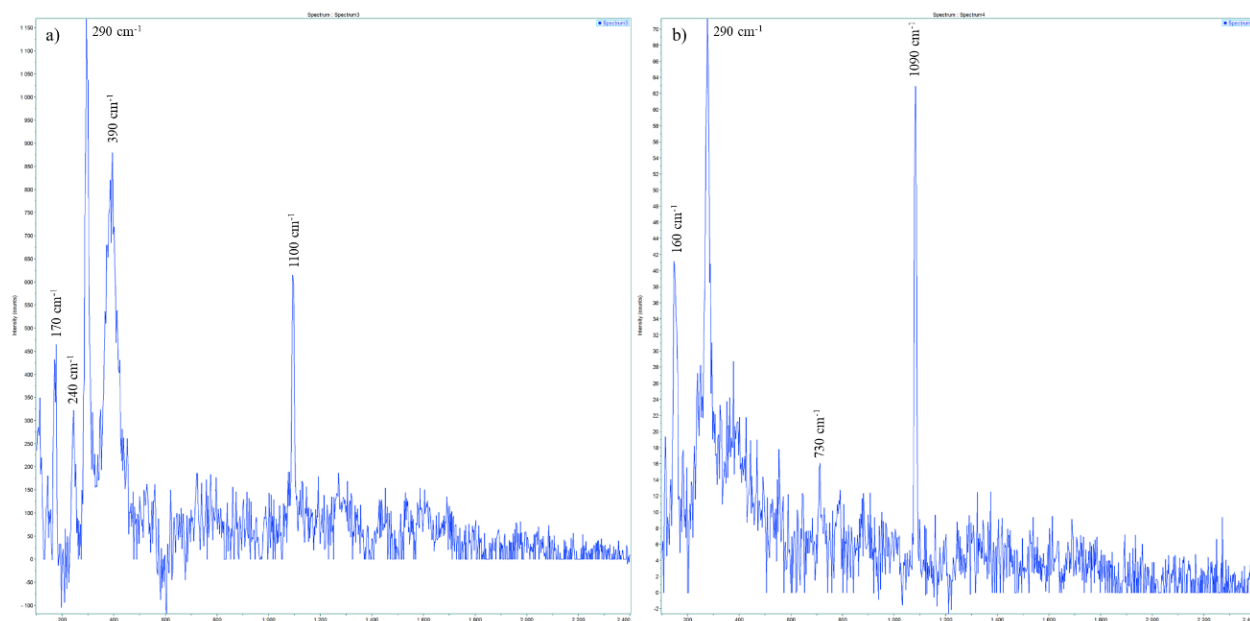


Figure S5.4. Raman spectra of the precipitate found on the top discs, T1 and T2, identifying the presence of a) goethite (α -FeOOH) and b) siderite (FeCO_3). Analysis was conducted using a Horiba XploRA with a dual excitation source (532 nm and 785 nm).

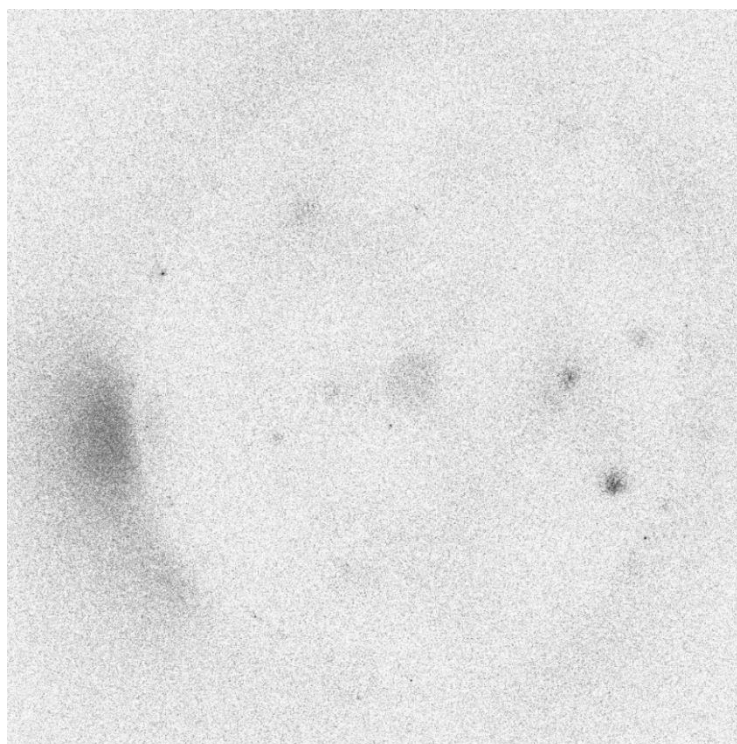


Figure S5.5. Autoradiography of the back of the top disc, T1, indicating contamination may have penetrated through the plastic.

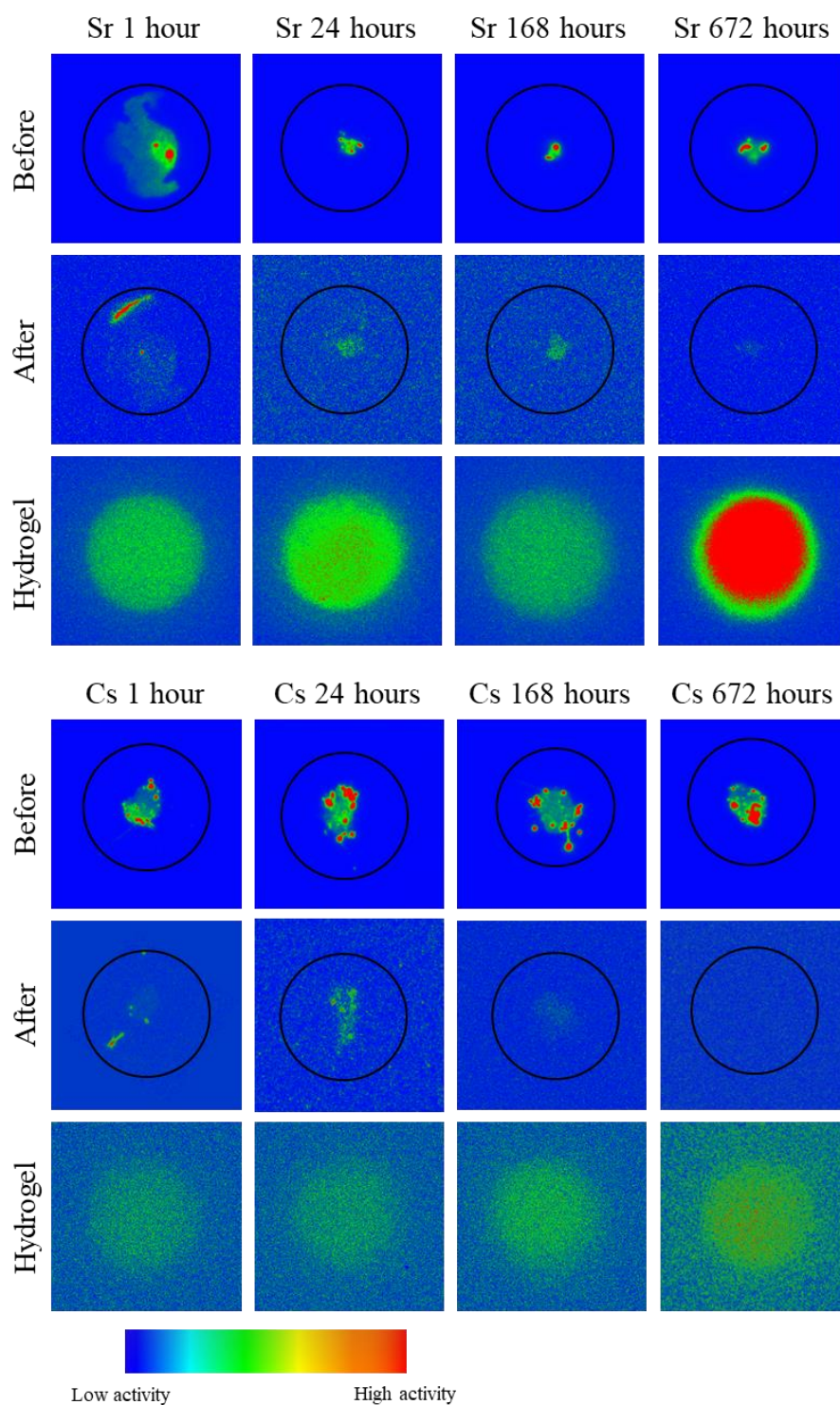


Figure S5.6. False-colour, contrast-adjusted autoradiography images of 20 Bq Sr-90 (top) and 20 Bq Cs-137 (bottom) on HDPE coupons (black circles) before and after hydrogel application. Autoradiography images of radioactive uptake in the hydrogels are below.

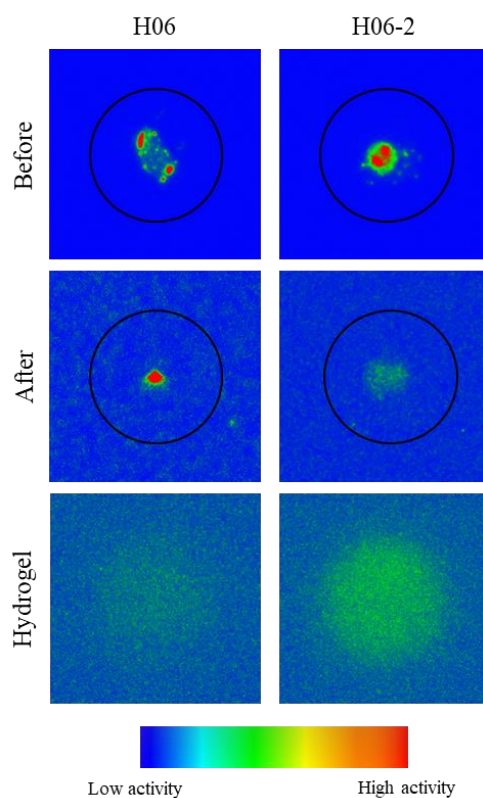


Figure S5.7. False-colour, contrast-adjusted autoradiography images of 20 Bq of mixed gamma standard on HDPE coupons before and after hydrogel application for 24 hours. Autoradiography images of radioactive uptake in the hydrogels are below.

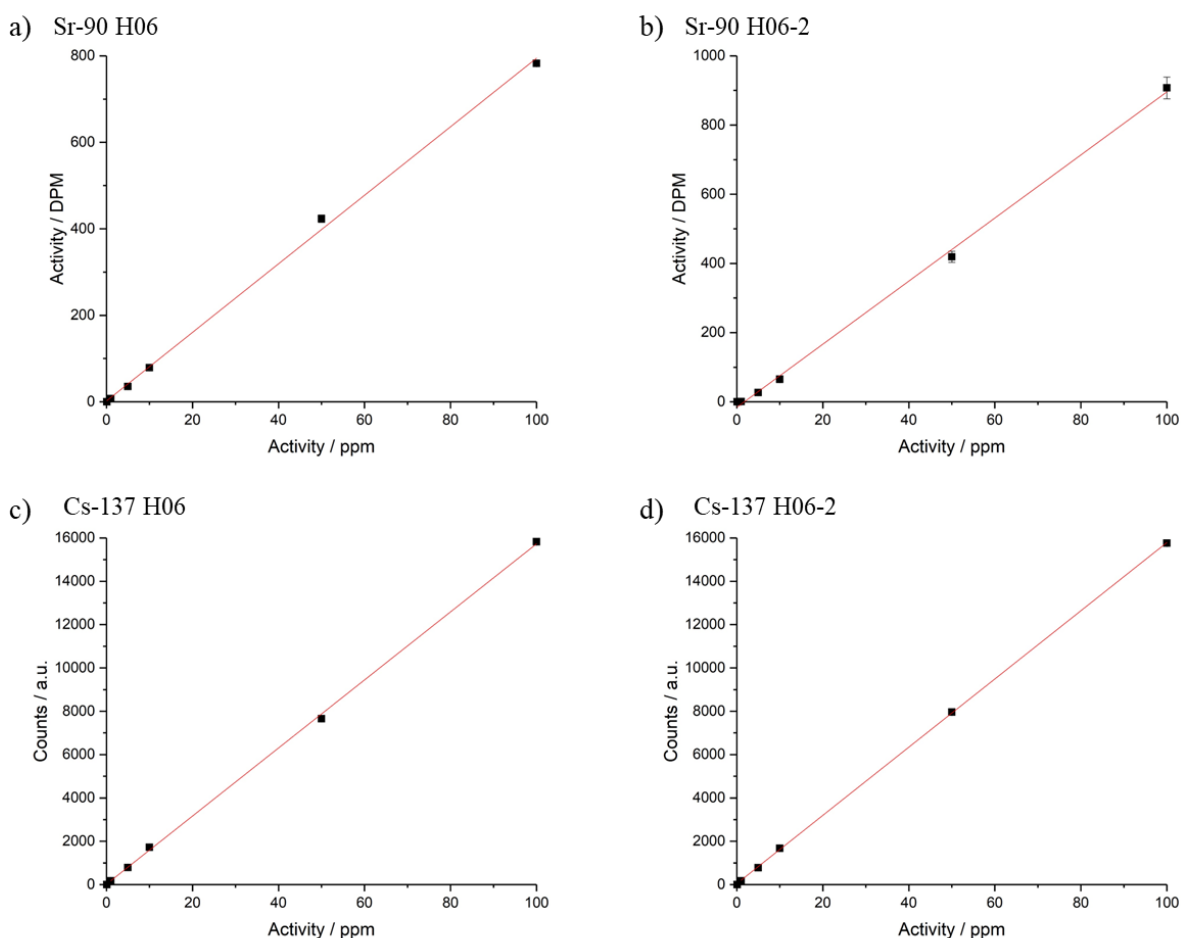


Figure S5.8. Calibration curves for a) H06 ($R^2 = 0.9991$) and b) H06-2 ($R^2 = 0.9981$) Sr-90 hydrogel standards measured with LSC, and c) H06 ($R^2 = 0.9996$) and d) H06-2 ($R^2 = 0.9999$) Cs-137 hydrogel standards measured with gamma spectroscopy. Error bars are estimated standard deviation from triplicate repeats.

Table S5.2. Hydrogel decontamination data for HDPE coupons contaminated with 20 Bq Sr-90 and 20 Bq Cs-137. DF = decontamination factor, %R = % activity removed.

Time / hours	Sr-90		Cs-137	
	DF	%R	DF	%R
1	1.5	32	2.2	56
24	2.2	56	2.0	50
168	1.6	38	2.5	59
672	2.5	60	2.7	63

Table S5.3. *Hydrogel decontamination data for HDPE coupons contaminated with 20 Bq mixed gamma standard. DF = decontamination factor, %R = % activity removed.*

Hydrogel	DF	%R	Cs-137 uptake / Bq
H06	42	97.6	0.3
H06-2	64	98.4	0.9

6. Radionuclide Associations in a Concrete Core Extracted from the Decommissioned Hunterston A Spent Nuclear Fuel Pond

Anna E. Denman ^a, Gareth T.W. Law ^b, Thomas Carey ^c, Nicholas T. Smith ^c, Gianni F. Vettese ^b, Joyce W.L. Ang ^b, Heikki Suhonen ^b, and Scott L. Heath ^{a,d}

^a. Research Centre for Radwaste Disposal and Williamson Research Centre for Molecular Environmental Science, Department of Earth and Environmental Sciences, The University of Manchester, Manchester, M13 9PL, UK

^b. Radiochemistry Unit, Department of Chemistry, The University of Helsinki, Helsinki, 00014 FI, Finland

^c. National Nuclear Laboratory, Chadwick House, Warrington Road, Birchwood Park, Warrington, WA3 6AE, UK

^d. Dalton Nuclear Institute, The University of Manchester, Manchester, M13 9PL, UK

Status: Manuscript in preparation for submission to *Journal of Hazardous Materials*

Highlights:

- Concrete core from the decommissioned Hunterston A spent nuclear fuel storage pond contaminated with Sr-90, Cs-137, Am-241 and Pu-238-241.
- Autoradiography identified areas of increased radioactivity on the painted surface and ingress of radionuclides into bulk concrete.
- Strong acids required for the extraction of radionuclides from concrete.
- Hydrogels used to decontaminate fission products and actinides from the painted surface.

Keywords: Contamination, Decommissioning, Legacy Materials, Spent Fuel Pond, Concrete

6.1. Abstract

Characterisation of a unique concrete core obtained from beneath the water level of the decommissioned Hunterston A spent nuclear fuel (SNF) storage pond has been conducted to aid understanding of long-term radionuclide contamination in nuclear infrastructure. Radionuclide contamination is primarily isolated to the protective coatings adhering to the concrete walls, with the majority of activity arising from fission products, Sr-90 and Cs-137, and actinides, Am-241 and Pu-238-241 as identified by gamma spectroscopy and liquid scintillation counting. Analysis of the core in cross-section showed that radionuclides had penetrated through the protective layers and into the bulk concrete below, with Cs-137 detected down to 10 mm into the bulk. Results from X-ray diffraction (XRD), scanning electron microscopy energy dispersive X-ray spectroscopy (SEM-EDX) and autoradiography suggest that Sr-90 contamination was isolated to the cement phases, through interactions with calcium silicate hydrate (CSH) phases, while Cs-137 was associated with aggregate phases, namely quartz and gabbro minerals. Decontamination experiments using cross-linked polymer hydrogels showed decontamination of the painted surface was possible after 1 hour of contact, with increasing levels of contamination removed with longer contact times. Hydrogels were able to remove both fission products and actinides.

6.2. Introduction

Decommissioning of nuclear reactors and surrounding structures result in the build-up of large volumes of nuclear waste causing challenges to governments worldwide.¹ The Nuclear Decommissioning Authority (NDA) estimates a lifetime total of over 4.5 million m³ of nuclear waste will be generated in the UK.² This waste requires characterisation and sorting into low, intermediate or high level waste (LLW, ILW, HLW) before specific containment and disposal routes can be followed. Decommissioning of nuclear sites is an immense time-consuming and costly operation, requiring extensive knowledge and characterisation of the facility in order to decontaminate the area as swiftly and safely as possible with minimal generation of additional waste.³ In addition, contaminated materials give rise to high doses of radiation and heat, increasing risk to workers and the surrounding environment.⁴ Spent nuclear fuel (SNF) from Magnox reactors was traditionally stored underwater in large cooling ponds until it reached safer activity and heat levels, after which it was reprocessed for future use, with the exception of Wylfa Magnox station which stored their waste in dry storage cells before off-site disposal

could take place.⁵ Whilst the water provides shielding from the radiation and dissipates the heat generated, storage in these ponds for extended periods of time has resulted in the corrosion and degradation of the waste containers.⁶ Delays in reprocessing resulted in a back-log of SNF which remained in wet storage over the recommended 6 month storage period resulting in the degradation of containment structures.^{7,8} Corrosion, fission and activation products (Sr-90, Cs-137, Pu-241 and Co-60) are present in the pond water, and a complex magnesium hydroxide based sludge has formed on the pond floor, creating a significant decommissioning challenge.⁹ These complex environments require as much information as possible on the activity and chemistry of the water and surrounding materials to be gathered to deduce the appropriate decontamination operations required.

Historically, decontamination of concrete structures has been split into two categories: chemical and physical decontamination. Physical decontamination methods (ultrasonic cleaning, grinding, scabbling) tend to produce rubble fragments which take up additional volume as well as the generation of secondary waste products. Scabbling uses a series of steel tips attached to a mechanical device to remove a thin layer of concrete from the surface and has been the most effective method for removing contaminated concrete, but dry procedures require careful control of airborne particles produced and any contaminated rubble fragments generated must be collected at the end. High-powered jet-washing is an alternative wet scabbling technique which minimises the volume of concrete requiring disposal, but this generates vast volumes of aqueous waste that will require additional treatment and disposal, and the spray can result in the contamination of the surroundings.¹⁰

Rapid identification of radionuclide species and the extent of their binding strength and penetration into nuclear materials could help reduce the overall volume of ILW produced during decommissioning and minimise cost of post operational clean out (POCO) procedures. Whilst some contamination can remain loosely bound to the pond wall surfaces, radionuclides can form stronger interactions with concrete, predominantly via surface-based mechanisms such as sorption or ion-exchange.¹¹ Radionuclides can penetrate further into the bulk material through diffusion or transport in cracks and pores, aided by water-ingress, particularly for surfaces that have not had any protective coatings applied. Fission products, such as Sr-90 and Cs-137, are of particular concern due to their intermediate half-lives, 29.1 and 30.2 years respectively, and mobility in aqueous environments.¹² Understanding the effect of long-term contamination of these radionuclides in aged concrete materials will help determine the extent

of their penetration and binding strength, aiding future decommissioning tasks and providing insight into any necessary changes required for new waste storage builds.

6.2.1. Hunterston A concrete core

Hunterston Nuclear Power Station, in Ayrshire, Scotland, was home to one of the largest storage ponds in the Magnox fleet where waste from both reactors was stored for many years. Decommissioning of the Hunterston A pond began in 2013, with initial steps involving the simultaneous ultra-high pressure jet-washing of the inner contaminated pond walls as the pond was drained.¹³ Novel methods using floating pontoons allowed workers to access the inner walls as the pond was drained, removing contamination from the top down, minimising the dose rates workers were subjected to and decreasing decommissioning costs.¹³

A concrete core (120 x 190 mm (ø x h)) was extracted from the inner, contaminated wall below water level where it had been exposed to the pond water for around 50 years (Figures S6.1 and S6.2). Several protective layers were applied to the concrete pond walls when it was built to minimise contamination and prevent the ingress of radionuclides into the bulk concrete. These consisted of an ordinary Portland cement layer finish, a waterproof rubber coating and an epoxy paint topcoat. The pond walls were made from ordinary Portland cement (OPC) with a mix of aggregates from the local environment, primarily quartz and olivine gabbro, to increase the concrete strength.

6.3. Experimental

6.3.1. Materials and sample preparation

To aid analysis and sample manipulation, the most active top 3 cm of the core was cut from the bulk concrete using a Norton Clipper CM501 saw with a diamond blade (500 mm) using deionised (DI) water (18 MΩ) as the lubricant. Mylar film coatings and waterproof tape was used to minimise any damage or alteration to the sample surface. This allowed for further sectioning for surface and bulk analysis (Figure S6.3). In addition, non-active coupons were prepared from the uncontaminated bottom part to allow for further characterisation and initial evaluation of hydrogel decontamination (Section 6.3.8.). Non-active coupons (30 x 30 x 10 mm (w x l x h)) were prepared using a Buehler IsoMet Low Speed precision cutter with a Diamond Wafering Blade (15 HC, 10.2 x 0.3 mm), using deionised (DI) water (18 MΩ) as the

lubricant. The coupons were ground to 2500 grit using silicon carbide grinding paper and polished down to 0.5 μm using Buehler micropolish II alumina suspension on a Buehler EcoMet 30 semi-automatic grinder and polisher. Finally, samples were washed with DI water (18 M Ω) and isopropyl alcohol (IPA) and left to air dry for 1 week prior to analysis contamination experiments.

6.3.2. Gamma spectroscopy

The concrete core was analysed using a GEM high-performance germanium (HPGe) detector. Data was analysed using the Genie™ 2000 gamma analysis software (Mirion Technologies, Canberra). Quantification of the concrete core was not possible due to the unique geometry and composition of the sample. Gamma spectroscopy of the depth-profile samples was performed to estimate activities and compare between samples in the same geometry.

Gamma analysis of the concrete coupons and hydrogels was conducted using a Canberra 2020 coaxial HPGe detector with an Ortec DSPEC-50 multi-channel analyser. Liquid samples from sequential extractions were performed against standards of known activity counted in the same geometry. Gamma spectroscopy of the hydrogels was performed against standards of known activity counted in the same geometry and timescale. Cs-137 was quantified using the diagnostic photon energy of 661.6 keV. Am-241 and Eu-152 were identified using their diagnostic photon energy peak at 59.5 and 121.8 keV, respectively. Limits of detection (LOD) were calculated by the GammaVision software. Peaks with greater intensity than 3σ above the background count were considered significant.

6.3.3. Autoradiography

Autoradiography of the concrete core was carried out to identify areas of increased activity present on the surface for further analysis. For the concrete core, the active face was exposed to a BAS-IP TR 2040 E (Fujifilm Corporation) imaging plate for 2 hours and scanned using a Fujifilm Fluorescent Image Analyser FLA-5000 (Fuji Photo Film Co., Ltd) with pixel sizes of 50 μm . Image optimisation was conducted using the AIDA image analysis software version 5.0 SP 2 (Elysia-Raytest GmbH) to improve the contrast and clearly identify areas of interest.

Analysis of the concrete coupons and hydrogels (see section 2.9 for details) was conducted on BAS-IP MS 2040 E (GE Healthcare) storage phosphor screens for 24 hours and scanned using an Amersham™ Typhoon Laser Scanner (Cytiva Life Sciences) with pixel sizes of 50 μm .

Images were optimised using the Amersham ImageQuant TL analysis software version 10.2 (Cytiva Life Sciences).

6.3.4. Scanning electron microscopy energy dispersive spectroscopy (SEM-EDX)

Analysis of non-active concrete thin-sections was conducted using a FEI Thermofisher Quanta 650 (E)SEM with high resolution Bruker Quantax energy dispersive spectrometer (EDX) to identify and map the phases in the bulk material. Quantitative evaluation of materials by scanning electron microscopy (QEMSCAN) was conducted for a typical concrete coupon to generate a map of the various minerals and phases in the sample matrix.

6.3.5. Powder X-ray diffraction (XRD)

XRD samples were prepared by grinding with a pestle and mortar and adding amyl acetate to form a homogeneous slurry which was deposited on a glass slide. Powder-XRD analysis of the cement and aggregate phases in the bulk concrete were conducted using a Bruker D2 Phaser diffractometer, equipped with a Göbel Mirror and Lynxeye XE-T detector with an axial 2.5° Soller slit and anti-scatter screen. XRD was conducted using Cu K α X-rays (wavelength 1.5406 Å) over incident angle range from 5 - 70°, with a step size of 0.03° at 0.3 s per step.

6.3.6. X-ray computed tomography (XCT)

Tomography analysis was conducted on a section of the uncontaminated core to map the aggregate distribution in the cement and identify potential areas for radionuclide penetration. XCT analysis was done using a Phoenix Nanotom nanoCT scanner (Waygate Technologies, Baker Hughes). Analysis of the data was conducted using ImageJ and Avizo (Thermo Fisher Scientific).

6.3.7. Sequential extraction

Thin-sections (10 x 10 x 3 mm (w x l x h)) of the core were prepared using the cutting methods described above (Section 6.3.1.). These thin-sections ran from the surface directly below the protective layers to a depth of 2 cm. After initial gamma analysis, the thin-sections were physically separated into cementitious and aggregate phases, which were removed, before the remaining cement was ground to a fine powder using a pestle and mortar for use in sequential extraction. The procedure used was adapted from the method by Li *et al.*, with alterations made to suit the nature of the sample (Table 6.1).^{14,15} The total sample mass was decreased from 1.0 g to 0.2 g due to the volume of sample available, as well as to minimise the exposure limit to

the powdered solid. The lixiviant volumes were reduced proportional to the sample mass (Table 6.1). Extraction times for fractions 4 and 5 were extended compared to the reference method.

Table 6.1. Chemical lixiviants and extraction times used in the sequential extraction of the cement phase.

Fraction	Lixiviant	Time / hours	Temperature / °C	Targeted Phase(s)
Exchangeable	1 M MgCl ₂ (pH 7.0)	5	RT	Sorbed Carbonate minerals
Carbonate	NaOAc (pH 5)	17	RT	
Reducible	0.04 M in 25% (v/v) HOAc	6	85	Fe/Mn oxides
	0.02 M HNO ₃ , 30% H ₂ O ₂			
Oxidisable	(pH 2.5)	7	85	Organic matter
	3.2% in 20% (v/v) HNO ₃	1	RT	
Residual	70% HNO ₃ , 60% HClO ₄	2	90	Residual
		12	120	
		6	160	

Before moving onto the next step, each extraction was centrifuged (5000 rpm, 10 minutes) and the leachate kept. The residue was then washed with 2 mL DI water (18 MΩ) and shaken for 20 minutes before centrifuging (5000 rpm, 10 minutes). This leachate was discarded. The leachates from each step were analysed using gamma spectroscopy and liquid scintillation counting (LSC). A blank sample was run alongside, and the leachates were diluted and acidified in 2% HNO₃ and analysed using inductively coupled plasma mass spectrometry (ICP-MS).

Liquid scintillation counting (LSC) samples were prepared by adding 0.5 mL of leachate to 10 mL proSafe HC+ liquid scintillation cocktail. Leachates from fractions 3 and 5 were diluted in DI water (18 MΩ) before scintillation cocktail was added to avoid colour quenching. Samples were left for 19 days to reach secular equilibrium for Sr-90 prior to analysis and were dark adapted for 2 hours to minimise photoluminescence effects. Samples were run using a LabLogic Hidex 300 SL with MikroWin 300SL control software. The Hidex 300 SL system uses three PMT detectors to automatically quench correct by triple to double coincidence ratio (TDCR). In addition, Sr-90 standards in solution had been prepared for calibration of solution analysis. Hydrogel standards had been prepared to calibrate the leaching of Sr-90 from hydrogels.

6.3.8. Hydrogel decontamination experiments

H06 hydrogels (20 x 20 mm (ø x h)) were synthesised as described by Moore *et al.*¹⁶ Polyvinylpyrrolidone (PVP) was dissolved in deionised (DI) water (18 MΩ) and combined with hydroxyethyl methacrylate (HEMA), *N,N'*-methylenebisacrylamide (MBAM) and azobisisobutyronitrile (AIBN). The mixture was stirred to remove any bubbles before being transferred to well plates (20 x 20 mm (ø x h)) and heated at 60 °C. Once cured the hydrogels were stored in deionised (DI) water (18 MΩ) until use. In addition to the H06 hydrogels, modifications were made to double the MBAM cross-linker concentration, which will be referred to as H06-2. Hydrogels were loaded in 2% HNO₃ 1 week prior to experiments to aid decontamination without affecting the hydrogel structure and functionality. H06 and H06-2 hydrogels were used for decontamination studies on concrete coupons (30 x 30 x 10 mm (w x l x h)) contaminated with Sr-90, Cs-137 or a mixed gamma solution (Table S6.1). A top stock of each radionuclide solution was diluted to achieve a working solution of 200 Bq/mL in 0.1 M HCl. 100 Bq of each Sr-90, Cs-137 or mixed gamma standard was spotted onto each concrete coupon surface and allowed to air dry for 1 week, resulting in an overall activity of 11.1 Bq/cm². Hydrogels were then placed on each coupon for a decontamination period of 1, 24, 168 and 672 hours. Replicates were not possible due to the limited quantity of material available for analysis.

For the concrete core, decontamination studies were conducted on both the painted surface and a section of concrete directly below the protective layers. Hydrogels were physically placed on the surfaces for select time periods of 1, 24 and 168 hours. For the painted surface, hydrogels were replaced with fresh ones in the same location after each decontamination period to determine the overall uptake of contamination with increasing contact time. For the bulk concrete, the same hydrogel was replaced on the concrete surface after each decontamination period to determine whether repeat use was possible to increase radionuclide removal from long-term contaminated concrete. Hydrogels and core samples were analysed with autoradiography and gamma spectroscopy before commencing the next decontamination test and analysed with LSC after the final decontamination period.

The decontamination factor (DF) for the hydrogels was:

$$DF = \frac{A_0}{A_f} \quad [1]$$

where A_0 is the radioactivity on the sample surface before decontamination and A_f is the activity on the sample surface after decontamination.¹⁷

This was then converted to the percentage of activity removed (%R):

$$\%R = \left(1 - \frac{1}{DF}\right) \times 100\% \quad [2]$$

6.4. Results and discussion

6.4.1. Concrete core surface characterisation

The core is primarily made from ordinary Portland cement (OPC) mixed with locally sourced aggregate. The radionuclide inventory of the core indicated the majority of activity was due to Sr-90, Cs-137, Am-241 and Pu-238-241 as determined by destructive radiometric analysis (Table 6.2). The fission products, Sr-90 and Cs-137, are of particular interest due to their mobility and relatively short half-lives. Previous work by Bower *et al.* showed the majority of the radionuclides were bound to the protective layers on a core removed from above the pond water level, with Sr-90 binding to titanium dioxide (TiO₂) pigment in the paint layer.¹⁸

Table 6.2. Radioisotopic inventory of the Hunterston A concrete core received from Magnox Ltd.

Radionuclide	Activity / Bq
Sr-90	1.53E+05
Cs-137	1.12E+05
Eu-152	8.29E+02
Eu-154	7.11E+02
Pu-238	3.81E+03
Pu-239	3.27E+03
Pu-240	4.03E+03
Pu-241	9.19E+04
Am-241	1.56E+04

Autoradiography of the top, painted face shows the activity is heterogeneously distributed across the surface (Figure 6.1). Raised areas, grooves and scratches on the painted surface

aligned with areas of increased radionuclide uptake. The highest area of activity in the top left corner of the core (Figure 6.1b), was of particular interest and was targeted for further analysis.

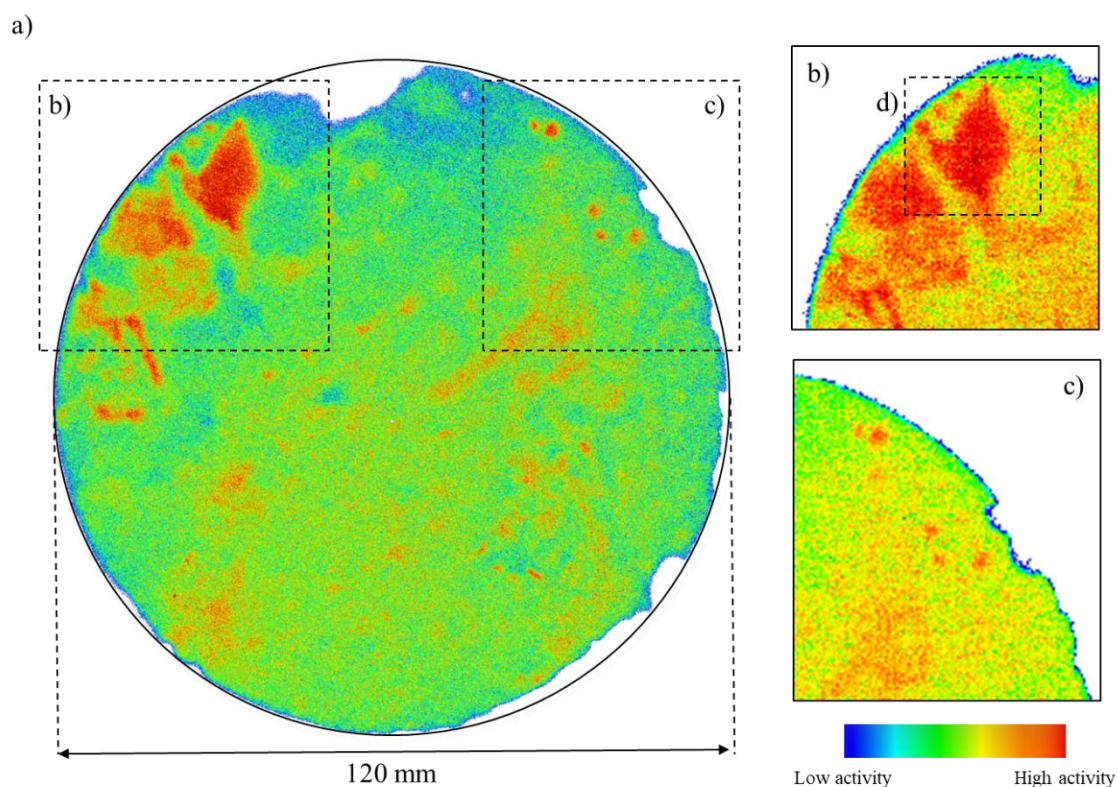


Figure 6.1. False-colour, contrast-adjusted autoradiography images of a) the active top face of the concrete core, highlighting areas of increased activity distributed heterogeneously on the surfaces (b and c). The active hot-spot (d) was cut through for depth analysis with autoradiography and gamma spectroscopy.

6.4.2. Concrete core bulk characterisation

The core was cut directly through a hot-spot (Figure 6.1d) to allow characterisation of the internal cross-section of the concrete and protective layers and to visualise any potential penetration of radionuclides through the protective coatings. In addition, smaller segments of the core were sectioned for analysis of the core's internal structure using XCT, characterisation of radionuclide binding strength and phases using sequential extraction methods and for use in hydrogel decontamination studies.

The SNF pond comprised large concrete walls made from OPC with locally sourced coarse and fine aggregates distributed throughout, and with protective coatings. XRD (Figure S6.4) and SEM-EDX analysis (Figure 6.2) of the cementitious phases in the concrete shows that

portlandite ($\text{Ca}(\text{OH})_2$), calcite (CaCO_3) and gypsum ($\text{CaSO}_4 \cdot 2\text{H}_2\text{O}$) dominated the material, with quartz (SiO_2) present throughout. SEM-EDX images show the high proportion of silica split between individual Si containing minerals and throughout the calcium-rich cementitious phase indicative of the presence of calcium silicate hydroxide (CSH) phases ($3\text{CaO} \cdot 2\text{SiO}_2 \cdot 3\text{H}_2\text{O}$). OPC undergoes hydration mechanisms during setting whereby the calcium aluminate and silicate phases react to form crystalline portlandite and various calcium hydrates, the majority of which consists of CSH.¹⁹ These CSH phases are of particular interest in terms of radionuclide contamination due to their high abundance and ability to undergo ion-exchange mechanisms with a multitude of radionuclides, including Sr, Cs and U.^{20–22} Strontium(II) has also been shown to replace calcium(II) in the CaO octahedral layer in CSH layers, and the added presence of aluminium silicate phases can lead to the formation of Cs-containing zeolite phases.^{23,24}

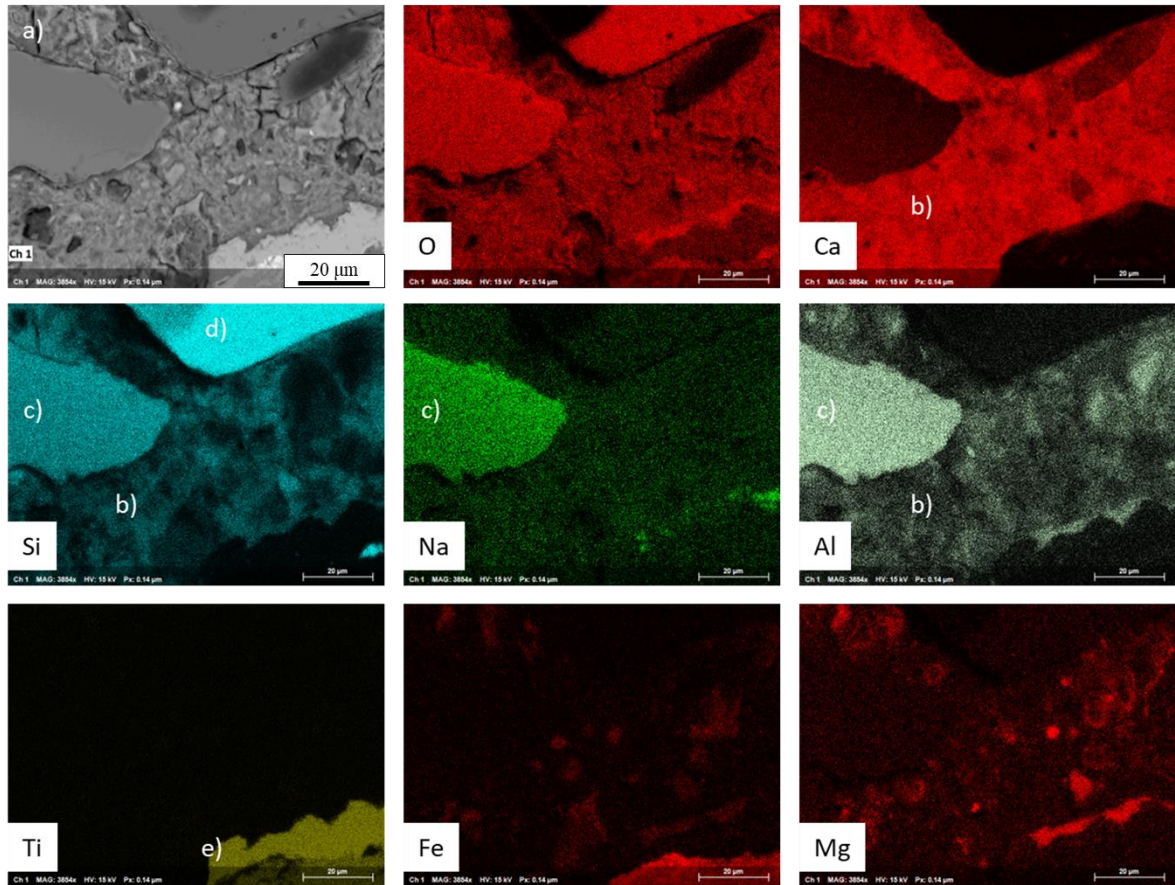


Figure 6.2. SEM image (a) and EDX maps of a section of the concrete core indicating the presence of b) CSH/CASH phases, c) mica and feldspathoidal minerals, d) quartz as well as e) TiO_2 minerals.

Analysis of the aggregate phases using XRD and SEM-EDX identified pyroxene and olivine minerals, consisting of gabbro aggregate (Figure 6.3). There are possible traces of mica and feldspar minerals present in the aggregates that can form vermiculite over time. These minerals can undergo ion-exchange with cesium(I), with higher exchange capacities for vermiculite due to calcium(II) and magnesium(II) cations forming part of the interlayer, and may retain Cs-137 in contaminated concrete.²⁵ These findings are in agreement with results obtained by Bower *et al.*¹⁸ Of note is the presence of Ti-Fe mineral phases in the concrete which could be ilmenite (FeTiO_3) and TiO_2 clasts from the local quarry (Figure S6.5).²⁶

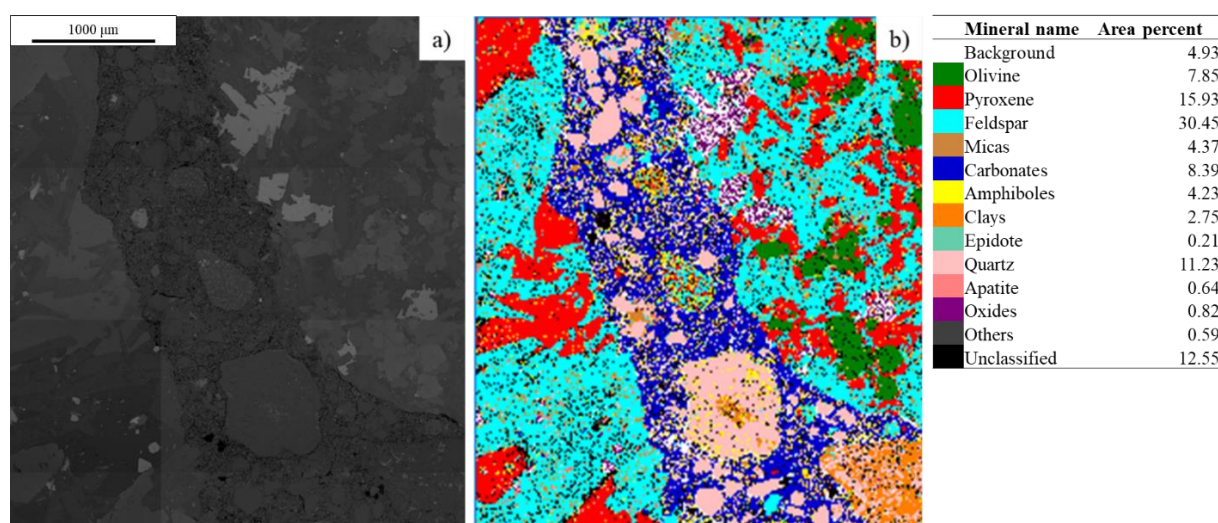


Figure 6.3. SEM images obtained via a) backscattered electron (BSE) analysis and b) quantitative evaluation of materials by scanning electron microscopy (QEMSCAN) of a section of typical concrete.

Calcium carbonate (CaCO_3) can be an indicator that corrosion of the cement paste may have taken place in the concrete structures over time. Water ingress can result in carbonation of Ca(OH)_2 , forming insoluble calcium carbonate, which at low concentrations can form an additional protective layer in the cement and prevent further corrosion and ingress of water.²⁷ Alkaline conditions can also lead to corrosion events in the cementitious phases of concrete materials whereby crystalline sodium carbonate precipitates can form, causing cracks in the cement. In alkaline environments such as SNF ponds, these cracks could aid radionuclide penetration into the concrete materials. Analysis of the structure in the concrete using X-ray computed tomography (XCT) showed pores were distributed throughout the cement, with some pores reaching up to 1 mm in diameter, and gaps between the aggregate and cement boundaries were identified which could aid the migration of radionuclides through the concrete (Figure

S6.6). However, extended corrosion is likely to have been prevented by the protective layers present on the concrete surface.

Autoradiography analysis of the interior cross-section of the core shows the majority of the activity was isolated in the first 1-2 mm of the core on the protective coatings (Figure 6.4). However, radionuclide penetration beneath these protective layers can be seen, indicating that some radionuclides have migrated into the bulk concrete via diffusion through the cement or along pores and cracks. The diffusion of radionuclides into the material is heterogeneous due to the complex concrete matrix. This is enhanced along boundaries between the cement and aggregate phases where activity can be seen to penetrate ~1 cm into the concrete (Figure 6.4b). Petit *et al.* conducted sorption studies with Cs reaching penetration depths of up to 6 cm in concrete over 50 years with the presence of cracks increasing the contamination depth.²⁸ Radionuclide ingress into concrete predominantly occurs via diffusion driven by the concentration gradient until the radionuclides are adsorbed on the cement or aggregate phases.²⁹

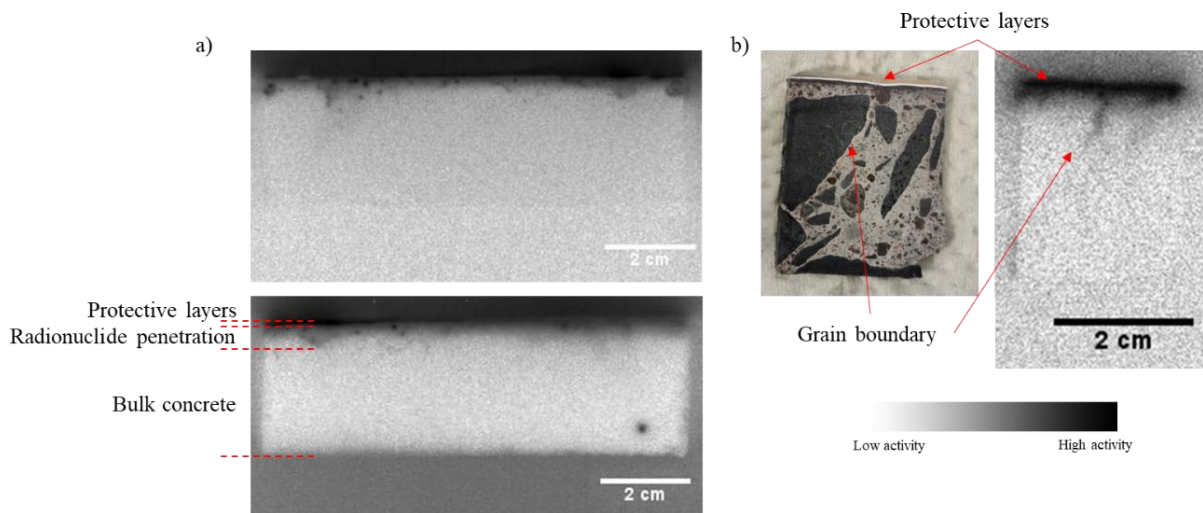


Figure 6.4. Contrast adjusted autoradiography images of a) the core cross-section after cutting through the active spot in figure 6.1d, indicating radionuclides had penetrated through the protective layers into the bulk concrete, b) aided by cracks and boundaries between the cement and aggregate phases.

Gamma spectroscopy of thin-sections taken from the top to 2 cm into the core bulk shows a decrease in Cs-137 activity with increasing depth (Figure 6.5). This is consistent with the autoradiography and shows the majority of the Cs-137 activity is isolated in the first 5 mm of the concrete core, in the protective layers and initial bulk layer. This activity rapidly declines

by a factor of 1000 as the radionuclides remain bound to the concrete and no longer travel further into the bulk. Whilst characterisation of Sr-90 penetration into the concrete bulk was not possible in this study, the solubility of Sr under alkaline conditions suggests that penetration into the bulk concrete is likely.³⁰ Research by Peterson *et al.* showed Sr was able to penetrate up to 1.0 mm into OPC cured at 60 °C and up to 1.6 mm with the addition of clinoptilolite after three weeks, a Si and Al based zeolite with high affinity for Sr and Cs.^{31,32} Future studies to assess the extent of this migration using radiotracers could greatly benefit future decommissioning tasks.^{33,34}

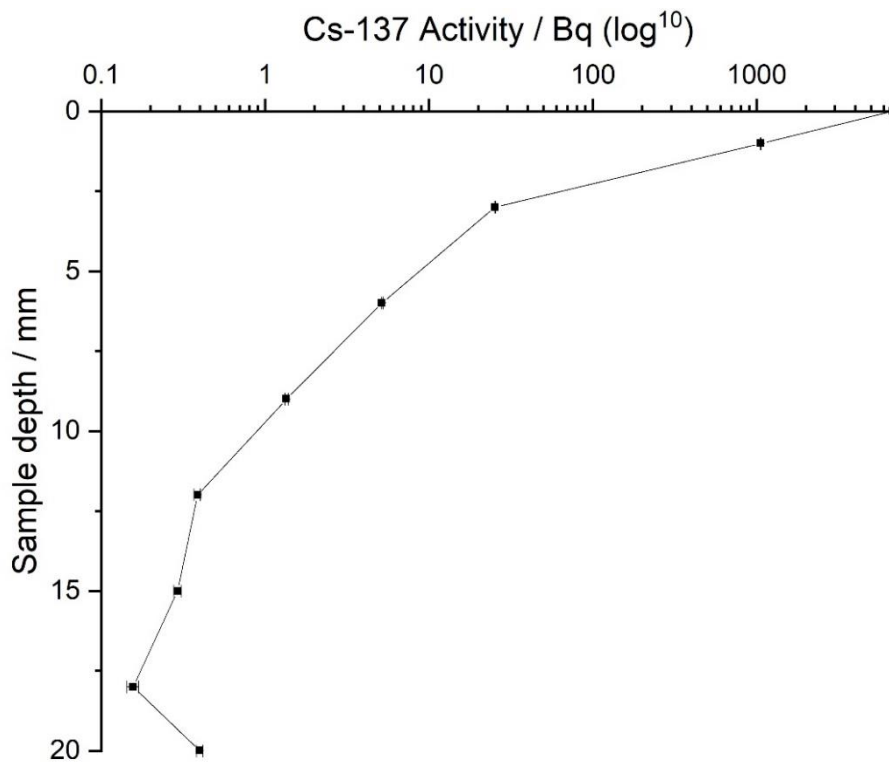


Figure 6.5. Cs-137 activity penetration profile for a section of the concrete core (log scale). The gamma spectrometer was not calibrated for the shape and geometry of these samples, therefore activities presented serve as an estimate to allow for comparison and assessment of general trend. Error bars are uncertainties from gamma spectroscopy (3σ).

Sequential extraction of the cement was conducted to identify phase associations of the radionuclides (Figure 6.6). Weakly bound radionuclides are more likely to be extracted in earlier fractions, whereas more strongly bound radionuclides will require harsher conditions. Due to the small quantities of material available and the initial low activity of the material, only Cs-137 was able to be accurately quantified. The majority of Cs-137 activity was present in the final, residual phase, ($32\% \pm 4$) followed by the oxidisable ($9\% \pm 2$) and Fe/Mn oxide phase

(6% \pm 2). There was also considerable Cs-137 activity present in the undigested solid (50% \pm 4) after all sequential extraction steps were complete, indicating Cs adsorption to crystalline silica and iron minerals was taking place.

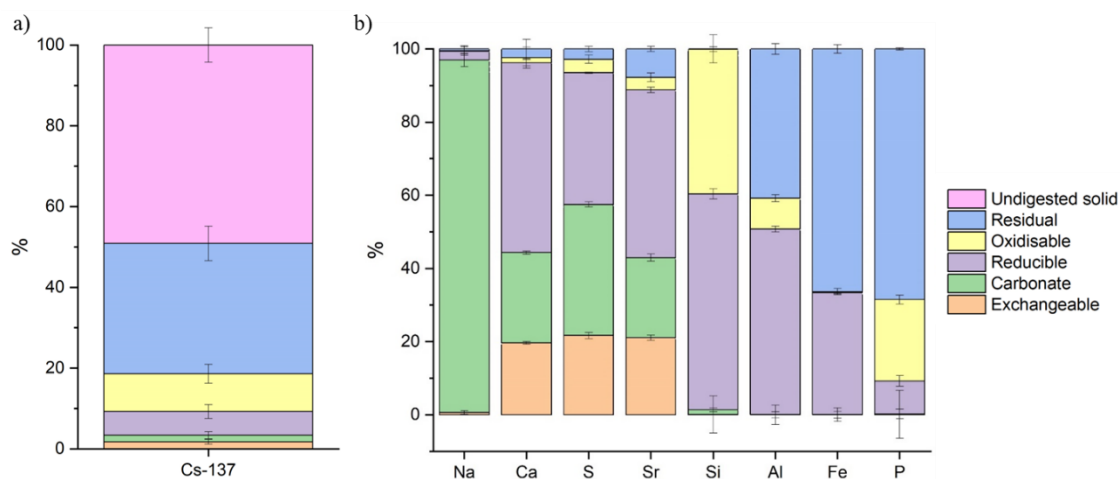


Figure 6.6. a) Percentage distribution of Cs-137 between the different phases targeted with the sequential extraction reactions of the concrete core samples at a depth of 3 mm. Solid activity was calculated based on the difference between the initial activity of the sample and the total activity leached out with each sequential extraction step. b) Percentage distribution of elements in the concrete core samples obtained using ICP-MS from the different phases targeted with the sequential extraction reactions. Error bars are uncertainties from gamma spectroscopy (3σ) for Cs-137 and estimated standard deviation from repeats for ICP-MS.

Analysis by ICP-MS showed higher quantities of Si (59% \pm 3) were present in the reducible, Fe/Mn oxide phase alongside Ca (51% \pm 4.) indicative of the soluble, amorphous CSH phases being leached out. A slight increase in Cs-137 activity can be seen in the Fe/Mn oxide phase, as some cesium(I) may have adsorbed to the CSH and CSAH phases.^{35–37} Crystalline silicate phases require stronger reagents such as HF and HClO₄ to be dissolved.^{38,39} These silicates will not have been digested under the conditions used and remain present in the solid phase, where higher activities of Cs-137 were found. Cesium is likely to be structurally incorporated with these more crystalline phases through ion-exchange or irreversible adsorption onto phyllosilicate edge sites.^{40,41}

Iron(II) was leached out in both the reducible (34% \pm 4) and residual fractions (65% \pm 1). Cesium(I) sorption to iron (oxy)hydroxide minerals occurs *via* weaker surface outer sphere complexation and would be expected to be released in the earlier Fe/Mn oxide phase as iron(III)

is reduced to soluble iron(II).⁴² The presence of impurities such as Si in iron (oxy)hydroxides can significantly increase the adsorption of cesium(I) in these phases, resulting in stronger interactions that require harsher conditions to leach Cs-137.⁴³ The Fe content in the residual phase is likely due to the presence of more crystalline primary iron phases such as iron oxide. There were also higher percentages of phosphorus ($68\% \pm 1$) leached out in the residual phase, indicating that crystalline iron phosphate compounds may have been present and adsorption of Cs-137 to these minerals may have occurred. The exact source of the phosphorus is unknown due to the age of the samples; however it is likely to have originated from aggregate material sourced from the local quarries. However, the actual concentration of phosphorus in the residual phase is relatively low ($98.1 \pm 1.2 \mu\text{g/L}$). It is more likely that the Cs-137 was strongly bound to silica and gabbro minerals distributed throughout the concrete.^{18,44–46}

Whilst Sr-90 activities in the extracted phases were too low to be detected through LSC, natural Sr from the cement was leached out during the sequential extraction and could be measured using ICP-MS. The Sr concentration was highest in the Fe-Mn oxides phase ($45\% \pm 4$), along with the majority of Ca and Si. These results support the previous statements that Sr is most likely incorporated in the CSH phases in the cement through ion-exchange with calcium(II).^{20,23} In addition, concrete coupons contaminated with 100 Bq Sr-90 showed preferential migration and adsorption of the Sr-90 with the cementitious phases in the concrete coupon (Figure S6.7) It is therefore reasonable to assume radioactive Sr-90 will behave in the same manner and would be leachable under reducible conditions when bound to CSH.

Autoradiography analysis of the underneath of the protective layers indicate radionuclide contamination was greatest within the protective layers, in line with the cross-section autoradiography images (Figure 6.7b) However, analysis of the bulk concrete directly below the protective layers shows radioactivity is distributed throughout the concrete, with increased radioactivity gathered in the grain boundaries between the aggregate and cement phases, as well as in some of the finer aggregate grains (Figure 6.7c). This supports the sequential extraction results that some radionuclides, such as Sr-90, are present within the cement phase, and that other radionuclides, such as Cs-137, were found to be bound to the aggregate phases.

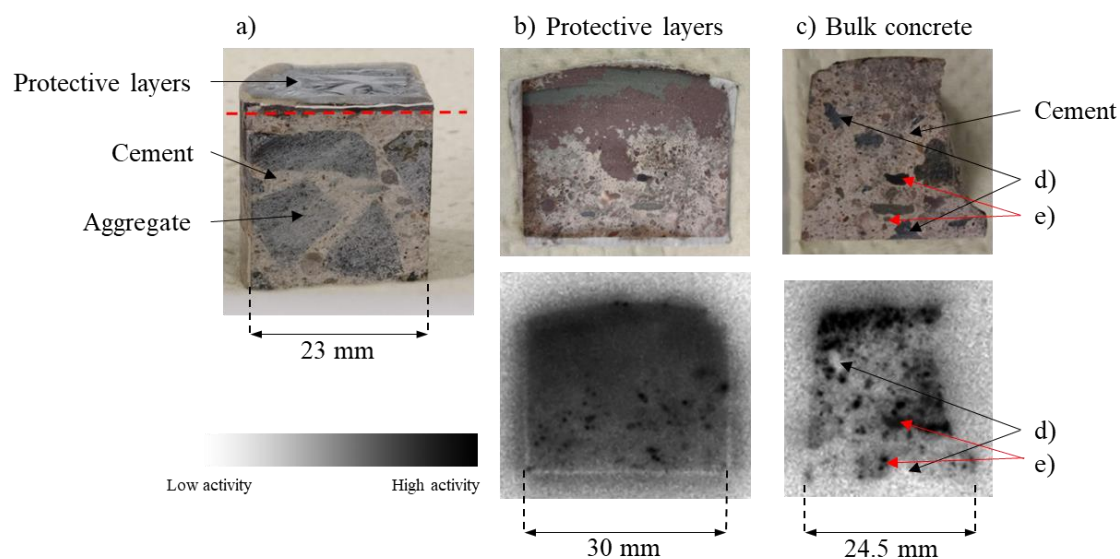


Figure 6.7. a) Image of the active section before removal of the protective layers for internal analysis (red dotted line indicates cutting path). Images (top) and contrast-adjusted autoradiography images (bottom) of b) the underside of the paint layer and c) the concrete directly beneath the protective layers. Activity is heterogeneously distributed throughout the concrete, congregating around the boundaries between cement and aggregate minerals (d - black), as well as in certain mineral phases (e - red).

6.4.3. Decontamination of the concrete core

Simple swabbing was ineffective at removing radionuclide contamination, but polymer based hydrogels have been identified as a potential decontamination route for radionuclides adsorbed to steel surfaces.¹⁶ Given the large number of concrete structures requiring decommissioning, a similar technology for concrete surfaces would be very useful. Previous decontamination methods have resulted in large volumes of secondary waste, either through the formation of increased waste volume due to inefficient packing of scabbling fragments or the generation of aqueous waste through water and chemical-based methods.⁴⁷ Alternative methods using gel or foam applications have been shown to remove contaminants from porous surfaces such as concrete, but can involve long contact times, multiple applications or additional equipment such as vacuums to remove the final product.^{17,48,49} The use of hydrogels for the decontamination of concrete surfaces is of interest due to their ability to target specific areas and leach radionuclides into the cross-linked polymer network, limiting secondary waste production.^{16,50}

Initial studies using concrete coupons contaminated with known quantities of Sr-90, Cs-137 and mixed gamma standard showed hydrogels were capable of removing a variety of radionuclides from the concrete surfaces simultaneously (Figures S6.7 and S6.8). Sr-90 removal after 1 hour was greater than Cs-137 with 25% and 4%, activity removed, respectively (Tables S6.2. And S6.3). Use of the modified H06-2 hydrogel resulted in greater removal of radionuclides for the mixed gamma standard contaminated sample, but only resulted in small variations for single Sr and Cs experiments.

Calibration curves were calculated for Sr-90 and Cs-137 uptake in H06 and H06-2 hydrogels (Figure S6.9). Due to the heterogeneous spread of activity and the hydrogels only decontaminating a small area on the sample surface (3.14 cm²), DF values were determined based on autoradiography data (Table 6.3). The following modifications were made to equation [1]:

$$DF = \frac{\text{Average intensity of decontamination area before (\%)}}{\text{Average intensity of decontamination area after (\%)}} \quad [3]$$

Table 6.3. *Hydrogel decontamination data for the painted surface after consecutive applications. DF = decontamination factor, %R = % activity removed.*

Time / hours	Paint 1		Paint 2	
	DF	%R	DF	%R
1	1.2	19	1.4	27
24	2.5	38	2.7	52
168	3.9	69	4.3	91

Hydrogels were placed in two areas on the painted surface, labelled “paint 1” where a higher concentration of activity was present, and “paint 2” which was less active, (Figure 6.8). The initial activity of the individual locations is unknown due to the heterogeneous spread of activity on the sample surface. Hydrogels were able to remove 18-27% of activity from the painted surface after just 1 hour of contact. Increasing the contact time between the hydrogel and the sample surface resulted in increased removal of radionuclides and after 1 week resulted in ~70% removal in the higher activity area, paint 1, and around >90% removal in the lower activity area, paint 2.

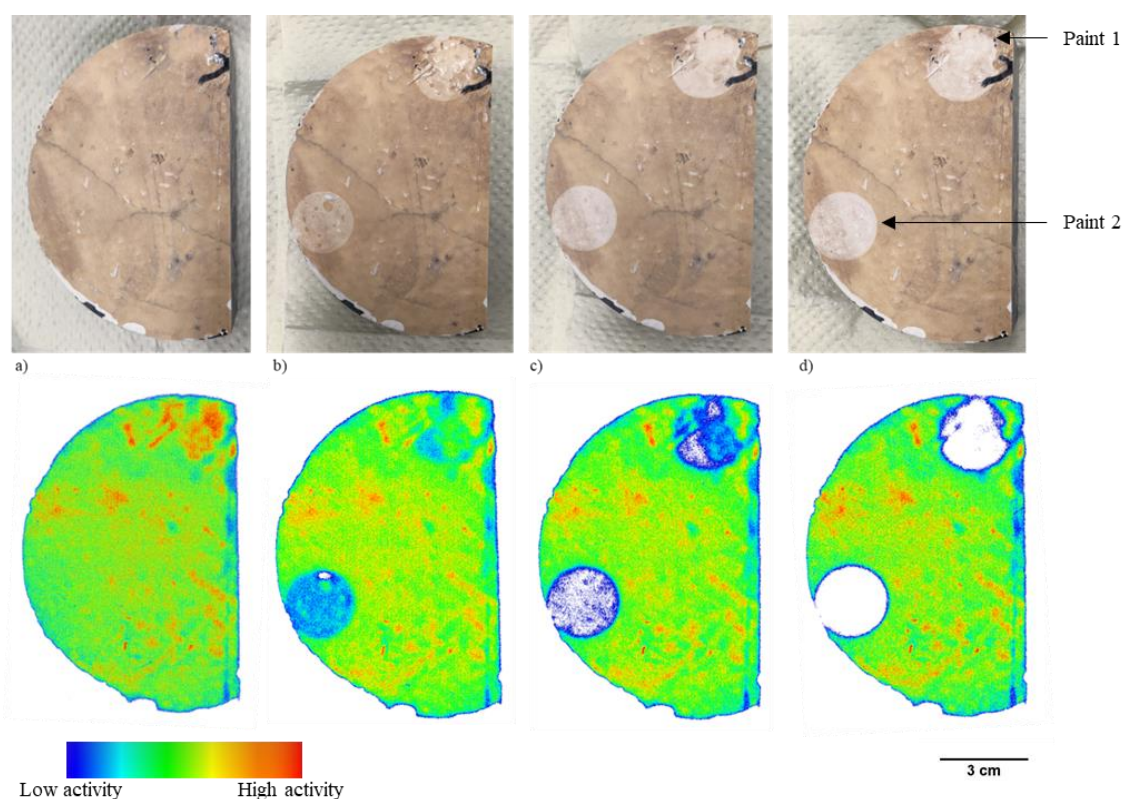


Figure 6.8. Contrast-adjusted, false-colour autoradiography images showing the progressive decontamination of a) the painted surface with consecutive hydrogel applications after b) 1, c) 24 and d) 168 hours of contact in areas “paint 1” and “paint 2”.

Hydrogels were not left on the concrete core surfaces over 168 hours, due to dehydration effects and increased adhesion of the hydrogel to the surfaces affecting the hydrogel integrity (Figure S6.10). Analysis of the hydrogels indicated that increased activities of Cs-137 and Sr-90 were removed with each additional hydrogel exposure (Figure 6.9). Results show that a total of 530 ± 40 Bq Cs-137 and 1000 ± 60 Bq Sr-90 were removed within a 3.14 cm^2 area on the painted surface and autoradiography shows significant removal of activity took place on the surface after consecutive applications. As calibration curves were not generated for Am-241 uptake this uptake was not quantifiable, however, preliminary experiments indicate that Am-241 was also taken up into the hydrogel after 1 hour of contact, indicating that the hydrogels can be used for the simultaneous removal of fission products and actinides from heavily contaminated painted concrete surfaces.

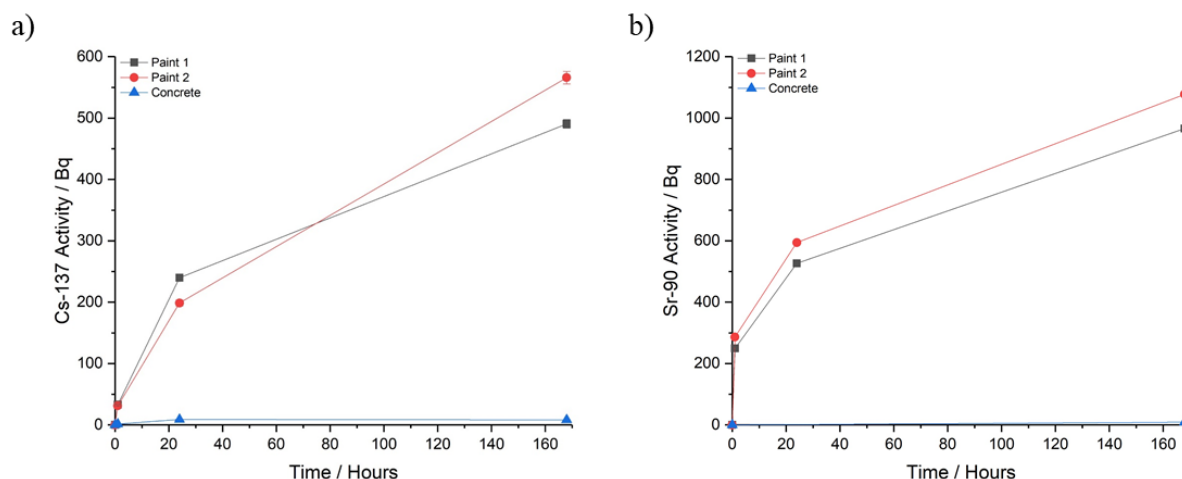


Figure 6.9. The cumulative activity taken up of for a) Cs-137 and b) Sr-90 into the hydrogels after consecutive decontamination experiments on the painted (black and red) and concrete (blue) surface. Error bars are uncertainties from gamma spectroscopy (3σ).

Compared to the decontamination of the painted surface, decontamination of the bulk concrete directly below the painted surface was less successful. In this instance, the same hydrogel was replaced for each consecutive time point. Visually there was almost no change to the activity on the sample surface as can be seen from the autoradiography images (Figure S6.11). However, radiometric analysis of the hydrogel showed small amounts of Cs-137 and Sr-90 activity present in the hydrogel after each exposure, indicating trace quantities may be removed (Figure 6.9). This is more likely due to the removal of loose concrete particulates from the surface. These results confirm the sequential extraction data that the majority of Cs-137 is strongly bound to the concrete and decontamination methods using hydrogels loaded with 2% HNO_3 are not strong enough to extract long-term contamination from the bulk concrete.

In addition to being a quick, easy to apply decontamination method that can be moulded to any shape, the hydrogels can also act as a final waste container for the radionuclides removed. As the hydrogels dry they become solid pucks that trap the radionuclides in their previously open-network structure. The only way to get the radionuclides back out is through re-hydration of the hydrogels and leaching methods. Therefore, it is possible to dispose of the hydrogels through acid dissolution or by burning the solid waste forms and mixing with cement grout, resulting in a $>90\%$ reduction in volume.⁵¹ This treatment could also include the removal of Sr and Cs to minimise the risk of these mobile species and to decrease the activity levels of the waste for disposal as LLW.

6.5. Conclusions

Novel research on a concrete core sample from the Hunterston A SNF pond was carried out to improve understanding of long term contamination of concrete structures. Autoradiography of the protective painted surface showed radioactivity was heterogeneously distributed on the surface after 50 years of contact with the pond water, with greater areas of radioactivity associated with defects on the surface. Analysis of the core cross-section showed radioactivity was predominantly associated with the protective coatings applied to the concrete walls, with some contamination penetrating into the bulk material to a maximum observable depth of 5 mm along the grain boundary of aggregates and the cement. Analysis of the surface directly below the protective layers indicated contamination in the concrete material was localised between the cement-aggregate boundaries and in gabbro and silicate aggregate clasts.

Analysis of the bulk concrete material with XRD and SEM-EDX identified the presence of silicate, gabbro and iron-titanium bearing minerals. Sequential extraction of the concrete material showed the majority of the activity was contained in the residual phase, indicating Cs-137 was strongly bound to silicate and gabbro aggregates (pyroxene and olivine), making release of radionuclides from these concrete materials extremely unlikely under natural conditions.

Hydrogels have been shown to successfully remove Sr-90 and Cs-137 after 1 hour of contact. Cs-137 uptake was significantly lower than Sr-90, due to stronger interactions occurring between the cesium(I) ions and the aggregate phases, compared to strontium(II) and the cement. Decontamination studies of the painted surface showed fission products and actinides were simultaneously taken up by the hydrogels after 1 hour of contact. Over 90% decontamination of the surface is possible with consecutive or longer application times. Hydrogels were unable to take up significant activity from the aged bulk concrete.

Overall, this research has shown the value of authentic samples to inform understanding of long-term radionuclide contamination of nuclear structures. Highlighting that protective layers previously used were unable to prevent radionuclide ingress into concrete structures and that Cs-137 remains strongly bound to the aggregate phases in concrete structures.

Declaration of competing interest

None.

Acknowledgements

Martin C. McGarvey at Magnox Ltd and the National Nuclear Laboratory (NNL) are acknowledged for the provision of the Hunterston A concrete core.

The EPSRC NNUF RADER Facility (EP/T011300/1) is acknowledged for access and analysis performed.

The University of Helsinki is acknowledged for the use of their facilities for the manipulation and analysis of the Hunterston A concrete core.

The authors would like to acknowledge Professor Peter Quayle and Dr Aula Alwatter for the synthesis of the hydrogels, Dr Lewis Hughes for the QEMSCAN analysis and Dr Abby Ragazzon-Smith for the ICP-MS analysis.

The authors would also like to acknowledge Professor Francis Livens for helpful discussions and support throughout.

Funding sources

The National Nuclear Laboratory (NNL) (Core Science Decontamination and Decommissioning R&D Theme) and the EPSRC Next Generation Nuclear Centre for Doctoral Training (NGN CDT) are acknowledged for their funding.

6.6. References

- 1 Focus Europe, *The World Nuclear Waste Report*, 2019.
- 2 Jacobs UK Ltd and AFRY Solutions UK Ltd, *2022 UK Radioactive Waste Inventory*, 2022.
- 3 B. Wealer, J. P. Seidel and C. von Hirschhausen, *Decommissioning of Nuclear Power Plants and Storage of Nuclear Waste*, Springer Fachmedien Wiesbaden, 2019.

- 4 S. A. Adeleye, D. A. White and J. B. Taylor, Kinetics of contamination of stainless steel in contact with radioactive solutions at ambient temperatures, *J. Radioanal. Nucl. Chem. Artic.*, 1995, **189**, 65–70.
- 5 Magnox Ltd, *Wylfa Site Environmental Management Plan Issue Ten*, 2021, vol. DP/EMP/ENG.
- 6 IEAE Nuclear Energy Series, *Decommissioning of Pools in Nuclear Facilities*, 2015, vol. NW-T-2.6.
- 7 M. J. Dunn and I. R. Topliss, The status of spent fuel treatment in the United Kingdom, *Advis. Gr. Meet. status trends spent fuel Reprocess.*, 1998, 61–65.
- 8 M. Forwood, The legacy of reprocessing in the United Kingdom, 2008, 1–54.
- 9 Magnox North, *Information in support of the application by Magnox North Ltd for authorisation under RSA93 to dispose of radioactive waste from the Hunterston A site*, 2010, vol. HNA/3800/T.
- 10 K. S. Dickerson, M. J. Wilson-Nichols and M. I. Morris, Contaminated concrete: occurrence and emerging technologies for DOE decontamination, 1995, 377.
- 11 J. Kořátková, J. Zatloukal, P. Reiterman and K. Kolář, Concrete and cement composites used for radioactive waste deposition, *J. Environ. Radioact.*, 2017, **178–179**, 147–155.
- 12 M. I. Ojovan, W. E. Lee and S. N. Kalmykov, in *An Introduction to Nuclear Waste Immobilisation*, Elsevier, 3rd edn., 2019, pp. 145–154.
- 13 C. Bertoncini, in *Proceedings of the International Conference on Environmental Remediation and Radioactive Waste Management, ICEM*, 2013, pp. 1–11.
- 14 X. D. Li, C. S. Poon, H. Sun, I. M. C. Lo and D. W. Kirk, Heavy metal speciation and leaching behaviors in cement based solidified/stabilized waste materials, *J. Hazard. Mater.*, 2001, **82**, 215–230.
- 15 X. Li, B. J. Coles, M. H. Ramsey and I. Thornton, Sequential extraction of soils for multielement analysis by ICP-AES, *Chem. Geol.*, 1995, **124**, 109–123.

- 16 J. J. Moore, T. P. Raine, A. Jenkins, F. R. Livens, K. A. Law, K. Morris, G. T. W. Law and S. G. Yeates, Decontamination of cesium and strontium from stainless steel surfaces using hydrogels, *React. Funct. Polym.*, 2019, **142**, 7–14.
- 17 US Environmental Protection Agency, *Decontamination of cesium, cobalt, strontium, and americium from porous surfaces.*, 2013.
- 18 W. R. Bower, K. Morris, J. F. W. Mosselmans, O. R. Thompson, A. W. Banford, K. Law and R. A. D. Patrick, Characterising legacy spent nuclear fuel pond materials using microfocus X-ray absorption spectroscopy, *J. Hazard. Mater.*, 2016, **317**, 97–107.
- 19 D. Marchon and R. J. Flatt, *Mechanisms of Cement Hydration*, Elsevier Ltd, 2016.
- 20 E. Wieland, J. Tits, D. Kunz and R. Dähn, Strontium uptake by cementitious materials, *Environ. Sci. Technol.*, 2008, **42**, 403–409.
- 21 J. Tits, G. Geipel, N. Macé, M. Eilzer and E. Wieland, Determination of uranium(VI) sorbed species in calcium silicate hydrate phases: A laser-induced luminescence spectroscopy and batch sorption study, *J. Colloid Interface Sci.*, 2011, **359**, 248–256.
- 22 J. Bu, R. Gonzalez Teresa, K. G. Brown and F. Sanchez, Adsorption mechanisms of cesium at calcium-silicate-hydrate surfaces using molecular dynamics simulations, *J. Nucl. Mater.*, 2019, **515**, 35–51.
- 23 J. Tits, E. Wieland, C. J. Müller, C. Landesman and M. H. Bradbury, Strontium binding by calcium silicate hydrates, *J. Colloid Interface Sci.*, 2006, **300**, 78–87.
- 24 S. L. Hoyle and M. W. Grutzeck, Incorporation of cesium by hydrating calcium aluminosilicates, *J. Am. Ceram. Soc.*, 1989, **72**, 1938–1947.
- 25 D. G. Schulze, Clay minerals, *Encycl. Soils Environ.*, 2005, 246–254.
- 26 A. S. Makarious, M. A. El-Kolaly, I. I. Bashter and W. A. Kansouh, Radiation distribution through ilmenite-limonite concrete and its application as a reactor biological shield, *Int. J. Radiat. Appl. Instrumentation. Part*, 1989, **40**, 257–260.
- 27 H. Zhang, Ed., in *Building Materials in Civil Engineering*, Woodhead Publishing

- Limited, 2011, pp. 46–80.
- 28 L. Petit, C. Martin, S. Leclercq, H. Catalette and D. Noel, in *Electric Power Research Institute*, 2004, pp. 575–590.
 - 29 P. Claisse, Transport properties of concrete, *Penetration Permeability Concr.*, 2020, 223–274.
 - 30 W. Bostick, B. Dunaway and M. Sanders, in *Waste Management*, 2016, pp. 1–23.
 - 31 V. K. Peterson, R. Siegele, A. Ray, W. K. Bertram and L. P. Aldridge, Strontium binding to cement paste cured at different temperatures, 262–265.
 - 32 A. Dyer, J. Hriljac, N. Evans, I. Stokes, P. Rand, S. Kellet, R. Harjula, T. Moller, Z. Maher, R. Heatlie-Branson, J. Austin, S. Williamson-Owens, M. Higgins-Bos, K. Smith, L. O’Brien, N. Smith and N. Bryan, The use of columns of the zeolite clinoptilolite in the remediation of aqueous nuclear waste streams, *J. Radioanal. Nucl. Chem.*, 2018, **318**, 2473–2491.
 - 33 M. C. Chaparro, M. W. Saaltink, J. M. Soler, L. J. Slooten and U. K. Mäder, Modelling of matrix diffusion in a tracer test in concrete, *Transp. Porous Media*, 2016, **111**, 27–40.
 - 34 N. Macé, P. Fichet, S. Savoye, J. Radwan, C. Lim, S. Lefèvre, J. Page and P. Henocq, Use of quantitative digital autoradiography technique to investigate the chlorine-36-labelled radiotracer transport in concrete, *Appl. Geochemistry*, 2019, **100**, 326–334.
 - 35 S. Bagosi and L. J. Csetényi, Cesium immobilisation in hydrated calcium silicate aluminate systems, *Cem. Concr. Res.*, 1998, **28**, 1753–1759.
 - 36 S. Kang, J. Lee, S. M. Park, D. S. Alessi and K. Baek, Adsorption characteristics of cesium onto calcium-silicate-hydrate in concrete powder and block, *Chemosphere*, 2020, **259**, 127494.
 - 37 E. Duque-Redondo, K. Yamada and H. Manzano, Cs retention and diffusion in C-S-H at different Ca/Si ratio, *Cem. Concr. Res.*, 2021, **140**, 106294.
 - 38 N. Singh and P. K. Gupta, Analysis of silicates materials: A review, *Rev. Anal. Chem.*,

- 2005, **24**, 1–7.
- 39 Z. Hu and L. Qi, Sample Digestion Methods, *Treatise Geochemistry Second Ed.*, 2013, **15**, 87–109.
 - 40 R. M. Cornell, Adsorption of cesium on minerals: A review, *J. Radioanal. Nucl. Chem. Artic.*, 1993, **171**, 483–500.
 - 41 A. Ben Said, F. Frances, A. Grandjean, C. Latrille and S. Faure, Study of a foam flotation process assisted by cationic surfactant for the separation of soil clay particles: processing parameters and scaling-up sensitivity, *Chem. Eng. Process. Process Intensif.*, 2019, **142**, 107547 1–30.
 - 42 S. Kikuchi, T. Kashiwabara, T. Shibuya and Y. Takahashi, Molecular-scale insights into differences in the adsorption of cesium and selenium on biogenic and abiogenic ferrihydrite, *Geochim. Cosmochim. Acta*, 2019, **251**, 1–14.
 - 43 H. Catalette, J. Dumonceau and P. Ollar, Sorption of cesium, barium and europium on magnetite, *J. Contam. Hydrol.*, 1998, **35**, 151–159.
 - 44 A. J. Fuller, S. Shaw, M. B. Ward, S. J. Haigh, J. F. W. Mosselmans, C. L. Peacock, S. Stackhouse, A. J. Dent, D. Trivedi and I. T. Burke, Cesium incorporation and retention in illite interlayers, *Appl. Clay Sci.*, 2015, **108**, 128–134.
 - 45 J. M. Zachara, S. C. Smith, C. Liu, J. P. McKinley, R. J. Serne and P. L. Gassman, Sorption of Cs⁺ to micaceous subsurface sediments from the Hanford site, USA, *Geochim. Cosmochim. Acta*, 2002, **66**, 193–211.
 - 46 B. Yıldız, H. N. Erten and M. Kış, The sorption behavior of Cs⁺ ion on clay minerals and zeolite in radioactive waste management: Sorption kinetics and thermodynamics, *J. Radioanal. Nucl. Chem.*, 2011, **288**, 475–483.
 - 47 K. E. Archibald, *Concrete Decontamination Scoping Tests*, 1995.
 - 48 H. M. Yang, C. W. Park and K. W. Lee, Enhanced surface decontamination of radioactive Cs by self-generated, strippable hydrogels based on reversible cross-linking, *J. Hazard. Mater.*, 2019, **362**, 72–81.

- 49 A. Gossard, A. Lilin and S. Faure, Gels, coatings and foams for radioactive surface decontamination: state of the art and challenges for the nuclear industry, *Prog. Nucl. Energy*, 2022, **149**, 104255.
- 50 V. V. Kusumkar, M. Galamboš, E. Viglašova, M. Daňo and J. Šmelková, Ion-imprinted polymers: synthesis, characterization, and adsorption of radionuclides, *Materials (Basel)*., 2021, **14**, 1083 1–29.
- 51 C. Madic and M. Hudson, *High-level liquid waste partitioning by means of completely incinerable extractants*, 1998.

6.7. Supporting information

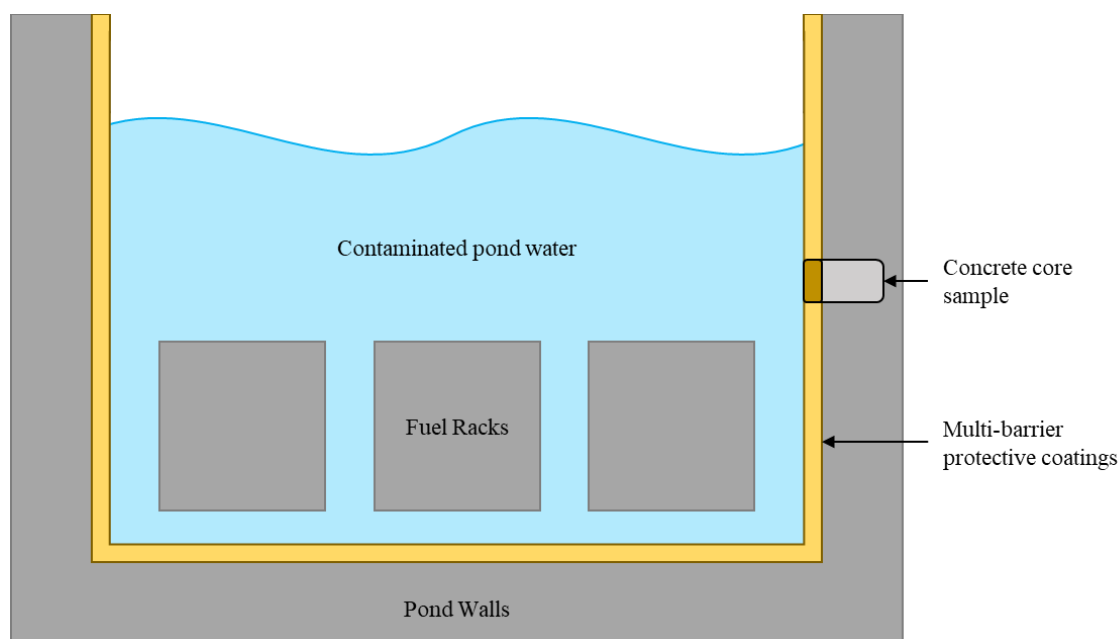


Figure S6.1. Schematic of the Hunterston A SNF storage pond and concrete core sampling location.

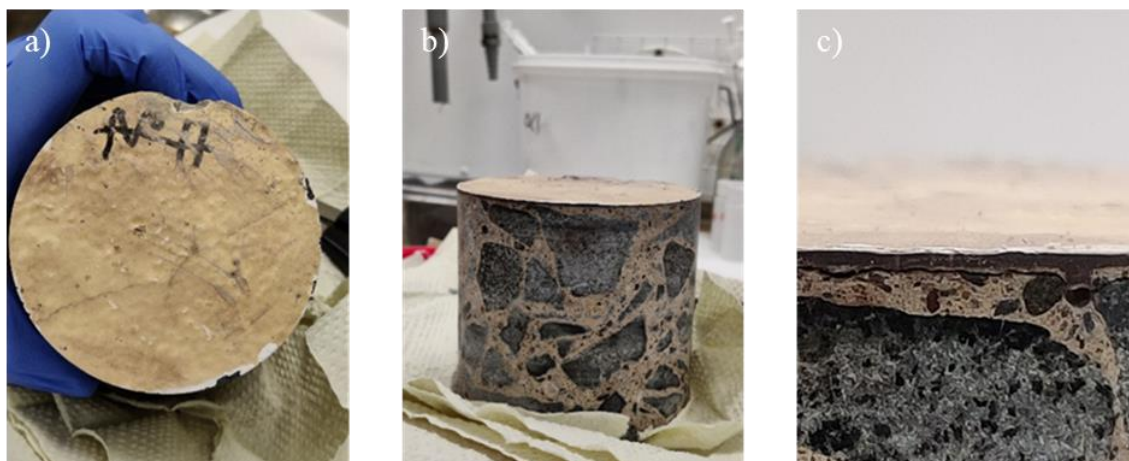


Figure S6.2. Images of the Hunterston A concrete core highlighting the a) active, painted surface, b) bulk concrete showing the heterogeneous distribution of aggregate in the cement matrix and c) multi-layered protective coatings and close up of finer aggregate.



Figure S6.3. Concrete core sectioned for analysis (red lines indicate cutting paths).

Table S6.1. Radionuclide inventory of a mixed gamma standard used for the assessment of hydrogel decontamination (adapted from IsoTrak Catalogue).⁵¹

Radionuclide											
Am- 241	Cd- 109	Co- 57	Ce- 139	Cr- 51	Sn- 113	Sr- 85	Cs- 137	Co- 60	Y- 88	Zn- 65	Mn- 54

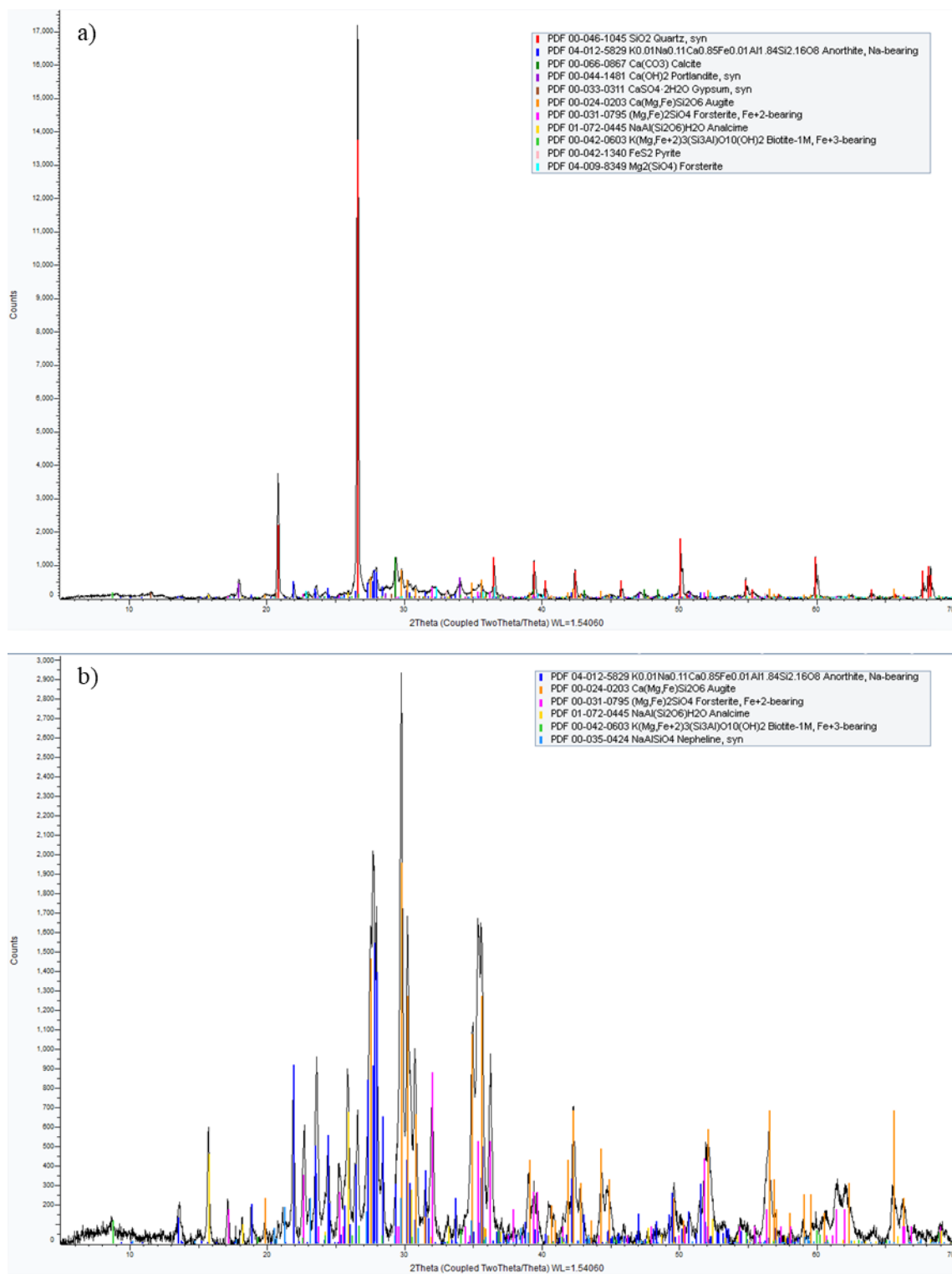


Figure S6.4. XRD spectra with assignment of the phases present in the a) cement and b) aggregate of the concrete core sample.

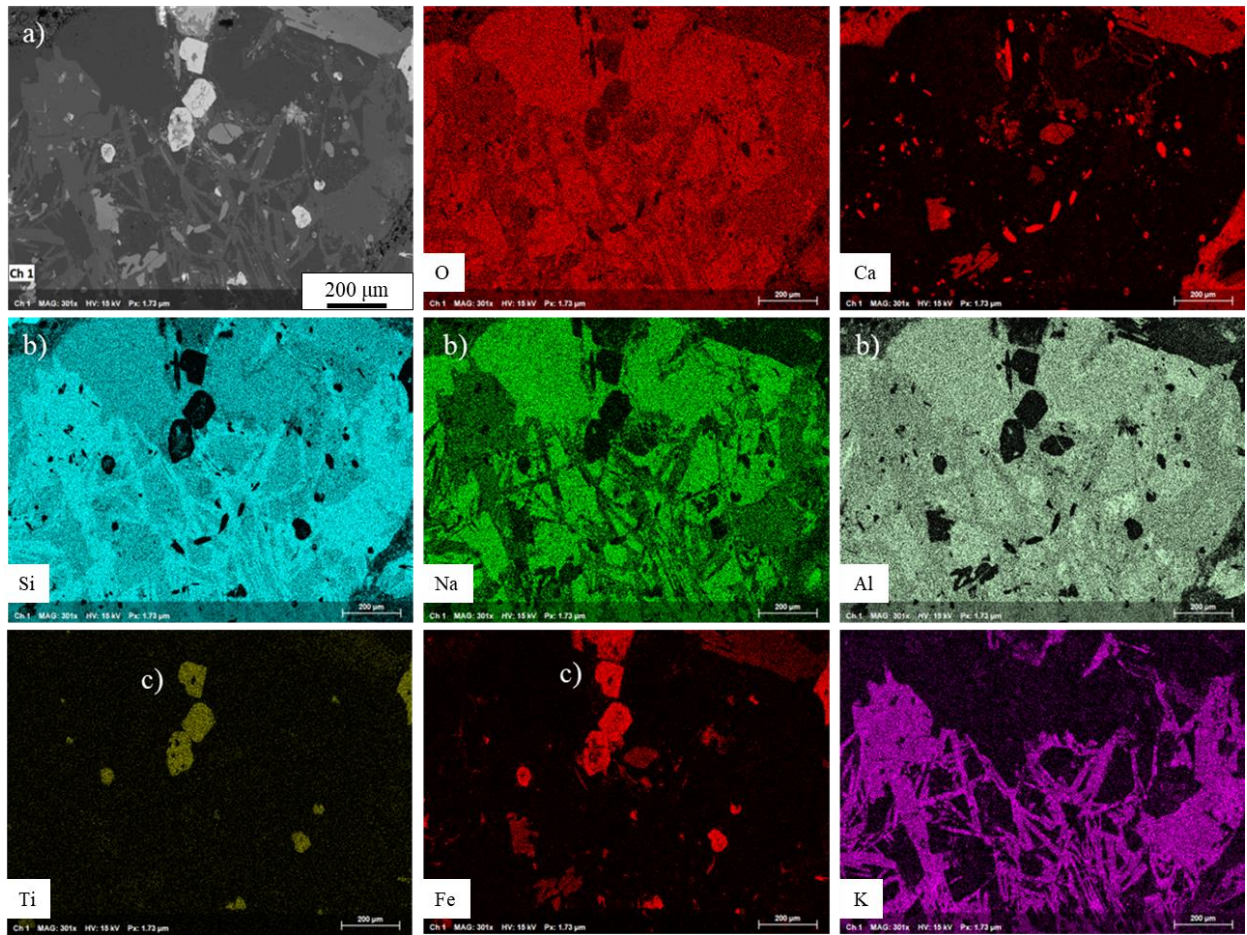


Figure S6.5. SEM images (a) and EDX maps of a section of the concrete core indicating the presence of b) mica and feldspathoidal minerals and c) Ti-Fe minerals.

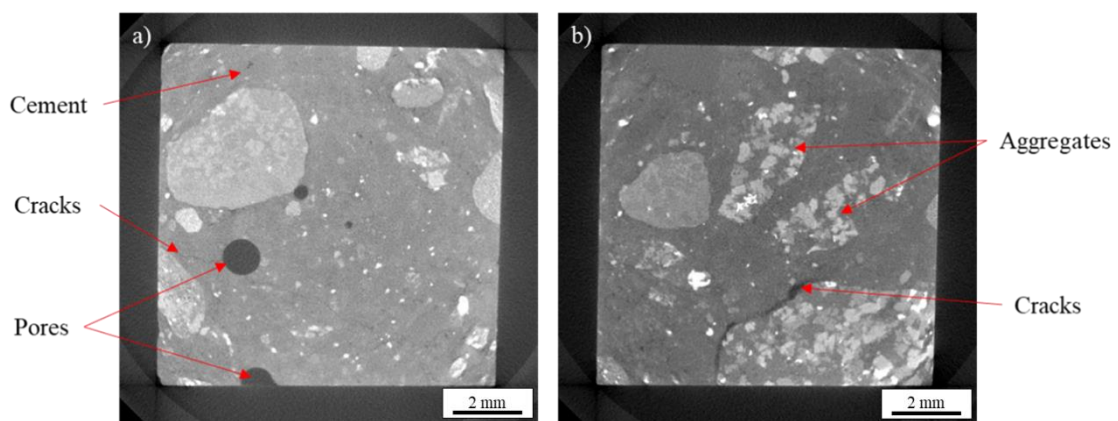


Figure S6.6. 2D grayscale X-ray micro-CT images of a section of the concrete core showing a) large pores and fine cracks and b) cracks between the aggregate and cement phases.

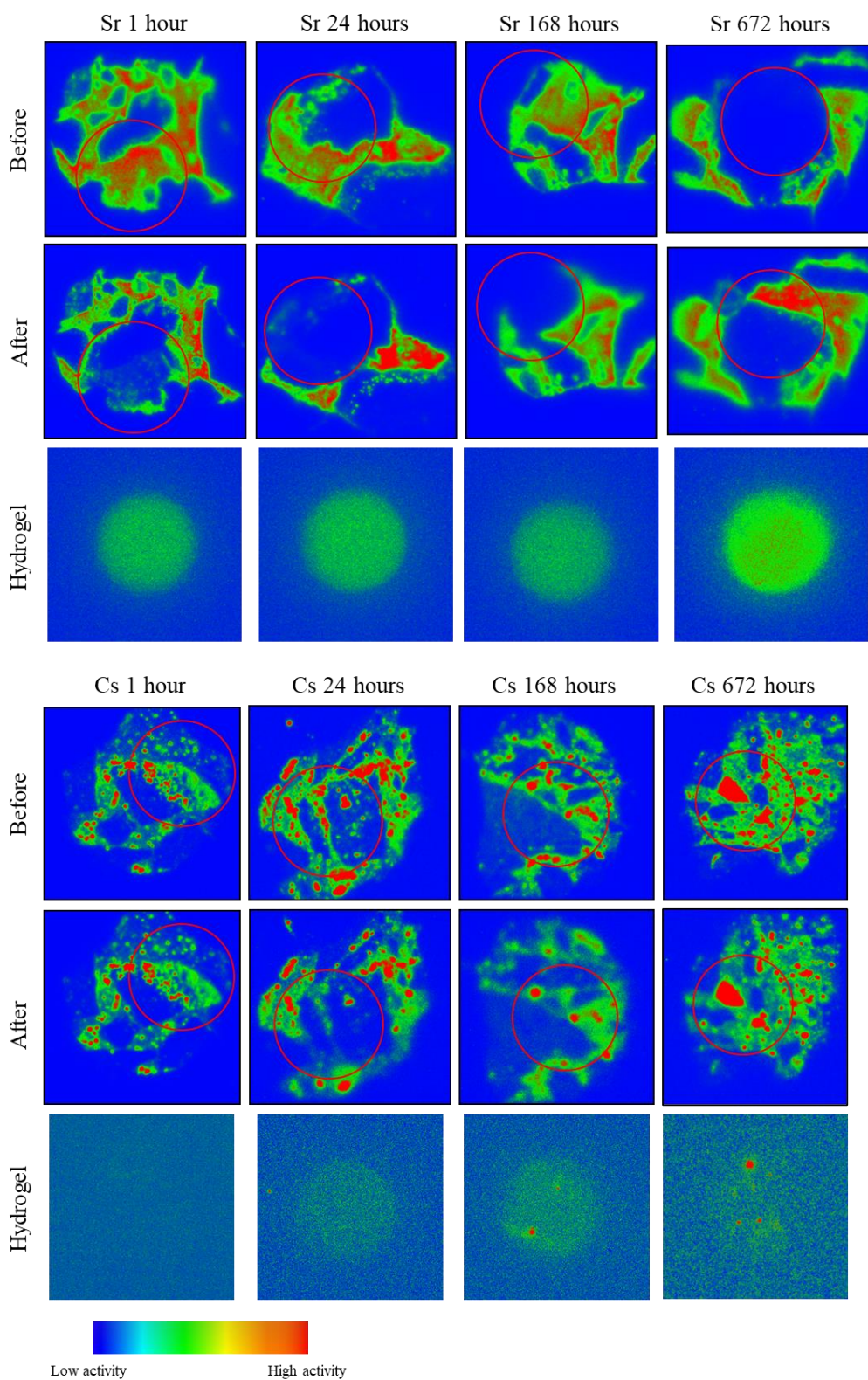


Figure S6.7. False-colour, contrast-adjusted autoradiography images of 100 Bq Sr-90 (top) and 100 Bq Cs-137 (bottom) on concrete coupons before and after H06 hydrogel application. Autoradiography images of radioactive uptake in each hydrogel is shown underneath.

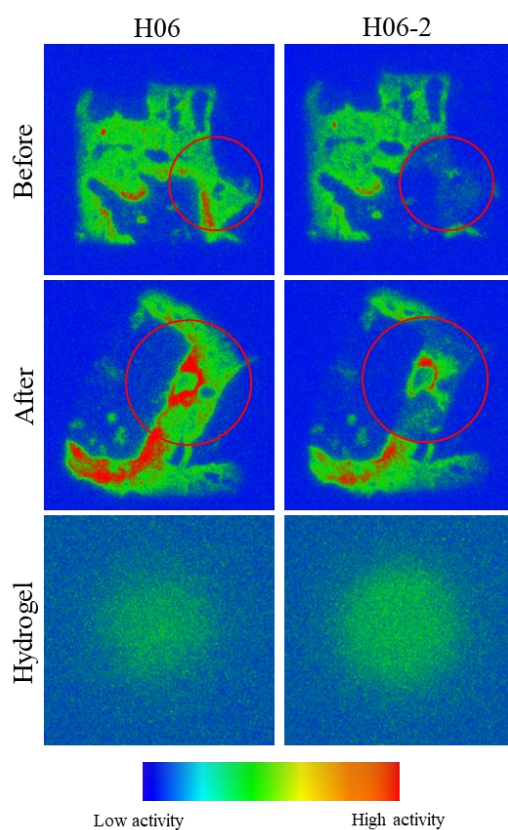


Figure S6.8. False-colour, contrast-adjusted autoradiography images of 100 Bq of mixed gamma standard on concrete coupons before and after 24 hours hydrogel application. Autoradiography images of radioactive uptake in each hydrogel is shown underneath.

Table S6.2. Hydrogel decontamination data for concrete coupons contaminated with 100 Bq Sr-90 and 100 Bq Cs-137. DF = decontamination factor, %R = % activity removed.

Radionuclide	Contact time / hours	H06		H06-2	
		DF	%R	DF	%R
Sr-90	1	1.4	26	1.3	24
	24	1.6	39	1.3	24
	168	1.4	28	1.4	30
	672	1.3	22	1.3	23
Cs-137	1	1	2.2	1	2.5
	24	1.2	15	1	6.4
	168	1.2	17	1	6.1
	672	1	4.2	1	6.2

Table S6.3. Hydrogel decontamination data for concrete coupons contaminated with 100 Bq of mixed gamma standard. DF = decontamination factor, %R = % activity removed.

Hydrogel	DF	% R	Cs-137 uptake / Bq
H06	1.2	16	0.23
H06-2	1.2	20	0.42

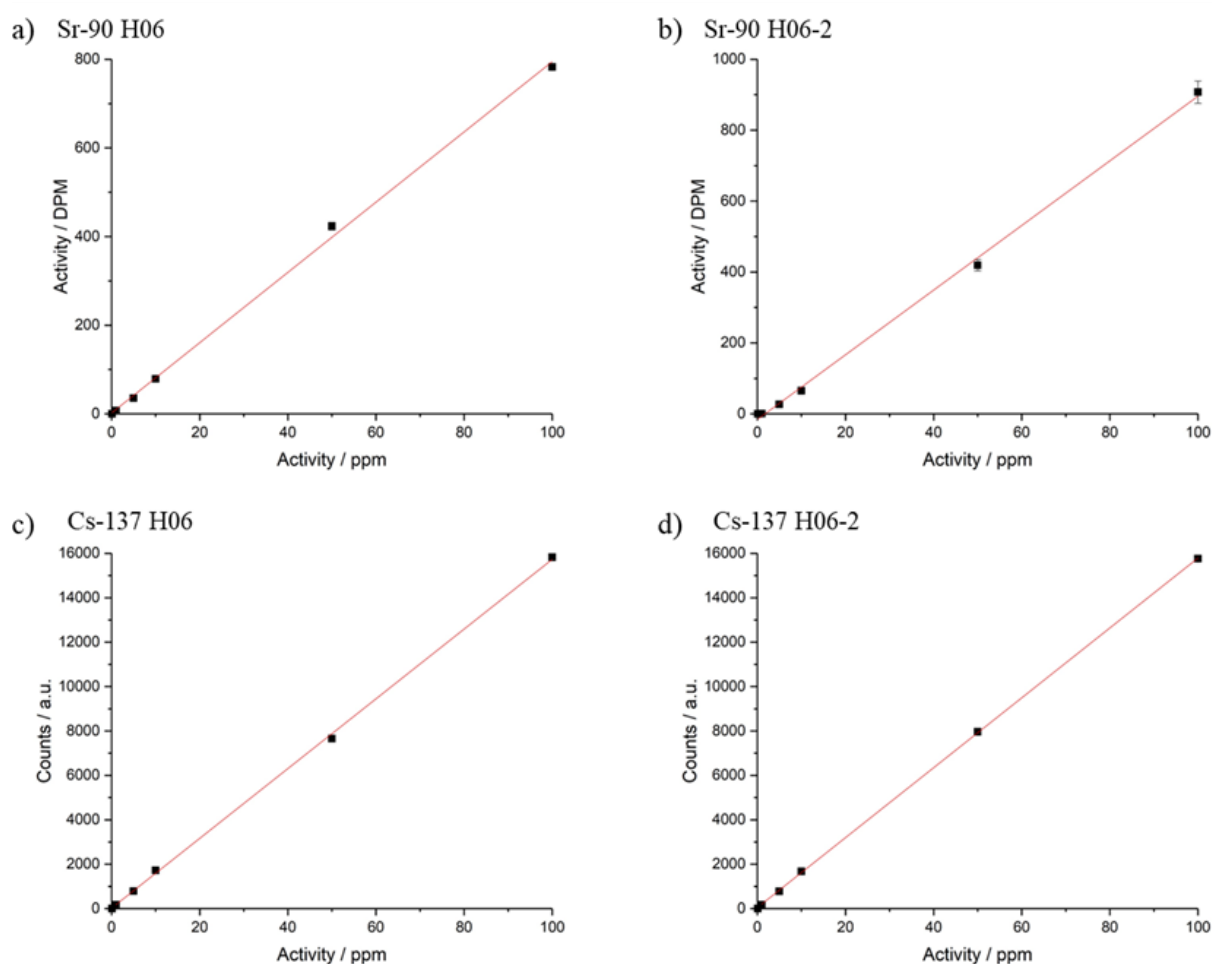


Figure S6.9. Calibration curves for a) H06 ($R^2 = 0.9991$), b) H06-2 ($R^2 = 0.9981$) Sr-90 hydrogel standards measured with LSC, c) H06 ($R^2 = 0.9996$) and d) H06-2 ($R^2 = 0.9999$) Cs-137 hydrogel standards measured with gamma spectroscopy. Error bars are estimated standard deviation from repeats.

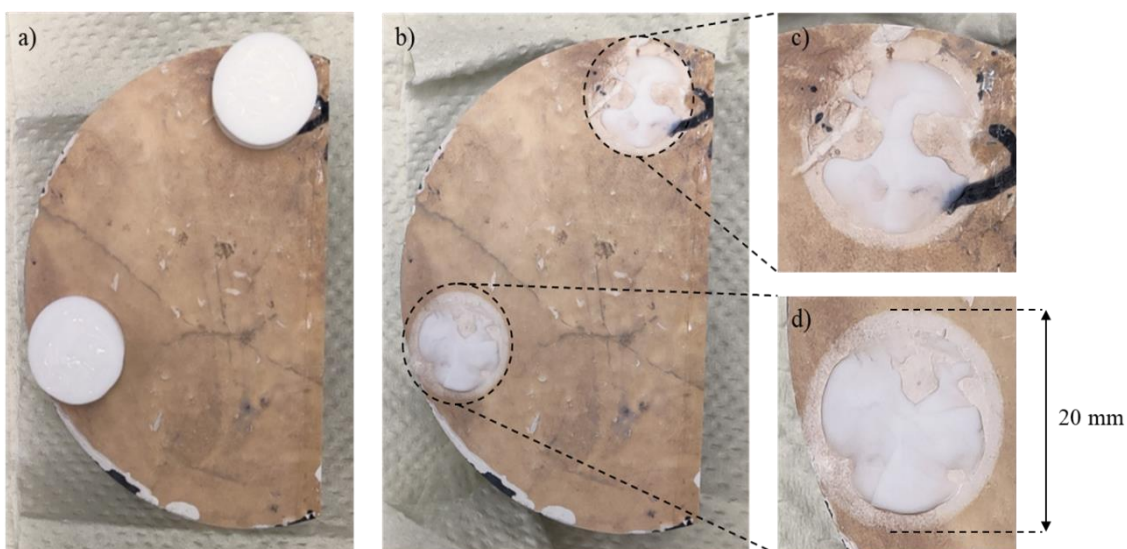


Figure S6.10. Images showing a) the hydrogel placement on the painted surface, b) the hydrogels stuck to the surface after 168 hours of contact, c and d) close ups of hydrogels in areas paint 1 and paint 2, respectively.

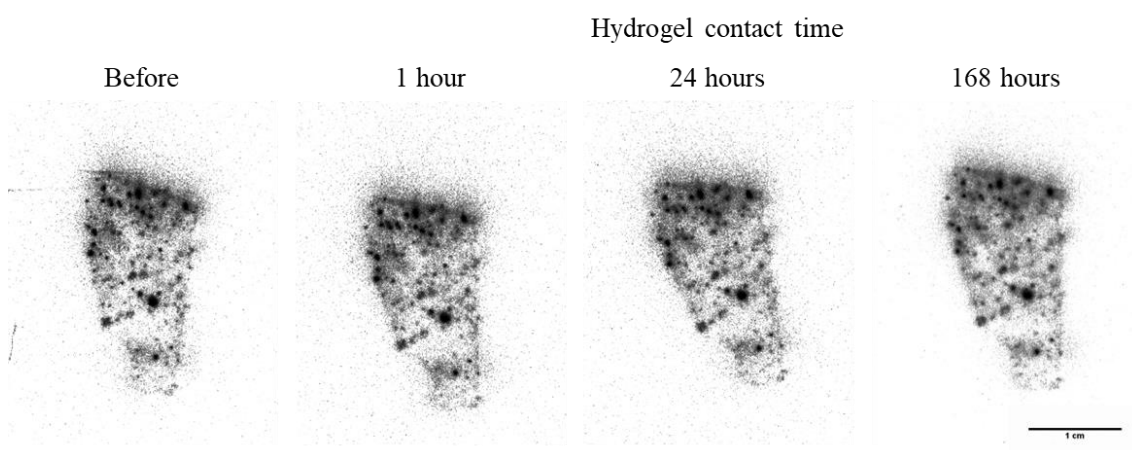


Figure S6.11. Contrast adjusted autoradiography images of the concrete bulk after consecutive decontamination experiments using H06-2 hydrogels.

7. Conclusions and Future Work

7.1. Conclusions

This PhD project has provided insight into the long-term radionuclide contamination of concrete and HDPE materials used in the Hunterston A SNF storage pond. Laboratory scale sorption studies and analysis of authentic samples were conducted to determine the extent of radionuclide contamination in aqueous alkaline conditions. The potential of LIBS analysis for standoff, *in-situ* analysis of radionuclide contaminated concrete and HDPE surfaces was assessed. The hypotheses and aims laid out in this project (Chapter 2) were tested and are summarised below.

Hypothesis 1 stated that “LIBS can be used to accurately identify and quantify Sr, Cs and Co contamination on concrete and HDPE surfaces in conditions representative of alkaline SNF pond environments”. This was explored in Chapter 4. Characteristic Sr, Cs and Co emission lines could be resolved from both the concrete and HDPE matrices and used for identification. Sr was present within the concrete matrix and could make quantification at low concentrations challenging, whereas the HDPE matrix had no interfering emissions. Despite this, LODs for each analyte were greater for the concrete matrix compared to the HDPE, presumably due to the porosity of concrete. LODs for concrete; 40 ng/cm² for Sr, 680 ng/cm² for Cs and 320 ng/cm² for Co; HDPE – 71 ng/cm² for Sr, 6000 ng/cm² for Cs and 2800 ng/cm² for Co. All three analytes could be characterised and quantified on both concrete and HDPE surfaces after exposure to individual 500 mg/L solutions in alkaline conditions with estimated uptake of Sr, Cs and Co as 0.72, 0.16 and 0.04 mg/cm² on concrete and 0.23, 0.03 and 0.25 mg/cm² on HDPE surfaces. However, when all three analytes and sample matrices were present in the same pond environment, Cs was only detectable on the concrete surfaces at lower concentrations (0.02 mg/cm²) and could not be identified within the HDPE and steel data, suggesting Cs sorption on these materials in conditions representative of SNF pond environments fell below the LOD for LIBS.

In addition, LIBS analysis of samples representative of waste discharge pipelines was able to distinguish Sr, Cs, Ru, Eu and Co emissions from the steel matrix for both biofilm and non-biofilm coated samples. Higher emission intensities for Cs and Ru were seen for the steel samples with a biofilm layer, whereas Eu was seen at greater emission concentrations for steel samples without biofilm present. The Sr and Co emission intensities remained relatively

constant for both samples. This shows promise for the use of LIBS to characterise complex radionuclide contaminated materials in waste pipelines.

Finally, depth-profiling of the samples showed Sr was primarily isolated to the surfaces; however, fluctuations in the LIBS emission intensity indicated that possible redeposition of the analytes had occurred, affecting the accuracy of the results.^{1,2} In addition, whilst initial depth-analysis of the HDPE coupons resulted in a consistent reduction of signal intensity with laser shot, the continuous firing of the laser on the sample surface resulted in melting of the plastic and incomprehensible spectra. Hence, depth-profiling with LIBS may not be a suitable technique for HDPE materials at the laser parameters used and accurate depth-profiling of heterogeneous, porous concrete materials with LIBS requires further work.

Building on the first hypothesis, the second hypothesis stated that “LIBS can be used for rapid, standoff, *in-situ* analysis of authentic radioactive contaminated materials”. This was explored in Chapters 5 and 6. LIBS could be used to measure the surface of the radioactively contaminated HDPE pontoons in Chapter 5. LIBS was able to identify the presence of Fe, Al and Mn emissions, indicating that metal oxide precipitates had formed on the pontoon surfaces and aided radionuclide contamination.³⁻⁵ In addition, Sr emission signals could be distinguished from the HDPE pontoon matrix, highlighting that LIBS can be used to characterise authentic radionuclide contaminated samples in air environments at distances of 8 cm. However, it is not possible to distinguish between stable and radio-Sr using LIBS alone. Finally, LIBS analysis of concrete coupons contaminated with 0.02 ng/cm² Bq Sr-90 and 0.03 ng/cm² Cs-137 (100 Bq each) did not identify Sr or Cs emission peaks, indicating the concentrations of radio-Sr and Cs fell below the LODs for analysis using LIBS in this project.

Hypothesis 3 stated that “hydrogels can be used to successfully decontaminate radioactivity from concrete and HDPE surfaces to minimise waste generation and aid future decommissioning tasks”. This was proven to be generally true in Chapters 5 and 6. Hydrogels were shown to successfully remove Sr-90, Cs-137 and multiple gamma radionuclides from model concrete and HDPE coupons after 1 hour of contact time. Sr-90 removal from concrete was more successful than Cs-137 over the same timescales with 26% and 2% removal, respectively. However, the opposite was seen for HDPE surfaces where 32% Sr-90 and 56% Cs-137 activity was removed after 1 hour.

Building on from the model coupons, hydrogels were able to remove both fission products and actinides simultaneously from the authentic Hunterston A samples. They removed 40-60% of activity from higher activity areas on the HDPE pontoon surfaces after 1 hour of contact time. Consecutive application of hydrogels showed they could be used to remove additional contamination with up to 80-90% removal of activity after four applications over a total of 872 hours. Hydrogels were able to remove radionuclide contamination from the painted surface of the concrete core as described in Chapter 6, with an average combined uptake of 530 ± 40 Bq Cs-137 and 1000 ± 60 Bq Sr-90 over three consecutive hydrogel applications. Removal of Am-241 was identified in the first two hydrogel applications and not in the final hydrogel, indicating complete Am removal may have taken place within the decontamination area. Whilst the hydrogels were able to remove radioactivity from the HDPE and painted surfaces, hydrogels were unable to remove significant activity from the aged concrete bulk. Quantification of the hydrogel after three consecutive applications determined 9 Bq Sr-90 and 8 Bq Cs-137 had been removed. Autoradiography showed little to no change in activity had occurred on the concrete surface, indicating the hydrogels used in this project could not be used to remove long-term radionuclide contamination from the bulk concrete.

The final objective for this project was to determine the effect of long-term radionuclide contamination on aged concrete and HDPE materials found in SNF storage pond facilities. This was explored in Chapters 5 and 6 using unique, authentic samples obtained from the decommissioned Hunterston A SNF storage pond. Radiometric analysis determined that activity on the painted concrete core was predominantly due to Sr-90, Cs-137, Am-241, Pu-238-241 and Eu-152. Activity was primarily isolated within the protective, painted surface; however, heterogeneous penetration of radionuclides into the bulk concrete was identified down to 5-10 mm, particularly along grain boundaries between the cement and aggregate phases. Sequential extraction of the concrete indicated that Sr was isolated within the cement phase, likely through adsorption and ion-exchange with CSH layers.^{6,7} Cesium was strongly bound to the concrete, determined to be silicate or gabbro aggregates, and could only be partially leached with strong acids.

Analysis of the six HDPE pontoon samples identified Sr-90, Cs-137, Am-241 and traces of Eu-152 activity at varying activities on the sample surfaces. The activity was heterogeneously spread on the sample surfaces in areas relating to the position of the samples on the pontoon structure. Increased radionuclide contamination was identified in areas of surface damage and

where build-up of chemical precipitates, such as Fe, Al and Mn oxides, may have occurred due to corrosion of the SNF containers and the alkaline aqueous conditions of the pond.⁸ Analysis of the pontoon cross-section identified potential diffusion of activity into the bulk and showed that initial jet-water decontamination methods were unsuccessful in removing activity from the pontoons during decommissioning.

7.2. Future Work

Carrying out long-term experiments to replicate phenomena occurring in nuclear reactor, reprocessing or storage environments is extremely challenging and virtually impossible over the timescale of a PhD project. The unique, authentic samples characterised in this project have provided invaluable insight into the interactions of radionuclides with concrete and HDPE surfaces in alkaline conditions, but many research avenues remain to be pursued.

Unfortunately, due to COVID-19, many of the experiments initially planned for this project could not be carried out. In particular, taking concrete and HDPE samples down to the Diamond Lightsource in Oxford for XRF/XAS beamtime analysis. Analysis of the contaminated painted surface using micro-XRF analysis was done by Bower *et al.*; however, the samples presented in this work contain higher activities and may have allowed for analysis of transuranic species, as well as fission products.⁹ In addition, analysis of the concrete surface below the protective layers could be conducted to further assess the binding mechanisms taking place within the bulk concrete.¹⁰ Initial assessment of the concrete cross-section identified radionuclide penetration into the concrete. As Cs-137 was the only radionuclide able to be monitored over increasing penetration depth further studies would be needed to determine how the different radionuclides may diffuse into the bulk concrete and to what extent. Tracer experiments could be used to determine diffusion pathways in the concrete and help identify new protective layers to prevent this.¹¹

Analysis of the HDPE pontoons showed radionuclide contamination was enhanced by the presence of chemical precipitates and possibly by biofilms. As this project did not focus on the microbiology of the SNF pond environment, future studies to assess the accumulation of organic and biological materials in aqueous, alkaline environments and the mechanisms in which radionuclides interact with these surfaces would greatly enhance our understanding of radionuclide contamination of pond structures. Studies using modified Robbins devices could

be used to model the behaviour of biofilm and chemical precipitate formation and subsequent radionuclide build-up in these phases on HDPE and painted surfaces in conditions representative of alkaline waste storage environments.^{12,13}

This project highlighted the use of hydrogels for the removal of fission product and actinide contamination on concrete and HDPE samples, whilst producing minimal secondary waste products. Minimising the production of nuclear waste produced during decommissioning operations is one of the key priorities of the Nuclear Decommissioning Authority (NDA) and hydrogels could help achieve this.^{14,15} Further research into improving the hydrogel composition to achieve greater decontamination factors on HDPE and concrete surfaces in shorter time frames would be beneficial. In addition, assessing the ability of hydrogels to remove contamination from within the sample bulk would make for an interesting future project.

Limits of detection (LODs) for LIBS measurement of Sr, Cs and Co on HDPE and concrete surfaces are in the range 40-6000 ng/cm². These mass concentrations correspond to activities of 0.2-23700 MBq/cm² which suggests LIBS will not be competitive with radiometric techniques. However, if LIBS could be used to detect longer-lived radionuclides, such as actinides, at concentrations of tens of ng/cm² then this would correspond to much lower activities (~20 Bq/cm² for Pu-239) and LIBS would be very attractive. Future work to determine the LODs of actinides such as Pu and Am on HDPE and concrete surfaces would be beneficial to determine the applicability of LIBS.

In addition, whilst LIBS analysis of Sr, Cs and Co contamination on steel has been widely researched, the identification of Ru and Eu on complex model waste pipeline samples highlights other avenues worth exploring.^{1,16-18} Further work to determine the LODs for these analytes on stainless steel and biofilm samples using LIBS could help provide quantitative analysis of metals uptake in these systems. In addition, research into the analysis of these materials using handheld-LIBS devices or probes could help determine whether these devices can be deployed for characterisation of real discharge pipelines used in the nuclear industry.¹⁹⁻

7.3. References

- 1 A. Lang, D. Engelberg, N. T. Smith, D. Trivedi, O. Horsfall, A. Banford, P. A. Martin, P. Coffey, W. R. Bower, C. Walther, M. Weiß, H. Bosco, A. Jenkins and G. T. W. Law, Analysis of contaminated nuclear plant steel by laser-induced breakdown spectroscopy, *J. Hazard. Mater.*, 2018, **345**, 114–122.
- 2 S. Singh, M. Argument, Y. Y. Tsui and R. Fedosejevs, Effect of ambient air pressure on debris redeposition during laser ablation of glass, *J. Appl. Phys.*, 2005, **98**, 1–8.
- 3 Y. Cao, M. Zhao, X. Ma, Y. Song, S. Zuo, H. Li and W. Deng, A critical review on the interactions of microplastics with heavy metals: mechanism and their combined effect on organisms and humans, *Sci. Total Environ.*, 2021, **788**, 147620.
- 4 S. Musić and M. Ristić, Adsorption of trace elements or radionuclides on hydrous iron oxides, *J. Radioanal. Nucl. Chem. Artic.*, 1988, **120**, 289–304.
- 5 J. L. Means, D. A. Crerar, M. P. Borcsik and J. O. Duguid, Adsorption of Co and selected actinides by Mn and Fe oxides in soils and sediments, *Geochim. Cosmochim. Acta*, 1978, **42**, 1763–1773.
- 6 E. Wieland, J. Tits, D. Kunz and R. Dähn, Strontium uptake by cementitious materials, *Environ. Sci. Technol.*, 2008, **42**, 403–409.
- 7 J. Tits, E. Wieland, C. J. Müller, C. Landesman and M. H. Bradbury, Strontium binding by calcium silicate hydrates, *J. Colloid Interface Sci.*, 2006, **300**, 78–87.
- 8 C. Bertoncini, in *Proceedings of the International Conference on Environmental Remediation and Radioactive Waste Management, ICEM*, 2013, pp. 1–11.
- 9 W. R. Bower, K. Morris, J. F. W. Mosselmans, O. R. Thompson, A. W. Banford, K. Law and R. A. D. Patrick, Characterising legacy spent nuclear fuel pond materials using microfocus X-ray absorption spectroscopy, *J. Hazard. Mater.*, 2016, **317**, 97–107.
- 10 A. M. Scheidegger, M. Vespa, D. Grolimund, E. Wieland, M. Harfouche, I. Bonhoure and R. Dähn, The use of (micro)-X-ray absorption spectroscopy in cement research, *Waste Manag.*, 2006, **26**, 699–705.
- 11 M. C. Chaparro, M. W. Saaltink, J. M. Soler, L. J. Slooten and U. K. Mäder, Modelling

- of matrix diffusion in a tracer test in concrete, *Transp. Porous Media*, 2016, **111**, 27–40.
- 12 A. J. McBain, in *Advances in Applied Microbiology*, Elsevier Inc., 2009, vol. 69, pp. 99–132.
 - 13 T. Coenye, K. De Prijck, B. De Wever and H. J. Nelis, Use of the modified Robbins device to study the in vitro biofilm removal efficacy of NitrAdineTM, a novel disinfecting formula for the maintenance of oral medical devices, *J. Appl. Microbiol.*, 2008, **105**, 733–740.
 - 14 Jacobs UK Ltd and AFRY Solutions UK Ltd, *2022 UK Radioactive Waste Inventory*, 2022.
 - 15 Nuclear Decommissioning Authority, Nuclear Decommissioning Authority strategy effective from March 2021, <https://www.gov.uk/government/publications/nuclear-decommissioning-authority-strategy-effective-from-march-2021/nuclear-decommissioning-authority-strategy-effective-from-march-2021#integrated-waste-management>.
 - 16 Y. Xie, J. Wang, Y. Hu, J. Zhang, Y. Gao, H. Li and S. Wang, Laser-induced breakdown spectroscopy for contamination analysis of Sr and Cs on 316L stainless steels in alkaline environment for spent nuclear fuel storage, *Appl. Surf. Sci.*, 2021, **566**, 150709.
 - 17 Y. Xie, J. Wang, Y. Hu, J. Zhang, Q. Zhang, M. Men, S. Wang, Z. Li, G. Liu and A. Mi, Corrosion and contamination of 316L stainless steel in simulated HNO₃-based spent nuclear fuel reprocessing environments with cesium and strontium, *Ind. Eng. Chem. Res.*, 2022, **61**, 9342–9355.
 - 18 V. Sturm, L. Peter and R. Noll, Steel analysis with laser-induced breakdown spectrometry in the vacuum ultraviolet, *Appl. Spectrosc.*, 2000, **54**, 1275–1278.
 - 19 B. J. Marquardt, S. R. Goode and S. Michael Angel, In-situ determination of lead in paint by laser-induced breakdown spectroscopy using a fiber-optic probe, *Anal. Chem.*, 1996, **68**, 977–981.
 - 20 I. Gaona, J. Serrano, J. Moros and J. J. Laserna, Evaluation of laser-induced breakdown

spectroscopy analysis potential for addressing radiological threats from a distance, *Spectrochim. Acta Part B*, 2014, **96**, 12–20.

- 21 B. T. Manard, E. M. Wylie and S. P. Willson, Analysis of rare earth elements in uranium using handheld laser-induced breakdown spectroscopy (HH-LIBS), *Appl. Spectrosc.*, 2018, **72**, 1653–1660.

8. Conference presentations, posters and awards

Awards:

- 2nd place in the Young Researchers Award at the Royal Society of Chemistry Radiochemistry Young Researchers Conference (July 2021)
- Exceptional abstract submitted to the Division of Nuclear Chemistry and Technology at ACS (March 2022)

Conference posters:

- PhLAME Workshop (October 2018)
- DEES Postgraduate Research Conference, Manchester, UK (November 2019)
- American Chemical Society Spring Conference, San Diego, USA (March 2022)

Conference oral presentations:

- PhLAME Workshop (October 2018, February 2019, February 2020, invited)
- NNL Decontamination Theme Seminar (November 2021, March 2023, invited)
- Sellafield Ltd Centre of Excellence Decontamination and Decommissioning Seminar (April 2022, invited)
- Dalton Nuclear Institute Seminar Series (August 2020, invited)
- DEES Postgraduate Research Conference, Manchester, UK (November 2019, accepted)
- Royal Society of Chemistry Radiochemistry Young Researchers Conference (July 2021, accepted)
- American Chemical Society Spring Conference, San Diego, USA (March 2022, accepted)
- Royal Society of Chemistry Spectroscopic Methods in Radiochemistry Research, Manchester, UK (July 2022, accepted)

- Environmental Radiochemical Analysis Conference, York, UK (September 2022, accepted)